



City Research Online

City, University of London Institutional Repository

Citation: Mathivanan, Sathya Narayanan (2019). Finite element characterisation of graphene-silicon hybrid waveguides. (Unpublished Doctoral thesis, City, University of London)

This is the accepted version of the paper.

This version of the publication may differ from the final published version.

Permanent repository link: <https://openaccess.city.ac.uk/id/eprint/22237/>

Link to published version:

Copyright: City Research Online aims to make research outputs of City, University of London available to a wider audience. Copyright and Moral Rights remain with the author(s) and/or copyright holders. URLs from City Research Online may be freely distributed and linked to.

Reuse: Copies of full items can be used for personal research or study, educational, or not-for-profit purposes without prior permission or charge. Provided that the authors, title and full bibliographic details are credited, a hyperlink and/or URL is given for the original metadata page and the content is not changed in any way.

City Research Online:

<http://openaccess.city.ac.uk/>

publications@city.ac.uk

Finite Element Characterisation of Graphene–Silicon Hybrid Waveguides



Sathya Narayanan Mathivanan

Department of Electrical and Electronic Engineering
School of Mathematics, Computer Science and Engineering
City, University of London

Submitted in partial fulfilment for the requirements of the degree of
Doctor of Philosophy

May 2019

Statement of Originality

I, Sathya Narayanan Mathivanan, confirm that the research included within this thesis is my own work or that where it has been carried out in collaboration with, or supported by others, that this is duly acknowledged below and my contribution indicated. Previously published material is also acknowledged below.

I attest that I have exercised reasonable care to ensure that the work is original, and does not to the best of my knowledge break any UK law, infringe any third party's copyright or other Intellectual Property Right, or contain any confidential material.

I accept that the College has the right to use plagiarism detection software to check the electronic version of the thesis.

I confirm that this thesis has not been previously submitted for the award of a degree by this or any other university.

The copyright of this thesis rests with the author and no quotation from it or information derived from it may be published without the prior written consent of the author.

Sathya Narayanan Mathivanan

May 2019

*I dedicate this thesis to my beloved dearest wife **Shreekarthika** and lovely
sons **Harinandh** and **Shivnandh**.*

Acknowledgements

First and foremost, I thank my supervisor eminent Professor B.M.A. Rahman for offering me a chance to pursue my doctoral research under his guidance. I express my sincere gratitude to my Prof. Rahman for his unwavering support during my PhD study, for his patience and motivation throughout my years with him. His guidance immensely deepened my understanding in my research area and have taught me how to identify, approach and resolve a research problem.

I thank Prof. Ken Grattan for his valuable guidance during my transfer process. My sincere thanks goes to Dr Arti Agrawal for her support and motivation especially during the OWTNM-2015 conference. My humble thanks goes to Dr Kejalakshmy for guiding me in understanding and in using the complex codes for modelling optical waveguides.

I thank Dr Ferdinand Katsriku and Dr Jonanthan Loo for their valuable guidance and recommendations. My heartfelt thanks to City, University of London for providing a place in their PhD programme which has greatly enhanced my career prospects. I am forever indebted to City, University of London, for their excellent facilities and financial support offered throughout my course.

I thank the supportive services provided by the research administrators and the visa compliance team. I thank my labmates for their stimulating discussions and very useful insights.

I am ever grateful to my dear friends Dr Yuvaraj, Dr Viswanathan and Dr Ramesh for supporting, motivating and inspiring me since my undergraduate degree.

Last but not least, I express my humblest sincerest heartfelt thanks to my devoted parents and in-laws, my beloved wife Shreekarthika Narayanan and lovely sons Harinandh Narayanan and Shivnandh Narayanan and my sweet sisters Viji and Raji and their families, for their trust on me even throughout the various challenges and struggles that we faced and supported me with their heart and soul that made me achieve my dream doctoral degree.

**‘One thing I have learned in a long life: that all our science,
measured against reality, is primitive and childlike - and yet it is
the most precious thing we have.’**

Albert Einstein (1879–1955)

**‘It doesn’t matter how beautiful your theory is, it doesn’t
matter how smart you are. If it doesn’t agree with experiment,
it’s wrong.’**

Richard P. Feynman (1918–1988)

Abstract

Recent years have witnessed remarkable progress in nanoscience and nonlinear optics research, paving entry of 2D materials such as graphene, phosphorene, silicene, and so on. Graphene has extraordinary optical, electrical, mechanical and thermal properties. The uniqueness of graphene lies in its modulation depth ($> 90\%$) and signal attenuation ($< 5\%$), achieved by controlling its Fermi level through gate voltage. It is envisioned that graphene-based modulators would be the ultimate high-speed modulator of the future, performing at speeds up to 10 times faster than existing ones.

The accuracy of such solutions lies in determining the permittivity (ϵ_r) of materials used. Graphene possesses complex conductivity ($\sigma(\omega) = \sigma_1 + j\sigma_2$) and permittivity ($\epsilon(\omega) = \epsilon_1 + j\epsilon_2$). Using Kubo formalism, we derived an analytical method for finding the conductivity of graphene ($\sigma_{g,\text{interband}} + \sigma_{g,\text{intra band}}$) and then the complex permittivity (ϵ_g). The values of $\epsilon(\omega)$ are plotted as a function of chemical potential (μ , eV), wavelength (λ , nm) and thickness of graphene layers (t_g).

Benchmarking was carried out using two solvers *viz.*, complex and perturbation to ascertain the suitability of the method. Effective mode index (n_{eff}) and absorption (α) are calculated for quasi-TE and quasi-TM guided modes of the waveguide. We found that the waveguide performance parameters are highly influenced by the position of graphene layers in the waveguide and the thickness and type of dielectric material that encapsulate the graphene layers. Two positions *viz.*, graphene-as-top layer and graphene-as-slot layer were analysed. Three dielectric materials, *h*BN, Al_2O_3 and HfO_2 , classified as low-, high- and very-high index, respectively, are chosen. For operation wavelength range (1.3–1.7 μm) and for varying dielectric layer thickness from 5 to 70 nm, the plots for n_{eff} and α (dB/ μm) are obtained.

Performance parameters such as extinction ratio (ER) and insertion loss (IL) were calculated for varying dielectric thickness (5–70 nm). ER and IL are achieved within the ranges 20–70 and 3–4 dB/ μm , respectively. We inferred that to enhance the modal properties (n_{eff} and α), graphene-as-top layer waveguide can have a combination of very high-index ($\epsilon_r = 25$) dielectric material (thickness $> 15 - 20$ nm) encapsulating graphene whereas a very high-index dielectric with reduced thickness ($< 5 - 10$ nm) encapsulating graphene is suitable for graphene-as-slot layer waveguide.

Contents

1	Introduction	1
1.1	Photonic materials	3
1.1.1	Photonic crystals	5
1.1.2	Current trends	6
1.2	Fundamentals	7
1.2.1	Light waves	7
1.2.2	n and ε	7
1.2.2.1	Mode Effective Index	8
1.2.2.2	Optical Absorption	8
1.2.3	Wave mechanics	8
1.2.4	Maxwell's equations	10
1.3	Waveguides	12
1.3.1	Silicon-on-Insulator	13
1.3.2	Waveguide Fabrication	15
1.3.2.1	Thin film deposition	15
1.3.2.2	Photolithography	19
1.3.2.3	Etching	21
1.4	Electro-absorption modulators	22
1.4.1	Modulation Mechanism	23
1.5	Numerical methods	23
1.6	Objectives of the thesis	25
1.7	Structure of the thesis	25
2	Finite Element Characterization of Waveguides	28
2.1	Introduction	28
2.2	Light-matter interaction	28
2.2.1	Optical modulators	30
2.2.1.1	Operation Principle	31
2.3	Theory of waveguides	32
2.3.1	Planar waveguides	34
2.3.2	Dielectric slab waveguide	34
2.3.3	Rib waveguide	35
2.3.3.1	Guided modes	35

2.3.3.2	Plasmonic waveguides	37
2.3.4	General solution to Maxwell's equations	39
2.3.4.1	Basic Equation	40
2.3.4.2	Analytical solution	40
2.4	Finite Element Method	43
2.4.1	Definition	46
2.4.2	Basic concepts	47
2.4.3	Implementation of FEM	50
2.4.4	Element Equations	52
2.4.5	Line Elements	52
2.4.6	Triangular Elements	54
2.4.7	Vector Field Formulation	56
2.4.8	The Matrix Equation	57
2.4.9	Shape Functions	58
2.4.10	Element Assembly	61
2.5	Summary	63
3	Graphene Photonics	64
3.1	Introduction	64
3.2	Physical Properties	66
3.2.1	Carbon Bonds	68
3.2.2	Crystal Structure	71
3.2.3	Mono-, bi- and trilayers	74
3.3	Electronic Band Structure	76
3.3.1	Tight Binding Model	76
3.4	Optical Conductivity	81
3.5	Dielectric Constants	84
3.5.1	Method	85
3.5.2	Results and Discussion	88
3.6	Plasmonics	96
4	Benchmarking Graphene-based Optical Waveguides	99
4.1	Introduction	99
4.2	Benchmarking	102
4.2.1	Study 1: Graphene-based Rib Waveguide	103
4.2.2	Study 2: Graphene-based Slot Waveguides	109
4.2.3	Study 3: Top Layer Graphene Waveguide	115
4.3	Conclusion	118
5	Characterization of Graphene–Silicon Hybrid Waveguides	120
5.1	Introduction	120
5.2	Characterisation of Optical Waveguides	121
5.2.1	Silicon Photonic Waveguides	122

5.2.2	Top- <i>versus</i> Slot-layered Graphene Waveguides	123
5.3	Characterisation of Slot Waveguides with Bilayer Graphene	127
5.3.1	Dielectric-encapsulated bilayer graphene waveguide	131
5.3.2	Graphene-on-Graphene slot waveguide	133
5.3.3	Summary	135
5.4	Characterisation of Trilayer Graphene-based Waveguides	137
5.4.1	Top- and slot-graphene waveguides	138
5.4.1.1	Top layer graphene	139
5.4.1.2	Slot layer graphene	140
5.4.1.3	Summary	141
5.4.2	ABA and ABC Stack Waveguides	142
5.4.2.1	Proposed waveguide designs	144
5.4.2.2	Results and Discussion	145
5.5	Summary	152
6	Conclusions and Suggestions for Future Research	153
6.1	Conclusions	153
6.2	Suggestions for Future Research	155
A	To calculate complex $\varepsilon(\omega)$ of graphene	157
	Bibliography	159

List of Figures

1.1	Propagation of a plane electromagnetic wave.	2
1.2	Energy band separation showing overlapping valence band (VB) and conduction band (CB) for metal and rest separated with a band gap energy, E_g	3
1.3	Photonic crystals of (a) one, (b) two and (c) three dimensions. Different lines show variation in dielectric constants ($\epsilon_1, \epsilon_2, \epsilon_3$) within the crystal.	5
1.4	The continuous spectrum of an electromagnetic spectrum.	7
1.5	Light ray travelling from medium 1 to medium 2. n_1 and n_2 , refractive indices of media; k_i, k_r , and k_t , incident, reflected and transmitted light rays, respectively.	8
1.6	A 1D wave function: a, $f(x)$; b, $f(x - 1)$; c, $f(x - 2)$; and d, $f(x - 3)$	9
1.7	Plot showing $\sin(\omega t)$ and $\cos(\omega t)$	10
1.8	Principle of refraction (a) and total internal reflection (b) of light rays in medium 1 and medium 2 of different refractive indices n_1 and n_2 , respectively.	13
1.9	Schematic of a SOI waveguide. Layers 1, 2 and 3 denote Si substrate, SiO ₂ and crystalline Si, respectively.	14
1.10	Common types of channel waveguides: (a) rib, (b) strip and (c) buried. Refractive indices n_1, n_2 and n_3 denote substrate, core and cladding (air), respectively, in each of the waveguides.	14
1.11	Electron micrograph of a fabricated Si rib waveguide.	15
1.12	Schematic of a plasma generation chamber: S, sheath; e_1 and e_2 , electrodes; p, plasma; AC, power.	16
1.13	Schematic of sputtering technique: (1) anode, (2) cathode, (3) plasma, (4) shutter, (5) substrate, (6) target and (7) diffusion.	17
1.14	Schematic of CVD process: (1) main gas flow region, (2) transport to surface, (3) gas phase reactions, (4) adsorption of film precursor, (5) nucleation and island growth, (6) surface diffusion, (7) redesorption of film precursor, (8) desorption of volatile surface reaction products and (9) step growth.	17
1.15	Schematic of oxidation process. Dotted lines ($a_1 \cdots a_2$) denote the Si-SiO ₂ interface after formation.	19
1.16	Steps involved in photolithography technique. (a) SoI wafer coated with thin polymer (photoresist), (b) exposure of UV light on the wafer covered by a mask and (c) waveguide pattern obtained after hard bake.	20

1.17	Schematic of chemical etching process: 1, silicon; 2, SiO ₂ ; 3, photoresist. (a) Unexposed photoresist after developing stage. (b) Oxide layer is etched in a HF + NH ₄ F solution. (c) Removal of photoresist with H ₂ SO ₄	21
1.18	Schematic of a typical electro-absorption modulator.	22
2.1	Number of papers published each year in a few relevant technical journals: (a) <i>Electronics Letters</i> ; (b) <i>Applied Optics</i> ; (c) <i>Electronic Letters</i> and <i>Ap- plied Optics</i> and <i>Bell Systems Technical Journal</i>	29
2.2	(a) Classical representation of a particle and field. (b) Corresponding quan- tum representation. In (b), dots mean the probability distribution of par- ticle position; field ϕ at x , $\phi(x)$	30
2.3	Incident (\mathbf{E}_i), reflected (\mathbf{E}_r) and transmitted rays (\mathbf{E}_t) at a plane interface between two dielectric media.	33
2.4	A planar waveguide. The refractive indices of guide, upper cladding, and substrate are denoted by n_g , n_c and n_s , respectively.	34
2.5	Ray of light in a dielectric slab waveguide.	35
2.6	A SOI rib waveguide with R_1 (air, $n = 1$), R_2 (Si, $n = 3.477$) and R_3 (SiO ₂ , $n = 1.444$). Here $h=rH$, for $r < 0.5$. For computational purposes broken lines denote air region which covers all around the waveguide.	36
2.7	A hybrid plasmonic waveguide: (1) metal; (2) dielectric; (3) silicon; (4) SiO ₂	37
2.8	Surface plasmons originating in a metal–dielectric interface. ε_1 denotes the real part of dielectric constant.	38
2.9	Coupling scheme of waveguide and plasmonic modes in a metal–dielectric interface.	38
2.10	Triangular elements used in FEM to cover chosen domain: (a) one element; (b) two elements with a common boundary.	45
2.11	A linear Lagrange triangle.	47
2.12	Quartic Hermite and quintic Argyris triangles.	47
2.13	Rectangular grid: domain division; (•) a node.	48
2.14	Mesh formation in FEM.	49
2.15	First (a) and second (b) order triangular elements.	54
2.16	A typical element.	58
3.1	(a) Fibre-optic cables transmitting information through light waves. (b) Map showing countries connected by undersea fibre optic cables.	65
3.2	Prominent allotropes of carbon: (a) diamond, (b) fullerene, (c) carbon nan- otube and (d) graphite. Dotted lines in (d) represent the van der Waals bonding (π bonds).	67
3.3	Publications on graphene.	67
3.4	Monolayer graphene: basis of all graphitic forms. (a) 0D bucky balls; (b) 1D nanotubes; and (c) 3D graphite.	68
3.5	Monolayer of graphene: (a) HRTEM image; (b) TEM image by Berkeleys TEAM05. C=C bond distance: 0.14 nm.	69

3.6	Depiction of electronic orbitals of ground state and excited state carbon atom.	69
3.7	Artistic imagination (NanoSmiths, 2018) showing strength of graphene monolayer (0.335 nm thick). A layer of graphene has a breaking strength of 42 N/m (intrinsic strength of a defect-free sheet) – 100 times more than that of the strongest hypothetical steel film of the same thickness.	70
3.8	Two atom basis superimposed forming a hexagonal lattice. Two carbon atoms (A and B) in each unit cell are shown in different colours (blue and red).	71
3.9	Honeycomb lattice of graphene layer: (a) lattice structure depicting Bravais lattice; (b) reciprocal lattice of the triangular lattice; (c) atoms (A and B) with nearest neighbours; (d) directions for reference to nearest neighbours.	72
3.10	(a) First Brillouin zone. (b) Dirac cone.	73
3.11	Bilayer stacking of graphene layers: (a) upper layer translated by δ_1 with respect to the lower – the A' sites on top of B sites; (b) upper layer translated by $-\delta_1$ with respect to the lower – the B' sites on top of A sites.	74
3.12	Trilayer graphene stack: (a) ABA, (b) ABC, (c) and (d) next layer moved one C–C bond distance, 0.142 nm.	75
3.13	Representation of tight binding model in graphene lattice.	76
3.14	Representation of electronic band structure in graphene. (a) Dirac cone; (b) cones at Dirac points K and K' ; (c) Brillouin zone in a graphene layer; and (d) unit cell of two-atom basis.	80
3.15	Graphene electron spectrum (Dirac cones) at K points of the Brillouin zone.	81
3.16	(a) Optical conductivity <i>versus</i> gate voltage. (b) Pauli blocking mechanism.	82
3.17	(a) Landau levels. (b) Schematic of Landau levels in Dirac cone.	84
3.18	Raman spectra of graphitic layers.	89
3.19	Contrast spectra of graphene sheets of varying thickness.	90
3.20	Benchmarking with Lu and Zhao. $\lambda = 1550$ nm; $t_g = 0.7$ nm; “theirs” refers to $\varepsilon(\omega)$ plots of Lu and Zhao and “ours” the $\varepsilon(\omega)$ plots from our study.	91
3.21	Benchmarking with Gosciniak and Tan. $\lambda = 1550$ nm; $t_g = 0.7$ nm; “theirs” refers to $\varepsilon(\omega)$ plots of Gosciniak and Tan and “ours” the $\varepsilon(\omega)$ plots from our study.	91
3.22	Benchmarking with Kwon. $\lambda = 1550$ nm; $t_g = 0.7$ nm; “theirs” refers to $\varepsilon(\omega)$ plots of Kwon and “ours” the $\varepsilon(\omega)$ plots from our study.	92
3.23	Complex dielectric constants of bilayer graphene ($t_g = 0.69$ nm) at $\lambda = 1550$ nm calculated and used in our study.	92
3.24	Complex dielectric constants deduced using Kubo formula for mono-, bi- and trilayer graphene of thickness (t_g) 0.4, 0.69 and 1.12 nm, respectively.	93
3.25	Complex dielectric constants of $\varepsilon(\omega)$ for two Fermi levels, $\mu = 0.4$ and $\mu = 0.509$ eV representing conditions ON and OFF, respectively; $t_g = 0.69$ nm.	94
3.26	Complex $\varepsilon(\omega)$ as a function of λ , values derived using our code.	96

4.1	(a) Accumulation of charge carriers in graphene–dielectric interface upon applying a voltage. (b) Depiction of light modulation using electrical signal.	100
4.2	Schematic of graphene based waveguide: (a) electric signal, (b) incident light and (c) modulated light pulse.	100
4.3	(a) Waveguide with active (A) and passive (P) materials. (b) A rib waveguide with graphene in layer 5. Layer 3 forms the core (Si), layers 1 and 2 are dielectric materials (e.g., SiO ₂) and layers 4 and 6 are termed buffer materials such as hBN, Si ₃ N ₄ or Al ₂ O ₃ that encapsulate graphene; V_g denotes applied gate voltage.	102
4.4	Waveguide redrawn from Gosciniak and Tan (2013) for validating complex and perturbation solvers. Since the waveguide is symmetric, half-structure was chosen as marked.	103
4.5	Mode effective index (n_{eff}) for validating perturbation and complex solvers.	104
4.6	Mode absorption (α) for validating perturbation and complex solvers. . . .	104
4.7	Electric field of quasi-TM E_y mode for chosen dielectric constants of graphene from Gosciniak and Tan (2013), simulated by using the complex solver. . . .	105
4.8	TM mode: $\text{Re}(n_{\text{eff}})$ and α for high- and low-index spacers between Si slab and Si ridge ($\lambda = 1550$ nm). Inset shows Fig. 3(a) in Gosciniak and Tan (2013).	106
4.9	$\text{Re}(n_{\text{eff}})$ and α for two supported modes, TM and TE, for high-dielectric spacer. Inset shows Fig. 3(b) in Gosciniak and Tan (2013).	107
4.10	$\text{Re}(n_{\text{eff}})$ and α for high- and low-index spacers between Si slab and Si ridge for TE mode; $\mu = 0.512$ eV. Inset shows Fig. 4(c) in Gosciniak and Tan (2013).	108
4.11	$\text{Re}(n_{\text{eff}})$ and α for high- and low-index spacers between Si slab and Si ridge for TM mode; $\mu = 0.512$ eV. Inset shows Fig. 4(d) in Gosciniak and Tan (2013).	109
4.12	Waveguides (a), (b), (c) and (d) represents figures chosen from Fig. 2a, 2b, 2e and 2f, respectively, from Lu and Zhao (2012) for benchmarking task. . . .	110
4.13	Waveguides redrawn from Fig. 2 of Lu and Zhao (2012) for benchmarking using our complex code.	111
4.14	Electric field plots of TM E_y mode for waveguide (a) shown in Fig. 2(a) of Lu and Zhao (2012); Si–(graphene/dielectric)–Si.	112
4.15	Electric field plots of TM E_y mode for waveguide (b) shown in Fig. 2(b) of Lu and Zhao (2012); Si–(graphene/dielectric)–Si, dielectric strip waveguide.	112
4.16	Electric field plots of TM E_y mode for waveguide (c) shown in Fig. 2(e) of Lu and Zhao (2012); Si–(graphene/dielectric)–Cu, width = 400 nm.	112
4.17	Electric field plots of TM E_y mode for waveguide (d) shown in Fig. 2(f) of Lu and Zhao (2012); Cu–(graphene/dielectric)–Si, width = 200 nm.	113
4.18	Mode profile and electric field of TM mode for waveguide in Fig. 2(a) of Lu and Zhao (2012). Table shows the comparison of n_{eff} and α values of theirs and ours.	114

4.19	Mode profile and electric field of TM mode for waveguide in Fig. 2(b) of Lu and Zhao (2012). Inset shows the comparison of n_{eff} and α values of theirs and ours.	115
4.20	Absorption versus wavelength plot as shown in Fig. 4(a) of Lu and Zhao (2012). Inset shows their plot.	116
4.21	TM mode absorption as a function of chemical potential (μ) for waveguide in Fig. 4(c) of Lu and Zhao (2012). Inset shows the plot from their study. .	116
4.22	(a) Three-dimensional illustration of the modulator. Source: Liu <i>et al.</i> (2011). (b) electric field plot obtained using our complex solver for their waveguide dimensions. Inset shows the electric field plot from their study (Liu <i>et al.</i> 2011).	117
4.23	Study of Liu <i>et al.</i> (2012) showing 2D (a) and 3D (b) models of double layer graphene modulator. Steps for fabrication is shown from (c) to (f). Source: Liu <i>et al.</i> (2012).	117
4.24	Waveguide designs taken from literature: (a) Liu <i>et al.</i> (2012); (b) Phatak <i>et al.</i> (2016); (c) Koester <i>et al.</i> (2012), Hu and Wang (2017); (d) Lu and Zhao (2012).	118
5.1	A rib waveguide in silicon-on-insulator. The refractive indices (n) air, Si and SiO ₂ are 1, 3.477 and 1.444, respectively.	121
5.2	A silicon nanowire.	122
5.3	Rectangular silicon waveguides: (a) strip and (b) rib. Dimensions of Si core are width $0.4\ \mu\text{m}$ and thickness $0.3\ \mu\text{m}$. In (b), the Si slab is of thickness $0.15\ \mu\text{m}$ and width $1\ \mu\text{m}$	123
5.4	Mode profiles of Si strip waveguide: (a) TM; (b) TM contour; (c) TE; (d) TE contour.	124
5.5	Mode profiles of Si rib waveguide: (a) TM; (b) TM contour; (c) TE; (d) TE contour.	125
5.6	Waveguides with graphene as top (a) and slot (b) layers. $t_{\text{graphene}} = 0.69\ \text{nm}$; $\lambda = 1550\ \text{nm}$; refractive indices (n) of Si, SiO ₂ and <i>h</i> BN are 3.4777, 1.444 and 1.98, respectively.	125
5.7	TM mode effective index plots of top-layer and slot-layer graphene.	126
5.8	TM mode absorption plots of top-layer and slot-layer graphene.	126
5.9	TE mode effective index plots of Si nanowire and waveguides with graphene as top layer; height-to-width ratio, w/a	128
5.10	TM mode effective index plots of Si nanowire and waveguides with graphene as top layer.	129
5.11	Silicon rib waveguides with graphene as slot layer: (a) graphene with encapsulated dielectric and (b) graphene directly on silicon and separated by a dielectric. Refractive indices of Si, SiO ₂ , <i>h</i> BN and Al ₂ O ₃ are 3.477, 1.444, 1.98 and 3.017, respectively.	129

5.12	TM and TE mode effective index (a, c) and absorption (b, d) for waveguides with dielectric layer encapsulated graphene and graphene-on-graphene configuration; (a) and (c) show the change in real part of n_{eff} ; $\lambda = 1550$ nm.	130
5.13	TM and TE mode profiles of low-index dielectric-encapsulated graphene layers. (a) TM; (b) TM electric field; (c) TE; (d) TE electric field. $\varepsilon(h\text{BN}) = 3.9204$; ON: $\varepsilon(0.4 \text{ eV}) = 4.7592 + j4.4441$; $\lambda = 1550$ nm.	132
5.14	TM and TE mode profiles of high-index dielectric-encapsulated graphene layers. (a) TM; (b) TM electric field; (c) TE; (d) TE electric field. $\varepsilon(\text{Al}_2\text{O}_3) = 9.1$; OFF: $\varepsilon(0.52 \text{ eV}) = -0.4998 + j0.5340$; $\lambda = 1550$ nm.	133
5.15	Mode effective index and absorption of TM and TE modes in a dielectric-encapsulated bilayer graphene waveguide. Plots (a) and (c) show the change of magnitude in real part of n_{eff} .	134
5.16	TM and TE mode profiles of waveguide with graphene- $h\text{BN}$ -graphene stack. (a) TM; (b) TM electric field; (c) TE; (d) TE electric field. $\varepsilon(h\text{BN}) = 3.9204$; ON: $\varepsilon(0.4 \text{ eV}) = 4.7592 + j4.4441$; $\lambda = 1550$ nm.	135
5.17	TM and TE mode profiles of waveguide with graphene- Al_2O_3 -graphene stack. (a) TM; (b) TM electric field; (c) TE; (d) TE electric field. $\varepsilon(\text{Al}_2\text{O}_3) = 9.1$; OFF: $\varepsilon(0.52 \text{ eV}) = -0.4998 + j0.5340$; $\lambda = 1550$ nm.	136
5.18	Mode effective index and absorption of TM and TE modes in a graphene-on-graphene slot waveguide. Plots (a) and (c) show the change of magnitude in real part of n_{eff} .	137
5.19	Top (a) and slot (b) waveguides with trilayer (1.12 nm) graphene, encapsulated with dielectric materials. Dotted lines indicate dielectric-graphene-dielectric stack.	138
5.20	Complex dielectric constants of trilayer graphene for Fermi level up to 2.0 eV.	139
5.21	Waveguide with trilayer (1.12 nm) graphene as top layer. Plots (a) and (c) show variations of real part of n_{eff} as a function of chemical potential, μ .	140
5.22	TM mode profile (a) and corresponding electric field, TM E_y (b) for trilayer graphene as top layer waveguide.	141
5.23	Slot waveguide with trilayer (1.12 nm) graphene. Plots (a) and (c) show variations of real part of n_{eff} as a function of chemical potential, μ .	141
5.24	TM mode profile (a) and corresponding electric field, E_y (b) for trilayer graphene as slot layer waveguide.	142
5.25	Effective refractive indices ($\text{Re}(n_{\text{eff}})$) of quasi-TE and quasi-TM modes of waveguide with HfO_2 -encapsulated trilayer graphene as top layer.	143
5.26	Effective refractive indices ($\text{Re}(n_{\text{eff}})$) of quasi-TE and quasi-TM modes of waveguide with HfO_2 -encapsulated trilayer graphene as slot layer.	144
5.27	Proposed designs for trilayer graphene with ABA Bernal and ABC rhombohedral stacking order in as a dielectric-encapsulated layer placed as slot (a) and as top (b); t_D , thickness of dielectric layer; t_G , thickness of graphene.	145
5.28	TE and TM mode effective index and optical absorption of waveguide with graphene-dielectric stack as top layer.	146

5.29	TE and TM mode effective index and optical absorption of waveguide with dielectric-graphene-dielectric stack as slot layer.	147
5.30	Mode profiles of dielectric-encapsulated trilayer graphene waveguide: (a) hBN ; (b) Al_2O_3 ; (c) HfO_2 . In (c) mode moves towards the graphene-dielectric stack.	147
5.31	TM (a) and TE (b) mode optical absorption for varying dielectric thickness in a graphene-as-top layer waveguide.	148
5.32	Optical absorption for TM modes of top-graphene (a) and slot-graphene (b) waveguides; $\mu = 0.53 eV$	149
5.33	TE and TM mode effective index of graphene-slot waveguide for varying wavelength (λ): ON, $0.4 eV$ (a, c); OFF, $0.53 eV$ (b, d).	150
5.34	Top-graphene: TM mode (a) extinction ratio and (b) insertion loss for varying dielectric layer thickness.	150
5.35	Slot-graphene: Extinction ratio (a) and insertion loss (b) for varying dielectric thickness.	151

List of Tables

1.1	List of few combinations optical materials	4
4.1	Benchmarking of results with Lu and Zhao (2012), obtained by using our complex code	113
A.1	Complex dielectric constant values, $\varepsilon(\omega) = \varepsilon_1 + j\varepsilon_2$, for $\mu = 0 - 1.0$ eV. . .	157

Chapter 1

Introduction

“Let there be light; and there was light”

Probably, Sunlight is the oldest of all “lights” mankind has ever seen or known after the Big Bang, just 13.7 billion years ago! Sunlight is the source of energy for all living beings on Earth. This proves one of the properties of light – it’s a form of energy! On an average, Sunlight takes 8 minutes and 20 seconds to reach the Earth.

The question “is light a wave or a particle” broadly remained till the dual nature of light was founded. Light holds both the properties of a wave and of a particle. A wave is simply an oscillation by which energy is transferred from one point to the other. Or a uniform disturbance (mechanical) that propagates through matter or space. The two most important ways of such transferring of energy through waves are classified as mechanical waves and electromagnetic (EM) waves; sound waves and light waves are classical examples, respectively. Former requires a medium, for instance air, to travel but latter do not require a medium for propagation. This thesis is wholly based on study of modal properties of electromagnetic waves. A propagating EM wave shown in Fig. 1.1 undergoes periodic changes in strengths of electric field and magnetic field.

A propagating light (EM) wave through a material medium can be controlled since it interacts with the atoms or molecules in the material. Such a medium is termed waveguide and have been a subject of study since the 1890s. Light wave act as a carrier in a waveguide. Most materials respond to an electric field applied as gate voltage. Only materials that allow/interact with EM waves and electric/magnetic fields can be used to design waveguides. Lithium niobate (LiNbO_3), lithium tantalate (LiTaO_3), potassium dihydrogen phosphate (KDP) and gallium arsenide (GaAs) are among several materials that are commonly used to design waveguides. JJ Thomson first proposed the structure

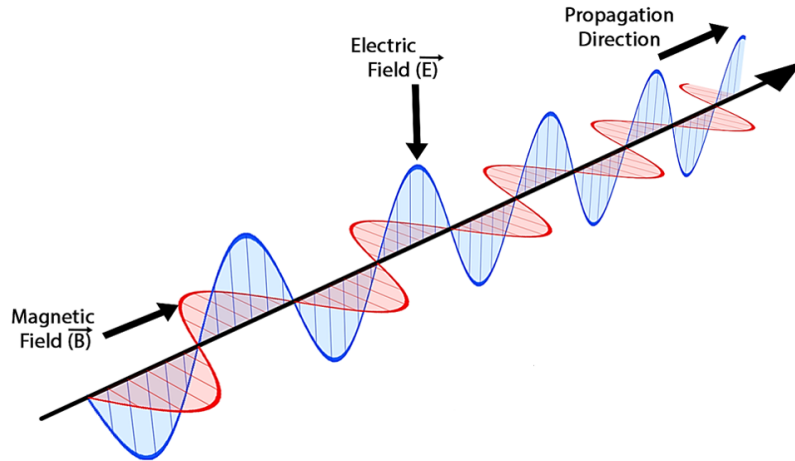


Figure 1.1: Propagation of a plane electromagnetic wave. Adapted from [1].

for guiding waves in 1893. Then Oliver Lodge (1894) tested it experimentally. In 1897, Lord Rayleigh derived the first mathematical analysis for electromagnetic waves. In 1964, Nelson and Reinhart observed phase modulation of light wave due to linear electro-optic effect. Devices based on electro-optic effect are used for analog/digital signal and information processing, optical computing and sensing, etc. Controlling the optical properties of light is the key aspect in photonics.

Thus the idea in electrooptic devices is to engineer the optical properties of a material by applying a voltage. Change in permittivity tensor of the material results in modification of phase, frequency, amplitude and propagation direction of the light wave. Therefore, studying propagation of light through such materials is important for designing electrooptic devices. An applied electric field affects redistribution of charges at the atomic level inside a material. This leads to linear (Pockels) and quadratic (Kerr) electrooptic effects. Optoelectronic materials are classified on the basis of both these effects. It is observed that Kerr electrooptic effect is exhibited by almost all crystals.

Combination of elements in groups III–V, II–VI and IV are important for designing modulator devices. Metals, insulators and semiconductor elements differ with separation between valence band and conduction band (Fig. 1.2). This is termed bandgap and denoted by E_g . Most elements in these groups respond to injection of electrons and holes by applying a voltage or through an optical pump. This results in change of absorptive properties due to change in carrier concentration. Here, the accuracy in determining the dielectric constant (ϵ) of the materials holds prime importance. Progress in crystal growth techniques such as molecular beam epitaxy (MBE), metal-organic chemical vapour

deposition (MOCVD) and atomic layer deposition (ALD) has led to growing different layers of materials one above the other with very high degree precision of layer alignment. Such designs result in heterojunction structures which play major role in optoelectronic device applications.

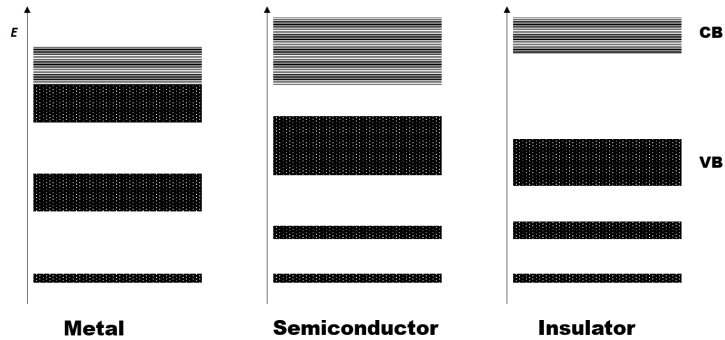


Figure 1.2: Energy band separation showing overlapping valence band (VB) and conduction band (CB) for metal and rest separated with a band gap energy, E_g .

Pockels effect denotes linear variation in refractive index (n) of a dielectric medium (crystal) with respect to applied electric field. A propagating wave through the crystal becomes dependent on the electric field vector. Such phenomenon is very useful for designing optical modulators using these materials. Modulating the light beam is the core principle on which these devices operate.

Optical modulators are of following types:

- acousto-optic
- electro-optic
- electroabsorption
- interferometric
- fibre-optic
- liquid crystal
- micromechanical

1.1 Photonic materials

Photonics is a word coined from photon and electronics. Photons are light particles with energy $E = h\nu$. Electronic devices integrated with light waves for modulation and trans-

Table 1.1: List of few combinations optical materials

$\text{NH}_4\text{H}_2\text{PO}_4$	KD_2PO_4	LiNbO_3	InP	GaAs
ZnSe	KH_2PO_4	SrTiO_3	GaInAsP	GaAlAs
ZnTe	CsH_2AsO_4	LiTaO_3	CaF_2	GaN
$\text{Bi}_{12}\text{SiO}_{20}$	BaTiO_3	KNbO_3	BaF_2	YAG
ZnO	ZnSe	ZnS	Si-Ge	Polymer optic materials

mission results in the birth of *photonics*. So, materials that are capable of molding the flow of light and that respond to electrical field are categorized as photonic materials. The type of atoms and lattice geometry of these materials govern their electrical, electronic and optical properties. The thickness of these layers are in terms of micrometer (μm) and nanometer (nm). These materials respond to light waves by reflecting or propagating or confining them. As is well-known, fibre optic cables made of materials that guide light are extensively used in telecommunications industry. Fibre optics deals with propagation and interaction of EM waves with material medium. Now the technology is moving towards identifying materials for high-speed computing as electronic devices have bandwidth limitation.

Photonics materials comprise a wide range of elements viz., semiconductor materials, nanomaterials, biophotonic materials and polymer materials (Table 1.1). The advent of 2D materials has opened the gates for new materials of one atomic layer thickness or few atomic layers. One such material is graphene and this thesis is based on it. Integrating these materials with other materials hexagonal boron nitride (hBN), hafnium oxide (HfO_2), molybdenum disulfide (MoS_2), etc. offers a huge potential for new range of electronic devices. Shortcomings observed in silicon photonics could be alleviated by integrating newly found materials with electronic components, for instance, optical interconnects.

Optical signals sent through optical fibres need to be converted to digital form for information processing. Therefore the speed of operation of the device that converts is crucial. Due to bandwidth limitation, electronic components cannot be tuned for high speed operations. Thus this limitation has led to the birth of 2-D optoelectronic materials. Electronic devices can be replaced with optical devices such as switches, connectors, receivers, modulators, filters and transmitters.

Materials exhibit weak nonlinearities when exposed to high intensity EM waves. Such nonlinearities arise from anharmonic motion of electrons with respect to an applied field. If a material is considered as a pool of charged particles, then an applied electric field will

induce an oscillation in the pool of electrons. At low intensities, in induced polarisation, the displacement of the electrons or dipole, P , is directly proportional to the magnitude of the electric field of the incident light wave given by, $P = \chi E$, where χ is the linear optical susceptibility, a function of the refractive index of the material. For instance, laser light generates very intense fields, which give rise to nonlinear optical effects and the expression for polarisation is given by,

$$P = \chi^{(1)}E + \chi^{(2)}E + \chi^{(3)}E + \dots \quad (1.1)$$

1.1.1 Photonic crystals

Photonic crystals are materials of which the refractive index (n) that vary periodically in 1, 2 or all 3 spatial dimensions [2]. Multilayers of such materials form two- and three-dimensional photonic structures that mold the flow of light (Fig. 1.3). The thickness of these layers are in terms of micrometer (μm) and nanometer (nm). These material respond to light waves by reflecting or propagating or confining them. As is well-known, fibre-optic cables made of materials that guide light are extensively used in telecommunications industry. Now the technology is moving towards identifying materials for high-speed computing.

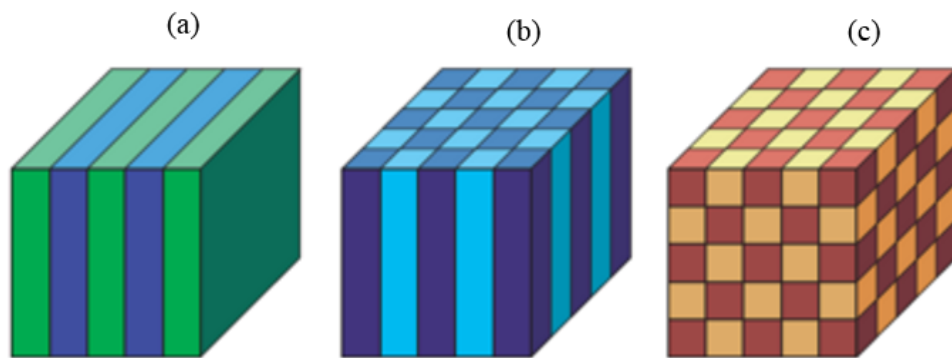


Figure 1.3: Photonic crystals of (a) one, (b) two and (c) three dimensions. Different lines show variation in dielectric constants (ε_1 , ε_2 , ε_3) within the crystal. Adapted from [2].

A crystal possesses long range periodic arrangement of atoms or molecules. An electron entering a crystal thus passes through a periodic potential. Therefore the type of atoms and lattice geometry govern the electrical, electronic and optical properties of the crystal. Similar to a crystal with atoms or molecules and periodic potential, a photonic crystal has macroscopic constituents with differing dielectric constants and periodic dielectric function or a periodic refractive index. Here, the photonic band gaps prevent EM wave

from propagating in particular directions and corresponding frequencies. When a photonic crystal prevents EM wave propagation in all directions irrespective of its polarization and source of emission, the crystal is said to have a perfect photonic band gap. Photonic band gap materials have a periodic dielectric profile, which prevents light of certain frequencies or wavelengths from propagating in one, two or any number of polarisation directions within the materials. This is synchronous to the electronic band gap and thus known as photonic band gap.

1.1.2 Current trends

Recent years have witnessed remarkable growth in nanoscience and nonlinear optics research, paving entry of 2D materials such as graphene [3], phosphorene [4], silicene [5] and so on. These materials offer exceptional properties which are in need for potential applications in nanoelectronics. Graphene has extraordinary optical, electrical, mechanical and thermal properties. Moreover, the optoelectronic and nonlinear properties of graphene makes it a suitable material for systems requiring extremely high operational bandwidth (12 THz) [6]. The uniqueness of graphene lies in its modulation depth ($> 90\%$) and signal attenuation ($< 5\%$), achieved by controlling its Fermi level through gate voltage. Graphene demonstrates strong light-matter interactions. Plasmons in graphene are tunable and operate in wide range of frequencies from terahertz to visible. It is envisioned that graphene-based modulators would be the ultimate high-speed modulator of the future, performing at speeds up to 10 times faster than existing ones.

Optical modulation has started getting attention in the recent years due to limitation imposed by electrical interconnects. On the other hand, optical interconnects have proven to be viable alternatives for ever growing demands of high speed computing, termed *Quantum Computing*, using qubits. Exploiting quantum aspects such as fermions of materials have shown possibilities of building future quantum computers. Recent studies have established Majorana Fermions (surface codes and colour codes) as the framework for quantum computation [7, 8] and a strategy to regulate the phase of Majorana state [9].

Intense research is being focussed on developing cost-effective, fast, high-performance optical modulators for optical interconnects. The 2D materials such as graphene, transition metal dichalcogenides (TMDs) and phosphorene have proven to be promising for implementing functions such as generation, propagation, modulation and detection of pho-

tons for integrated photonic circuits [10].

1.2 Fundamentals

1.2.1 Light waves

Light waves are characterized as wavelength (λ), frequency (ν) and speed (c), forming the simple equation, $c = \lambda\nu$. James Clerk Maxwell, in 1865, proposed that light waves are indeed electromagnetic waves comprising oscillating electric and magnetic fields. Speed of light was measured to be 299,792,458 m/s. Light particles are defined as photons, a quantization of EM energy, which behaves like particles as well as waves. Energy equation of photon is given as $E = h\nu$, where h denotes Planck's constant, 6.62×10^{-34} J/s. Figure 1.4 shows the complete chart of electromagnetic spectrum.

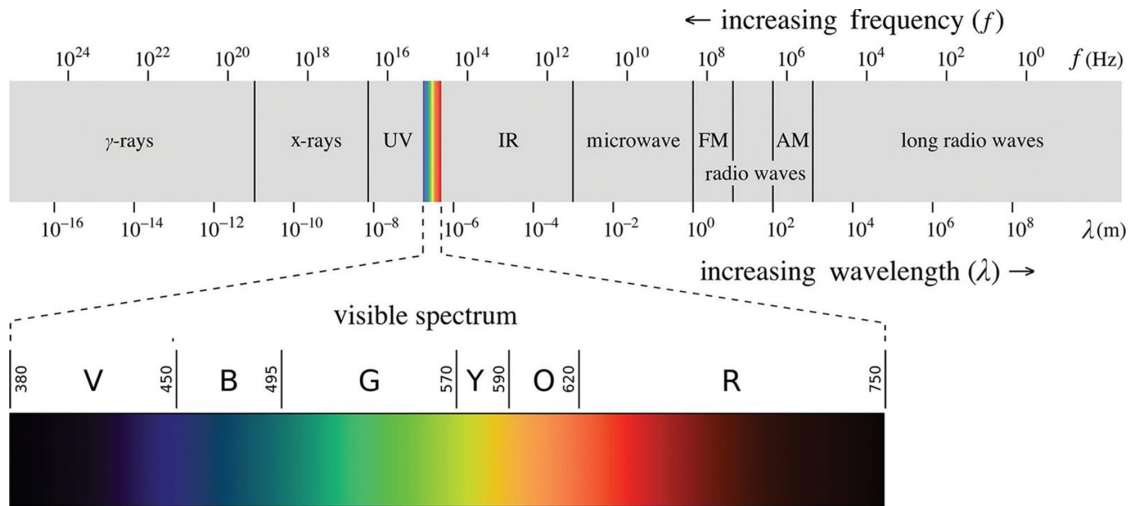


Figure 1.4: The continuous spectrum of an electromagnetic spectrum [11].

1.2.2 n and ε

Refractive index (RI) is the prime property of an optical waveguide which is used to study propagating modes, intensity distribution, insertion loss and cutoff wavelengths. It is a dimensionless physical quantity denoted by n . It is actually a complex number with real and imaginary parts: $n = n' - jn''$, where n' the real part and n'' the absorption coefficient which shows the level of absorption of light wave within the waveguide. In an ideal transparent material, $n = n'$, indicating $n'' = 0$. According to Snell's law light ray undergoes reflection and refraction when passing from one medium to another (Fig. 1.5), given by, $n_1 \sin \theta_1 = n_2 \sin \theta_2$ where n_1 and n_2 denote indices of refraction in medium 1 and medium 2, respectively.

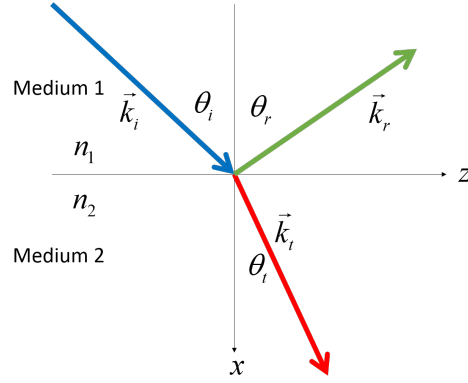


Figure 1.5: Light ray travelling from medium 1 to medium 2. n_1 and n_2 , refractive indices of media; k_i , k_r , and k_t , incident, reflected and transmitted light rays, respectively.

Dielectric constant or permittivity (ϵ) is square of refractive index, given by, $\epsilon_r = n^2$. In this study, we deal with materials having a complex dielectric constant, $\epsilon_1 + j\epsilon_2$. This part is dealt in detail with Chapter 3.5.

1.2.2.1 Mode Effective Index

The term “effective index” (n_{eff}) is derived from the word “refractive index” (n). It denotes the measure of overall delay experienced by the guided light wave inside a medium; for instance, a three-layer waveguide medium. Refractive index (n) is the inherent property of a material whereas n_{eff} refers to the property of the waveguide, which depends on the refractive indices of the individual materials that make the waveguide.

1.2.2.2 Optical Absorption

Optical absorption occurs when the energy of an incoming photon is transferred to an electron in the valence band which moves to the conduction band if the photon energy (E_p) is larger than the bandgap energy (E_g). The photon absorbed in this process results in an electron–hole pair. Photons with energy smaller than the bandgap energy, $E_p < E_g$, are not absorbed and the waveguide is transparent for lights with wavelengths longer than $\lambda = hc/E_g$. The optical absorption coefficient is denoted by α which is the most important factor for electro-absorption modulators and photodetectors [2].

1.2.3 Wave mechanics

Mathematically, a wave represents a function that propagates with respect to time. Figure 1.6 shows displacement of a function $f(x)$, moving with $x - x_0$ where $x_0 = 1, 2, 3$. This

represents a wave moving along positive x -axis whereas $x + x_0$ will denote a wave function along negative x -axis.

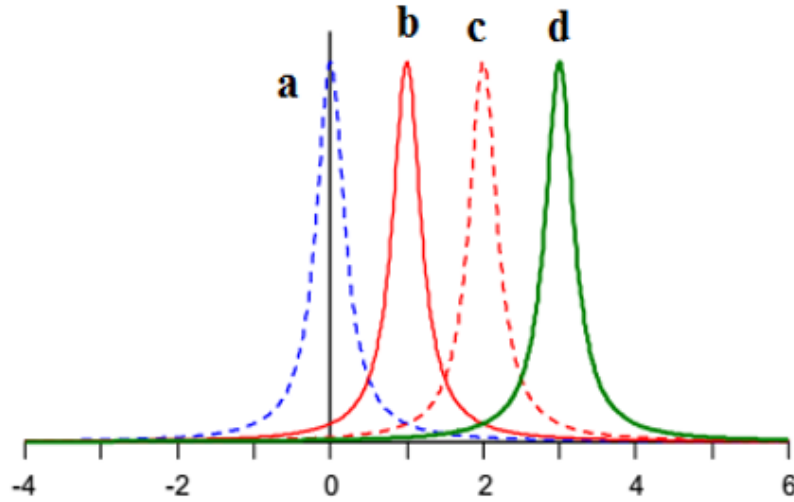


Figure 1.6: A 1D wave function: a, $f(x)$; b, $f(x - 1)$; c, $f(x - 2)$; and d, $f(x - 3)$.

The 1D wave equation for light waves is given by

$$\frac{\partial^2 E}{\partial x^2} - \mu\epsilon \frac{\partial^2 E}{\partial t^2} = 0 \quad (1.2)$$

where $E(x, t)$ is the electric field, μ the magnetic permeability and ϵ the dielectric permittivity. Here, x is the propagation direction.

The electric field of a light wave is then given by

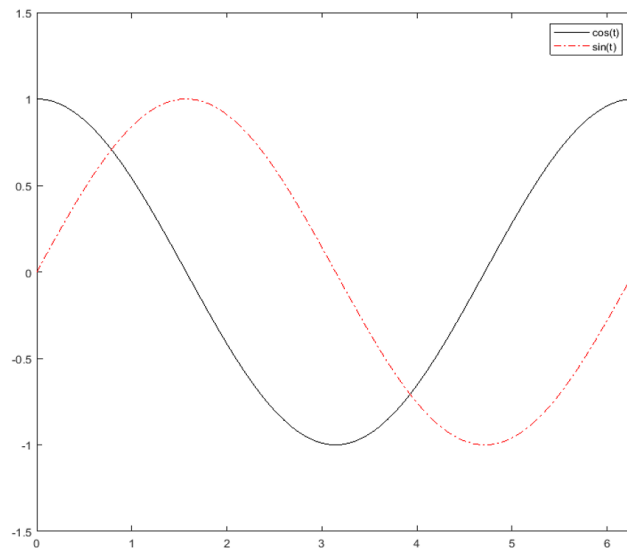
$$E(x, t) = A \cos(kx - \omega t - \theta) \quad (1.3)$$

where A is the amplitude and θ the absolute phase of the wave.

Figure 1.7 shows the plot of $\sin \omega t$ with respect to time t and ω the angular frequency. Both ω and frequency (ν) are related by $\omega = 2\pi\nu$. Such a propagating optical wave is expressed as:

$$E = E_0 \sin(kz \pm \omega t) \quad (1.4)$$

where the phase is $(kz \pm \omega t)$, kz denotes the wave propagation in z direction with k the propagation constant determining the progression rate of the wave with distance z . Wavelength and propagation constant are related as $\lambda = 2\pi/k$. Below equation addresses

Figure 1.7: Plot showing $\sin(\omega t)$ and $\cos(\omega t)$.

the mathematical description of a sinusoidal wave:

$$y(r, t) = y_0 \sin \left[\frac{2\pi}{\lambda}(r - vt) \right] \quad (1.5)$$

where $y(r, t)$ is the displacement of wave at position r and time t , y_0 the amplitude of the wave, λ the wavelength, v the speed of wave which equals to $\lambda \times f$ and t the time.

Phase angle of the wave is given by,

$$\phi = \frac{2\pi}{\lambda}(r - vt) \quad (1.6)$$

Other aspects of wave are interference, superposition, diffraction and polarization. These effects are not dealt in this thesis but can be studied from various books [12].

1.2.4 Maxwell's equations

In electromagnetism, Maxwell's equations play a pivotal role providing complete description of how electric and magnetic fields behave under space and time constraints [13]. Using divergence theorem and Stokes' theorem, Maxwell's equations transform the following basic equations from integral form to differential form.

Gauss' law for electric field:

$$\oint_S \vec{E} \cdot \hat{n} \, da = \frac{q_{\text{in}}}{\epsilon_0} \quad \text{Divergence theorem} \quad \vec{\nabla} \cdot \vec{E} = \frac{\rho}{\epsilon_0} \quad (1.7)$$

Gauss' law for magnetic field:

$$\oint_S \vec{B} \cdot \hat{n} \, da = 0 \quad \text{Divergence theorem} \quad \vec{\nabla} \cdot \vec{B} = 0 \quad (1.8)$$

Faraday's law:

$$\oint_C \vec{E} \cdot d\vec{l} = -\frac{d}{dt} \int_S \vec{B} \cdot \hat{n} da \quad \xrightarrow{\text{Stokes' theorem}} \quad \vec{\nabla} \times \vec{E} = -\frac{\partial \vec{B}}{\partial t} \quad (1.9)$$

Ampere–Maxwell law:

$$\int_C \vec{B} \cdot d\vec{l} = \mu_0 \left(I_{\text{enc}} + \varepsilon_0 \frac{d}{dt} \int_S \vec{E} \cdot \hat{n} da \right) \quad \xrightarrow{\text{Stokes' theorem}} \quad \vec{\nabla} \times \vec{B} = \mu_0 \left(\vec{J} + \varepsilon_0 \frac{\partial \vec{E}}{\partial t} \right) \quad (1.10)$$

where \vec{E} denotes the electric field vector; \vec{B} the magnetic field vector; ρ the electric charge density; \vec{J} the electric current density; ε_0 the electric permittivity of free-space, $\varepsilon_0 = 8.854 \times 10^{-12} \text{F/m}$, $\varepsilon = \varepsilon_0 \varepsilon_r$, ε_r the relative permittivity; μ_0 the magnetic permeability of free-space, $\mu_0 = 4\pi \times 10^{-7} \text{H/m}$ and $\mu = \mu_0 \mu_r$.

Using differential form of Maxwell equations, the wave equation is derived from Faraday's law (1.9) by taking curl on both sides of equation (1.9) as follows:

$$\vec{\nabla} \times (\vec{\nabla} \times \vec{E}) = \vec{\nabla} \times \left(-\frac{\partial \vec{B}}{\partial t} \right) = -\frac{\partial (\vec{\nabla} \times \vec{B})}{\partial t} \quad (1.11)$$

Applying vector operator identities and Laplacian to vector field components, yield the following linear second-order wave equation

$$\nabla^2 \vec{E} = \mu_0 \varepsilon_0 \frac{\partial^2 \vec{E}}{\partial t^2} \quad (1.12)$$

where \vec{E} is the electric field vector, denoting an electric field (wave) propagating from one point to other.

Similarly, Ampere–Maxwell law yields

$$\nabla^2 \vec{B} = \mu_0 \varepsilon_0 \frac{\partial^2 \vec{B}}{\partial t^2} \quad (1.13)$$

where \vec{B} is the magnetic field vector.

As we have seen earlier, waves are actually propagation of energy in the form of electric and magnetic fields. For an electromagnetic field, the expressions for energy density (U_E) and energy flux (U_H) are derived using Poynting's theorem and Maxwell's equations:

$$U_E = \frac{1}{2} \varepsilon \vec{E}^2 \quad U_H = \frac{1}{2} \mu \vec{H}^2 \quad (1.14)$$

where U_E and U_H denote energy per unit volume of electric and magnetic fields, respectively. Both vector quantities yield energy associated with an EM wave as $\vec{S} = \vec{E} \times \vec{H}$, known as Poynting vector.

Further, the constitutive relations are used to define the properties of the medium through which the EM wave propagates. Using E the electric field (V/m), B the magnetic flux density (V-s/m²), D the electric displacement flux density (C/m²) and H the magnetic field (A/m), following relations are derived:

In isotropic media,

$$D = \varepsilon E \quad B = \mu H \quad (1.15)$$

In anisotropic media,

$$D = \hat{\varepsilon} \cdot E \quad B = \hat{\mu} \cdot H \quad (1.16)$$

where $\bar{\varepsilon}$ is the permittivity tensor and $\bar{\mu}$ the permeability tensor given by

$$\hat{\varepsilon} = \begin{bmatrix} \varepsilon_{xx} & \varepsilon_{xy} & \varepsilon_{xz} \\ \varepsilon_{yx} & \varepsilon_{yy} & \varepsilon_{yz} \\ \varepsilon_{zx} & \varepsilon_{zy} & \varepsilon_{zz} \end{bmatrix} \quad \hat{\mu} = \begin{bmatrix} \mu_{xx} & \mu_{xy} & \mu_{xz} \\ \mu_{yx} & \mu_{yy} & \mu_{yz} \\ \mu_{zx} & \mu_{zy} & \mu_{zz} \end{bmatrix} \quad (1.17)$$

1.3 Waveguides

History of communications dates back when scientists attempted to use lens and mirrors to transmit light waves. It led to the search for appropriate transmission medium. Invention of laser gave a thrust of optical communications with first laser operating at $\lambda = 694$ nm and optical frequency of 5×10^{14} Hz. But free-space propagation is not a suitable way of communication as the beam is scattered by atmospheric factors such as rain, fog, snow, etc. Also, electronic components impose a limitation on bandwidth of optical communication. Therefore, the need for allowing light to propagate through another medium was identified.

Optical waveguides confine and guide light within a media of higher refractive index (n) than its surroundings i.e., cladding. Guiding light works according to the principle of total internal reflection (Fig. 1.8(a)). When a light ray hits the interface of two media with different refractive indices (n_1 and n_2), with a certain angle of incidence (θ_i), a part of the light is refracted (or transmitted) and other part is reflected back within the medium. This principle is known as total internal reflection. The reflected ray follows a zig-zag path within the medium (Fig. 1.8(b)).

If the waves propagate in the z -direction as $\exp(j\beta z)$, then the longitudinal propagation constant β is related to the ray angle ϕ by

$$\beta = n_1 k \cos \phi \quad (1.18)$$

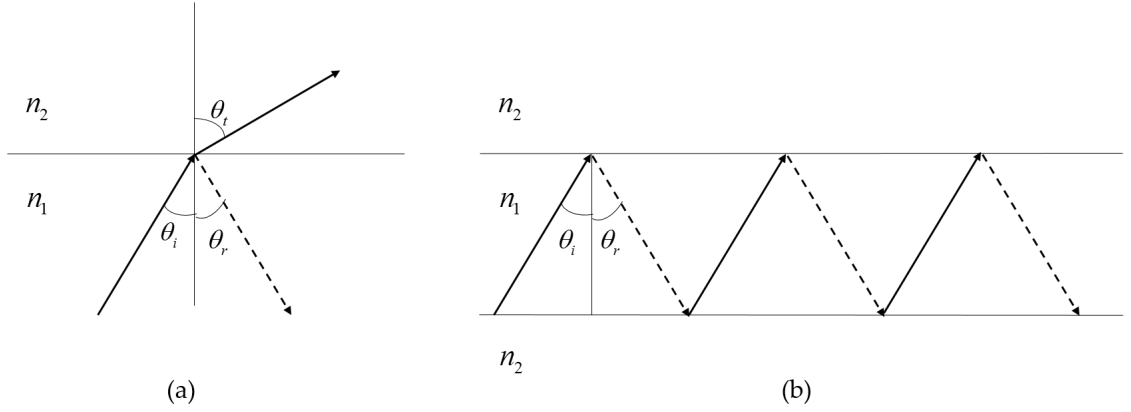


Figure 1.8: Principle of refraction (a) and total internal reflection (b) of light rays in medium 1 and medium 2 of different refractive indices n_1 and n_2 , respectively.

The propagation constant β is constrained for guided modes by

$$n_1 k \geq \beta \geq n_2 k \geq n_3 k \quad (1.19)$$

The aspect of confining, controlling and routing light on nanoscale has gained significant attention since the advent of 2-D materials. Light is confined to the order of sub-wavelength scale in these devices. Through proper choice of materials, mode confinement can be achieved at nanoscale.

1.3.1 Silicon-on-Insulator

Waveguide is the building block of photonic circuits. A 1D waveguide is termed planar and 2D the channel, which confine light in one-dimension and two-dimension, respectively. Photonic crystals can confine light in all the three dimensions. Silicon-on-Insulator (SOI) is the most extensively used platform used in microelectronics industry. Figure 1.9 shows a conventional SOI waveguide structure. Layer 2 is a buried SiO_2 with $n = 1.46$ and layer 3 the crystalline Si with $n \approx 3.5$. Thickness of these layers are of the order of a micron but varies according to fabrication methods.

From Maxwell's equations that govern the light wave propagating through this waveguide (Fig. 1.9) with conductivity $\sigma = 0$ and magnetic permeability $\mu = \mu_0$:

$$\nabla \times E = -\mu_0 \frac{\partial H}{\partial t} \quad (1.20)$$

$$\nabla \times H = \varepsilon \frac{\partial E}{\partial t} = \varepsilon_0 n^2 \frac{\partial E}{\partial t} \quad (1.21)$$

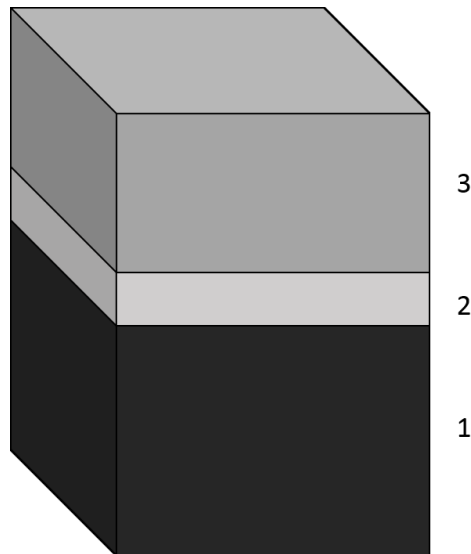


Figure 1.9: Schematic of a SOI waveguide. Layers 1, 2 and 3 denote Si substrate, SiO₂ and crystalline Si, respectively.

where E is the electric field, H the magnetic field, μ_0 the free-space permeability, ϵ_0 the free-space permittivity and n the refractive index of the medium. Components of electric field and magnetic field are denoted by (E_x, E_y, E_z) and (H_x, H_y, H_z) , respectively.

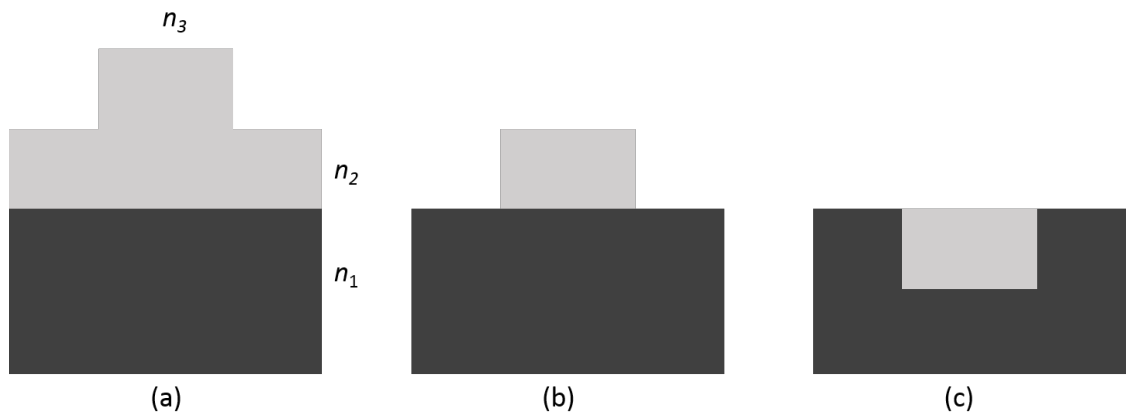


Figure 1.10: Common types of channel waveguides: (a) rib, (b) strip and (c) buried. Refractive indices n_1 , n_2 and n_3 denote substrate, core and cladding (air), respectively, in each of the waveguides.

Figure 1.10 shows the most common waveguide structures in use. Refractive index, n_2 , of layer 2 is higher than those of substrate (n_1) and cladding (n_3) such that the light wave is confined within layer 2. Silicon waveguides are capable of supporting multiple modes with dimensions even less than the operating wavelength.

1.3.2 Waveguide Fabrication

Fabrication involves step-by-step processes of thin film deposition, photolithography and etching. Thin film deposition is carried out by methods viz., sputtering, chemical vapour deposition (CVD) and thermal oxidation (SiO_2). Waveguide dimensions are controlled by thickness of thin film and pattern followed for photolithography. Figure 1.11 shows a micrograph of an actual SOI rib waveguide wherein a deposited oxide layer provides an upper cladding, and the buried oxide layer providing the lower cladding.

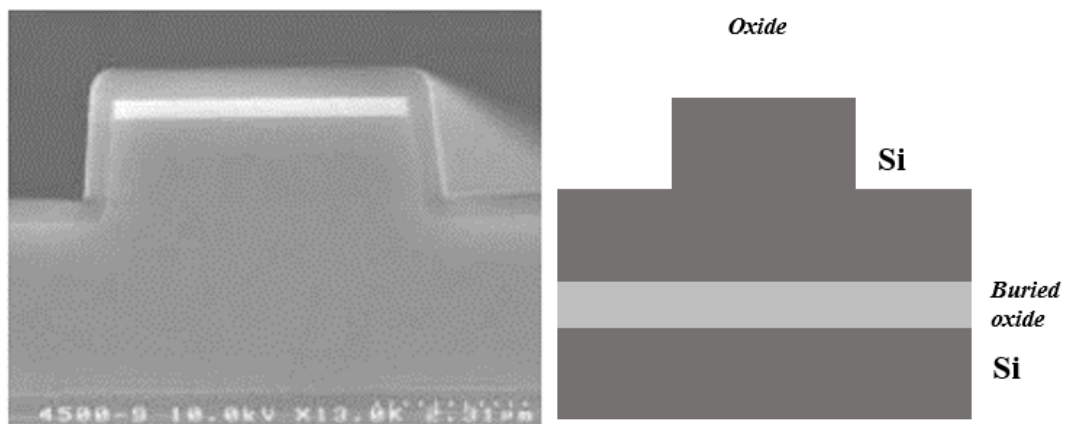


Figure 1.11: Electron micrograph of a fabricated Si rib waveguide. Reproduced from [14].

Most common fabrication processes include Separation by IMplanted OXYgen (SIMOX), Bond and Etch-back SOI (BESOI), wafer splitting and silicon epitaxial growth [14]. Other techniques include electron-beam lithography (EBL), holographic/composition lithography and anisotropic dry etching [15].

1.3.2.1 Thin film deposition

Deposition processes are carried out in vacuum chambers evacuated to around 10^{-6} Torr. Thermal evaporation is a conventional technique followed for depositing desired material onto the substrate. Plasma gas is prevalent in all stages of fabrication viz., deposition, etching, removal of photoresist and ion implantation. Plasma is composed of ionized gas comprising ions, electrons and neutral particles. It can be achieved by applying AC or DC voltage to a gas contained in a pressurised chamber. Figure 1.12 shows a plasma setup.

Plasma gas is sent to the evacuated pressurised chamber which is stabilised to the order of 10^{-3} and 10^{-2} Torr. Inside the chamber, electrons lose their energy through collision with gas atoms. In turn, excited gas atoms emits energy with a distinctive glow

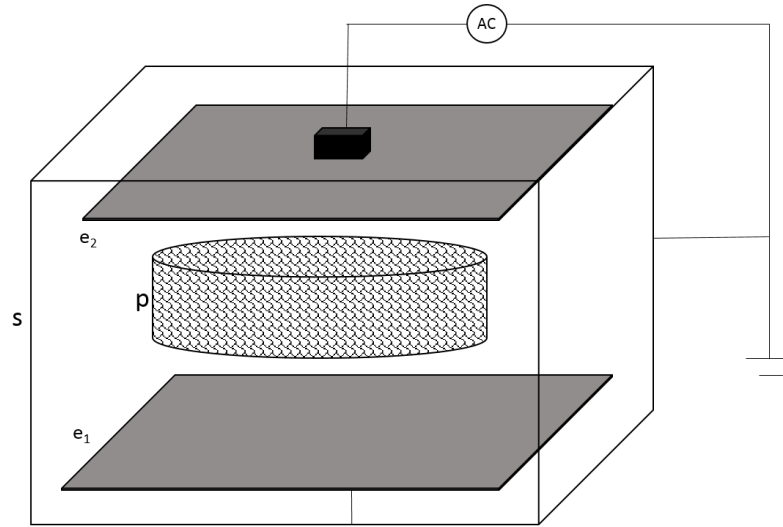


Figure 1.12: Schematic of a plasma generation chamber: S, sheath; e_1 and e_2 , electrodes; p, plasma; AC, power. Adapted from [14].

which varies according to the constituents of gas atoms. Sheath (S) refers to the dark region which contains very few electrons. In Si processing, plasma is derived from CF_4 gas. Using plasma gas, the etch rate can be controlled.

(a) Sputtering: This technique employs inert gas ions (e.g., argon) to strike the target and eject metallic atoms. Thus, the sputtered atoms migrate to the target wafer. The inert gas is ionized inside a plasma chamber. This technique uses a 13.56 MHz power and hence called RF sputtering. Figure 1.13 shows a schematic of sputtering process. The formed plasma potential makes inert gas ions to strike the target and eject the atoms which then travels to the wafer layer.

Energetic ions bombard the target element and eject the atoms. These atoms, called sputtered particles then deposit on thin films onto the substrate. This is called sputter deposition based on plasma used. Cathode and anode face each other inside a vacuum chamber. An inert gas (argon) is then introduced into the chamber which reaches a pressure of 1–10 Pa. High voltage to the range of 2 keV, applied between the electrodes, ignites a glow discharge. Argon ions are driven towards the target which ejects free atoms due to heavy bombardment. Ejected atoms are finally guided to the target wafer.

(b) Chemical vapour deposition: This is the most common technique for epitaxial growth of silicon. As the name indicates, deposition of desired film occurs due to chemical

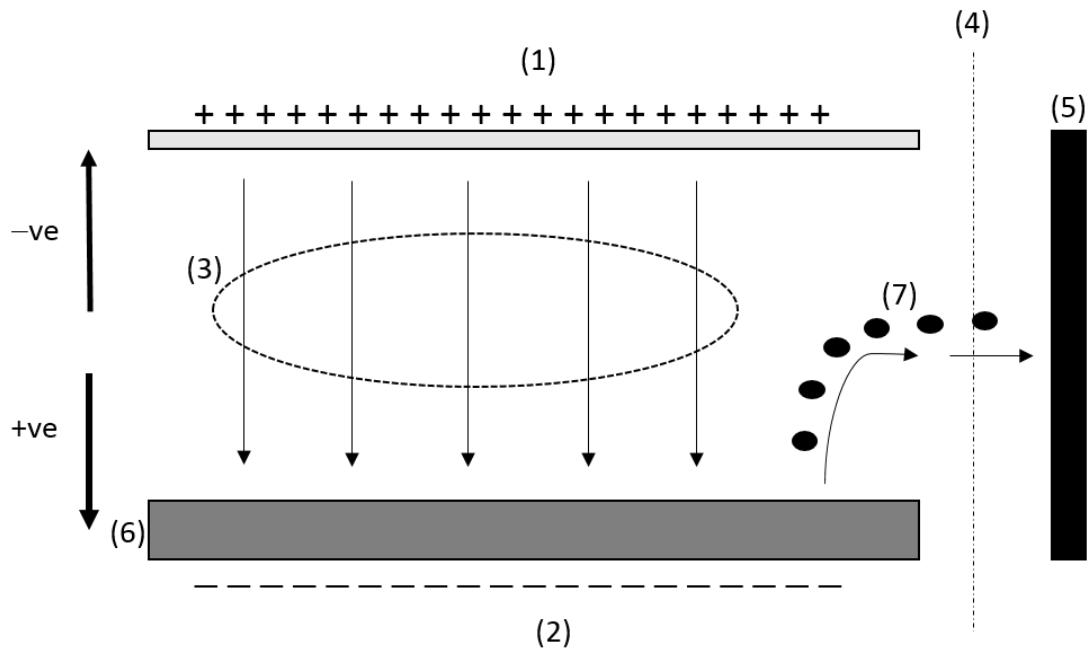


Figure 1.13: Schematic of sputtering technique: (1) anode, (2) cathode, (3) plasma, (4) shutter, (5) substrate, (6) target and (7) diffusion. Adapted from [14].

reactions. It is a process by which a solid film is deposited onto the surface of Si wafer by gas phase reactions at the surface. Figure 1.14 shows the schematic of a CVD process. Here, dichlorosilane (SiH_2Cl_2) is used as source gas. Wafer surface temperature is raised to the order of $> 1000^\circ\text{C}$ which is the driving factor behind the chemical reaction. CVD processes such as gas transport mechanism and chemical reaction kinetics are explained in various studies [16, 17].

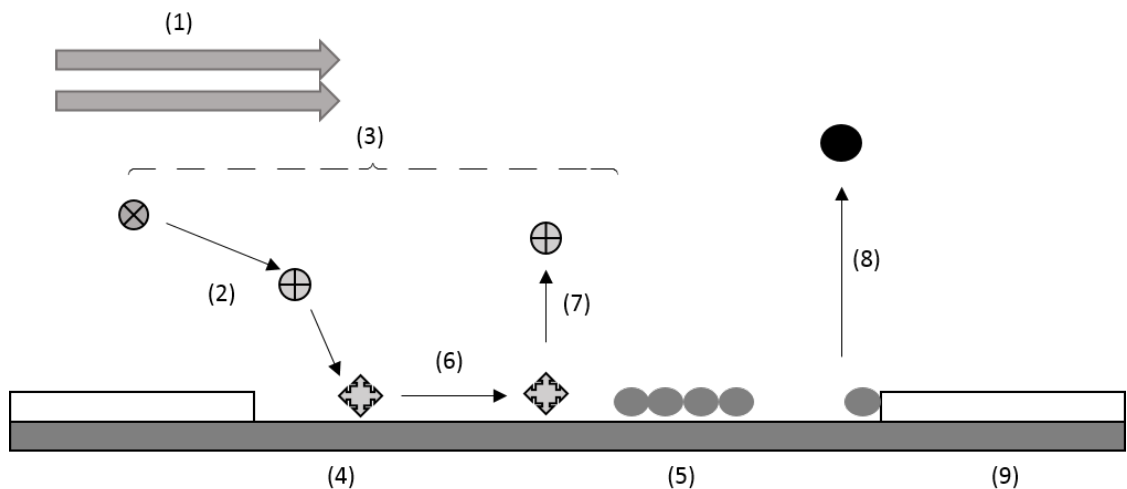


Figure 1.14: Schematic of CVD process: (1) main gas flow region, (2) transport to surface, (3) gas phase reactions, (4) adsorption of film precursor, (5) nucleation and island growth, (6) surface diffusion, (7) redesorption of film precursor, (8) desorption of volatile surface reaction products and (9) step growth. Adapted from [14].

1.3. Waveguides

Gas phase reactions play vital role here. Deposition takes place due to the chemical reaction between the reactants on the substrate. Reactant gases are pumped into the vacuum (reaction) chamber. Under optimum temperature and pressure conditions, the reactants undergo reactions on the substrate. Conditions vary according to the choice of film deposition. Finally, products of the reaction are deposited onto the substrate. Key parameters in this technique include reaction rates, gas transportation mechanism and diffusion processes. Following steps define the CVD technique:

- (a) reactants are transported to the reaction zone
- (b) gas phase reactions start
- (c) reactants are transported to surface of substrate
- (d) physical and chemical adsorption occur
- (e) desorption of volatile by-products
- (f) moving by-products away from reaction zone

Following are some of the reaction types from this technique:



Major advantage of CVD process is that high growth rates can be achieved and the possibilities of growing epitaxial films. On the other hand, it is a complex process which involves high temperatures and emission of toxic and corrosive gases.

(b) Thermal oxidation: The basic model reactions for this technique are as follows [18]:

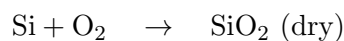


Figure 1.15 shows the simple schematic of oxidation technique. Chemical reactions occur at both the boundaries of oxide layer and diffusion process takes place. Oxygen is supplied to a quartz oxidation tube which has silicon slices placed flat on a quartz boat. Silicon slices are usually circular in shape with 22 mm diameter and $200\ \mu\text{m}$ thickness. The oxide thickness after formation are measured using interferometric techniques.

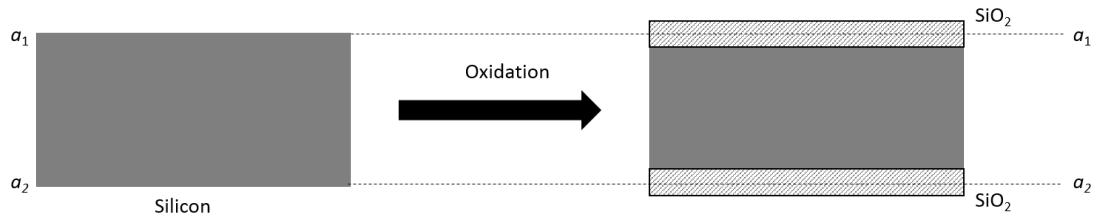


Figure 1.15: Schematic of oxidation process. Dotted lines ($a_1 \cdots a_2$) denote the Si–SiO₂ interface after formation [14].

Oxidant diffusion and Si/SiO₂ interface chemical reaction are the major controlling factors in this technique. Thickness of oxide deposition varies linearly with time.

1.3.2.2 Photolithography

Photolithography is a technique by which layers of thin films are patterned, etched and then coated [19]. It is the process of transferring the image of an integrated circuit to a substrate under controlled conditions. First, substrates are coated with photoactive material called photoresist. Then a pattern is aligned and projected on the substrate via UV light. The image is then developed. This process involves mask, photoresist, aligner, developer and setup for baking.

Geometric shapes are transferred on a mask to a polished surface. Optical radiation is used to image the mask on a Si wafer with the help of photoresist layers. This technique involves following steps:

- step 1: surface (wafer) cleaning
- step 2: barrier layer formation
- step 3: spin coating with photoresist
- step 4: soft baking to densify resist
- step 5: mask alignment to register patterns

1.3. Waveguides

- step 6: exposure
- step 7: development
- step 8: hard baking
- step 9: post process cleaning

In this technique, a mask-defined pattern is transferred onto the wafer surface. A photoresist i.e., a photosensitive polymer, is used to print the pattern on the wafer. Figure 1.16 shows the steps involved in this process.

Preparation of wafer: The wafer should be free from any contaminants and desorbed of

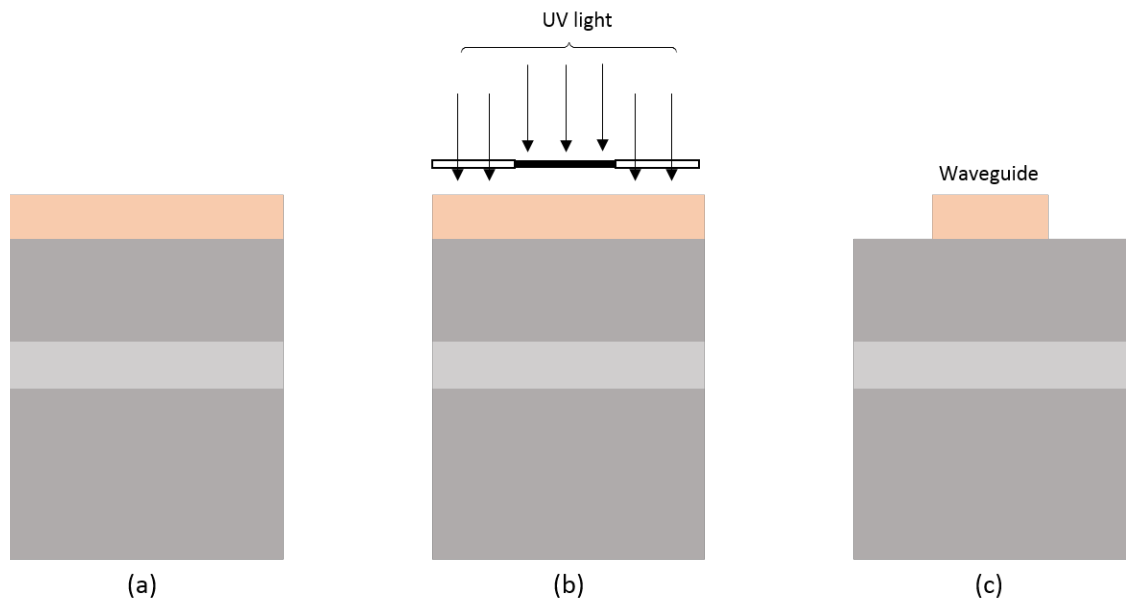


Figure 1.16: Steps involved in photolithography technique. (a) SoI wafer coated with thin polymer (photoresist), (b) exposure of UV light on the wafer covered by a mask and (c) waveguide pattern obtained after hard bake [14].

moisture. Cleaning is carried out by a wet process and then rinse and dry. Then baking at $T = 150^{\circ}\text{C}$ results in surface dehydration, which is done prior to applying photoresist. Finally wafer is coated with an adhesive such as hexamethyldisilazane.

Photoresist: Wafer is then coated with a liquid photoresist. Coating process involves dispensing the resist (1–10 mL) to the center of wafer and spun at a speed 1–5 krpm. Resist is thus distributed throughout the wafer.

Soft bake: It drives off the solvents in the resist and improves the uniformity and adhesiveness of the resist. This step is carried out at $T = 100^{\circ}\text{C}$ that lasts for few minutes.

1.3. Waveguides

UV exposure: Resist-coated wafer is placed in the mask-aligner with a submicron precision. Required pattern is defined in the mask. Then UV light is exposed onto the wafer. Mask has transparent regions through which light passes through and photosensitive elements of resist are activated which are removed later on. This is known as positive resist. In a process wherein unexposed areas are removed is called negative resist.

Photoresist developing: At this stage, wafer is treated with a developing solution. Depending on process (positive or negative), solution dissolves (activated or unactivated resist) and thus desired pattern is formed in the wafer.

Hardbake: This is the final stage wherein resist solvents are cleared and strengthening the adhesiveness of resist to the surface of the wafer takes place. Temperature is $90 - 140^{\circ}\text{C}$ which lasts for several minutes depending on requirement. Care should be taken such that pattern deformation does not occur. Pattern is then printed on photoresist.

1.3.2.3 Etching

This is the process of removal of layers from the wafer surface. It involves two approaches viz., wet and dry. Controlled and monitored material removal is carried out through physical (mechanical) or chemical (reactive) process. Figure 1.17 shows a wafer with SiO_2 on Si. Slanted lines denote hardened resist on SiO_2 layer. To remove oxide layer uncovered by resist, the wafer is immersed in a HF or $\text{HF} + \text{NH}_4\text{F}$ solution. Chemical reactions do not affect Si or protected oxide layers but etches away the exposed oxide layer. Chemicals making up such solution are called etchants. Different etchants are used for different materials. For instance, a solution of $\text{HCl} + \text{HNO}_3 + \text{H}_2\text{O}$ is used for indium tin oxide (ITO).

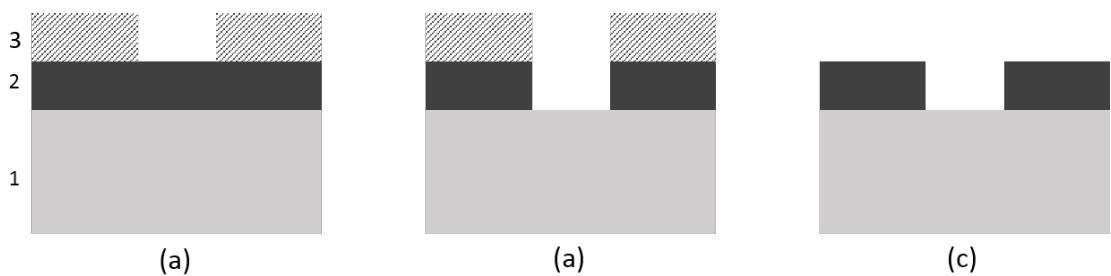


Figure 1.17: Schematic of chemical etching process: 1, silicon; 2, SiO_2 ; 3, photoresist. (a) Unexposed photoresist after developing stage. (b) Oxide layer is etched in a $\text{HF} + \text{NH}_4\text{F}$ solution. (c) Removal of photoresist with H_2SO_4 [14].

Temperature, etching time and etch rate are vital in this process. Types of etching are wet, dry and plasma. Mechanical ways of etching are ultrasonic agitation or cleaning, using abrasive compounds for polishing and supercritical cleaning.

1.4 Electro-absorption modulators

An electro-absorption modulator is basically a semiconductor device that introduces changes in incident light intensity by means of absorption. The materials that make such modulator are responsible for inducing a change in absorption spectrum due to an applied electric field. Change in refractive index (n) is caused by the electrical signal which results in change of real ($\text{Re}(n)$) and imaginary ($\text{Im}(n)$) parts of refractive indices of the material. Change in $\text{Re}(n)$ is termed electro-refraction and change in $\text{Im}(n)$ is termed electro-absorption. An EAM works on the ON-OFF principle thereby encoding information on an optical signal, termed modulation. Schematic of a typical EAM is shown in Fig. 1.18.

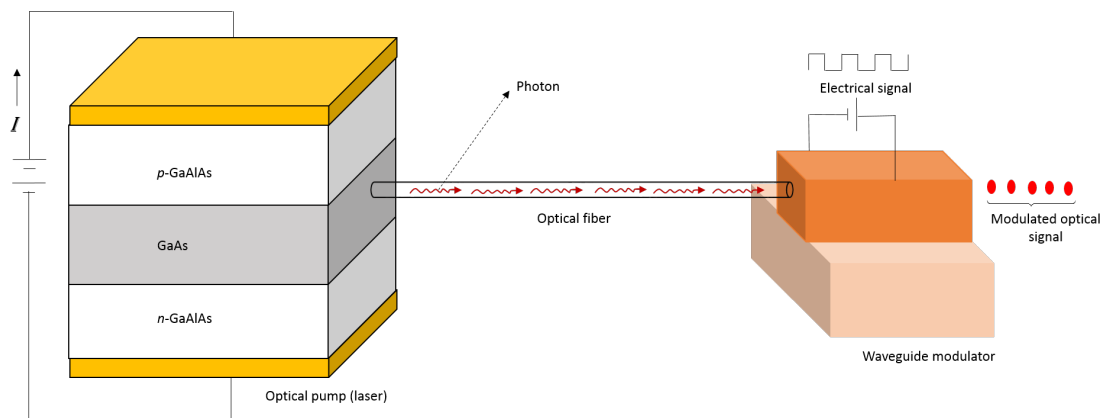


Figure 1.18: Schematic of a typical electro-absorption modulator [14, 20].

Our study deals with electroabsorption modulators (EAMs) wherein the modulation is achieved by controlling the incoming light beam by an applied voltage. In 1958, Franz and Keldysh developed the theory of optical absorption by crystals when subjected to an electric field. In 1963, Tharmalingam [21] derived expression for absorption coefficient (α) in the presence of a uniform field. The absorption factor plays a vital role in governing the performance of an EAM.

1.4.1 Modulation Mechanism

As already stated, the fundamental principle of an EAM is that the incident light beam is absorbed by the medium, which is controlled with an electrical signal. Then the nature of optical output will be based on the electrical signal that modulates the incident light. The primary E -field effects that apply to semiconductor materials are Pockels effect, Kerr effect and Franz–Keldysh effect [22, 23].

Absorption in a semiconductor waveguide results from inter-band and free carrier absorption [15]. In the former, photons with energy greater than the band gap ($\hbar\omega > E_g$) of the material are absorbed by the excitation of electrons from valence band (VB) to conduction band (CB). The latter is due to concentration of free carriers affecting both real and imaginary parts of n . Absorption changes in semiconductors are given by following Drude–Lorentz equation:

$$\Delta\omega = \frac{e^3\lambda_0^2}{4\pi^2c^3\varepsilon_0n} \left(\frac{N_e}{\mu_e(m_{ce}^*)^2} + \frac{N_h}{\mu_h(m_{ch}^*)^2} \right) \quad (1.22)$$

where e is the electronic charge, c the velocity of light, μ_e the electron mobility, μ_h the hole mobility, m_{ce}^* the effective mass of electrons, m_{ch}^* the effective mass of holes, N_e the free electron concentration, N_h the free hole concentration, ε_0 the permittivity of free-space and λ_0 the free-space wavelength.

Wavelength of incident light also plays a crucial role in absorption. A pure Si shows an absorption of 2.83 dB/cm at $\lambda = 1.15 \mu\text{m}$ and 0.004 dB/cm at $\lambda = 1.52 \mu\text{m}$ [24].

1.5 Numerical methods

Numerical methods or techniques [25] evolved for designing devices using software that are based on theoretical methods for predicting the performance and behaviour of a system before experimentation. Results from theoretical methods have always aided experimental research in terms of cost and time. Some of the popular names include Newton, Euler, Lagrange, Gauss, Jacobi, Fourier, Chebyshev and so on. Theoretical methods have roots in mathematics, for instance, Gauss–Jordan and Jacobi methods. Ordinary differential equations are used in methods such as Adams and Moulton, Runge–Kutta, Rayleigh–Ritz for problems in mechanics, aerodynamics and acoustics, respectively. Numerical methods form a bridge between mathematics and physics, especially. Invention of computers in mid-

1940s greatly reduced the time involved in working out calculations which were done using pen and paper. A new branch called “Computational Methods” was born encompassing physical, chemical and biological sciences, all branches in engineering as well as economics. Present day software helps research visualize the outcomes in a more advanced way.

On this regard, this thesis is wholly based on the Finite Element Method (FEM) or Finite Element Analysis (FEA) which is one of the most widely used technique for design and analysis in engineering. Following are the fields where such methods are most commonly used to develop software for testing, research and development:

- mechanical, aerospace, civil and automotive engineering
- structural and stress analysis
- flow of fluids
- heat transfer
- electromagnetic fields
- soil mechanism
- acoustics
- biomechanics

Numerical methods have been widely used in the study of optical guided-wave devices due to the availability of faster and cheaper computer power. These methods are concerned with finding numerical solutions to the Helmholtz’s wave equation derived from Maxwell’s equations. For planar structures, or for structures with 1D index variation, the approximate methods yield satisfactory results. However, for accurate characterization of 3D structures, a fully numerical method such as finite difference or finite element method is required.

We will be focussing only on electromagnetic study using FEM. Photonics, a branch of electromagnetics, is the study of governing light for practical applications, for example, fibre optics. Lasers and light beams carry energy and information for various applications. Techniques are grouped under *Computational Photonics* that employ numerical methods. Results from computations help us identify pitfalls and optimize design before

fabrication. This is termed *simulation* showing the propagation of EM wave in the material of study. Nowadays we have a range of customised software especially in photonics based on FEM, mostly in two-dimensional (2D) domains, categorized as time-domain and frequency-domain methods. There are numerous methods proposed for both domains till date. Time-domain techniques study a system and analyse the response with respect to time whereas frequency-domain study a system's response with respect to a range of frequencies. This thesis follows the studies based on frequency-domain.

1.6 Objectives of the thesis

This thesis is devoted to study the following:

1. to benchmark H-field full vectorial FEM (perturbation and complex) with chosen studies in literature;
2. to derive an analytical method for obtaining complex dielectric constants ($\varepsilon_1 + j\varepsilon_2$, where ε_1 and ε_2 denote real and imaginary parts) of graphene for entire voltage range 0–2 eV;
3. to study fabrication possibilities and build a model to implement FEM for characterizing proposed waveguide designs;
4. to conduct a detailed investigation of H-field and E-field modal profiles of proposed rib and slot waveguides;
5. to ascertain the influence of dielectric layers with different (low-, high- and very high) refractive indices on mode effective index and absorption;
6. to evaluate device performance parameters such as operation wavelength range, modulation depth and insertion loss;
7. to determine potential trade-offs between these performance metrics for practical applications;

1.7 Structure of the thesis

This thesis comprises six chapters. Chapters 1 and 2 are devoted to the fundamentals of light wave propagation, different methods in fabrication of optical waveguides and the

explanation of Finite Element Method. Chapter 3 explains the significance of graphene, beginning with physical and unique properties of this wonder material. Our method and results we obtained in the study of dielectric constants of graphene are also presented in this chapter. Chapter 4 is devoted for the benchmarking task we carried out as a precursor for characterising graphene-based waveguides. In Chapter 5 we discuss our results in detail and propose waveguide designs based on our findings. Chapter 6 concludes this thesis and provides suggestions for future research.

Chapter 1 provides the recent trends in nanoelectronics with the advent of 1D and 2D materials. The need of these materials and their exceptional properties are given. Fundamentals such as wave mechanism and Maxwell's equations are explained for the study of light wave propagation in a material medium. We move on to the background of waveguides and the phenomena behind propagation. Few basic silicon-on-insulator designs were discussed. Waveguide fabrication and the methods involved are explained with schematic of the processes such as thin film deposition, CVD, sputtering, photolithography and etching. Finally the modulation mechanism is briefly discussed.

Chapter 2 begins with fundamentals of interaction between light and matter and the principle of operation in modulators. Planar, slab and rib waveguide theories are discussed. A brief about plasmonic waveguides is given. Finite element method (FEM) is explained in detail with an introduction to Maxwell's equations.

Chapter 3 deals with physical, electrical and optical properties of graphene. The physical properties of mono-, bi- and trilayers of graphene are explained. The electronic band structure that gives rise to the Dirac cone is discussed. Optical conductivity ($\sigma(\omega) = \sigma_1 + j\sigma_2$) of graphene is introduced here since it leads to derivation of complex relative permittivity ($\varepsilon(\omega) = \varepsilon_1 + j\varepsilon_2$) of graphene in the next section. We followed two methods in the literature [26,27] and formed our analytical method for deriving complex dielectric constants of graphene. We benchmarked the plots of complex dielectric constants of graphene from three studies [6,28,29]. A brief introduction to plasmonics is given.

Chapter 4 is devoted for benchmarking of modal properties from three studies [6,20,29]. The task of benchmarking is carried out to validate our complex and perturbation solvers with published results. This helps to debug and identify the limitations in our solvers and find ways to increase mesh dimensions handled by the solvers. The effective index (n_{eff}),

absorption (α) and electric field intensity plots are benchmarked and the results obtained using our methods are given.

Chapter 5 presents the characterization of waveguides we carried out in this study. Mode profiles, effective index, absorption and performance parameters (ER, IL) are evaluated. This chapter is divided into three parts. First part discusses the characterisation of silicon nanowires (strip and rib waveguides). An introduction to influence of positioning of graphene layers (top *versus* slot) in the waveguide is given. Second part deals with characterisation of waveguides with bilayer graphene. We discuss here the influence of dielectric layers on modal properties of graphene-based waveguides.

Third part in Chapter 5 deals with characterization of trilayer graphene-based waveguides. Results using low-, high-, and very high-index dielectric materials encapsulating graphene layers are presented. Our proposed waveguide designs are given. We discuss the modal solutions of proposed designs in detail in this final part. Conclusion and suggestions for future research are given in Chapter 6.

Chapter 2

Finite Element Characterization of Waveguides

2.1 Introduction

Dielectric waveguides are being studied since the early years of 19th century [30]. Achievement of lasing action in semiconductors by research groups in 1962 [31–33] led to the realization of light guidance in p - n junction [34, 35]. Further, heterostructure laser was developed in late 1960s [36]. In 1964, it was found that guiding action of a p - n junction could be used in a modulator via the electro-optic effect [37]. Such inventions in optical waveguide research resulted in rapid growth of potential applications in communication systems. Figure 2.1 shows rapid rise in this field of research between 1964 and 1980.

In this chapter, we discuss the waveguide design, characteristics and numerical method for characterization. First we discuss the interaction between light and matter. Here, matter refers to the materials (e.g., silicon, graphene and so on) that are used to design the waveguide. Next, the optical modulators which is the core study of this thesis. Second, we move on to the theoretical aspects of waveguides. Here we study the interaction phenomena of light with material using equations. Finally, we discuss the Finite element method used for characterization of waveguide. Basic concepts and steps involved in finite element study are discussed in detail.

2.2 Light–matter interaction

Interaction of light with matter results in following phenomena: reflection, refraction, emission, absorption and transmission. Light constitutes photons of energy, $E = h\nu$. Depending on the structure of matter and wavelength of light, this energy is either absorbed

2.2. Light–matter interaction

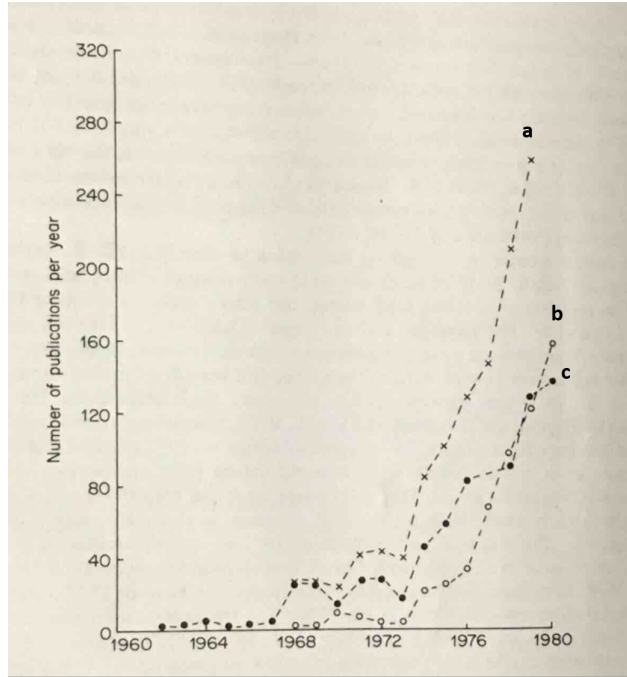


Figure 2.1: Number of papers published each year in a few relevant technical journals: (a) *Electronics Letters*; (b) *Applied Optics*; (c) *Electronic Letters and Applied Optics* and *Bell Systems Technical Journal*. Reproduced from Adams (1981) [38].

or reflected. There are other phenomena viz., fluorescence and diffraction. When light is incident on a surface or traverses a material medium, interactions with electrons of atoms or molecules that are present in the lattice take place. An electron, upon absorbing a photon, use the energy to move to an excited state of higher energy and then fall to lower energy by dissipating it in the form of a photon. Such process happens in few nanoseconds. The difference in energy between higher and lower states decides the frequency of emitted photon. A light photon has neither mass nor charge but it interacts with electrons, atoms and molecules. A light beam is nothing but a stream of photons of well-defined energy depending on the wavelength of the light. Thus the energy of photon is given by

$$E_p = h\nu = \frac{hc}{\lambda} = \hbar\omega, \quad \nu = \frac{c}{\lambda}; \quad \omega = 2\pi\nu; \quad \hbar = \frac{h}{2\pi} \quad (2.1)$$

where E_p is the energy of photon in joules, h the Planck's constant (6.625×10^{-34} J s), \hbar the reduced Plancks constant equals to $h/2\pi$, c the speed of light (2.998×10^8 m/s), λ the wavelength of light and $\omega = 2\pi\nu$ the angular frequency.

Interference and polarization phenomena of light proved wave nature of light and photoelectric effect the particle nature. The “true” nature of light was understood only

after Maxwell’s formulation of EM theory. Light is *made* of electromagnetic waves which are governed by Maxwell’s equations. Electric and magnetic fields at x at time t are denoted by $E = E(x, t)$ and $H = H(x, t)$ [39]. These fields are not classical but quantum in nature. Similar to Schrödinger and Heisenberg treatments for quantization of material systems, the electric and magnetic fields of light are quantized.

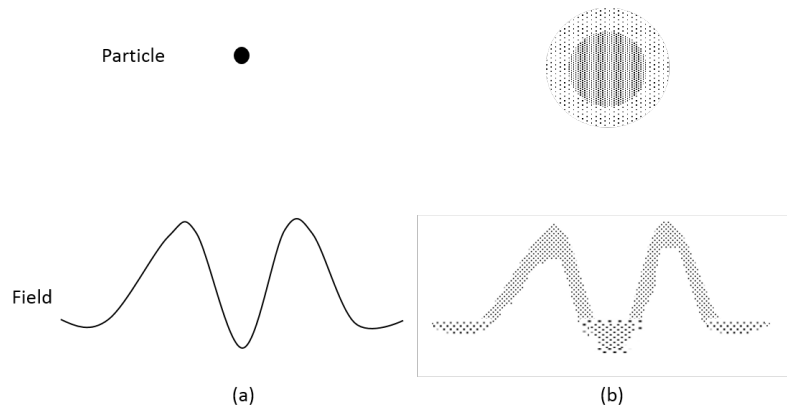


Figure 2.2: (a) Classical representation of a particle and field. (b) Corresponding quantum representation. In (b), dots mean the probability distribution of particle position; field ϕ at x , $\phi(x)$ [39]

Figure 2.2(b) shows the quantization of light photon. The electric field $E(x)$ is defined by a functional $\psi[E(x)]$, within a certain range. A quantum field is a field with vector potential.

2.2.1 Optical modulators

Electrooptic (EO) effect is a widely applied phenomena which forms the working principle of modulators. Materials that respond to electrical and optical fields are used to make devices based on EO effect. Most external modulators were made from materials such as KDP, ADP, BaTiO₃ and LiNbO₃, InP and polymer materials. The list also includes ZnO, ZnS and GaAs. Franz–Keldysh effect marked the arrival of electroabsorption modulators. Initially a high voltage was required to achieve large extinction ratio [23]. Light wave modulation is carried out by changing the absorption (α) or refractive index (n). The major figures of merit of a modulator are as follows [10]:

- modulation speed
- modulation depth
- operation wavelength range

- energy consumption
- insertion loss

The ability to modulate optical signals at particular data transmission rate (bit/s) is known as modulation speed. Modulation depth is nothing but extinction ratio (ER) which is the ratio of maximum to minimum transmittance (T_{\max}/T_{\min}). An ER > 7 dB is preferred in most applications especially involving high data rate transfers and ER \lesssim 4 dB for short-distance data transfers. Modulators are expected to operate at telecommunication wavelength, $\lambda = 0.85, 1.3, 1.5 \mu\text{m}$. Energy consumption is measured with fJ/bit. Energy efficient modulators should operate with few fJ/bit for higher data connection speed. Insertion loss (IL) refers to the system energy efficiency. Derivations and explanations for ER and IL are provided in further chapters.

2.2.1.1 Operation Principle

Modulation happens in a waveguide when change in absorption (α) or refractive index (n) occurs. These changes are based on Pockel's effect, Franz-Keldysh effect, quantum confined Stark effect (QCSE), exciton-bleaching or tunable carrier density effect and plasma or injected carrier effect [23]. Many reported waveguide structures are single waveguide, Mach-Zehnder, directional coupler etc. First, the design procedure of a waveguide modulator is considered. The absolute values of the absorption coefficient (α) and refractive index (n) and their change with applied voltage (V) or carrier injection are determined. At the initial stage, such values are taken from literature. Mixed crystals such as ternary or quaternary are used for semiconductor waveguides and necessary parameters are obtained using linear or quadratic approximation of binary materials by extrapolating the fractional content values.

Waveguide characteristics are strongly dependent on the waveguide core and cladding materials as the optical confinement factor depends on the refractive index profile. There are five important factors pertaining to intensity modulators:

- on/off ratio
- voltage required for on/off
- 3-dB bandwidth

- insertion loss
- chirping

The on/off ratio is an important parameter which is usually 15 or 20 dB. It is defined as the ratio of incident light intensity (P_{in}). It is given as follows:

$$\left[\frac{\text{on}}{\text{off}} \right] = -10 \log_{10} \left(\frac{P_{\text{out}}}{P_{\text{in}}} \right) \quad (2.2)$$

In electroabsorption materials, the transmitted light intensity is calculated using the absorption coefficient with the incident light intensity as follows:

$$\frac{P_{\text{out}}}{P_{\text{in}}} = \exp(-\Gamma \cdot \Delta\alpha \cdot L) \quad (2.3)$$

where Γ is the optical confinement factor, $\Delta\alpha$ the change in absorption coefficient and L the sample length.

The change in absorption coefficient ($\Delta\alpha$) strongly depends on the applied voltage (V_{in}) and wavelength of incident light (λ). Normally, the smaller the applied voltage, the better for operation of electronic circuits. For instance, a 2 V peak-to-peak voltage is needed for high-speed operation (>10 Gb/s). The 3-dB bandwidth is determined by the device capacitance when the device is operated in reverse bias condition, except when it is operated by carrier injection with very slow speed such as a few nanoseconds. When the speed is limited by the device capacitance, the 3-dB bandwidth is calculated as follows [23]:

$$[f_{3\text{dB}}]_1 = \frac{1}{\pi RC} \quad (2.4)$$

where R is the load resistance and C the capacitance. The device capacitance is proportional to the length of the sample (L , say $5 \mu\text{m}$) and width W .

2.3 Theory of waveguides

Waveguides are the most basic components of an optoelectronic system. They form the building blocks of such systems. A suitable combination of active (Si, graphene) and passive materials (hBN, SiC, SiON) makes an efficient waveguide. For effective propagation in a waveguide, refractive index (n) of core material should be higher than other layers, such that $n_1, n_2 < n_3$ and $n_3 > n_4$.

2.3. Theory of waveguides

Materials are chosen based on their optoelectronic properties and response to electrical and optical signals. An electro-optic modulator requires a nonlinear material that could modulate optical signal with electrical input at ultrafast rate. Reflecting, propagating and confining light waves within a specified volume are the fundamental characteristics of a waveguide. Materials with excellent optical and electrical properties are of particular interest for designing waveguides. A multilayer rib waveguide is made of layers with differing refractive indices to reduce leaky modes. In our study, we will be studying modes that effectively confine EM field within core Si and graphene.

Dielectric slab waveguides have been studied extensively in literature. To begin with, the standard problem of reflection and refraction at an interface between two isotropic dielectric media is considered. This results in Snell's laws, Fresnel's laws for reflection and transmission coefficients and the expressions for phase shift on reflection of a plane wave at a dielectric interface. This leads to derivation of the eigenvalue equation for a three-layer dielectric interface. Electromagnetic mode treatment of dielectric slab yields an identical eigenvalue equation.

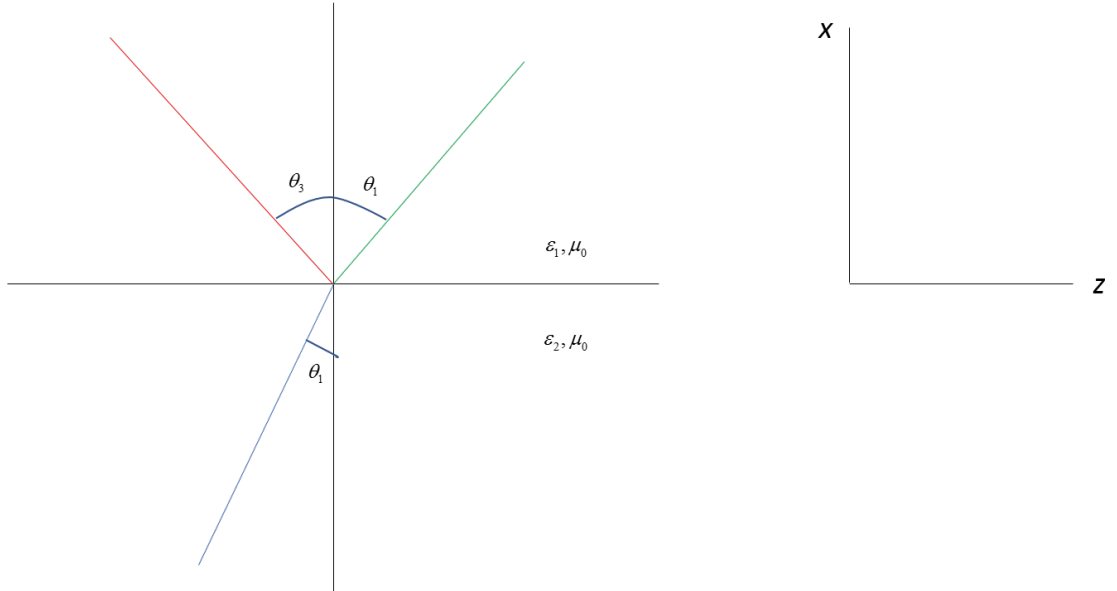


Figure 2.3: Incident (\mathbf{E}_i), reflected (\mathbf{E}_r) and transmitted rays (\mathbf{E}_t) at a plane interface between two dielectric media.

Figure 2.3 shows a plane interface ($x = 0$) in the $y - z$ plane between two media characterized by ε_1, μ_0 and ε_2, μ_0 . A plane wave is incident in the $x - z$ plane from medium q on this interface. Here we assume that the incident (\mathbf{E}_i), reflected (\mathbf{E}_r) and transmitted (\mathbf{E}_t) rays are coplanar and corresponding equations are given as follows:

1. Incident wave: $\mathbf{E}_i = \mathbf{E}_1 e^{-j\omega t} \exp[ikn_1(-x \cos \theta_1 + z \sin \theta_1)]$
2. Reflected wave: $\mathbf{E}_r = \mathbf{E}_3 e^{-j\omega t} \exp[ikn_1(x \cos \theta_3 + z \sin \theta_3)]$
3. Transmitted wave: $\mathbf{E}_t = \mathbf{E}_2 e^{-j\omega t} \exp[ikn_1(x \cos \theta_2 + z \sin \theta_2)]$

where $k = \omega(\mu_0 \varepsilon_0)^{1/2} = 2\pi/\lambda$; n_1 and n_2 are the refractive indices in media 1 and 2; θ_1 , θ_2 and θ_3 are incident, refraction and reflection angles, respectively.

2.3.1 Planar waveguides

There are various types of waveguides and out of which is the planar waveguide. This two-dimensional waveguide enables confining light in one direction (y) and allow to spread in other direction (x). Geometry of simple planar waveguide is shown in Fig. 2.4. For a 3-layer asymmetric planar waveguide, the refractive indices are related as $n_c < n_s < n_g$ such that incoming light is confined within the guiding core. When indices of substrate (n_s) and upper cladding (n_c) are equal, $n_s = n_c$, yields a symmetric guide.

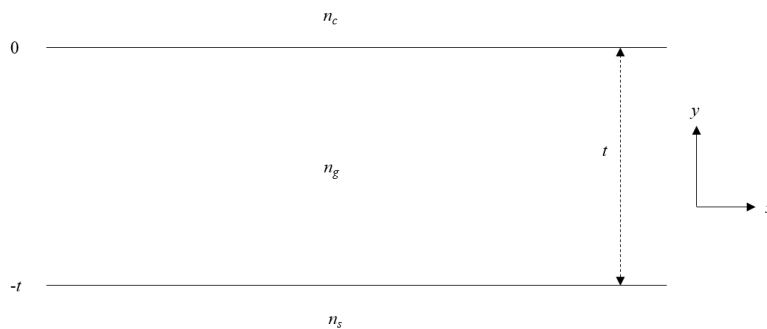


Figure 2.4: A planar waveguide. The refractive indices of guide, upper cladding, and substrate are denoted by n_g , n_c and n_s , respectively.

In the waveguide shown in Fig. 2.4, refractive index (n) is taken as a constant value within chosen regions of the waveguide. Many waveguides have graded index since the refractive index changes gradually.

2.3.2 Dielectric slab waveguide

Consider a three-layer dielectric slab waveguide (Fig. 2.5) with material refractive indices n_1 , n_2 and n_3 such that $n_1 > n_2 \geq n_3$. This variation in refractive indices of the material results in an asymmetric waveguide for $n_2 \neq n_3$ and a symmetric waveguide for $n_2 = n_3$.

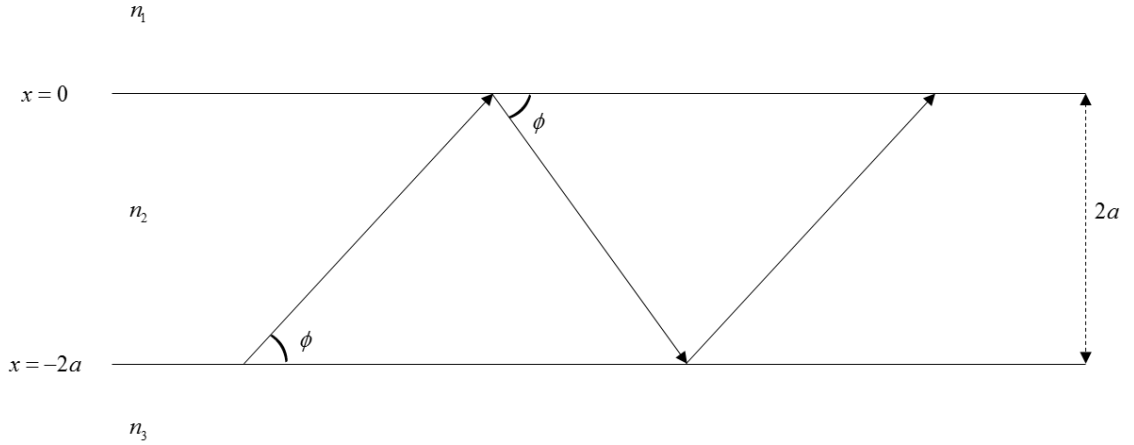


Figure 2.5: Ray of light in a dielectric slab waveguide.

As shown in Fig. 2.5, light ray undergoes total internal reflection at each interface, thus light is trapped within the core layer of the waveguide. This is known as guided mode. Waves propagate in the z -direction as $\exp(i\beta z)$. The longitudinal propagation constant, β , is related to the ray angle ϕ by $\beta = n_1 k \cos \phi$ and hence it follows the propagation constant β is constrained for guided modes as follows:

$$n_1 k \geq \beta \geq n_2 k \geq n_3 k \quad (2.5)$$

Here the minimum value of β for guided propagation, or the cut-off condition, for the mode is $n_2 k$.

2.3.3 Rib waveguide

Silicon-on-Insulator (SOI) waveguides with dimensions greater than hundreds of nanometers support multiple modes but are not preferred for photonic circuits as presence of multiple modes will affect the performance. A simple expression for single-mode condition (SMC) was first proposed by Soref *et. al* [40]

$$\frac{W}{H} \leq 0.3 + \frac{r}{\sqrt{1-r^2}} \quad (\text{for } 0.5 \leq r < 1) \quad (2.6)$$

where r is the ratio of slab height to overall rib height and W/H is the ratio of waveguide width to overall rib height.

2.3.3.1 Guided modes

Maxwell's equations in terms of refractive index n_j ($j = 1, 2, 3$) of the three layers, and assuming the magnetic permeability is everywhere the same as that of free space μ_0 , are given by [38],

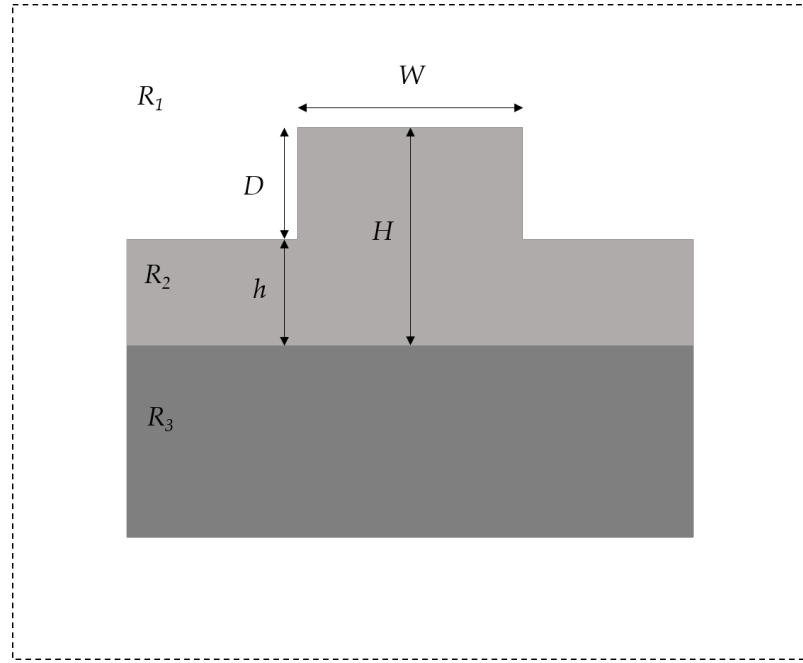


Figure 2.6: A SOI rib waveguide with R_1 (air, $n = 1$), R_2 (Si, $n = 3.477$) and R_3 (SiO₂, $n = 1.444$). Here $h=rH$, for $r < 0.5$. For computational purposes broken lines denote air region which covers all around the waveguide.

$$\nabla \times \mathbf{H} = n_j^2 \varepsilon_0 \frac{d\mathbf{E}}{dt} \quad (2.7)$$

$$\nabla \times \mathbf{E} = -\mu_0 \frac{d\mathbf{H}}{dt} \quad (2.8)$$

$$\nabla \cdot \mathbf{E} = 0 \quad (2.9)$$

$$\nabla \cdot \mathbf{H} = 0 \quad (2.10)$$

where cross denotes a vector product, \mathbf{H} and \mathbf{E} are respectively the magnetic and electric field vectors and ε_0 and μ_0 denote dielectric permittivity and magnetic permeability of vacuum, respectively, n the refractive index of the medium and t the time variable.

To obtain a complete description of all modes supported by dielectric waveguides, the Maxwell's equations (2.1)–(2.4) must be solved. Modes of slab waveguide can be classified as transverse electric (TE) and transverse magnetic (TM). The TE modes have no electric field component along the direction of wave propagation whereas TM modes have no longitudinal magnetic field component.

We now move on to plasmonic waveguides made of materials with complex refractive indices, in other words, complex dielectric constants ($\varepsilon_1 + j\varepsilon_2$), where ε_1 denotes the real part and ε_2 the imaginary part. Chapter 3 deals with complex dielectric constants in detail.

2.3.3.2 Plasmonic waveguides

Electromagnetic wave propagating through a material (polarizable) medium is polarized and couples with the medium. This coupled mode of excitation results in a polariton. In a cloud of electrons or an electron plasma, such coupled modes are termed plasmon-polaritons [41, 42]. Resulting polaritons in bulk traverse through an unbounded medium whereas surface polaritons that result due to the coupling of incident radiation with surface dipole excitation and propagate along the interface between two media. Existence of surface plasmons is in the boundary of semiconductor layers in the plasmonic waveguide. Such waveguides are made of semiconductor materials whose electrons behave similar to a quasifree electron gas.

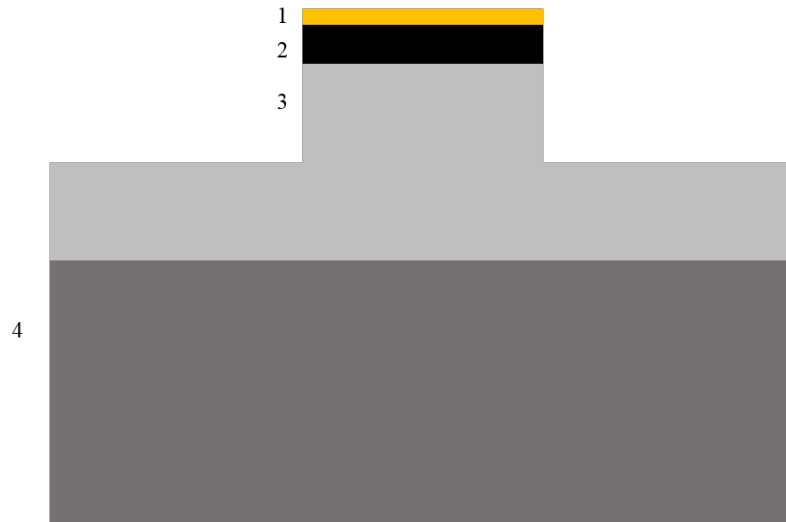


Figure 2.7: A hybrid plasmonic waveguide: (1) metal; (2) dielectric; (3) silicon; (4) SiO₂.

Figure 2.7 shows a typical hybrid plasmonic waveguide. In a graphene-based plasmonic waveguide, usually graphene is sandwiched between dielectric layers. As phonons are quanta associated with vibration of a crystal lattice, plasmons are quanta of oscillations of surface charges induced by external electric fields in the boundary.

Surface plasma waves occur in a dielectric–metal interface (Fig. 2.8), where dielectric has a positive dielectric constant ($+\epsilon_1$) and metal with negative real part of dielectric constant ($-\epsilon_1$). Properties of plasmonic waves are based on solving Maxwell’s equations for interface between two semi-infinite and isotropic dielectric media. In such waveguides, the thickness of metal layer is much lower than the dielectric layer. For example, in a graphene–silicon hybrid waveguide, the graphene–boron nitride (BN) interface acts as

2.3. Theory of waveguides

metal–dielectric for certain gate voltages; thickness of graphene is 0.33 nm to that of BN is 10 nm. Strong light confinement can be achieved in a plasmonic waveguide.

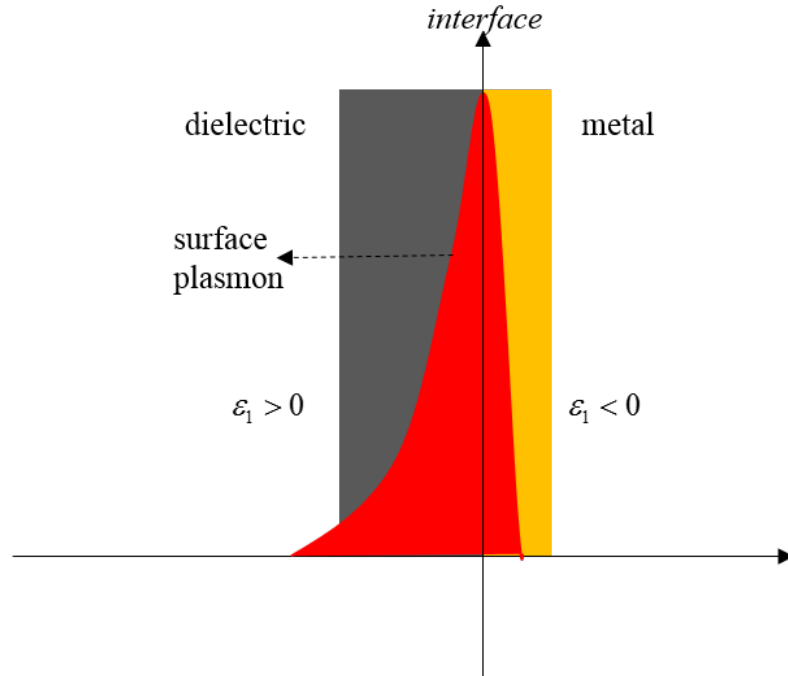


Figure 2.8: Surface plasmons originating in a metal–dielectric interface. ϵ_1 denotes the real part of dielectric constant.

A waveguide mode that arises in a dielectric couples with the surface plasmon mode in the metal. This results in an evanescent wave as the wave amplitude exponentially decreases with increasing distance from the metal–dielectric interface. Figure 2.9 shows the scheme of coupling of waveguide mode with dielectric mode in a plasmonic waveguide.

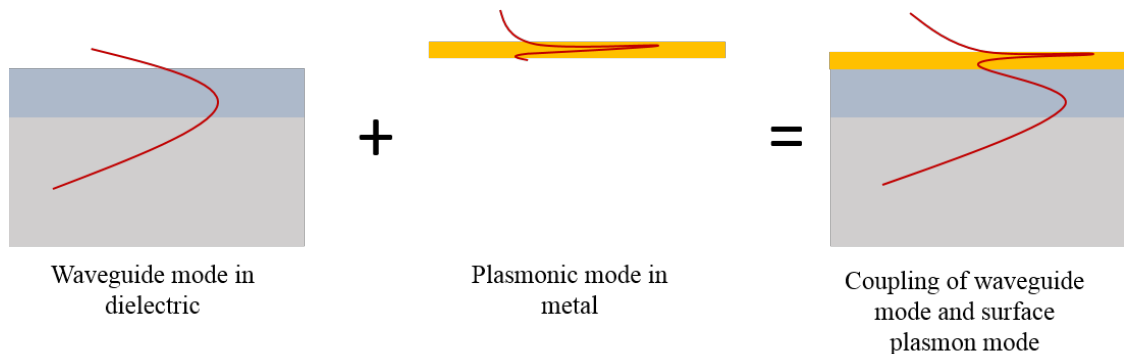


Figure 2.9: Coupling scheme of waveguide and plasmonic modes in a metal–dielectric interface.

2.3.4 General solution to Maxwell's equations

Maxwell's equations govern the propagation of light through optical media and its interaction with the optical media. Thus derived equations are valid for entire frequency spectrum and differential form are stated as follows:

$$\begin{aligned}
 \nabla \times E + \frac{\partial B}{\partial t} & \text{ Faraday's Law} \\
 \nabla \times H - \frac{\partial D}{\partial t} & \text{ Maxwell - Ampere Law} \\
 \nabla \cdot D = \rho & \text{ Gauss' Law} \\
 \nabla \cdot B = 0 & \text{ Gauss' Law Magnetic}
 \end{aligned} \tag{2.11}$$

Considering a lossless dielectric isotropic material, the electric \mathbf{E} and magnetic \mathbf{H} field vectors are related through the constitutive equations

$$D = \varepsilon_0 \mathbf{E} + P$$

$$B = \mu_0 \mathbf{H}$$

where D is the electric flux density (coulombs/m²), B the magnetic flux density (webers/m²), ρ the charge density, μ_0 the magnetic permeability of vacuum ($= 4\pi \times 10^{-7}$ F/m) and ε_0 the vacuum dielectric permittivity.

Assuming a complex time dependence through the factor $\exp(j\omega t)$, where j is an imaginary unit, ω the angular frequency and t the time. Substituting for B and D , the time derivatives in the above equations may be rewritten as follows:

$$\nabla \times E + j\omega\mu H = 0 \tag{2.12}$$

$$\nabla \times H - j\omega\varepsilon E = 0 \tag{2.13}$$

Taking curl of above equations and substituting from Maxwell's equations yields,

$$\nabla \times \nabla \times E - \omega^2 \mu \varepsilon E = 0 \tag{2.14}$$

$$\nabla \times \nabla \times H - \omega^2 \mu \varepsilon H = 0 \tag{2.15}$$

Using the following vector identity

$$\nabla \times \nabla \times A = \nabla(\nabla \cdot A) - \nabla^2 A \tag{2.16}$$

the first terms of equations 2.14 and 2.15 becomes

$$\nabla(\nabla \cdot E) - \nabla^2 E - \omega^2 \mu \varepsilon E = 0 \tag{2.17}$$

$$\nabla(\nabla \cdot H) - \nabla^2 H - \omega^2 \mu \varepsilon H = 0 \quad (2.18)$$

These equations can be written as follows:

$$\nabla^2 E + k^2 E = 0 \quad (2.19)$$

$$\nabla^2 H + k^2 H = 0 \quad (2.20)$$

where $k = \omega \sqrt{\varepsilon \mu_0}$.

Equations 2.17 and 2.18 or 2.19 and 2.20 provide the general solution to Maxwell's equations using properties of the material and angular frequency of the incoming electromagnetic signal. To obtain an optical mode, these equations need to be solved for the chosen waveguide structure.

2.3.4.1 Basic Equation

Expanding the curl operator in equation 2.17 using rectangular coordinate system results in

$$\frac{\partial^2 \mathbf{E}}{\partial x^2} + \frac{\partial^2 \mathbf{E}}{\partial y^2} + \frac{\partial^2 \mathbf{E}}{\partial z^2} = -\omega^2 \mu \varepsilon \mathbf{E} \quad (2.21)$$

The field vector \mathbf{E} can be separated into the individual components such that there is an equivalent differential equation for each of the vector components:

$$\frac{\partial^2 \mathbf{E}_x}{\partial x^2} + \frac{\partial^2 \mathbf{E}_x}{\partial y^2} + \frac{\partial^2 \mathbf{E}_x}{\partial z^2} = -\omega^2 \mu \varepsilon \mathbf{E}_x \quad (2.22)$$

$$\frac{\partial^2 \mathbf{E}_y}{\partial x^2} + \frac{\partial^2 \mathbf{E}_y}{\partial y^2} + \frac{\partial^2 \mathbf{E}_y}{\partial z^2} = -\omega^2 \mu \varepsilon \mathbf{E}_y \quad (2.23)$$

$$\frac{\partial^2 \mathbf{E}_z}{\partial x^2} + \frac{\partial^2 \mathbf{E}_z}{\partial y^2} + \frac{\partial^2 \mathbf{E}_z}{\partial z^2} = -\omega^2 \mu \varepsilon \mathbf{E}_z \quad (2.24)$$

2.3.4.2 Analytical solution

Consider the planar waveguide shown in Fig. 2.4, the field quantities are taken to be varying along only one direction. In this 3-layer (substrate, core, cladding) waveguide structure, assuming the incoming light is confined along y-axis, the partial derivative along x-axis is written as $\frac{\partial}{\partial x} = 0$. Now we introduce a parameter ϕ such that

$$\phi = \begin{cases} \mathbf{E}_x & \text{For TE mode} \\ \mathbf{H}_x & \text{For TM mode} \end{cases} \quad (2.25)$$

then equations 2.19 and 2.20 can be written as

$$\frac{\partial^2 \phi}{\partial y^2} + (k_0^2 n^2 - \beta^2) \phi = 0 \quad (2.26)$$

2.3. Theory of waveguides

where $n = \varepsilon^2$ and β the phase constant.

For two-dimensional waveguides, the TE mode has no longitudinal component of the electric field, $E_z = 0$. The non-vanishing field components are defined as follows:

$$\mathbf{H}_y = \frac{\beta}{\omega\mu} \mathbf{E}_x \quad (2.27)$$

$$\mathbf{H}_z = \frac{1}{j\omega\mu} \frac{\partial \mathbf{E}_x}{\partial y} \quad (2.28)$$

$$\mathbf{E}_x = \frac{\beta}{\omega\varepsilon} \mathbf{H}_y \frac{1}{j\omega\mu} \frac{\partial \mathbf{E}_x}{\partial y} \quad (2.29)$$

For TM modes, there is no magnetic field along the propagation direction, $H_z = 0$. The only non-vanishing field components are given as follows:

$$\mathbf{E}_y = \frac{\beta}{\omega\varepsilon} \mathbf{H}_x \quad (2.30)$$

$$\mathbf{E}_z = \frac{1}{j\omega\varepsilon} \frac{\partial \mathbf{H}_x}{\partial y} \quad (2.31)$$

$$\mathbf{H}_x = \frac{\beta}{\omega\mu} \mathbf{E}_y \frac{1}{j\omega\mu} \frac{\partial \mathbf{E}_z}{\partial y} \quad (2.32)$$

Solutions to equation 2.26 are either exponential or sinusoidal functions of y in each regions of the waveguide. The particular function is dependent on the factor $(k_0^2 n^2 - \beta^2)$. In the 3-layered waveguide, for a guided wave, the phase constant β will satisfy the condition $kn_s \leq \beta \leq kn_f$. Equation 2.26 will then have following solution [43]:

$$\phi = \begin{cases} A_c \exp(-\alpha_c y) & 0 \leq y \\ A_f \cos k_f y + B_f \sin k_f y & -t \leq y \leq 0 \\ A_s \exp[\alpha_s (y + t)] & y \leq -t \end{cases} \quad (2.33)$$

where A_f , B_f , A_c and A_s are arbitrary constants determined by boundary conditions which must be satisfied at the interface of two media. Values α_c , α_s and k_f are given as:

$$\alpha_c = \sqrt{\beta^2 - k^2 n_c^2} \quad (2.34)$$

$$\alpha_s = \sqrt{\beta^2 - k^2 n_s^2} \quad (2.35)$$

$$k_f = \sqrt{k^2 n_f^2 - \beta^2} \quad (2.36)$$

These are well-confined modes normally referred to as TE₀/TM₀ and TE₁/TM₁ modes. For $\beta > kn_f$, the function ϕ must be exponential in all three regions, which would imply

infinite energy in the upper and lower cladding of the waveguide [44]. Of course, such a mode will not exist. A substrate radiation mode is obtained for a value of $kn_s > \beta > kn_c$ and this mode is confined at the interface of the upper cladding but varies sinusoidally in the substrate. Such a mode can only be supported over short distances as it losses energy from the guiding region to the substrate region and hence not very useful in transmission of signal. It may, however, prove useful in tapered coupler applications. The number of modes that can be supported by a waveguide depends on the thickness of the waveguiding layer and on the material properties of the waveguide as well as the frequency. This implies that for a given waveguide thickness and given refractive indices, there is a cut-off frequency, ω_c below which waveguiding cannot occur. In optical waveguide applications, the wavelength is of fixed value, the problem is therefore to determine the refractive index values for which a particular mode can be supported. It can be shown that for the asymmetric waveguide, the refractive indices are related through the following equation,

$$\Delta n = n_f - n_s \geq \frac{(2m + 1)^2 \lambda_0^2}{32n_f t^2}$$

where $m = 0, 1, 2, \dots$ is the mode number, λ_0 the vacuum wavelength and t the thickness of the waveguiding layer.

The properties of planar waveguides can be thus studied using analytical methods. Exact analytical solutions can also be obtained for planar guides with stepped refractive index values but for a continuously graded index guide, it is rather difficult to obtain exact analytical solutions. Planar waveguides have a limited range of use due to 1-D optical confinement, whereas in many applications, 2-D optical confinement is preferred which can be provided by channel or 3-D waveguides. It is not possible to obtain exact analytical solutions to such waveguides, except in very special cases, and many practical waveguides have complex structures with arbitrary index distribution. The propagation mode is often a hybrid mode, E_{mn}^x (the main components of the electromagnetic field being E_x and H_y) or E_{mn}^y (the main components of the electromagnetic field being E_y and H_x) modes, where subscripts m and n refer to the mode order such that $m, n = 1, 2, 3, \dots$, corresponding to the total number of extrema appearing in distribution of the electric fields in both x and y directions. In reality, one of the modes is dominant, TE^y in the case of E_{mn}^x mode and TM^y in the case of E_{mn}^y mode where the existence of such modes compounds the complexity of obtaining an analytical solution. Amongst the many reasons,

following factors show the difficulties in obtaining an exact analytical solution to Maxwell's equations:

- the electromagnetic field may extend beyond the guiding core
- anisotropic and non-linear optical materials may be used to extend the range of waveguide applications
- materials with complex refractive index $(n_1 + jn_2)$ such as graphene

2.4 Finite Element Method

The characteristics of light wave propagation in a waveguide are studied using numerical methods through which modelling and simulations of different waveguides can be carried out. This reduces time and cost involved in choosing a suitable design before experimentation. These methods are adopted for finding approximate solutions to boundary value problems using partial differential equations. To name few: Galerkin and moment methods, Transfer matrix method, Finite-element-based methods, Finite-difference-based methods, Transmission line matrix method, Monte Carlo method, etc., broadly classified as computational photonics. The book written by Rahman and Agrawal [45] explains solving waveguide problems using Finite Element method in detail.

Finite element method is relatively a new and powerful numerical method used in the analysis of optical waveguide problems. Using this approach, any optical waveguide cross-section can be divided into triangular elements and the field components within the elements are approximated by polynomial functions. The versatility of the method ensures that each element can be of a different dielectric material, anisotropic, non-linear or lossy. The finite element formulation is usually established using a variational technique [46, 47].

Vector variational formulations of Maxwell's equations provide a means of solving wave propagation problems where all six electromagnetic field components are required whereas scalar formulations are inadequate [48]. Such formulation also provides a better convergence where the natural boundary condition is that of Dirichlet. Using a standard procedure, a variational formulation can be obtained as follows [49]:

1. Find the variational integral whose first variation is zero for the given boundary conditions.

2.4. Finite Element Method

2. Choose an appropriate trial function and expand the field components as a sum of the trial functions.
3. Substitute the trial fields in the variational integral and find the first variation and equate it to zero
4. The resulting simultaneous equations from the weak formulation of the boundary value problem are equivalent to a standard eigenvalue matrix equation of the form $Ax - \lambda x = 0$. This equation can then be solved by one of several standard matrix algorithms.

Different variational formulations have been proposed for use with FEM. The simplest of these is the scalar approximation, which is useful where the field can be said to be predominantly TE or TM. It has been applied to the analysis of different types of waveguide problems [50–52]. For practical waveguides, the scalar formulation is not accurate since the modes are hybrid. To overcome this shortcoming of the scalar approximation, a vector formulation with at least two field components is used. Both the \mathbf{E} and \mathbf{H} field vector variational formulations or combinations of the two have been used. The natural boundary condition for the \mathbf{E} field is that of a magnetic wall. This implies a conducting electric boundary wall, $\mathbf{n} \times \mathbf{E} = 0$. Such a condition is however difficult to implement on arbitrarily shaped guide walls. Therefore, \mathbf{E} -field formulation requires special care in preserving the continuity of the transverse components of the fields. It is difficult to implement the natural boundary condition using this method for guides with arbitrary index distribution. However, the two axial components on which the formulation is based are the least essential of the six vector field components. Also, this method suffers from spurious modes which can be reduced at the expense of increased computational cost [52].

Vector \mathbf{H} field formulation has been extensively used due to its ability to solve generally anisotropic waveguide problems [46, 47]. Since the natural boundary condition is that of an electric wall there is no need to explicitly enforce this condition. This formulation can be given as follows [47]:

$$\omega^2 = \frac{\int (\nabla \times H)^* \cdot \varepsilon^{-1} \cdot (\nabla \times H) d\Omega}{\int H^* \cdot \mu^{-1} \cdot H d\Omega} \quad (2.37)$$

where ε and μ are the permittivity and permeability of a loss-free medium. Applying Raleigh–Ritz procedure to equation 2.37 will yield a similar matrix equation as in the

vector \mathbf{E} formulation. A serious shortcoming of this equation is the appearance of spurious solutions which are attributed to the fact that the divergence condition $\nabla \cdot \mathbf{H} = 0$ is not satisfied. Rahman and Davies, in their study, enforced this divergence condition by imposing a ‘penalty’ function that could eliminate these spurious modes [46].

Almost all natural phenomena can be described using differential/integral equations. Deriving such equations may not pose difficulty, however, solving them by analytical methods is a formidable task. Nowadays many simulation programs are used which has reduced the time required for calculations to a great extent. Finite element method is a theoretical method wherein the domain of study is “built” using a finite number of elements. This method is built using mathematical equations that define field in each element. Therefore, the shape of elements plays a significant role in this method. In other words, it is a method by which a complex domain is ”broken” into smaller elements and assigning approximating functions in each element to solve them mathematically [45]. Elements are chosen such that the shape and size of each element covers as closely as possible the geometry of the chosen domain (Fig. 2.10).

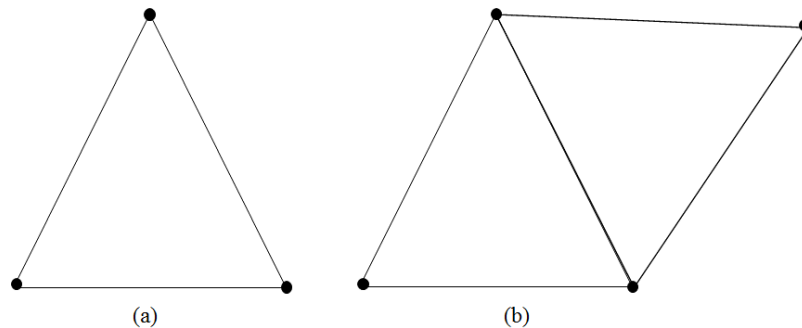


Figure 2.10: Triangular elements used in FEM to cover chosen domain: (a) one element; (b) two elements with a common boundary. Source: Rahman and Agrawal [45].

Investigation of light wave propagation is of prime importance in the characterization of waveguides. In this regard, finite element method (FEM) has been established as one of the most powerful and versatile methods used in the analysis of optical waveguides [46,47, 53–55] in numerical modelling. FEM allows each element to have a different but piecewise-constant refractive index ($\varepsilon_r = n^2$) which enables applying FEM to analyse arbitrarily shaped diffused anisotropic waveguides. Optical waveguides are characterized by solving Maxwells equations which involves calculating eigenfunctions, or modes of the waveguide, at a fixed frequency and the eigenvalues that correspond to the axial propagation constant

of the wave in the waveguide. The graphene/silicon hybrid waveguide has hybrid nodes and is generally anisotropic [49].

The basic idea of the finite element method is to divide the region of interest into a large number of finite elements or sub-regions. These elements may be one, two or three-dimensional. The idea of representing a given domain as a collection of discrete elements is not new, it is recorded that ancient mathematicians estimated the value of π by representing the circle as a polygon with a large number of sides. FEM has been used to solve complex engineering problems such as structural analysis in aircrafts, fluid flow, heat transfer and mass transport. Later on, this method found its way in solving electromagnetic field problems. Waveguide problems are described by using integral or differential equations. Then these equations are solved using numerical methods. FEM has established itself as one of the most powerful and accurate technique for solving problems associated with integrated optical waveguides and microwave devices. The versatility of the method allows elements of various shapes to be used to represent an arbitrary cross-section [49].

2.4.1 Definition

Finite elements, as the name suggests, the domain of study will be divided into smaller elements of finite size and numbers, with each element having a suitable approximating function [45]. These elements construct a finite element space comprising field variables of partial differential equations and integral equations. Elements are of 1D, 2D and 3D of which 2D denotes a triangular element. The 2D element is mostly used for studying waveguides. A finite element (K, P, N) is defined as follows [56]:

- $K \subseteq R^n$ a domain with piecewise smooth boundary – the element domain
- P a finite-dimensional space of functions on K – the shape function
- $N = \{N_1, N_2, \dots, N_k\}$ a basis for P – the nodal variables

Let us now see how to form triangular finite elements. Consider K as any triangle, P_k the set of polynomials of degree $\leq k$. Dimensions of P_k will follow the relation:

$$\dim P_k = \frac{1}{2}(k+1)(k+2) \quad (2.38)$$

2.4. Finite Element Method

Let us consider z_1, z_2 and z_3 the vertices of triangle K and L_1, L_2 and L_3 linear functions defining the lines joining the vertices of K (Fig. 2.11).

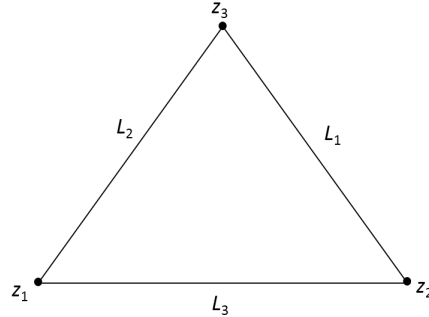


Figure 2.11: A linear Lagrange triangle.

In Fig. 2.11, $k = 1$, therefore using equation 2.38, $\dim P_1 = 3$. Using this equation we can derive for $k = 2, 3, 4, \dots$. Apart from Lagrange, we have other elements called Hermite and Argyris (Fig. 2.12). In quartic Hermite, $k = 4$ yields 15 dimensions and quintic Argyris, $k = 5$ results in 21 dimensions [56].

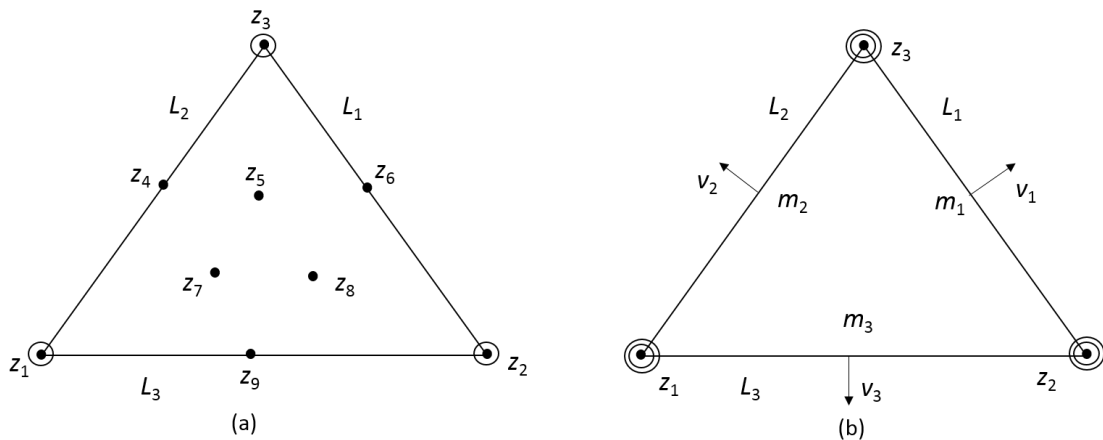


Figure 2.12: Quartic Hermite and quintic Argyris triangles.

2.4.2 Basic concepts

The major key ideas in FEM are

- 1 discretization of the region of interest into elements
- 2 using interpolating polynomials to describe the variation of the field within each of the elements

Instead of differential equations for the system under investigation, variational expressions are derived and the piecewise continuous function is approximated by a piecewise

continuous polynomial within each element. From the equivalent discretized model contribution from each element, an overall system is assembled. This can be regarded as a sub-class of the Ritz–Galerkin method in which the trial functions are replaced with polynomial functions. In the classical analytical procedure where the region is not subdivided into regions, only the simplest structures with basic material properties can be considered. The finite difference method is the simplest of all the discretization procedures and in the traditional version uses a rectangular grid (Fig. 2.13) with nodes at the intersections of the orthogonal straight lines. Such an approach is not particularly suited to irregular geometries with curved boundaries and interfaces since the intersections with the gridlines could be at points other than at the nodes. It is not well suited to the analysis of problems in which there are steep variations of the field [49].

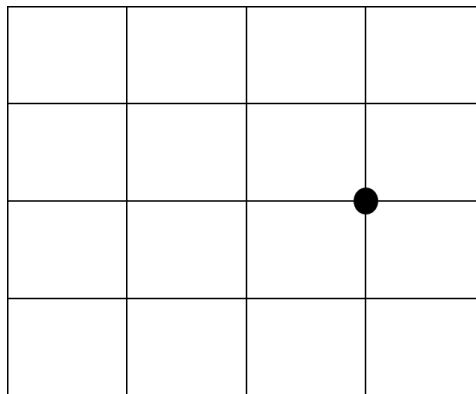


Figure 2.13: Rectangular grid: domain division; (●) a node.

On the other hand, FEM allows the domain to be subdivided into elements or sub-regions. These elements can be of various shapes such as triangles and rectangles thus enabling the use of irregular grid for complex waveguide structures. The method can therefore be easily used to analyse problems with steep variations of the field and can be adapted quite readily to anisotropic and inhomogeneous problems. The accuracy of this method could be systematically increased by increasing the number of elements. The method does not rely on the variational method for its establishment; it could be established by using the Galerkin method, which is a weighted-residual method. The importance of this last point is that the method could be applied in cases where no variational formulation exists or cannot be found [49].

The steps involved in FEM can be summarized as follows:

1. discretize the domain under investigation into sub-domains or elements. The accu-

2.4. Finite Element Method

racy of the method depends on the level of discretization. It is recommended to use more elements in areas where the field is thought to have steep variations. It is also not advisable to use elements across physical boundaries or interfaces. For symmetrical domains, the mesh should follow the same type of symmetry.

2. the functional for which the variational principle should be applied for the elements are then derived. In deciding on the interpolation function, certain continuity conditions must be satisfied by the interpolation function across inter-element boundaries. These requirements are normally obvious from physical consideration of the problem. It is however also necessary that the function have to be an admissible member of the Ritz and Galerkin methods. It follows that the polynomial function has to remain unchanged under a linear transformation from one coordinate system to the other.
3. assemble all the element contributions to for a global matrix.
4. solve the system of equations that is obtained, in this case a matrix equation.

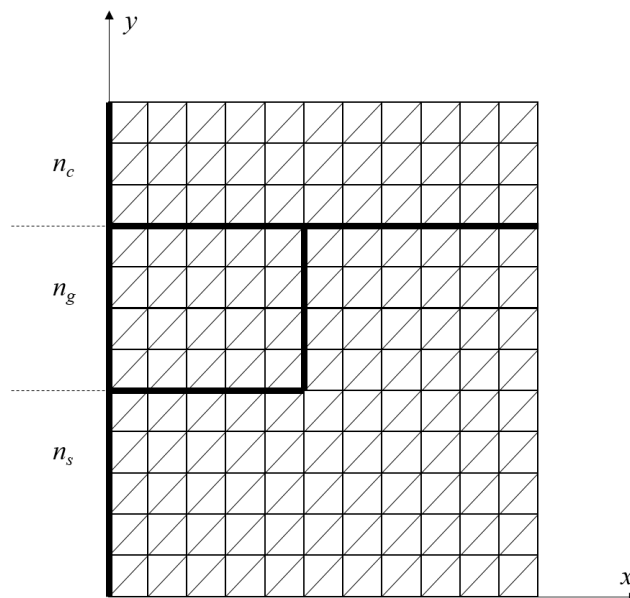


Figure 2.14: Mesh formation in FEM. Adapted from Rahman and Agrawal [45].

Figure 2.14 shows how FEM discretization can be applied to a waveguide with different regions, viz., a cladding (n_c), guide (n_g) and substrate (n_s). The elements used in this case are triangular since it is much easier to represent an arbitrary cross-section with triangles rather than with rectangles. In 2-D waveguide analysis, the triangles can be of any order

but the most commonly used triangles are of first and second orders.

2.4.3 Implementation of FEM

Consider the following Helmholtz equation:

$$\nabla^2\phi + k^2\phi = 0 \quad (2.39)$$

as the governing equation in a waveguide problem, defined within the domain Ω , where ϕ is the electric or magnetic field component ∇^2 is a Laplacian operator defined as

$$\nabla^2 = \frac{\partial^2}{\partial x^2} + \frac{\partial^2}{\partial y^2} + \frac{\partial^2}{\partial z^2} \quad (2.40)$$

In equation 2.39, k^2 is a constant related to frequency and given also that Γ_f and Γ_n are boundaries within the said domain, then the following boundary conditions may be defined:

- (1) on the boundary Γ_f (Dirichlet boundary condition)

$$\phi = \hat{\phi} \quad (2.41)$$

- (2) on the boundary Γ_n (Neumann boundary condition)

$$\frac{\partial\phi}{\partial n} = n \cdot \nabla\phi = \hat{\psi} \quad (2.42)$$

where \mathbf{n} is the outward normal unit vector. The gradient operator, is defined by the following matrix differential operator

$$\nabla = \begin{bmatrix} \partial/\partial x \\ \partial/\partial y \\ \partial/\partial z \end{bmatrix} \quad (2.43)$$

in the Cartesian system of co-ordinates. Taking into consideration the stated boundary conditions, the functional for equation 2.39 could be written as (Koshiba, 1990)

$$F = \frac{1}{2} \iiint_{\Omega} [(\nabla\phi)^2 - k^2\phi^2] d\Omega - \iint_{\Gamma_n} \phi\hat{\psi} d\Gamma \quad (2.44)$$

The stationary requirement of the above functional, $\delta F = 0$, coincides with the governing equation of the problem. The Neumann boundary condition is automatically satisfied in the variational procedure as such it is referred to as the natural boundary condition. The Dirichlet boundary condition however needs to be imposed and is therefore called the

forced boundary condition. The functional for each of the elements of the region could then be written as

$$F = \frac{1}{2} \iiint_e [(\nabla\phi)^2 - k^2\phi^2] d\Omega - \iint_{\Gamma_e} \phi\hat{\psi} d\Gamma \quad (2.45)$$

The functional for the whole of the domain can then be regarded as a summation of the element functions

$$F = \sum_e F_e \quad (2.46)$$

For the n nodes within each element, the field ϕ can be approximated as follows:

$$\phi = \sum_{i=1}^n N_i\phi_i \quad (2.47)$$

where ϕ_i is the i th nodal parameter of the element e and N_i is the interpolation or shape function. The above equation could be written in Matrix form as follows

$$\phi = \{N\}^T \{\phi\}_e \quad (2.48)$$

where the component of the vector $\{\phi\}_e$ is ϕ_i and that of the vector $\{N\}^T$ is the interpolation function N_i , T denotes a transpose, $\{\cdot\}$ and $\{\cdot\}^T$ denotes a column and row vector, respectively.

For convergence of the solution, the shape function N_i must satisfy certain conditions when the functional contains first order derivatives:

- the variable ϕ and its derivatives must include constant terms, and
- the variable ϕ must be continuous at the interface of two adjacent elements.

The first of the two conditions is also known as the completeness condition and is simple to satisfy provided complete polynomial expressions are used in each element. The second of the two conditions is called the compatibility condition. First order elements are the most fundamental and first order polynomials are used with them but higher order elements are used with higher order polynomials. Since the number of nodes within each element coincides with the number of terms in a complete polynomial expansion, the nodes are simply arranged to satisfy the compatibility condition.

2.4.4 Element Equations

To obtain the element equations it is necessary to perform a coordinate transformation. This is because the interpolation function is defined using the local coordinates and hence it is necessary to find a means of linking the global derivatives in terms of the local derivatives. Secondly, the element volume over which the integration has to be carried out needs to be expressed in terms of local coordinates with change of limits as may be appropriate.

Assuming the local coordinates ξ_1 , ξ_2 and ξ_3 have as a corresponding set, the following global coordinates x , y and z as follows:

$$x = x(\xi_1, \xi_2, \xi_3) \quad (2.49)$$

$$y = y(\xi_1, \xi_2, \xi_3) \quad (2.50)$$

$$z = z(\xi_1, \xi_2, \xi_3) \quad (2.51)$$

Using partial differentiation rules, the transformation relation for differentiation can be written as follows

$$\begin{bmatrix} \frac{\partial}{\partial \xi_1} \\ \frac{\partial}{\partial \xi_2} \\ \frac{\partial}{\partial \xi_3} \end{bmatrix} = [J] \begin{bmatrix} \frac{\partial}{\partial x} \\ \frac{\partial}{\partial y} \\ \frac{\partial}{\partial z} \end{bmatrix} \quad (2.52)$$

where the matrix $[J]$ is a Jacobian matrix defined as

$$[J] = \begin{bmatrix} \frac{\partial x}{\partial \xi_1} & \frac{\partial y}{\partial \xi_1} & \frac{\partial z}{\partial \xi_1} \\ \frac{\partial x}{\partial \xi_2} & \frac{\partial y}{\partial \xi_2} & \frac{\partial z}{\partial \xi_2} \\ \frac{\partial x}{\partial \xi_3} & \frac{\partial y}{\partial \xi_3} & \frac{\partial z}{\partial \xi_3} \end{bmatrix} \quad (2.53)$$

The global matrix of the derivatives can then be obtained through an inversion of the Jacobian matrix to give

$$\begin{bmatrix} \frac{\partial}{\partial x} \\ \frac{\partial}{\partial y} \\ \frac{\partial}{\partial z} \end{bmatrix} = [J]^{-1} \begin{bmatrix} \frac{\partial}{\partial \xi_1} \\ \frac{\partial}{\partial \xi_2} \\ \frac{\partial}{\partial \xi_3} \end{bmatrix} \quad (2.54)$$

2.4.5 Line Elements

Line elements (1D) are the most fundamental of all the elements used. These elements can be of

- a) first order
- b) second order, and

c) third order

These are normally used for solving 1D problems. It is necessary to introduce the line coordinates L_1 and L_2 . The relationship between line and Cartesian coordinates is given by

$$\begin{bmatrix} L_1 \\ L_2 \end{bmatrix} = \frac{1}{l_e} \begin{bmatrix} x_2 & -1 \\ -x_1 & 1 \end{bmatrix} \begin{bmatrix} 1 \\ x \end{bmatrix} \quad (2.55)$$

where x_1 and x_2 are the Cartesian coordinates of the edge of the line and the length of the element l_e is given by

$$l_e = x_2 - x_1 \quad (2.56)$$

If the local coordinate is now defined as ξ_1 then

$$L_1 = \xi_1 \quad (2.57)$$

$$L_2 = 1 - L_1 = 1 - \xi_1 \quad (2.58)$$

The transformation relation for differentiation is then given by

$$\frac{d}{dx} = -\frac{1}{l_e} \frac{d}{d\xi_1} \quad (2.59)$$

For integration, the transformation relation is given by

$$\int_e f(x) dx = l_e \int_0^1 f(\xi_1) d\xi_1 \quad (2.60)$$

Using equations 2.59 and 2.60 both the differentiation and integration formulae could be written as

$$\frac{df}{dx} = \frac{1}{l_e} \left(-\frac{\partial f}{\partial L_1} + \frac{\partial f}{\partial L_2} \right) \quad (2.61)$$

$$\begin{aligned} \int_e L_1^k L_2^l dx &= l_e \int_0^1 \xi_1^k (1 - \xi_1)^l d\xi_1 \\ &= l_e \frac{k!l!}{(k+l+1)!} \end{aligned} \quad (2.62)$$

The shape function vector for the linear element and its derivative are given as

$$\{N\} = \begin{bmatrix} L_1 \\ L_2 \end{bmatrix} \quad (2.63)$$

and

$$\{N_x\} = \frac{d\{N\}}{dx} = \frac{1}{l_e} \begin{bmatrix} -1 \\ 1 \end{bmatrix} \quad (2.64)$$

respectively. The modal coordinates (L_1, L_2) of the linear element are given as follows: node 1: $(1, 0)$ node 2: $(0, 1)$ For the quadratic element, the shape function and its derivatives are defined as

$$\{N\} = \begin{bmatrix} L_1(2L_1 - 1) \\ L_2(2L_2 - 1) \\ 4L_1L_2 \end{bmatrix} \quad (2.65)$$

$$\{N_x\} = \frac{l}{l_e} \begin{bmatrix} 1 - 4L_1 \\ 4L_2 - 1 \\ 4(L_1 - L_2) \end{bmatrix} \quad (2.66)$$

The nodal coordinates for nodes 1, 2 and 3 are given as $(1, 0)$, $(0, 1)$ and $(\frac{1}{2}, \frac{1}{2})$, respectively.

2.4.6 Triangular Elements

In practical, most electromagnetic problems are of the two-dimensional type. This makes the use of triangular elements a common practice. These elements can be of either first order, second order or higher order (Fig. 2.15). In applying the first order elements, it can be seen that nodes occur at the vertices of the triangles while nodes are also defined at the middle of the edges for second order elements. In this work, only first order triangular elements are used since the second order elements are costly in terms of the computational time. Since adjacent elements will have common nodes, it is important to adopt a numbering system that will assign to this common nodes of the same numbers.

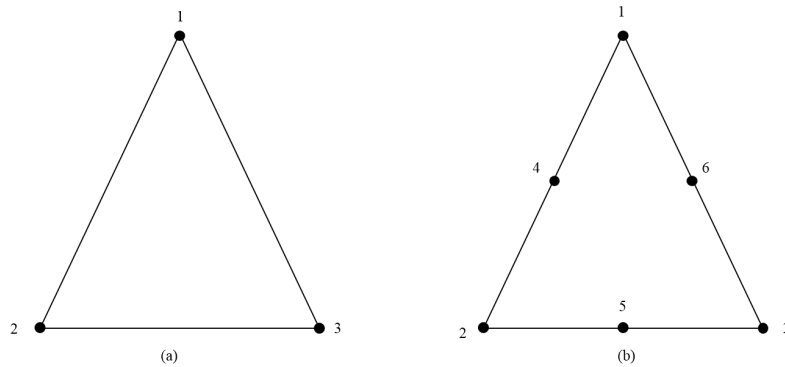


Figure 2.15: First (a) and second (b) order triangular elements.

Triangular elements shown in Fig. 2.15 are used in two-dimensional problems. For such an element, the area coordinates L_1 , L_2 and L_3 are introduced. The equation relating the Cartesian coordinates to the area coordinates is given by

$$\begin{bmatrix} 1 \\ x \\ y \end{bmatrix} = \begin{bmatrix} 1 & 1 & 1 \\ x_1 & x_2 & x_3 \\ y_1 & y_2 & y_3 \end{bmatrix} \begin{bmatrix} L_1 \\ L_2 \\ L_3 \end{bmatrix} \quad (2.67)$$

or

$$\begin{bmatrix} L_1 \\ L_2 \\ L_3 \end{bmatrix} = \begin{bmatrix} 1 & 1 & 1 \\ x_1 & x_2 & x_3 \\ y_1 & y_2 & y_3 \end{bmatrix}^{-1} \begin{bmatrix} 1 \\ x \\ y \end{bmatrix} = \frac{1}{2A_e} \begin{bmatrix} a_1 & b_1 & c_1 \\ a_2 & b_2 & c_2 \\ a_3 & b_3 & c_3 \end{bmatrix} \begin{bmatrix} 1 \\ x \\ y \end{bmatrix} \quad (2.68)$$

where (x_1, y_1) , (x_2, y_2) and (x_3, y_3) are the Cartesian coordinates of the vertex k , where $k = 1, 2, 3$ of the triangle. The coefficients a_k , b_k and c_k are defined as

$$a_k = x_l y_m - x_m y_l \quad (2.69)$$

$$b_k = y_l - y_m \quad (2.70)$$

$$c_k = x_m - x_l \quad (2.71)$$

The subscripts k , l and m are cyclical around the three vertices of the triangle. The area A_e of the element is given as

$$2A_e = \begin{bmatrix} 1 & 1 & 1 \\ x_1 & x_2 & x_3 \\ y_1 & y_2 & y_3 \end{bmatrix} \quad (2.72)$$

If the local coordinates ξ and η are defined as

$$L_1 = \xi \quad (2.73)$$

$$L_2 = \eta \quad (2.74)$$

$$L_3 = 1 - L_1 - L_2 = 1 - \xi - \eta \quad (2.75)$$

then the transformation relation for differentiation will be given by the following:

$$\begin{bmatrix} \frac{\partial}{\partial \xi} \\ \frac{\partial}{\partial \eta} \end{bmatrix} = [J] \begin{bmatrix} \frac{\partial}{\partial x} \\ \frac{\partial}{\partial y} \end{bmatrix} \quad (2.76)$$

where

$$[J] = \begin{bmatrix} x_1 - x_3 & y_1 - y_3 \\ x_2 - x_3 & y_2 - y_3 \end{bmatrix} \quad (2.77)$$

or

$$\begin{bmatrix} \frac{\partial}{\partial x} \\ \frac{\partial}{\partial y} \end{bmatrix} = [J]^{-1} \begin{bmatrix} \frac{\partial}{\partial \xi} \\ \frac{\partial}{\partial \eta} \end{bmatrix} \quad (2.78)$$

with

$$[J]^{-1} = \frac{1}{2A_e} \begin{bmatrix} b_1 & b_2 \\ c_1 & c_2 \end{bmatrix} \quad (2.79)$$

The relation for integration is given as

$$\iint f(x, y) dx dy = 2A_e \int_0^1 \int_0^{1-\xi} f(\xi, \eta) d\xi d\eta \quad (2.80)$$

Using equations (2.70) through to (2.77), the formulae for both differentiation and integration can be given by

$$\frac{\partial f}{\partial x} = \frac{1}{2A_e} \left(b_1 \frac{\partial f}{\partial L_1} + b_2 \frac{\partial f}{\partial L_2} + b_3 \frac{\partial f}{\partial L_3} \right) \quad (2.81)$$

$$\frac{\partial f}{\partial y} = \frac{1}{2A_e} \left(c_1 \frac{\partial f}{\partial L_1} + c_2 \frac{\partial f}{\partial L_2} + c_3 \frac{\partial f}{\partial L_3} \right) \quad (2.82)$$

$$\begin{aligned} \iint_e L_1^k L_2^l L_3^m dx dy &= 2A_e \int_0^1 \xi^k \left[\int_0^{1-\xi} \eta^l (1-\xi-\eta)^m d\eta \right] d\xi \\ &= 2A_e \frac{k!l!m!}{(k+l+m+2)} \end{aligned} \quad (2.83)$$

We now move on to the vector field formulation that leads to accurate characterisation of general waveguides.

2.4.7 Vector Field Formulation

This formulation requires at least two field components, namely, **E**-field and **H**-field. Former approach was first applied by English and Young [48]. This formulation is suitable for generally anisotropic and loss-less problems. The natural boundary condition corresponds to a magnetic wall and as such it is essential to enforce the electric wall as the boundary condition ($\mathbf{n} \times \mathbf{E} = 0$). Such a condition is quite difficult to impose for an irregular structure. It also requires an additional integral to ensure the continuity of the fields at the dielectric interfaces. The H-field formulation, on the other hand, has as its natural boundary condition the electric wall and the magnetic field is continuous everywhere. As such it is suitable for dielectric waveguide problems as no boundary conditions need to be imposed. This formulation is given as

$$\omega^2 = \frac{\int (\nabla \times H)^* \cdot \hat{\epsilon}^{-1} \cdot (\nabla \times H) d\Omega}{\int H^* \cdot \mu^{-1} \cdot H d\Omega} \quad (2.84)$$

The above formulation leads to non-physical or spurious solutions since the divergence condition $\nabla \cdot H = 0$ is not satisfied. Various methods exist for detecting these spurious modes. A simple way is to examine the field profiles, since these modes are characterised by inconsistency and a random variation of the field they are easy to identify. The mathematical idea underpinning the physical solution is that the condition $\nabla \cdot H = 0$ is obeyed by the eigenvector. By calculating $\nabla \cdot H$ for each eigenvector, it is possible to identify the true solutions from the spurious ones. The objective, however, is not simply to detect these modes, but to eliminate them or at least suppress them. The penalty-function method proposed by Rahman and Davies [46] is one the best established methods for eliminating

these spurious solutions. The method includes an additional term α , the penalty term, a dimensionless number in the variational formulation, which now is written as:

$$\omega^2 = \frac{\int (\nabla \times H)^* \cdot \hat{\varepsilon}^{-1} \cdot (\nabla \times H) d\Omega + \left(\frac{\alpha}{\varepsilon}\right) \int (\nabla \cdot H)^* (\nabla \cdot H) d\Omega}{\int H^* \cdot \mu^{-1} \cdot H d\Omega} \quad (2.85)$$

2.4.8 The Matrix Equation

It has been stated that the vector formulation leads to a standard eigenvalue problem of the form

$$Ax - \lambda Bx = 0 \quad (2.86)$$

where x represents the engen vector, which holds the nodal field values. If in equation 2.84, the numerator is written as

$$x^T \cdot Ax = \int (\nabla \times H)^* \cdot \hat{\varepsilon}^{-1} \cdot (\nabla \times H) d\Omega \quad (2.87)$$

and the denominator as

$$x^T \cdot Bx = \int H^* \cdot \mu \cdot H d\Omega \quad (2.88)$$

then the functional

$$J = \int (\nabla \times H)^* \cdot \hat{\varepsilon}^{-1} \cdot (\nabla \times H) d\Omega - k_0^2 \int H^* \cdot \mu \cdot H d\Omega \quad (2.89)$$

can be written as

$$J = x^T \cdot Ax - \lambda \cdot x^T \cdot Bx \quad (2.90)$$

To find a stationary solution, it is required that

$$\frac{\partial J}{\partial x} = 0 \quad (2.91)$$

Applying this minimisation procedure to equation 2.89, the following eigenvalue equation 2.86 is obtained

$$Ax - \lambda Bx = 0$$

which can be solved using any standard matrix routine to obtain the field values at the nodes.

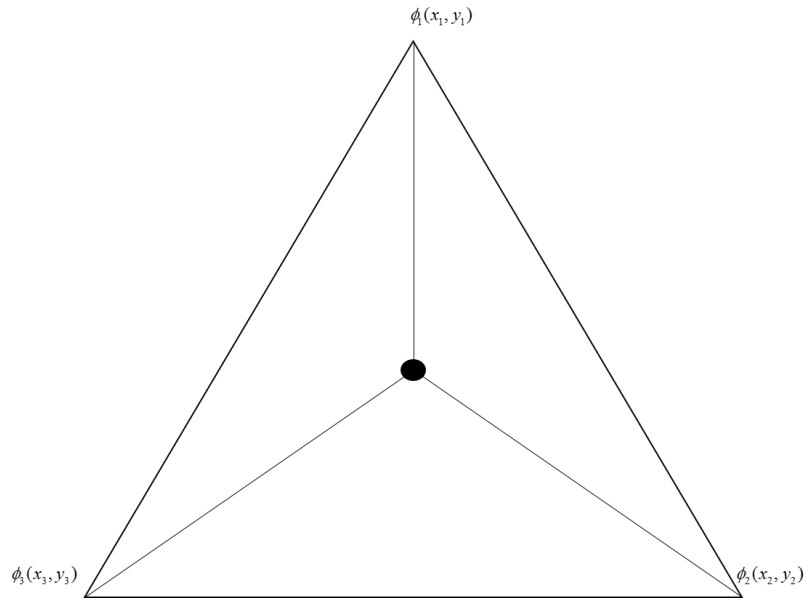


Figure 2.16: A typical element.

2.4.9 Shape Functions

The shape functions are a set of interpolation functions, defined in terms of complete polynomials and which are normalised over each element. If a typical element, as shown in Fig. 2.16 is considered, then the shape function is chosen so that it uniquely defines the field within the element under consideration.

At the nodal points, they take on values equal to the nodal values ϕ_1 , ϕ_2 and ϕ_3 . It is important therefore that the functions are expressed in terms of their nodal values. Within the triangle, the field value can be adequately modelled by the expression

$$\phi = a + bx + cy \quad (2.92)$$

where a , b and c are constants. These constants can be represented in terms of the coordinates of the nodes. The nodal values of ϕ can then be expressed as

$$\phi = a + bx_1 + cy_1 \quad (2.93)$$

$$\phi_2 = a + bx_2 + cy_2 \quad (2.94)$$

$$\phi_3 = a + bx_3 + cy_3 \quad (2.95)$$

The above system of equations can be solved to determine a , b and c as

$$a = \frac{\phi_1(x_2y_3 - x_3y_2) + \phi_2(x_3y_1 - x_1y_3) + \phi_3(x_1y_2 - x_2y_1)}{2A_e} \quad (2.96)$$

2.4. Finite Element Method

$$b = \frac{\phi_1(y_2 - y_3) + \phi_2(y_3 - y_1) + \phi_3(y_1 - y_2)}{2A_e} \quad (2.97)$$

$$c = \frac{\phi_1(x_3 - x_2) + \phi_2(x_1 - x_3) + \phi_3(x_2 - x_1)}{2A_e} \quad (2.98)$$

where A_e is the area of the triangle. Substituting these values into equation 2.92 will yield

$$\phi(x, y) = N_1\phi_1 + N_2\phi_2 + N_3\phi_3 \quad (2.99)$$

or

$$\phi(x, y) = [N]\{\phi\} \quad (2.100)$$

$$N_1 = \frac{1}{2A}[(x_2y_3 - x_3y_2) + (y_2 - y_3)x + (x_3 - x_2)y] \quad (2.101)$$

$$N_2 = \frac{1}{2A}[(x_3y_1 - x_1y_3) + (y_3 - y_1)x + (x_1 - x_3)y] \quad (2.102)$$

$$N_3 = \frac{1}{2A}[(x_1y_2 - x_2y_1) + (y_1 - y_2)x + (x_2 - x_1)y] \quad (2.103)$$

The above can be rewritten as

$$N_1 = a_1 + a_2x + a_3y \quad (2.104)$$

$$N_2 = a_4 + a_5x + a_6y \quad (2.105)$$

$$N_3 = a_7 + a_8x + a_9y \quad (2.106)$$

An important property of shape function is that

$$N_1 + N_2 + N_3 = 1 \quad (2.107)$$

The **H**-field components H_x , H_y and H_z can be written as

$$H_x(x, y) = N_1H_{x1} + N_2H_{x2} + N_3H_{x3} \quad (2.108)$$

$$H_y(x, y) = N_1H_{y1} + N_2H_{y2} + N_3H_{y3} \quad (2.109)$$

$$H_z(x, y) = N_1H_{z1} + N_2H_{z2} + N_3H_{z3} \quad (2.110)$$

In matrix form, the above equations can be expressed as

$$H = \begin{bmatrix} H_x \\ H_y \\ H_z \end{bmatrix} = \begin{bmatrix} N_1 & 0 & 0 & N_2 & 0 & 0 & N_3 & 0 & 0 \\ 0 & N_1 & 0 & 0 & N_2 & 0 & 0 & N_3 & 0 \\ 0 & 0 & N_1 & 0 & 0 & N_2 & 0 & 0 & N_3 \end{bmatrix} \begin{bmatrix} H_{x1} \\ H_{y1} \\ H_{z1} \\ H_{x2} \\ H_{y2} \\ H_{z2} \\ H_{x3} \\ H_{y3} \\ H_{z3} \end{bmatrix} \quad (2.111)$$

2.4. Finite Element Method

In a simplified form this is equivalent to $H=[N]H$, where $[N]$ is the 3×9 matrix shown above and H is the 9×1 column vector which represents the components of the field.

Similarly, the expression for $\nabla \times H$ could be written as

$$\nabla \times H = [Q] \cdot H \quad (2.112)$$

where

$$[Q] = \begin{bmatrix} 0 & -\frac{\partial N_1}{\partial z} & \frac{\partial N_1}{\partial y} & 0 & -\frac{\partial N_2}{\partial z} & -\frac{\partial N_2}{\partial y} & 0 & -\frac{\partial N_3}{\partial z} & -\frac{\partial N_3}{\partial y} \\ \frac{\partial N_1}{\partial z} & 0 & -\frac{\partial N_1}{\partial x} & \frac{\partial N_2}{\partial z} & 0 & -\frac{\partial N_2}{\partial x} & \frac{\partial N_3}{\partial z} & 0 & -\frac{\partial N_3}{\partial x} \\ -\frac{\partial N_1}{\partial y} & -\frac{\partial N_1}{\partial x} & 0 & -\frac{\partial N_2}{\partial y} & \frac{\partial N_2}{\partial x} & 0 & -\frac{\partial N_3}{\partial y} & \frac{\partial N_3}{\partial x} & 0 \end{bmatrix} \quad (2.113)$$

The \mathbf{Q} -matrix, after evaluation, i.e., finding the derivative of the shape, with $j\beta z$ being the z -variation, becomes

$$[Q] = \begin{bmatrix} 0 & j\beta N_1 & a_3 & 0 & j\beta N_2 & a_6 & 0 & j\beta N_3 & a_9 \\ -j\beta N_1 & 0 & -a_2 & -j\beta N_2 & 0 & -a_5 & j\beta N_3 & 0 & -a_8 \\ -a_3 & a_2 & 0 & -a_6 & a_5 & 0 & -a_9 & a_8 & 0 \end{bmatrix} \quad (2.114)$$

The \mathbf{B} -matrix can also be calculated in a similar fashion from equation 2.87. Since μ is a scalar quantity, it can be taken outside the integral to give

$$x^T \cdot B \cdot x = \mu \int H^* \cdot H d\Omega \quad (2.115)$$

since $H = [N] H$

$$B_e = \int_{\Delta} [N]^* \cdot [N] d\Omega \quad (2.116)$$

The solution of the above expressions yields a 9×9 matrix. The integration is carried out using equation 2.83 and the resulting B_e matrix is as follows:

$$B_e = \begin{bmatrix} \frac{A}{6} & 0 & 0 & \frac{A}{12} & 0 & 0 & \frac{A}{12} & 0 & 0 \\ 0 & \frac{A}{6} & 0 & 0 & \frac{A}{12} & 0 & 0 & \frac{A}{12} & 0 \\ 0 & 0 & \frac{A}{6} & 0 & 0 & \frac{A}{12} & 0 & 0 & \frac{A}{12} \\ \frac{A}{12} & 0 & 0 & \frac{A}{6} & 0 & 0 & \frac{A}{12} & 0 & 0 \\ 0 & \frac{A}{12} & 0 & 0 & \frac{A}{6} & 0 & 0 & \frac{A}{12} & 0 \\ 0 & 0 & \frac{A}{12} & 0 & 0 & \frac{A}{6} & 0 & 0 & \frac{A}{12} \\ \frac{A}{12} & 0 & 0 & \frac{A}{12} & 0 & 0 & \frac{A}{6} & 0 & 0 \\ 0 & \frac{A}{12} & 0 & 0 & \frac{A}{12} & 0 & 0 & \frac{A}{6} & 0 \\ 0 & 0 & \frac{A}{12} & 0 & 0 & \frac{A}{12} & 0 & 0 & \frac{A}{6} \end{bmatrix} \quad (2.117)$$

The area of each element or triangle is denoted by A_e . The coefficients of the A_e matrix can also be calculated using equation 2.83. Making the following substitutions $H=[N]H$ and $\nabla \times H = [Q] \cdot \{H\}$, yields

$$x^T \cdot A_e \cdot x = \int \{H\}^* \cdot [Q]^* \hat{\varepsilon}^{-1} \cdot [Q] \{H\} d\Omega \quad (2.118)$$

A simplification of the above will yield an A_e matrix of the form

$$A_e = \int [Q]^* \hat{\varepsilon}^{-1} \cdot [Q] d\Omega \quad (2.119)$$

For isotropic media, ε is a scalar quantity and hence can be factored out of the integral sign. For anisotropic media, ε is a tensor defined by a 3×3 matrix as follows:

$$\varepsilon = \begin{bmatrix} \varepsilon_{11} & \varepsilon_{12} & \varepsilon_{13} \\ \varepsilon_{21} & \varepsilon_{22} & \varepsilon_{23} \\ \varepsilon_{31} & \varepsilon_{32} & \varepsilon_{33} \end{bmatrix} \quad (2.120)$$

Finding the inverse of ε , $[P]$ (Appendix), equation 2.119 can be rewritten as

$$A_e = \int [Q]^* \cdot [P] \cdot [Q] d\Omega \quad (2.121)$$

Carrying out necessary algebraic calculations yields a 9×9 matrix. Using the integration formula of 2.87, the integrals can be evaluated as

$$\int N_1^2 d\Omega = \frac{A}{6} \quad (2.122)$$

$$\int N_1 d\Omega = \frac{A}{3} \quad (2.123)$$

$$\int d\Omega = A \quad (2.124)$$

For instance, the $A_{e_{11}}$ matrix is given as

$$A_{e_{11}} = p_{22}\beta^2 \frac{A}{6} + p_{23}a_3j\beta \frac{A}{3} + p_{32}a_3j\beta \frac{A}{3} + p_{33}a_3^2 A \quad (2.125)$$

The other 80 elements of the A_e matrix can be found in a similar way.

2.4.10 Element Assembly

The next stage in the finite element method is the assembly of the element matrices $[A_e]$ and $[B_e]$ into global matrices $[A]$ and $[B]$ respectively. An appropriate matrix solver is then used to obtain the eigenvalues and eigenvectors of the equation. The assembly of the global matrix is done with respect to the nodes of the domain. Where two or more nodes are common to more than one element then it is advisable to add the contribution of each adjacent element to the global matrix when the calculation for the common node is carried.

As previously noted, for every element in the discretised variational formulation, there is an expression of the form

$$\{H\}[N]\{H\}^T = \{H_1 \cdots H_9\} \begin{bmatrix} N_{11} & \cdot & \cdot & \cdot & N_{19} \\ \cdot & \cdot & & & \cdot \\ \cdot & & \cdot & & \cdot \\ \cdot & & & \cdot & \cdot \\ N_{91} & \cdot & \cdot & \cdot & N_{99} \end{bmatrix} \begin{bmatrix} H_1 \\ \cdot \\ \cdot \\ \cdot \\ H_9 \end{bmatrix} \quad (2.126)$$

Each term in the matrix N_{ij} relates to two nodal field values where the indices, i and j , correspond to the nodal field values of the vectors $\{H\}$ and $\{H\}^T$ according to the local numbering of an element. If a scalar formulation is considered, then only one field component need be taken into account H_x for example and the expression can be written as

$$\{ H_{x_1} \quad H_{x_2} \quad H_{x_3} \} \begin{bmatrix} N_{11} & N_{12} & N_{13} \\ N_{21} & N_{22} & N_{23} \\ N_{31} & N_{32} & N_{33} \end{bmatrix} \begin{bmatrix} H_1 \\ H_2 \\ H_3 \end{bmatrix} \quad (2.127)$$

The global matrix G_{pq} may be defined as

$$G = \begin{bmatrix} G_{11} & \cdot & \cdot & \cdot & G_{18} \\ \cdot & \cdot & & & \cdot \\ \cdot & & \cdot & & \cdot \\ \cdot & & & \cdot & \cdot \\ G_{81} & \cdot & \cdot & \cdot & G_{88} \end{bmatrix} \quad (2.128)$$

If P is the total number of nodal points of the structure, the order of the global matrix is $P \times P$, which defines the size of the matrix when only one unknown field component is considered for each node. The terms of the global matrix, G_{pq} , are the field contributions of two nodes, p and q according to the global numbering system. Each term of the global matrix G_{pq} consists of a local contribution from only one element, unless the nodes lie on a shared boundary. The terms of the global matrix, G_{11} , for the first node with respect to itself will be defined as

$$G_{11} = N_{11}^A \quad (2.129)$$

where N_{11}^A is the term for the element matrix for the element A . The terms of the global matrix for other nodes which do not lie on a shared boundary can be found in a similar manner: $G_{12} = N_{13}^A$, $G_{24} = N_{32}^B$, etc. When the nodes are on a shared boundary, then the contributions of each element are added to the node, for example,

$$G_{22} = N_{33}^A + N_{33}^B \quad (2.130)$$

2.5 Summary

This chapter has presented the general formulation of the Finite element method for optical waveguide problems. Various aspects of implementation of the method have been explained including domain discretisation, shape functions and field representations. The development of the vector **H**-field formulation of eliminating spurious modes has been reviewed. In addition, this chapter provided the theory behind different waveguide designs and the guided modes. The operation principle of the optical modulator is also explained.

Chapter 3

Graphene Photonics

3.1 Introduction

Photonics has shown exotic ways to overcome the speed limitation in electronics. Electronic interconnections (e.g., copper cables) suffer from bandwidth issues and loss due to performance restrictions in terms of energy consumption, speed, cross-talk and dispersion. On the other hand, optical interconnections have shown promising alternatives with better performance such as higher bandwidth and lower loss. An optical modulator is a device that modulates, i.e., varies the fundamental characteristics, of light propagating through an optical waveguide. Intense research is currently under way in light modulation to develop cost-effective, compact, efficient, high speed broadband optical modulators for high-performance optical interconnects [57]. Idea of optical interconnects in the 1970s arose to overcome the limitation set by electrons moving in the solid. Keyes [58] envisaged that optical elements would be much faster than their electrical counterparts due to greater velocity of optical signals.

An optical interconnect is a dielectric waveguide that operates at optical frequencies. In a broader picture, an optical fibre (Fig. 3.1(a)) that transmits information using light is such a waveguide. Fibre optic communications are in the forefront of long distance as well as undersea data telecommunications (Fig. 3.1(b)). Technology started adopting light waves for data transmission since 1960s [59]. As it took years and years of research to fully evolve communications through optical waves, it would take at least a decade of research to realise ultrafast devices for optical interconnects. Now that a range of two-dimensional materials such as graphene, phosphorene and silicene have been identified, technology is slowly adapting to blend such materials with existing ones such as silicon for high-speed high-performance devices.

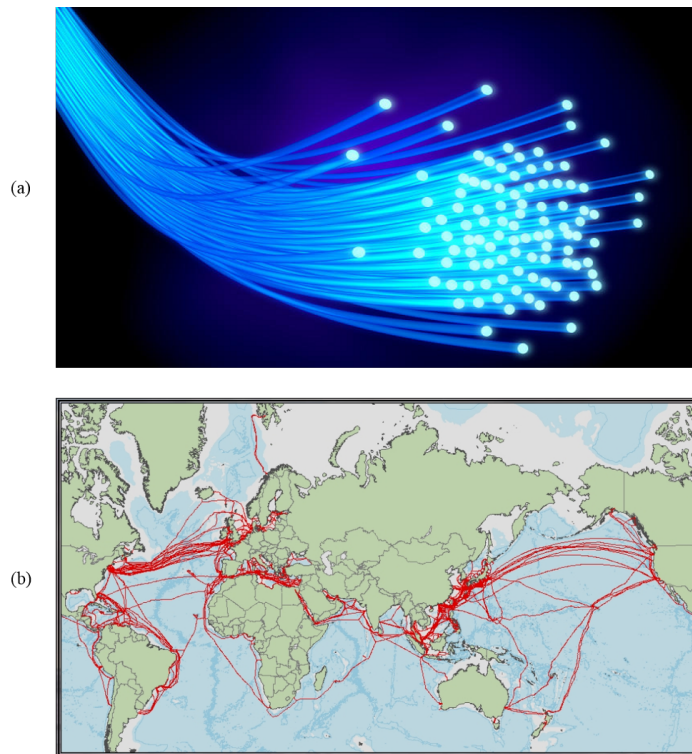


Figure 3.1: (a) Fibre-optic cables transmitting information through light waves. (b) Map showing countries connected by undersea fibre optic cables. Source: [60].

Two-dimensional layered materials exhibit a range of physical behaviours from that of an insulator to a semiconductor with narrow-gap to a semimetal or metal. Such materials offer numerous opportunities for diverse photonic and optoelectronic applications. For instance, graphene has been widely used for devices operating at extremely broad spectral range from ultraviolet, visible and near-infrared to mid-infrared, far-infrared and extending to terahertz and microwave regions, due to its unique electro-optical properties [10]. These materials have been shown to be compatible with various photonic structures, for example, well developed fibre and silicon devices. Intense research is now underway to integrate 2D materials with current optical fibres and CMOS technology. Two-dimensional materials also provide mechanical flexibility, easy fabrication and integration and robustness. Additionally, generation, propagation, modulation and detection of photons can be accomplished [61].

In these 2D nanostructures, the sea of electrons or electron gas play pivotal role in electro-optical properties of the material. For example, applying an electric field perturbs the electrons that couple with incoming light wave and that the collective excitations induces surface plasmons. They then confine or trap optical waves into regions

(metal–dielectric interface) much smaller than their wavelengths. In case of a boron nitride–graphene–boron nitride (BN) stack, the combined thickness could be 20.7 nm, where graphene is of just 0.7 nm thick and BN each 10 nm. Such a combination operates within a range of wavelength, $\lambda=800\text{--}2000$ nm. Therefore, plasmonic resonances play a crucial role. Plasmonic circuits tightly confine the electromagnetic waves at the metal–dielectric interface which is identified to be a potential solution for electro-optic modulation. Plasmons in graphene are discussed in Section 3.6.

Graphene has been studied theoretically in depth as early as 1947 [62], however the monolayer was thought to be unstable. In 1986, Boehm *et al.* [63] in their study proposed the first observation of graphene monolayer. They introduced the name “graph-ene” deriving it from the combination of “graphite” (graph) and the suffix (ene) that refers to polycyclic aromatic hydrocarbons. Experimental discovery of graphene happened in an unusual way – a scotch tape method – whereby Novoselov *et al.* [3] prepared graphene films by mechanical exfoliation or repeated peeling from pyrolytic graphite. This accidental discovery led to award of Nobel prize in Physics for Andre Geim and Konstantin Novoselov in 2010 for their “groundbreaking experiments regarding the two-dimensional material graphene” [64]. In following sections, we discuss the physical, electrical and optical properties of graphene in detail.

3.2 Physical Properties

Graphene is precisely a monolayer of carbon atom that forms a tightly packed two-dimensional (2D) honeycomb lattice. Actually, this lattice is the basic structure of graphitic materials. In the history of carbon allotropes, graphite is the oldest known allotrope which was discovered in a mine near Borrowdale in Cumbria, England, around 16th century. Coincidentally, graphene, the youngest known allotrope of carbon, was exfoliated firstly by two British researchers in Manchester, England, in 2004. After this accidental “discovery”, graphite is seen as a graphene sheet stack that bond the layers together due to van der Waals interaction. Note that the interlayer distance is 0.335 nm. The weaker nature of van der Waals bonding makes exfoliation of graphene sheets possible. The other allotropes such as 0D fullerenes (bucky ball) and 1D carbon nanotubes can be termed as graphene sphere (C_{60}) and rolled up graphene sheets, respectively. Another prominent allotrope of

3.2. Physical Properties

carbon is diamond which consists of four club-like orbitals forming a tetrahedron.

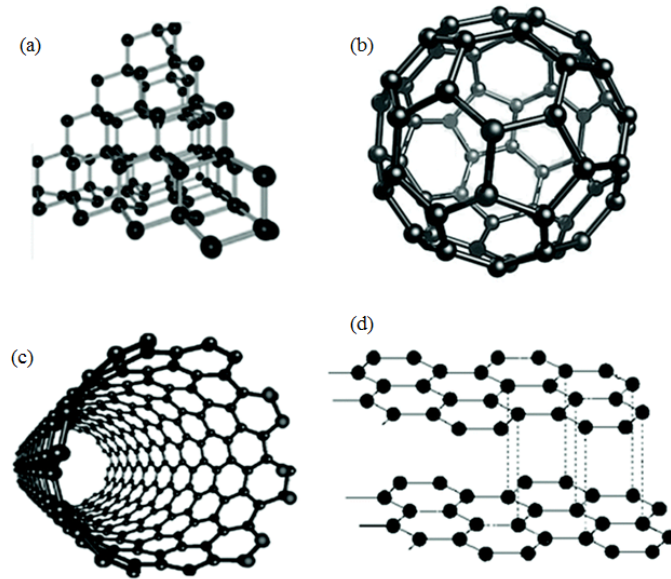


Figure 3.2: Prominent allotropes of carbon: (a) diamond, (b) fullerene, (c) carbon nanotube and (d) graphite. Dotted lines in (d) represent the van der Waals bonding (π bonds). Adapted from Ref. [65].

Figure 3.2 shows allotropes of carbon. Diamond is one of the hardest natural materials with all four valence electrons in $2s$ and $2p$, with 2 in each, involved in the formation of σ bonds with other carbon atoms. Diamond is an insulator with large band gap, $E_g = 5.47\text{ eV}$. On the other hand, the π bonds in graphite are weaker and responsible for good electronic conduction properties. Fullerene is a C_{60} molecule which has the form of a sphere (football), wherein some hexagonal bonding carbon atoms are replaced by pentagon formation that causes crumbling leading to a sphere-like formation. Carbon nanotubes are further classified as SWNT and MWNT, meaning single wall nanotube and multiwall nanotubes, respectively.

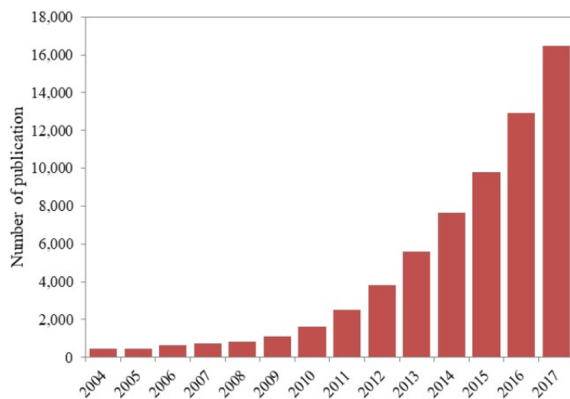


Figure 3.3: Publications on graphene [66].

Graphene is considered a rising star amongst the 2D class of materials. Figure 3.3 shows a spike in number of papers published on graphene after 2004 and significantly increasing afterwards the award of Nobel prize in 2010. Graphene exhibits exceptionally high crystal and electronic quality [67]. Potential applications such as

3.2. Physical Properties

optical interconnects, environmental monitoring, medicinal, biosensing and security devices of such material has been proposed by numerous studies [10]. Graphene has a unusual electronic spectrum that led to start of “relativistic” solid state physics, where quantum relativistic phenomena is observed. It represents a new class of materials that are just one atom thick, offering insights to low-dimensional physics which are currently studied by various research groups for applications. Not only graphene but also other 2D materials such as transition metal dichalcogenides (TMDs) and black phosphorus have shown promising applications in electronics, photonics and optoelectronics.

Graphene is basically an allotrope of Carbon. Other allotropes include diamond, graphite, fullerenes and carbon nanotubes (Fig. 3.4). Of these allotropes of carbon, the youngest is two-dimensional graphene which represents a single layer graphite sheet. Layers of graphene are classified as mono (0.4 nm), bi (0.69 nm), tri (1.12 nm) and few or multiple layers ≤ 10 [68]. Thickness of Bilayer graphene (BLG) is taken as 0.7 nm by most simulation studies [6, 29] as single layer thickness is very

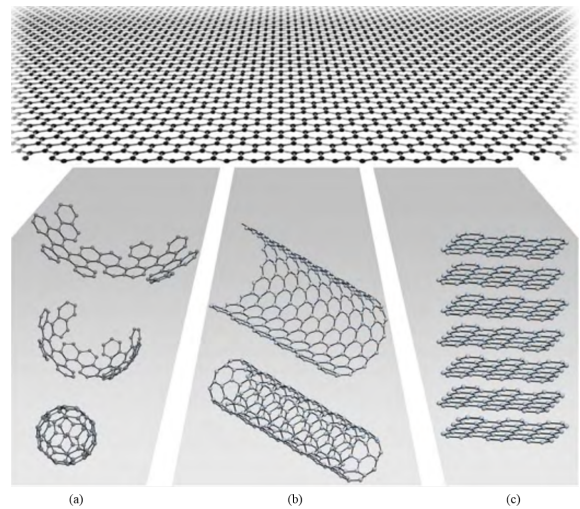


Figure 3.4: Monolayer graphene: basis of all graphitic forms. (a) 0D bucky balls; (b) 1D nanotubes; and (c) 3D graphite. Source: Geim and Novoselov [67].

thin. Further, bilayer is considered the most energetically stable stack of two graphene layers [69]. Thickness of graphene has been a subject of discussion as atomic force microscopy (AFM) measurements were proven to be inaccurate [70]. Figure 3.5 shows HRTEM and TEM images taken by two research groups showing hexagonal lattice formation in graphene layer.

3.2.1 Carbon Bonds

Graphene is made of chain of carbon atoms which have been extensively studied by various research groups. We have various studies for carbon and its bonding with other elements. Therefore, here we present a fundamental part which is needed in understanding the physical properties of graphene. A ground state carbon atom has six electrons in the configuration $1s^2 2s^2 2p^2$, depicting two electrons in the inner orbital $1s$ and 4 electrons

3.2. Physical Properties

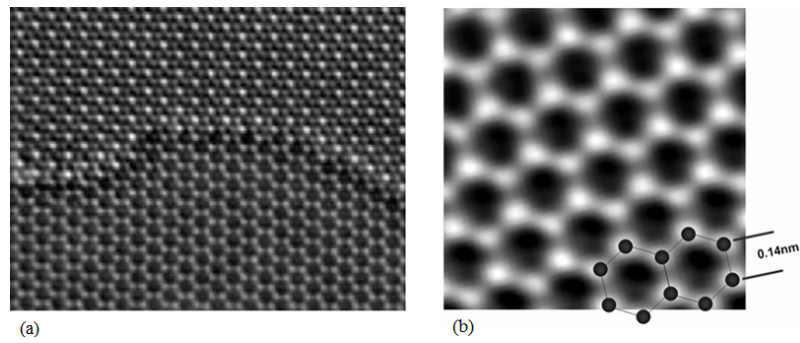


Figure 3.5: Monolayer of graphene: (a) HRTEM image by Ref. [71]; (b) TEM image by Berkeleys TEAM05 [72]. C=C bond distance: 0.14 nm.

in the outer orbitals $2s$ and $2p$. The $2p$ orbitals ($2p_x, 2p_y, 2p_z$) are approximately 4 eV higher than the $2s$ orbital. Figure 3.6 shows the ground state and excited state electronic configurations for a carbon atom.

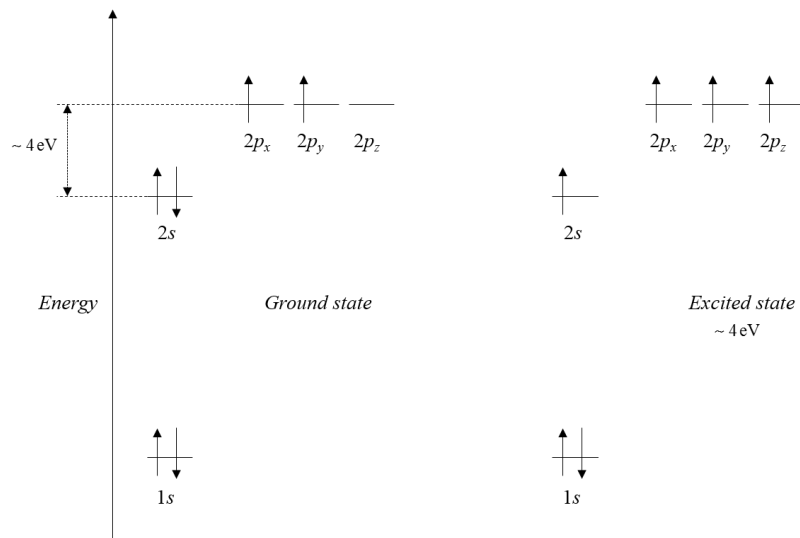


Figure 3.6: Depiction of electronic orbitals of ground state and excited state carbon atom [73].

Two electrons in the innermost orbital ($1s$) is close to the nucleus and are irrelevant for chemical bonding or reactions. Four electrons in $2s$ and $2p$, with two electrons in each, are responsible for the bonding nature of carbon atoms. As the $2p$ orbitals are 4 eV higher than the $2s$ orbitals, it is energetically favourable to place two electrons in the latter and two in the former. At the time of bonding, one electron from $2s$ orbital is easily excited to $2p$ ($2p_z$ to be exact) state for forming covalent bonds with other atoms. Therefore, we now have four equivalent quantum-mechanical states as follows:

$$|2s\rangle, |2p_x\rangle, |2p_y\rangle \text{ and } |2p_z\rangle$$

3.2. Physical Properties

This quantum-mechanical superposition of state $|2s\rangle$ with n $|2p_j\rangle$ states is termed as sp^n hybridisation. In case of graphene, the superposition of the $2s$ and two $2p$ orbitals ($|2p_x\rangle, |2p_y\rangle$ states), results in sp^2 hybridisation. The following represents the 3 quantum-mechanical states of the sp^2 hybridisation in graphene [73]:

$$\begin{aligned} |sp_1^2\rangle &= \frac{1}{\sqrt{3}}|2s\rangle - \sqrt{\frac{2}{3}}|2p_y\rangle, \\ |sp_2^2\rangle &= \frac{1}{\sqrt{3}}|2s\rangle - \sqrt{\frac{2}{3}}\left(\frac{\sqrt{3}}{2}|2p_x\rangle + \frac{1}{2}|2p_y\rangle\right), \\ |sp_3^2\rangle &= -\frac{1}{\sqrt{3}}|2s\rangle + \sqrt{\frac{2}{3}}\left(-\frac{\sqrt{3}}{2}|2p_x\rangle + \frac{1}{2}|2p_y\rangle\right). \end{aligned} \quad (3.1)$$

These orbitals are oriented along the xy -plane with mutual angles 120° and the remaining $2p_z$ orbital remains unhybridised and is perpendicular to the plane. A hexagonal structure of graphene is akin to the benzene ring which has carbon atoms linked by σ bonds. The C–C bond length in graphene is 0.142 nm [74]. Bonding plays a major role in physical and chemical properties of the metal and a strong bond obviously denotes higher the material strength or in other words, strength of the thin film of graphene (Fig. 3.7). It takes an elephant to stand on a pencil to tear a film of graphene!!

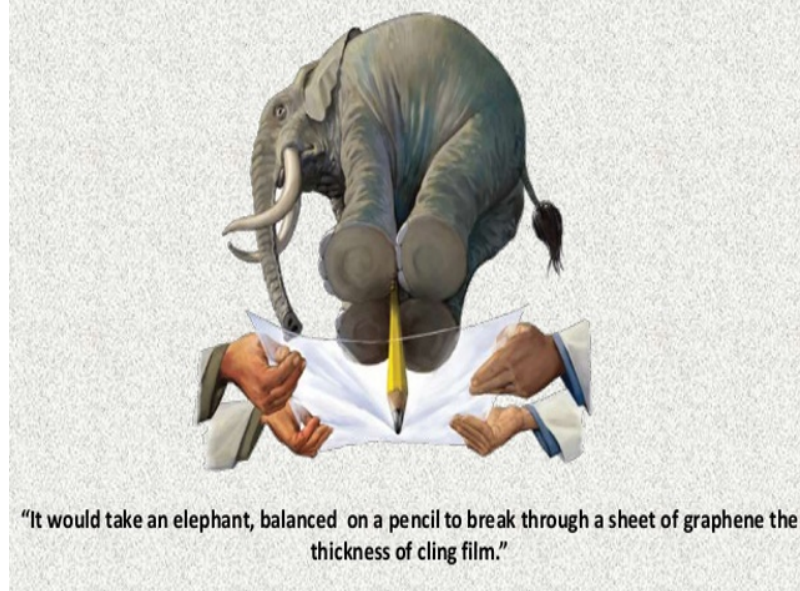


Figure 3.7: Artistic imagination [75] showing strength of graphene monolayer (0.335 nm thick). A layer of graphene has a breaking strength of 42 N/m (intrinsic strength of a defect-free sheet) – 100 times more than that of the strongest hypothetical steel film of the same thickness [64].

The unhybridised $2p_z$ orbital has one extra electron (because of sp^2 hybridisation) that forms π -bonds and is half-filled [76]. Such half-filled bands play major role in the physics

of strongly correlated systems because of their strong tight-binding character and the large Coulomb energies [74]. Plasmons in graphene are caused by electron oscillations which is due to the electronic structure which in turn is the resultant of bonding nature of C=C in graphene. So the study of basic bonding structure of graphene is required to understand the unique properties of this *wonder* material. A detailed discussion on chemical bonding of graphene is out of scope of this thesis. So we now move on to overview of crystal structure and stacking or orientation of layers in graphene when its thickness exceeds 0.335 nm – the thickness of monolayer [77].

3.2.2 Crystal Structure

In graphene, carbon atoms condense in a honeycomb lattice due to sp^2 hybridisation. This honeycomb lattice, with 2 carbon atoms in the basis (Fig. 3.8), is not termed a Bravais lattice because two neighbouring sites (A and B) are not equivalent. Each unit cell contains one lattice point and a two-atom basis. Any lattice point can be reached by adding an integral number of primitive vectors. The vectors \mathbf{d}_A and \mathbf{d}_B from a lattice point to an atom in the basis and are used in calculating the structure factor as follows:

$$|a_1| = |a_2| = \sqrt{3}l, \quad |\mathbf{d}_A| = |\mathbf{d}_B| = \frac{l}{2}, \quad \phi = 120^\circ \quad (3.2)$$

From equation 3.2, $\phi = 120^\circ$ denotes the angle between orbitals in sp^2 hybridisation. Figure 3.9 illustrates graphene crystal lattice with sublattices A and B . Vectors \mathbf{a}_1 and \mathbf{a}_2 form the basis vectors of the triangular Bravais lattice. Its primitive lattice vectors are \mathbf{a}_1^* and \mathbf{a}_2^* . The shaded region in Fig. 3.9(b) denotes the first Brillouin zone with centre Γ and two inequivalent corners K and K' . From Fig. 3.9(c), a site on the A sublattice has its nearest neighbours in the directions (Fig. 3.9(d)) north-east, north-west and south. Similarly, a site on the B sublattice has nearest neighbours in the directions north, south-west and south-east. Both A and B form a two-atom basis for a triangular

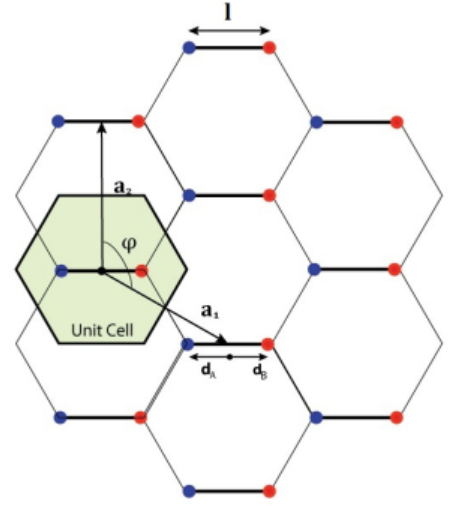


Figure 3.8: Two atom basis superimposed forming a hexagonal lattice. Two carbon atoms (A and B) in each unit cell are shown in different colours (blue and red) [78].

3.2. Physical Properties

Bravais lattice [73].

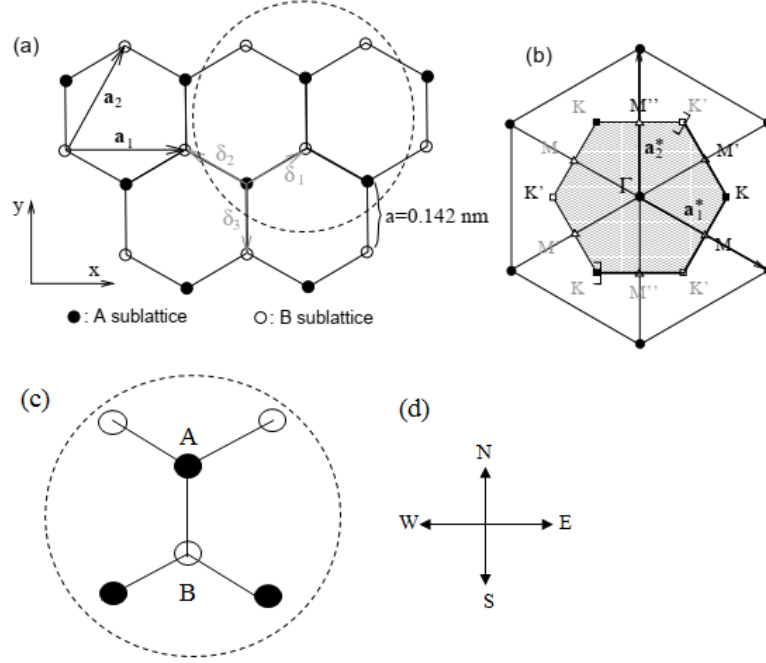


Figure 3.9: Honeycomb lattice of graphene layer: (a) lattice structure depicting Bravais lattice; (b) reciprocal lattice of the triangular lattice; (c) atoms (A and B) with nearest neighbours; (d) directions for reference to nearest neighbours. Adapted from Ref. [73].

The distance between *nearest-neighbour* (nn) carbon atoms is 0.142 nm. The three vectors that connect a site on *A* with a *nn* in *B* is given by

$$\begin{aligned}\delta_1 &= \frac{a}{2} (\sqrt{3}\mathbf{e}_x + \mathbf{e}_y), \\ \delta_2 &= \frac{a}{2} (-\sqrt{3}\mathbf{e}_x + \mathbf{e}_y), \\ \delta_3 &= -a\mathbf{e}_y\end{aligned}\tag{3.3}$$

and the basis vectors \mathbf{a}_1 and \mathbf{a}_2 ,

$$\begin{aligned}\mathbf{a}_1 &= \sqrt{3}a\mathbf{e}_x \\ \mathbf{a}_2 &= \frac{\sqrt{3}a}{3} (\mathbf{e}_x + \sqrt{3}\mathbf{e}_y).\end{aligned}\tag{3.4}$$

Modulus of basis vectors $|\mathbf{a}_1|$ and $|\mathbf{a}_2|$ yields the lattice spacing

$$\tilde{a} = \sqrt{3}a = 0.24 \text{ nm}\tag{3.5}$$

and the area of the unit cell is

$$A_{\text{unit cell}} = \frac{\sqrt{3}\tilde{a}^2}{2} = 0.051 \text{ nm}^2\tag{3.6}$$

Therefore, the density of carbon atoms is

$$n_C = \frac{2}{A_{\text{unit cell}}} = 39 \text{ nm}^{-2} = 3.9 \times 10^{15} \text{ cm}^{-2}\tag{3.7}$$

3.2. Physical Properties

From Fig. 3.9(b), the reciprocal lattice is spanned by the vectors given by

$$\begin{aligned}\mathbf{a}_1^* &= \frac{2\pi}{\sqrt{3}a} \left(\mathbf{e}_x - \frac{\mathbf{e}_y}{\sqrt{3}} \right) \\ \mathbf{a}_2^* &= \frac{4\pi}{3a} \mathbf{e}_y\end{aligned}\quad (3.8)$$

Actually, all sites of the reciprocal lattice represent equivalent wave vectors, such that, any wave (vibrational lattice excitation or quantum-mechanical electronic wave packet) propagating on the lattice with a wave vector differing by a reciprocal lattice vector has the same phase up to a multiple of 2π , given by

$$\mathbf{a}_i \cdot \mathbf{a}_j^* = 2\pi\delta_{ij} \quad (3.9)$$

where $\delta_{ij} = 1$ if $i = j$ and $\delta_{ij} = 0$ if $i \neq j$.

From equation 3.9, the reciprocal vectors are calculated as follows:

$$\begin{aligned}\mathbf{a}_1^* &= 2\pi \frac{\mathbf{a}_2 \times \mathbf{a}_3}{\mathbf{a}_1 \cdot \mathbf{a}_2 \times \mathbf{a}_3}, \\ \mathbf{a}_2^* &= 2\pi \frac{\mathbf{a}_3 \times \mathbf{a}_1}{\mathbf{a}_1 \cdot \mathbf{a}_2 \times \mathbf{a}_3}, \\ \mathbf{a}_3^* &= 2\pi \frac{\mathbf{a}_1 \times \mathbf{a}_2}{\mathbf{a}_1 \cdot \mathbf{a}_2 \times \mathbf{a}_3},\end{aligned}\quad (3.10)$$

where \mathbf{a}_1 and \mathbf{a}_2 are primitive vectors of the crystal and \mathbf{a}_3 the \hat{z} unit vector. The first Brillouin zone which is the unit cell of reciprocal lattice and the behaviour of relativistic particle are shown in Fig. 3.10. In the figure, \mathbf{b}_1 and \mathbf{b}_2 denote \mathbf{a}_1^* and \mathbf{a}_2^* , respectively. Closer to the points K and K' , the energy of electrons in graphene depend linearly on their wavenumber. This behaviour is similar to that of a relativistic particle whose behaviour is governed by the Dirac equation,

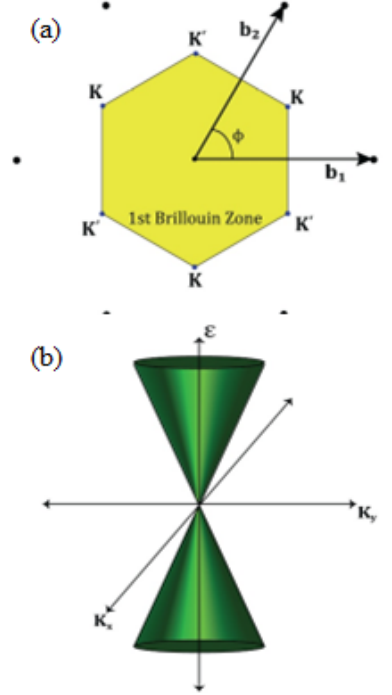


Figure 3.10: (a) First Brillouin zone. (b) Dirac cone. Adapted from Ref. [78].

$$|\mathbf{b}_1| = |\mathbf{b}_2| = \frac{4\pi}{3l}, \quad \phi = 60^\circ \quad (3.11)$$

The crystallographic points play a major role in defining the electronic properties of graphene as their low-energy excitations are centred around the two points, K and K' . Electronic properties are discussed in detail in Section 3.3.

3.2.3 Mono-, bi- and trilayers

A single atomic plane is a 2D crystal. In case of graphene, the atomic plane is made of carbon atoms. The thickness of monolayer graphene (MLG) is 0.335 nm. As seen in previous sections, a single layer of graphene is where the carbon atoms are arranged on a honeycomb lattice. Whereas in a bilayer, the second layer is shifted over one carbon-carbon bond length (0.142 nm) with respect to the first layer. MLG are zero-gap semiconductors with the low-energy electrons behaving as massless Dirac fermions. They are chiral as their wavefunction has two components – pseudospin with direction pinned to the electro momentum [74]. Bilayer graphene (BLG) are distinct 2D systems – zero-gap semiconductors with low energy chiral electrons but with quadratic low-energy dispersion. Applying a perpendicular electric field to the bilayer opens a gap between valence and conduction bands and transforms charge neutral bilayers to insulators [79].

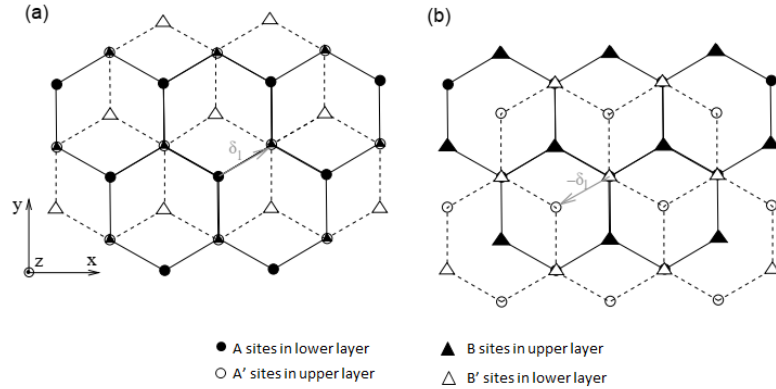


Figure 3.11: Bilayer stacking of graphene layers: (a) upper layer translated by δ_1 with respect to the lower – the A' sites on top of B sites; (b) upper layer translated by $-\delta_1$ with respect to the lower – the B' sites on top of A sites. Source: Ref. [73]

Let us consider the case of bilayer graphene (BLG) of thickness 0.69 nm [68]. Inter-layer spacing is roughly $d = 2.4a = 0.34$ nm. In a bilayer stack, the layers are arranged such that the upper layer atoms are placed at the hexagon centres of lower layer. The layers are translated with respect to each other with displacement given by either δ_i or $-\delta_i$, where $i = 1, 2$ or 3 . Figure 3.11 shows two possibilities of stacking bilayer graphene.

Now we move on to trilayer graphene of thickness 1.12 nm [68]. From the bilayer graphene wherein the second layer is translated with respect to first by δ_i , the third layer may be considered to be translated with respect to second either by δ_i or $-\delta_i$. Former leads to ABA stacking and latter the ABC stacking. It is generalised as follows:

3.2. Physical Properties

- Layers translated with respect to their lower neighbour by δ_i leads to rhombohedral stacking, also called ABC stacking, which has 6 atoms per unit cell. However, structural defects are often present in domains with ABC stacking [69].
- In alternate translation $(\delta_i, -\delta_i, \delta_i, -\delta_i, \dots)$, such stacking results in a hexagon or ABA or Bernal stacking. This is the most common stacking found in natural graphite crystals [69].

In 2011, three research groups [80–82] reported experimental findings that ABC-stacked trilayers are distinct from all other graphene multilayers. Measurements of quantization sequence of Hall conductance confirmed that low-energy electrons in ABC trilayers exhibit a cubic dispersion unlike mono- and bilayers. Applying a perpendicular electric field in ABA trilayers, increases the overlap between valence and conduction bands which enhances the conductivity [83]. Figure 3.12 shows trilayer ABA and ABC stacking order with layers shifted to one C–C distance (0.142 nm) with respect to the next layer.

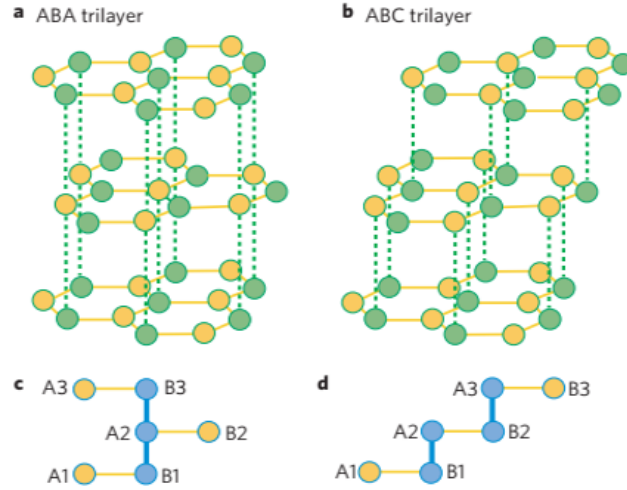


Figure 3.12: Trilayer graphene stack: (a) ABA, (b) ABC, (c) and (d) next layer moved one C–C bond distance, 0.142 nm. Reproduced from Ref. [80].

In a layer of graphene, one s -orbital ($2s^2$) and two p -orbitals ($2p_x, 2p_y$) hybridize leading to sp^2 hybridisation, forming σ -bond between carbon atoms which are separated by 0.142 nm. The σ -band provides robustness to the lattice. Based on Pauli principle, these bonds form a deep valence band since they have a filled shell. The remaining p -orbital ($2p_z$) stands perpendicular to the planar structure and forms covalent π -bonds with nearest neighbouring carbon atoms. This π -band has only one electron from each atom and thus half-filled.

Mono- and bilayer graphene have simple electronic spectra and both are zero-gap semiconductors. For three layers and beyond, the spectra becomes complicated since several charge carriers appear and valence and conduction bands start overlapping [67]. Therefore, graphene layers are distinguished as single-, double- and few- (3 to < 10 layers). Increasing layers of graphene approaches the 3D limit of graphite at 10 layers [84].

3.3 Electronic Band Structure

Given the electronic configuration of carbon ($1s^2 2s^2 2p^2$), three electrons are involved in forming strong covalent σ bonds and one electron per atom forms the π bonds. At low energies, the π electrons are responsible for electronic properties whereas the σ electrons form energy bands far away from the Fermi energy [73]. Charge carriers in graphene constitute a 2D gas of massless Dirac fermions (i.e., carrier transport is governed by the relativistic Dirac equation). Fig. 3.6, there is an energy difference (~ 4 eV) the $2s$ and $2p$ orbitals, which leads to hybridisation of these orbitals. Of the four valence electrons in carbon atom, one electron in each of $2s$, $2p_x$ and $2p_y$ orbitals form σ bonds with three nearest neighbours and the remaining one electron in $2p_z$ forms π bond with nearest neighbours. The electrons forming π bonds determine the energy spectra of graphene represented using the tight binding model.

3.3.1 Tight Binding Model

A free-electron model defines how charge carriers behave in a metallic solid and thus represents the electronic structure. In case of materials with closed shell atoms (e.g., graphene), the free electron model may not be appropriate. A tight binding model (Fig. 3.13) brings together the wavefunctions of atoms and their interaction to represent the electronic structure of such systems. The simplest model is the system with one atom per unit cell with one valence orbital $\phi(r)$.

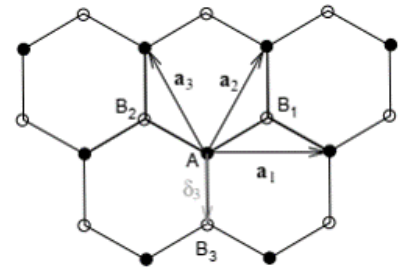


Figure 3.13: Representation of tight binding model in graphene lattice. Source: [73].

The general form of Bloch wave function is used in this model:

$$\psi = \sum_{\mathbf{R}} e^{i\mathbf{k}\cdot\mathbf{R}} \phi(\mathbf{r} - \mathbf{R}) \quad (3.12)$$

3.3. Electronic Band Structure

where \mathbf{R} represents the set of lattice vectors \mathbf{a}_1 and \mathbf{a}_2 and $\phi(\mathbf{r})$ the envelope function. Since there is a overlap of atomic wave functions, ϕ is approximated by a linear combination of set of atomic wave functions.

Using equation 3.12, the wave function for an atom in an unit cell is given by

$$\psi_{\mathbf{k}}(r) = \frac{1}{\sqrt{N}} \sum_m \exp(j\mathbf{k} \cdot \mathbf{R}_m) \phi(\mathbf{r} - \mathbf{R}_m) \quad (3.13)$$

This idea is extended to two atoms in an unit cell system. As seen in previous sections, long range order of hexagonally arranged carbon atoms make up a layer of graphene. This arrangement is seen as a lattice with a two-atom basis in a unit cell. Lattice vectors are given as

$$\mathbf{a}_1 = \frac{a}{2}(3, \sqrt{3}), \quad \mathbf{a}_2 = \frac{a}{2}(3, -\sqrt{3}) \quad (3.14)$$

and vectors for reciprocal lattice are given by

$$\mathbf{b}_1 = \frac{2\pi}{3a}(1, \sqrt{3}), \quad \mathbf{b}_2 = \frac{2\pi}{3a}(1, -\sqrt{3}) \quad (3.15)$$

where the carbon-carbon bond distance, $a \approx 0.142$ nm. The Bravais lattice vectors are given by

$$\mathbf{R}_j = m_j \mathbf{a}_1 + n_j \mathbf{a}_2 \quad (3.16)$$

where m_j and n_j are integers. Each ion on site R_j yields an electrostatic potential and the overall potential energy is given as $\sum_j^N V(\mathbf{R}_l - \mathbf{R}_j)$ where N is the number of lattice sites and \mathbf{R}_l and \mathbf{R}_j the lattice sites. This is a periodic function with respect to an arbitrary translation by lattice vector \mathbf{R}_i .

The points K and K' at the corners of Brillouin zone (see Fig. 3.10) in graphene are important for the electronic spectra and are called Dirac points. Their positions in momentum space are given

$$K = \left(\frac{2\pi}{3a}, \frac{2\pi}{3\sqrt{3}a} \right), \quad K' = \left(\frac{2\pi}{3a}, -\frac{2\pi}{3\sqrt{3}a} \right) \quad (3.17)$$

the three nearest neighbour vectors are

$$\delta_1 = \frac{a}{2}(1, \sqrt{3}), \quad \delta_2 = \frac{a}{2}(1, -\sqrt{3}), \quad \delta_3 = -a(1, 0) \quad (3.18)$$

and the six nearest neighbour vectors are located at

$$\delta'_1 = \pm a_1, \quad \delta'_2 = \pm a_2, \quad \delta'_3 = \pm(a_2 - a_1). \quad (3.19)$$

3.3. Electronic Band Structure

From the orbital representation of graphene (Fig. 3.6), we understand that electron in $2p_z$ orbital forms σ bond, which is taken into account in this model. Therefore, in a unit cell, we have two $2p_z$ orbitals denoted by ϕ_1 and ϕ_2 . The total wave function is then given by

$$\phi = b_1\phi_1 + b_2\phi_2 \quad (3.20)$$

where b_1 and b_2 denote constants, $|b_1|^2 + |b_2|^2 = 1$. The nearest-neighbour atoms exert atomic potential on these two electrons and the Hamiltonian is given by

$$H = \frac{\nabla^2}{2m} + \sum_{\mathbf{R}} (V_{\text{atom}}(\mathbf{r} - \mathbf{r}_1 - \mathbf{R}) + V_{\text{atom}}(\mathbf{r} - \mathbf{r}_2 - \mathbf{R})) \quad (3.21)$$

where \mathbf{r}_1 and \mathbf{r}_2 denote positions of the two atoms. The constants b_1 and b_2 are obtained by solving the Schrödinger equation,

$$H\psi = E\psi \quad (3.22)$$

For the total wave function with constants (b_1 and b_2) and states (ϕ_1 and ϕ_2), using bra and ket vectors, above equation becomes

$$\langle \phi_j | H | \psi \rangle = E \langle \phi_j | \psi \rangle \quad (3.23)$$

where $j = 1, 2$.

Considering only nearest neighbours $\mathbf{R} = 0, \mathbf{a}_1, \mathbf{a}_2$ terms in $|\psi\rangle$,

$$\langle \phi_1 | \psi \rangle = b_1 + b_2 \langle \phi_1 | \phi_2 \rangle (1 + e^{-i\mathbf{k}\cdot\mathbf{a}_1} + e^{-i\mathbf{k}\cdot\mathbf{a}_2}) \quad (3.24)$$

$$\langle \phi_2 | \psi \rangle = b_2 + b_1 \langle \phi_2 | \phi_1 \rangle (1 + e^{-i\mathbf{k}\cdot\mathbf{a}_1} + e^{-i\mathbf{k}\cdot\mathbf{a}_2}) \quad (3.25)$$

Here $\langle \phi_1 | \phi_2 \rangle = \langle \phi_2 | \phi_1 \rangle$. From equation 3.21, the atomic Hamiltonian for two atoms, a_1 and a_2 is given by

$$H_1 = \frac{\nabla^2}{2m} + V_{\text{atom}}(\mathbf{r} - \mathbf{r}_1) \quad (3.26)$$

$$H_2 = \frac{\nabla^2}{2m} + V_{\text{atom}}(\mathbf{r} - \mathbf{r}_2) \quad (3.27)$$

Therefore,

$$H = H_1 + \Delta H_1 = H_2 + \Delta H_2 \quad (3.28)$$

We now use a simple relation as ϕ_j are eigenfunctions of H_j ,

$$H_j |\phi_j\rangle = \varepsilon_j |\phi_j\rangle \quad (3.29)$$

3.3. Electronic Band Structure

where ε_j represents the energy of $2p_z$ orbitals. As we have only carbon atoms in a layer of graphene, $\varepsilon_1 = \varepsilon_2$, which is now denoted by ε_0 . Setting $\varepsilon_0 = 0$,

$$\langle \phi_1 | H | \psi \rangle = \langle \phi_1 | H_1 + \Delta H_1 | \psi \rangle = \langle \phi_1 | \Delta H_1 | \psi \rangle \quad (3.30)$$

$$\langle \phi_2 | H | \psi \rangle = \langle \phi_2 | H_2 + \Delta H_2 | \psi \rangle = \langle \phi_2 | \Delta H_2 | \psi \rangle \quad (3.31)$$

As we are studying a two-atom basis, so only the nearest neighbours are relevant for atoms 1 and 2 when calculating the terms of $\langle \phi_j | \Delta H_j | \psi \rangle$. So the terms for above two equations are given as follows:

$$\langle \phi_1 | \Delta H_1 | \psi \rangle = b_1 \beta + b_2 \gamma_1 f^*(\mathbf{k}) \quad (3.32)$$

$$\langle \phi_2 | \Delta H_2 | \psi \rangle = b_2 \beta + b_1 \gamma_1 f(\mathbf{k}) \quad (3.33)$$

where

$$\begin{aligned} \beta &= \langle \phi_1 | \Delta H_1 | \phi_1 \rangle \\ \gamma_1 &= \langle \phi_1 | \Delta H_1 | \phi_2 \rangle = \langle \phi_2 | \Delta H_2 | \phi_1 \rangle \\ f(\mathbf{k}) &= 1 + e^{i\mathbf{k} \cdot \mathbf{a}_1} + e^{i\mathbf{k} \cdot \mathbf{a}_2} \end{aligned} \quad (3.34)$$

Using equations (3.25) through (3.33), transforming the Schrödinger equation (3.23) into an eigenvalue equation as

$$\begin{pmatrix} \beta & f^*(\mathbf{k})(\gamma_1 - \gamma_0 E) \\ f(\mathbf{k})(\gamma_1 - \gamma_0 E) & \beta \end{pmatrix} \begin{pmatrix} b_1 \\ b_2 \end{pmatrix} = E \begin{pmatrix} b_1 \\ b_2 \end{pmatrix} \quad (3.35)$$

where β is the variation in energy of $2p_z$ orbital, exerted by carbon atoms in a graphene layer. The above equation leads to the dispersion relation $E = E(\mathbf{k})$. From Schrödinger equation (3.23) and Bloch equation (3.13), the two basis wave functions are assumed as

$$\psi_{(1,2)} = \sum_{\mathbf{R}} e^{i\mathbf{k} \cdot \mathbf{R}} \phi_{(1,2)}(\mathbf{r} - \mathbf{R}) \quad (3.36)$$

The energy variation, β , is considered negligible as it corresponds to a minor rigid shift on the energy band. Using this fact, equation (3.35) is simplified further since the hopping parameter, γ_0 , is small. Then the dispersion relation becomes

$$\begin{aligned} E(\mathbf{k}) &= \pm \gamma_1 |f(\mathbf{k})| \\ &= \pm \gamma_1 \sqrt{1 + 4 \cos\left(\frac{k_y \sqrt{3}a}{2}\right) \cos\left(\frac{k_x a}{2}\right) + 4 \cos^2\left(\frac{k_x a}{2}\right)} \end{aligned} \quad (3.37)$$

where k_x and k_y are components of \mathbf{k} . The above equation leads to the energy band structure of graphene shown in Fig. 3.14(a), which can be obtained using MATLAB codes.

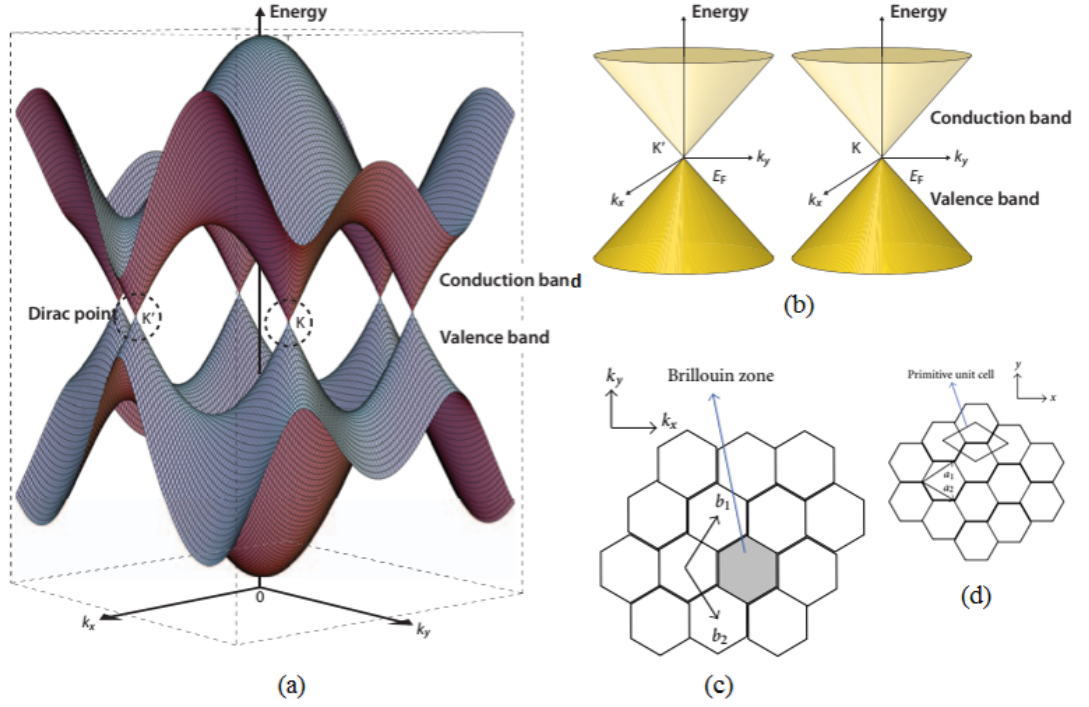


Figure 3.14: Representation of electronic band structure in graphene. (a) Dirac cone; (b) cones at Dirac points K and K' ; (c) Brillouin zone in a graphene layer; and (d) unit cell of two-atom basis. Adapted from Refs [85, 86].

The electronic band structure shown in Fig. 3.14(a) represents how the valence and conduction bands cross each other at six points in the corners of the 2D hexagonal Brillouin zone (BZ) in Fig. 3.14(c). Both these bands meet at K and K' , called Dirac points. Each BZ has three K and three K' points. Fig. 3.14(b) depicts the cones at K and K' separately and each carbon atom contributes an electron ($2p_z$) each for conduction. The electrons and holes behave like relativistic particles near the Dirac points with half-spin due to the linear dispersion relation in equation (3.37). So the charge carriers of graphene are termed as Dirac Fermions that make graphene a zero-gap semiconductor. Importantly, the Fermi level in graphene can be controlled by applying a gate voltage (V_{gate}), which is a unique property. The electronic and optical properties vary with respect to change in chemical potential. This variation and its influence on material properties such as dielectric constant (ϵ) is discussed in the next section.

The region close to K and K' is termed a low-energy region where the Hamiltonian is approximated by a first-order expansion. Firstly, around K point, $\mathbf{k} = \boldsymbol{\kappa} + K$, and by first-order expansion of $f(\mathbf{k})$, equation (3.35) becomes,

$$-\frac{\sqrt{3}\gamma_1 a}{2} \begin{pmatrix} 0 & \kappa_x - i\kappa_y \\ \kappa_x + i\kappa_y & 0 \end{pmatrix} \begin{pmatrix} b_1 \\ b_2 \end{pmatrix} = \epsilon(\boldsymbol{\kappa}) \begin{pmatrix} b_1 \\ b_2 \end{pmatrix} \quad (3.38)$$

3.4. Optical Conductivity

Secondly, above dispersion relation simplifies to

$$\varepsilon(\kappa) = \mp \hbar v_F |\kappa| \quad (3.39)$$

where v_F is termed the Fermi velocity and it is given by

$$v_F = \frac{\sqrt{3} \gamma_1 a}{2 \hbar} \quad (3.40)$$

As the two-dimensional energy spectrum is linear, the electrons always move at a constant speed, v_F . Using literature values for $\gamma_1 = 2.9 \text{ eV}$ [87] and $a = 0.426 \text{ nm}$ [88], the Fermi velocity is calculated to be, $v_F \approx 10^6 \text{ m/s}$. This shows the charge carriers in graphene move in a similar manner of light, as if they are relativistic particles with zero mass.

The Hamiltonian in terms of Fermi velocity at \mathbf{K} is

$$H = \hbar - v_F \hat{\kappa} \cdot \sigma \quad (3.41)$$

where

$$\hat{\kappa} = -i\nabla = -i \left(\hat{x} \frac{\partial}{\partial x} + \hat{y} \frac{\partial}{\partial y} \right) \quad (3.42)$$

and σ the Pauli matrices are given by $\sigma = (\sigma_x, \sigma_y)$.

3.4 Optical Conductivity

We have seen the electron band structure of graphene in previous section. It is very simple, near the energy $\varepsilon = 0$, the energy bands form cones at Dirac points K and K' in the two-dimensional Brillouin zone (Fig. 3.15) with Fermi velocity, $v_F \approx 10^6 \text{ m/s}$. One of the unique properties of graphene is that the quasiparticles such as plasmons and fermions obey a linear dispersion relation. As a consequence, an additional symmetry that is chiral in nature exists for these quasiparticles. This chiral symmetry fixes the direction of pseudospin – parallel

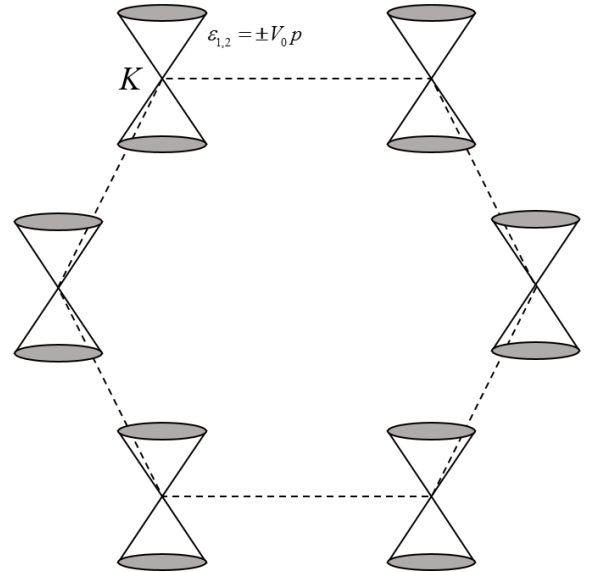


Figure 3.15: Graphene electron spectrum (Dirac cones) at K points of the Brillouin zone.

or antiparallel – to the directions of motion of electrons and holes, respectively, which

3.4. Optical Conductivity

also has an immediate and dominant effect on the electronic and optical properties of graphene [89].

Modulation mechanism in a graphene modulator is wholly based on electron–photon interaction. Charge carrier density or carrier concentration (n_g) levels play a major role in this phenomena, which is unique in graphene, as this levels can be adjusted through doping or by applying an external gate voltage.

$$n_g = \frac{\epsilon_0 \epsilon_r}{t e} V_g = \gamma V_g \quad (3.43)$$

where $\epsilon_0 \cong 8.854 \times 10^{-12}$ F/m is the permittivity of free space, ϵ_r the relative permittivity of substrate (SiO₂, $\epsilon_r = 3.9$), t the thickness of SiO₂ (e.g., 300 nm) and $e \cong 1.602 \times 10^{-19}$ C the electronic charge. Using these values, the proportionality coefficient γ between charge carriers and applied gate voltage is $\gamma \cong 7.3 \times 10^{10}$ cm⁻²V⁻¹ [90].

Studies based on conductivity of graphene (σ_g) gained prominence when it is found that this property “never falls below a minimum value” [90], even when n_g tends to zero. Adjusting the chemical potential with electric field thus provides unique effects which can be exploited in realising electronic devices at the nanolevel. Another important phenomena, unusual half-integer quantum Hall effect, has been observed in graphene which is also due to the effect of electric field on both electron and hole carriers [92]. Figure 3.16(a) shows variation of optical conductivity (σ) as a function of gate voltage (V_g). For both polarities, σ linearly increases with increasing V_g . The Pauli blocking mechanism is shown in Fig. 3.16(b). In stage I, interband transitions occur as graphene absorbs incident light. In stage II, the carriers relax

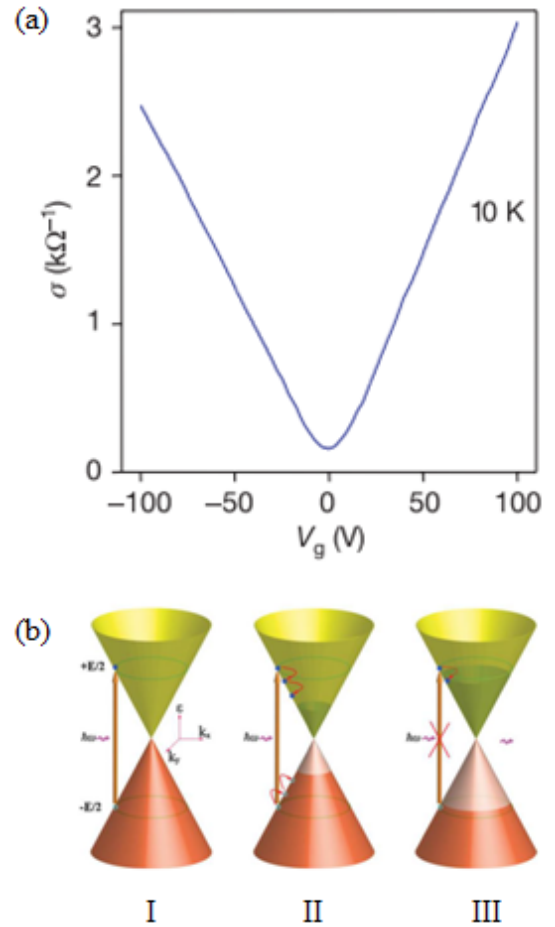


Figure 3.16: (a) Optical conductivity *versus* gate voltage. Reproduced from Ref. [90]. (b) Pauli blocking mechanism. Adapted from Ref. [91].

3.4. Optical Conductivity

and redistribute given by Fermi–Dirac distribution. Stage III shows saturable absorption when further absorption is blocked, which is termed Pauli blocking, as no two electrons can be in the same quantum state. At this stage, no light will be absorbed and graphene is transparent.

Optical absorption in graphene occurs from two transitions or contributions *viz.*, intra-band and interband. Former happens within cones and latter between the lower (valence band) and upper (conduction band) cones. The term transitions refer to the production of electron–hole pairs. The intraband transitions exists even at zero energy, $\varepsilon = 0$. When Fermi energy is at the Dirac point, the Fermi surface shrinks to a point, so the intraband transitions disappear and only interband transitions between the lower and upper cones exist [93]. The change in optical conductivity of graphene under excitation arises from both intra- and interband contributions. Kubo formula is used for describing the complex conductivity of graphene including both the transitions [91, 94, 95]:

$$\sigma = \sigma_{\text{intra}} + \sigma'_{\text{inter}} + j\sigma''_{\text{inter}} \quad (3.44)$$

where “intra” denotes the transitions within valence bands whereas “inter” the electron transitions between valence and conduction bands.

$$\sigma_{\text{intra}} = \sigma_0 \frac{4\mu}{\pi} \frac{1}{\hbar\tau_1 - i\hbar\omega} \quad (3.45)$$

$$\sigma'_{\text{inter}} = \sigma_0 \left(1 + \frac{1}{\pi} \arctan \frac{\hbar\omega - 2\mu}{\hbar\tau_2} - \frac{1}{\pi} \arctan \frac{\hbar\omega + 2\mu}{\hbar\tau_2} \right) \quad (3.46)$$

$$\sigma''_{\text{inter}} = -\sigma_0 \frac{1}{2\pi} \ln \frac{(\hbar\omega + 2\mu)^2 + \hbar^2\tau_2^2}{(\hbar\omega - 2\mu)^2 + \hbar^2\tau_2^2} \quad (3.47)$$

where μ is the chemical potential (in eV), $\sigma_0 = e^2/4\hbar \cong 60.8\mu\text{S}$ is the universal optical conductance, $\hbar = h/2\pi$, h the Planck’s constant (6.626176×10^{-34} joule-seconds), $\omega = 2\pi\nu$, ν the frequency of optical pump and $\tau_1 = 8.3 \times 10^{11} \text{ s}^{-1}$ and $\tau_2 = 10^{13} \text{ s}^{-1}$ the relaxation rates of intra- and interband transitions, respectively [96]. The complex conductivity of graphene takes the final form,

$$\sigma(\omega) = \sigma_1(\omega) + j\sigma_2(\omega) \quad (3.48)$$

where $\sigma_1(\omega)$ and $\sigma_2(\omega)$ denote the real and imaginary parts of $\sigma(\omega)$.

In the next section, we discuss a very important parameter, dielectric constant or permittivity, of graphene. It is denoted by ε and this parameter plays a very crucial role in the electro-optic modulation phenomena on which this thesis is mainly based on.

3.5 Dielectric Constants

Optical properties of a material are mostly based on their electronic band structure and dielectric screening factors. The dielectric function $\varepsilon(\mathbf{q}, \omega)$ is dependent on wave vector \mathbf{q} and frequency ($\omega = 2\pi\nu$). The uniqueness of graphene is that the chemical potential can be controlled through external voltage, i.e., tuning Fermi level (E_F) by electrical gating (V_g). The dielectric function ($\varepsilon(\omega)$) of graphene is a complex term since it is derived from conductivity ($\sigma(\omega)$), which is also a complex term as seen in previous section. Both ε and σ consist of interband and intraband contributions.

To obtain $\varepsilon(\omega)$, we need to calculate $\sigma(\omega)$ first. Stauber *et al.* [27] has presented a detailed study on optical conductivity of graphene. They used Kubo formula and introduced a correction to the real part of $\sigma(\omega)$. Their study has included the following cubic term in the density of states ($\rho(E)$) with usual Dirac cone approximation,

$$\rho(E) = \frac{2E}{\sqrt{3}\pi t^2} + \frac{2E^3}{3\sqrt{3}\pi t^4} + \frac{10E^5}{27\sqrt{3}\pi t^6} \quad (3.49)$$

A graphene layer confines electrons in a two-dimensional system which results in quantum-mechanical phenomenon such as Landau levels. These quantized behaviours of Dirac fermions in graphene are studied experimentally in infrared spectroscopy experiments [99] as well as using scanning tunnelling microscopy (STM) and scanning tunnelling spectroscopy (STS). The measurements show Landau-level spectra and rich level-splitting in graphene layers of varying thickness. Based on these results, the presence of number of layers and stacking order (random or ABA or ABC) in graphene sample can be identified. In graphene, Landau levels are not equidistant, therefore all optical transition frequencies are different from each other. The optical transitions are of two types:

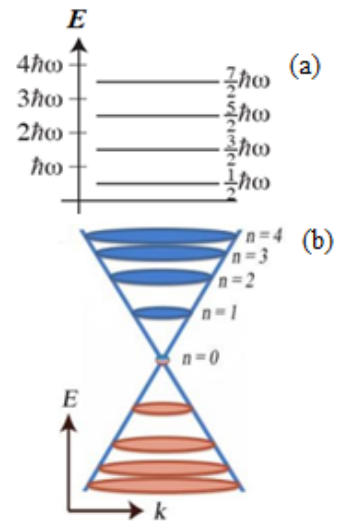


Figure 3.17: (a) Landau levels [97]. (b) Schematic of Landau levels in Dirac cone [98].

- a) intraband: transition between electron (hole) states;
- b) interband: transition between electron and hole states, i.e., valence and conduction bands.

For calculating the dielectric constant of graphene layers, it is very important to know the number of layers present in the sample as it will impact the dielectric constant values which are very crucial for electro-optic modulation. Next section we will discuss the method we used in this study to obtain the complex dielectric constant values ($\varepsilon_1 + j\varepsilon_2$) for various voltage levels ($\mu = 0 - 1$ eV). The concept of electro-optic modulation using graphene layer is based on its uniqueness on controlling of Fermi level (chemical potential, μ) by applying a gate voltage (V_g).

3.5.1 Method

Several studies have obtained the conductivity equation [26,27,94,100], $\sigma(\omega)$, from Kubo formula and identified the range of complex dielectric constants, $\varepsilon_1 + j\varepsilon_2$, for graphene [6,28,29]. Here ε_1 and ε_2 denote the real and imaginary parts of $\varepsilon(\omega)$. The factors such as angular frequency (ω), chemical potential (μ), scattering rate (Γ) and temperature (T) influence the conductivity as well as the permittivity of graphene. So the first step is to derive the equation for optical conductivity $\sigma(\omega)$ and then calculate the permittivity $\varepsilon(\omega)$ at various voltage levels (in eV).

Under an external electric field, a material polarize ($\mathbf{P} = \chi_e \mathbf{E}$) or carry a current $\mathbf{j} = \sigma \mathbf{E}$, where χ_e is the electric susceptibility and σ the conductivity. In case if the electric field (\mathbf{E}) is not strong enough, both these parameters are independent of \mathbf{E} . They then depend only on the material properties which is termed linear response since χ_e and σ are independent of the electric field [101].

An electric field varies in space and time sinusoidally given by

$$\mathbf{E}(t) = \mathbf{E} \cos(\omega t) \quad (3.50)$$

In a solid, the response will be a first order with an electric current given by

$$j_\alpha(t) = \sigma_{\alpha\beta}^{(1)} \mathbf{E}_\beta \cos(\omega t) + \sigma_{\alpha\beta}^{(2)} \mathbf{E}_\beta \sin(\omega t) \quad (3.51)$$

In terms of complex notations, equation (3.51) is equivalent to

$$j(t) = \text{Re}[\sigma(\omega) \mathbf{E} e^{-i\omega t}] \quad (3.52)$$

3.5. Dielectric Constants

with complex conductivity $\sigma = \sigma^{(1)} + j\sigma^{(2)}$ where real part denoting the in-phase or dissipative and imaginary part the out-of-phase or reactive response to the \mathbf{E} field.

Optical conductivity of a material is studied through the material's response to an external electric field given by

$$\mathbf{E}(\mathbf{r}, t) = \mathbf{E}_0 e^{i\mathbf{q}\cdot\mathbf{r} - i\omega t} \quad (3.53)$$

Conductivity is calculated from following relation, within this linear response:

$$J_\alpha(\mathbf{r}, t) = \sigma_{\alpha\beta}(\mathbf{q}, \omega) E_\beta(\mathbf{r}, t) \quad (3.54)$$

To find expression for conductivity, we start with the Hamiltonian of the system,

$$H = \int d^d r \left[\frac{1}{2m} \psi^\dagger(x) (\mathbf{p} - e\mathbf{A})^2 \psi(x) - e\phi(x) \psi^\dagger(x) \psi(x) \right] + H_{\text{int}} \quad (3.55)$$

From above equation, the current is found by

$$\begin{aligned} \mathbf{j} &= -\frac{\delta H}{\delta \mathbf{A}} \\ &= \underbrace{\frac{-ie\hbar}{2m} \left(\psi^\dagger(x) \nabla \psi(x) - \psi(x) \nabla \psi^\dagger(x) \right)}_{j_p} - \underbrace{\frac{e^2}{m} \mathbf{A} \psi^\dagger(x) \psi(x)}_{j_d} \end{aligned} \quad (3.56)$$

where j_p is the paramagnetic current and j_d the diamagnetic current.

The observed current is the expectation value of current operation given by,

$$J(\mathbf{r}, t) = \langle \mathbf{j}_p(\mathbf{r}, t) \rangle - \frac{ne^2}{m} \mathbf{A}(\mathbf{r}, t) \quad (3.57)$$

where n denotes the electron density which is a vital parameter.

We have seen in previous sections that the π electrons in graphene are responsible for conduction. Therefore, the dispersion of such electrons in the first Brillouin zone is given by

$$E(\mathbf{k}) = s\hbar v_F |\mathbf{k}| \quad (3.58)$$

where \hbar is the reduced Planck's constant and v_F the Fermi velocity, $\sim 10^6$ m/s; here, $s = +1$ refers to the conduction band and $s = -1$ the valence band; $|\mathbf{k}| = 0$ refers to the Dirac point, thus, $E(|\mathbf{k}| = 0) = 0$ eV.

The uniqueness in graphene is the tuning of Fermi level by electrical gating or external voltage. This applied gate voltage (V_g) alters the carrier density, $n_g = C(V + V_0)$. Accordingly, the Fermi level gets shifted by

$$E_F = \hbar v_F \sqrt{\pi \cdot n_g} \quad (3.59)$$

3.5. Dielectric Constants

where V_0 is the offset voltage; C refers to the capacitance estimated from a simple capacitor model (especially for devices involving two layers of graphene separated by a dielectric) given by

$$\alpha = \frac{\varepsilon_0 \varepsilon_d}{t_d e} \quad (3.60)$$

where $\varepsilon_0 \cong 8.854 \times 10^{-12}$ F/m is the permittivity of free space, ε_d the permittivity of dielectric and t_d the thickness of dielectric between two graphene layers [6].

In an undoped graphene, under thermal equilibrium, the mobile (π) electrons in CB and holes in VB act similar to intrinsic carriers in a semiconductor. Therefore, in terms of density of states (DOS), the sheet carrier density ρ_g of such intrinsic carriers is given by

$$\rho_g(E) = \frac{g_s g_v}{2\pi(\hbar v_F)^2} |E| \quad (3.61)$$

where g_s refers to the two-fold spin degenerate and g_v the two valleys in the first Brillouin zones (K and K'); $g_s = g_v = 2$ [102]. The charge carrier density is given by,

$$n = \int_0^{\infty} dE \rho_g(E) f(E) \quad (3.62)$$

where $f(E)$ is the Fermi–Dirac distribution given by

$$f(E) = \left(1 + \exp \left[\frac{E - E_F}{k_B T} \right] \right)^{-1} \quad (3.63)$$

where k_B is the Boltzmann constant, T the absolute temperature and E_F the Fermi level. Using dimensionless variables $u = E/k_B T$ and $\eta = E_F/k_B T$, equation (3.62) can be rewritten as,

$$n = \frac{2}{\pi} \left(\frac{k_B T}{\hbar v_F} \right)^2 \mathfrak{S}_1(+\eta) \quad (3.64)$$

Similarly, the symmetric hole density is given by,

$$p = \frac{2}{\pi} \left(\frac{k_B T}{\hbar v_F} \right)^2 \mathfrak{S}_1(-\eta) \quad (3.65)$$

where $\mathfrak{S}_j(\eta)$ is termed the Fermi–Dirac integral with $j = 1$.

The Fermi level, under no external bias and no optical illumination, is unique and exactly at the Dirac point, $E_F = 0$ eV, and the intrinsic carrier concentration is derived using above equations as,

$$n = p = n_i = \frac{\pi}{6} \left(\frac{k_B T}{\hbar v_F} \right)^2 \quad (3.66)$$

3.5. Dielectric Constants

The above equation is an ideal equation which has carrier concentration (n) dependent only on Fermi velocity (v_F). At room temperature, this value is $n_i \approx 9 \times 10^{10} \text{ cm}^{-2}$ taking into account the intrinsic electron and hole sheet densities [102].

In previous sections, we have seen that modulation in a graphene-based waveguide is carried out by tuning Fermi level in graphene through electric gating and the Fermi level shift is given by

$$\Delta E_F = \hbar v_F \sqrt{\pi |n|} \quad (3.67)$$

where \hbar the Planck constant (h) divided by 2π and v_F the Fermi velocity ($\approx 10^6 \text{ m/s}$).

Using Kubo formula, the derived equation for conductivity is given as follows [26]:

$$\begin{aligned} \sigma(\omega) = & \frac{\sigma_0}{2} \underbrace{\left(\tanh \frac{\hbar\omega + 2\mu}{4k_B T} + \tanh \frac{\hbar\omega - 2\mu}{4k_B T} \right)}_{\text{interband}} \\ & - i \frac{\sigma_0}{2\pi} \underbrace{\log \left[\frac{(\hbar\omega + 2\mu)^2}{(\hbar\omega - 2\mu)^2 + (2k_B T)^2} \right]}_{\text{interband}} \\ & + i \underbrace{\frac{4\sigma_0}{\pi} \frac{\mu}{\hbar\omega + i\hbar\gamma}}_{\text{intraband}} \end{aligned} \quad (3.68)$$

where μ is the Fermi level, γ the intraband scattering rate, σ_0 the universal conductivity defined by $e^2/(4\hbar)$, k_B the Boltzmann constant ($1.38 \times 10^{-23} \text{ m}^2 \text{ kg s}^{-2} \text{ K}^{-1}$), ω the angular frequency ($= 2\pi\nu$) and T the temperature in kelvin.

Using equation (3.68), the complex dielectric function can be obtained as follows [6]:

$$\varepsilon(\omega) = 1 + j \frac{\sigma(\omega)}{\omega \varepsilon_0 t_g} \quad (3.69)$$

where t_g is the thickness of graphene layer, ε_0 the permittivity of free space ($8.8542 \times 10^{-12} \text{ m}^{-3} \text{ kg}^{-1} \text{ s}^4 \text{ A}^2$) and $\omega = 2\pi\nu$ with $\nu = c/\lambda$; (velocity of light, $c = 3 \times 10^8 \text{ ms}^{-1}$ and λ the wavelength of incident light in μm).

3.5.2 Results and Discussion

We have seen in previous sections the uniqueness of graphene layer is that the Fermi level (E_F) can be tuned by applying a gate voltage (V_g). This property makes graphene layers most suitable for electro-absorption modulators. In simple terms, electrons in graphene couple with photons and thus light modulation is achieved by tuning the Fermi energy of graphene with electrical gating. Equations (3.68) and (3.69) shows expressions for $\sigma(\omega)$

and $\varepsilon(\omega)$, respectively. From equation (3.69), it is obvious that the dielectric constant $\varepsilon(\omega)$ depends on wavelength (λ) and t_g the thickness of graphene layer. In this section, we present our results on change in dielectric constant ($\varepsilon(\omega)$) with respect to Fermi level or chemical potential, layer thickness and wavelength of incident light.

We have chosen the thickness of graphene layers from an experimental study [68] as follows:

- a) Monolayer: 0.4 nm
- b) Bilayer: 0.69 nm
- c) Trilayer: 1.12 nm

Figure 3.18 shows Raman spectra of graphite with mono-, bi- and trilayers. Technically, graphene is a monolayer of carbon atom of diameter 0.3 nm, so a thickness of monolayers graphene taken as 0.33–0.4 nm is agreeable.

As yet, a broad consensus has not been reached among research groups in treating the thickness of monolayer or bilayer graphene as given above. Most theoretical studies [6, 29, 103] used bilayer thickness of graphene as 0.7 nm. Studies [103–105] have taken thickness of graphene layer as 1 nm. In case of 2D materials, thickness measurement is very crucial as their electronic and thermal conduction properties heavily depend on layer thickness and difference of 0.1 or 0.01 will influence the results.

Novoselov *et al.* [3] used 1-mm-thick platelets of highly-oriented pyrolytic graphite (HOPG) as starting material to prepare single, double and few layer graphene. They found that thin flakes of this material with thickness, $d < 10$ nm attach strongly to SiO₂. This is an important finding when thickness of graphene required for electronic devices is still unclear. At $d < \approx 1.5$ nm, graphene films are not visible to the naked eye. Also, single-layer graphene has rarely been observed to be flat so some areas of film are ruptured or folded back. The step heights for single and double folds are found to be 0.4 and 0.8 nm, respectively (see Supplementary Material in Ref. [3]).

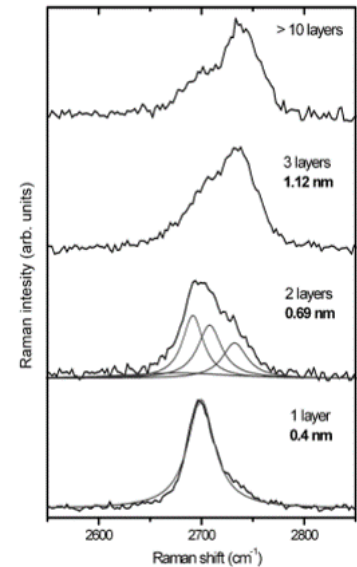


Figure 3.18: Raman spectra of graphitic layers. Source: [68].

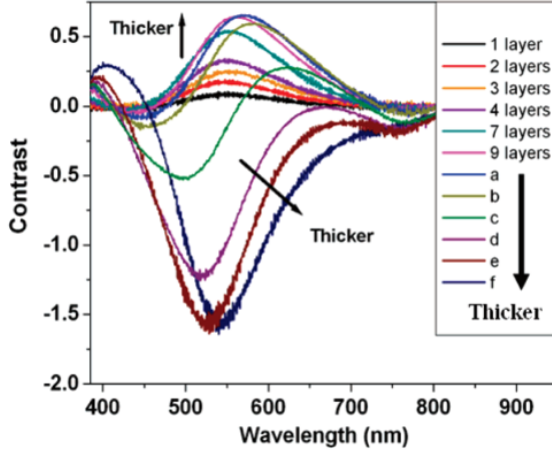


Figure 3.19: Contrast spectra of graphene sheets of varying thickness. Source: [77].

contrast peak position as shown in the figure remains steady at $\lambda = 550$ nm for layers up to 10. Beyond 10-layer thickness, the contrast spectra peak shifts towards higher wavelength (a and b), and negative contrast starts occurring for increasing number of layers (c-f). It is obvious that when samples become thick that the reflections from surface is more intense than that from the substrate leading to negative contrast [77].

We now move on to our results from the analytical expression (equations 3.68 and 3.69) we derived for calculating the dielectric constants of graphene [26, 27, 94]. Using equation (3.69), we can obtain a range of dielectric constants for varying thickness of graphene layers (t_g), chemical potential (μ) and wavelength (λ). Permittivity or dielectric constant ($\epsilon(\omega)$) depends on conductivity of the material which is derived using Kubo formula. First, we benchmarked our analytical expression with studies [29], [6] and [28]. Plots from equation 3.69 are plotted against theirs as shown in Figs 3.20, 3.21 and 3.22, respectively.

Plots in the figure show similar trend with $\text{Re}(\epsilon_1)$ peaks at $\mu = 0.4$ eV and becomes negative beyond $\mu = 0.5$ eV. When the electric gating (V_g) causes $\text{Re}(\epsilon_1)$ to negative values, the corresponding effect is termed “epsilon near zero” (*enz*) effect. For instance, $\mu(0.52 \text{ eV}) = -0.4998 + j0.5340$ is one such *enz* value, where TM mode attenuation peaks. The *enz* effect is that when the fundamental TM mode starts attenuating rapidly, which will be discussed in Chapters 4 and 5. An interactive MATLAB code was written (Appendix A) for the analytical expression (3.68 and 3.69) to obtain range of complex dielectric constants ($\epsilon_1 + j\epsilon_2$) for varying chemical potential μ , wavelength λ and thickness of graphene layer t_g . Thickness of graphene layer was taken as 0.7 nm. Using equation (3.69), the values obtained were plotted against the chemical potential, $\mu = 0 - 1.0$ eV.

Figure 3.19 shows the contrast spectra taken for varying thickness of graphene layers. Samples a-f are more than 10-layer thick. Contrast spectra is calculated as follows:

$$C(\lambda) = \frac{R_0(\lambda) - R(\lambda)}{R_0(\lambda)} \quad (3.70)$$

where $R_0(\lambda)$ is the reflection spectrum from SiO_2/Si substrate and $R(\lambda)$ the reflection spectrum graphene sheet. The con-

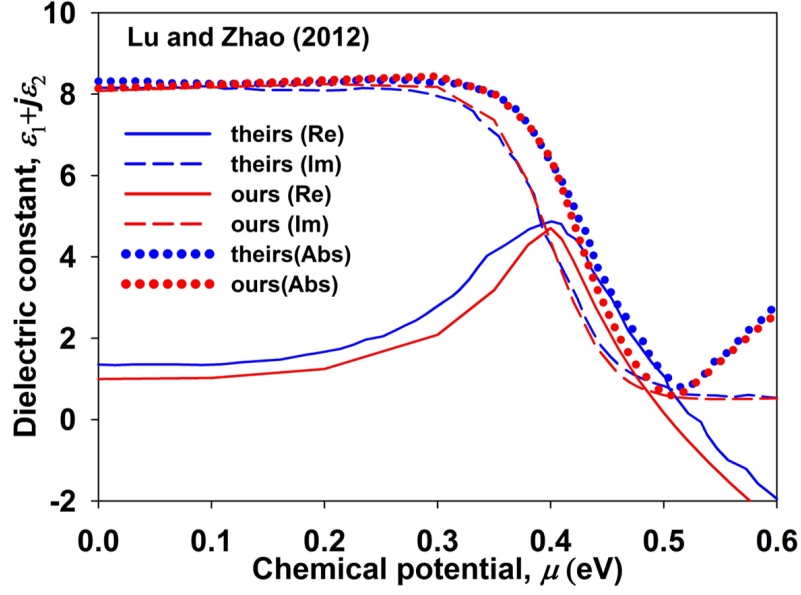


Figure 3.20: Benchmarking with Lu and Zhao [29]. $\lambda = 1550$ nm; $t_g = 0.7$ nm; “theirs” refers to $\varepsilon(\omega)$ plots of Lu and Zhao [29] and “ours” the $\varepsilon(\omega)$ plots from our study.

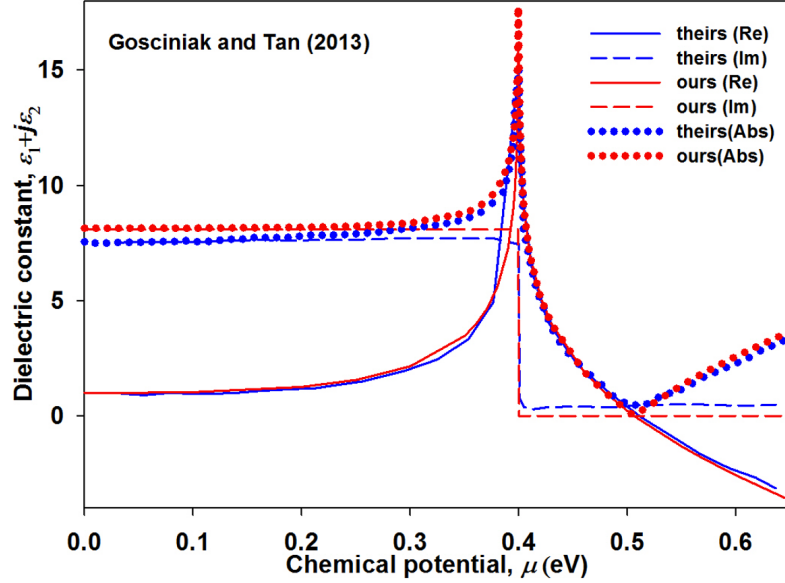


Figure 3.21: Benchmarking with Gosciniak and Tan [6]. $\lambda = 1550$ nm; $t_g = 0.7$ nm; “theirs” refers to $\varepsilon(\omega)$ plots of Gosciniak and Tan [6] and “ours” the $\varepsilon(\omega)$ plots from our study.

We will now move on to the discussion of dielectric constant plot in detail, which is crucial for electro-optic modulation. Figure 3.23 shows the plot obtained using analytical expressions (3.68) and (3.69) derived for bilayer graphene (0.69 nm) at the telecommunication wavelength, $\lambda = 1550$ nm.

In this plot, we have varied only the Fermi level (E_F) or chemical potential (μ), keeping λ and t_g constant. The applied gate voltage alters the carrier density (n_g) in graphene

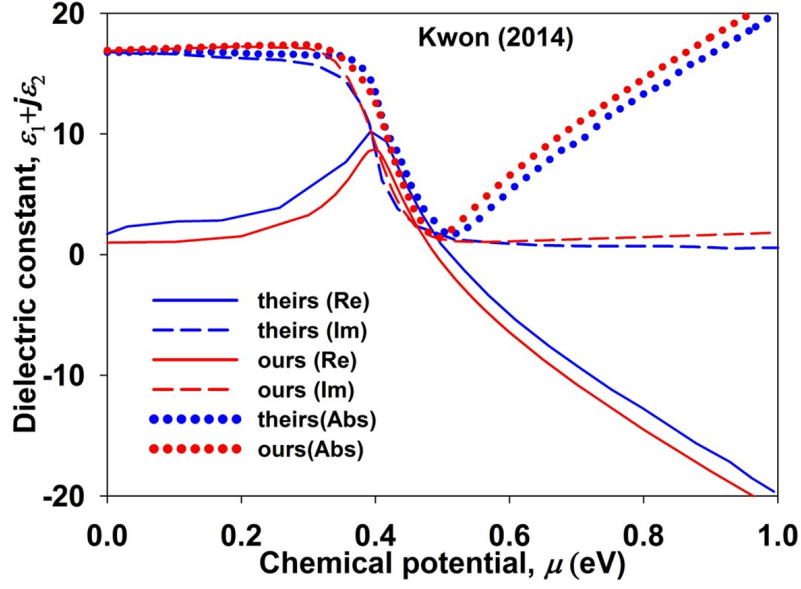


Figure 3.22: Benchmarking with Kwon [28]. $\lambda = 1550$ nm; $t_g = 0.7$ nm; “theirs” refers to $\varepsilon(\omega)$ plots of Kwon [28] and “ours” the $\varepsilon(\omega)$ plots from our study.

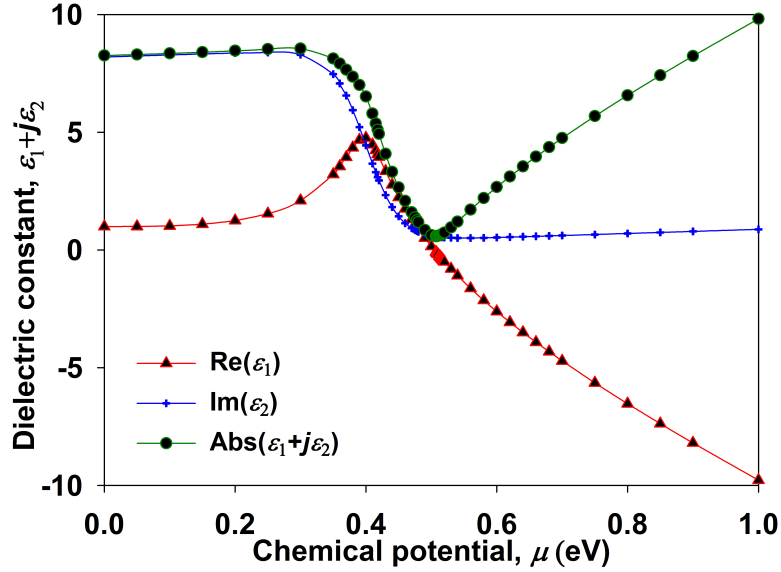


Figure 3.23: Complex dielectric constants of bilayer graphene ($t_g = 0.69$ nm) at $\lambda = 1550$ nm calculated and used in our study.

and shifts the Fermi level accordingly. This change in Fermi level influences the optical property (refractive index, n) of graphene which undergoes a range of variations. Plots shown in Figs 3.20, 3.21, 3.22 and 3.23 show variation of complex dielectric constant ($\varepsilon_1 + j\varepsilon_2$), which is the square of refractive index, $\varepsilon_r = n^2$.

The chemical potential (μ) varies from 0 to 1 eV. Real part of dielectric constant, $\text{Re}(\varepsilon_1)$, reaches a peak at $\varepsilon(0.4 \text{ eV}) = 4.7592 + j4.4441$. Beyond 0.50, the $\text{Re}(\varepsilon_1)$ gate-dependent dielectric constant becomes negative, $\varepsilon(0.51 \text{ eV}) = -0.0839 + j0.5728$. This is

a transition point for transformation of graphene from dielectric to metallic. The attenuation of fundamental TM mode increases rapidly when μ is between 0.5 eV and 0.52 eV, showing the *enz* effect. Altogether, huge variations in waveguide parameters such as mode effective index (n_{eff}) and mode absorption (α in dB/ μm), can be observed from $\varepsilon(0.4 \text{ eV})$ to $\varepsilon(0.7 \text{ eV})$, which will be discussed in further sections. We interpolated 55 voltage levels from 0 to 1.0 eV for calculating the variations in complex dielectric constants $\varepsilon_1 + j\varepsilon_2$. The range of values we calculated using derived method are given in Appendix A.

Next we shall study the variations of $\varepsilon(\omega)$ with respect to change in graphene layer thickness (t_g).

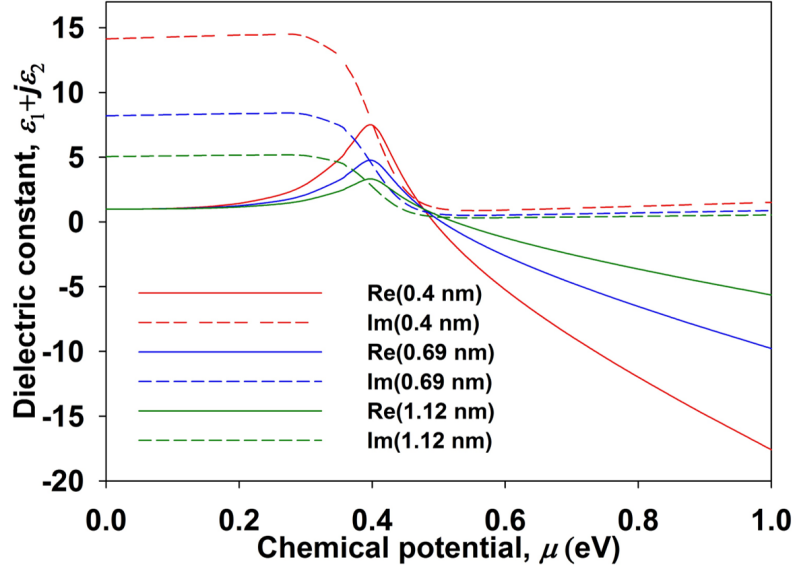


Figure 3.24: Complex dielectric constants deduced using Kubo formula for mono-, bi- and trilayer graphene of thickness (t_g) 0.4, 0.69 and 1.12 nm, respectively.

Equation (3.69) shows the dependence of $\varepsilon(\omega)$ on t_g . For the plot shown in Fig. 3.23, we used bilayer graphene of $t_g = 0.69 \text{ nm}$ to deduce the complex values for $\varepsilon(\omega)$. Figure 3.24 shows variations of complex $\varepsilon(\omega)$ for mono-, bi- and trilayers of graphene as a function of Fermi level. Graphene layer thickness (mono, bi and tri) values are taken from an experimental study [68]. Plots show similar trend with all three layers showing a peak at $\mu = 0.4 \text{ eV}$. As the layer thickness increases the amplitude of peaks for $\text{Re}(\varepsilon(\omega))$ decreases. Both real and imaginary parts of $\varepsilon(\omega)$ undergoes rapid change in the chemical potential window between 0.3 and 0.5 eV. In this region of change, the waveguide properties such as n_{eff} and α undergoes drastic changes which are discussed in detail in next section. These changes are very unique of graphene that form the basis for electro-optic modulation – ON/OFF condition.

3.5. Dielectric Constants

Both inter- and intraband transitions contribute to the trend of $\varepsilon(\omega)$. The sign of $\text{Re}(\varepsilon(\omega))$ beyond 0.4 eV changes due to intraband absorption. The interband transitions do not happen when $\mu > 0.4$ eV and intraband dominates beyond this Fermi level [28, 29]. Since the drop of $\text{Re}(\varepsilon(\omega))$ is drastic and due to *enz* effect, it is quite difficult to pinpoint the voltage level where graphene crosses the transition point (μ_t) to metallic. For instance, Ref. [29] has $\mu_t = 0.515$ eV with $\varepsilon(\omega) = -0.048 + j0.323$, whereas Ref. [6] has $\mu_t = 0.51$ eV with $\varepsilon(\omega) = -0.50 + j0.50$. Note the difference in $\text{Re}(\varepsilon(\omega))$ for both studies. Our calculations yield $\mu_t = 0.5070$ eV with $\varepsilon(\omega) = -0.0839 + j0.5728$.

Kwon [28] has discussed in his study the reason for these variances which arise due to the analytic expression used for conductivity (σ_g). In their study, $\mu_t = 0.513$ eV with $\varepsilon(\omega) = -0.202 + j1.32$ and has pointed out $\mu_t = 0.514$ eV with $\varepsilon(\omega) = -0.026 + j0.212$ in another study (see Ref. [22] in [28]). However, owing to the steep fall in $\text{Re}(\varepsilon(\omega))$ beyond $\mu = 0.4$ eV, these variations are not critical when considering the *enz* effect. Similarly, irrespective of layer thickness, the $\text{Im}(\varepsilon(\omega))$ shows a steady trend from 0 eV, starts decreasing beyond 0.36 eV, drops rapidly from 0.4 to 0.507 eV and steadies thereafter (see plot of $\text{Im}(\varepsilon_2)$ in Fig. 3.23).

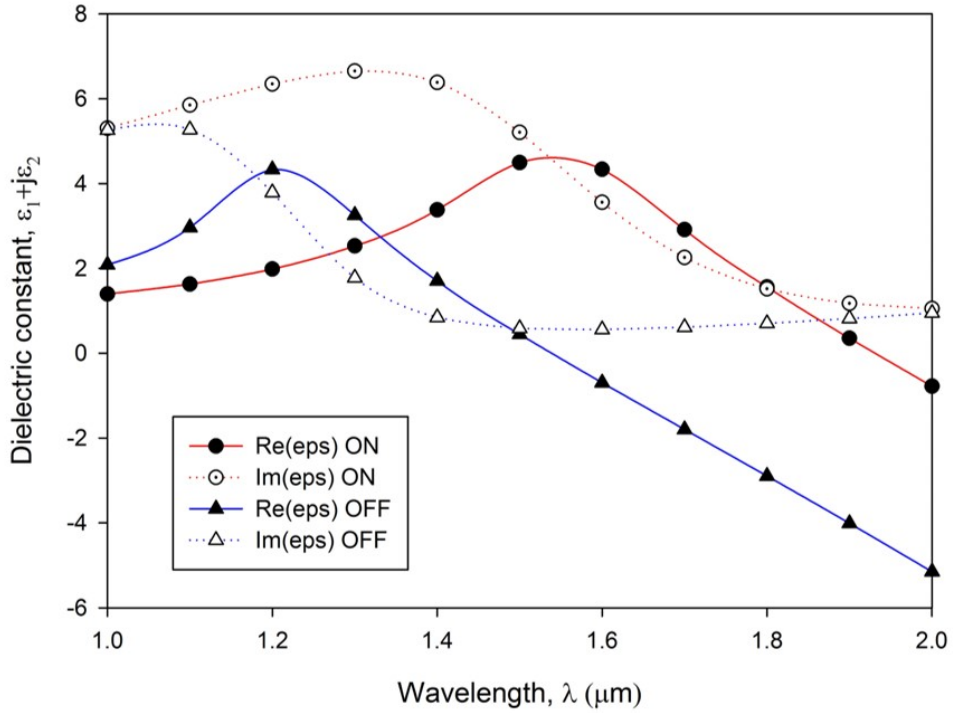


Figure 3.25: Complex dielectric constants of $\varepsilon(\omega)$ for two Fermi levels, $\mu = 0.4$ and $\mu = 0.509$ eV representing conditions ON and OFF, respectively; $t_g = 0.69$ nm.

Operation wavelength range is an important parameter in assessing performance of

a modulator. For use in optical data transmission systems, modulators are required to operate in one or more of the major telecom windows: $\sim 0.85, 1.3$ and $1.5 \mu\text{m}$ [10]. Graphene optical modulators have been found to accommodate extremely broad operation bandwidth covering from visible to microwave regions [20, 106]. Figure 3.25 shows the variations in $\varepsilon(\omega)$ as a function of wavelength (λ), calculated using equation (3.69).

Figure 3.25 is plotted over a wavelength range 1000–2000 nm for a bilayer graphene. This covers the typical fibre optic communication bandwidth, 1300–1600 nm. Both plots show similar trend but $\text{Re}(\varepsilon(\omega))$ has absorption peaks at different wavelengths:

$$\text{ON} : \mu = 0.4 \text{ eV}; \text{Re}(\varepsilon(\omega)) = 4.4944 \text{ at } \lambda = 1500 \text{ nm}$$

$$\text{OFF} : \mu = 0.509 \text{ eV}; \text{Re}(\varepsilon(\omega)) = 4.3328 \text{ at } \lambda = 1200 \text{ nm}$$

For a lower potential, $\mu = 0.4 \text{ eV}$, the peak in $\text{Re}(\varepsilon(\omega))$ moves towards longer wavelengths, $\lambda = 1500 \text{ nm}$ and vice versa for higher potential. Even though the $\varepsilon(\omega)$ varies for μ and λ , graphene layer has a constant absorption of $\pi\alpha = 2.293\%$ from visible to infrared wavelengths; $\alpha = e^2/\hbar c \approx 1/137$, c is the speed of light [87]. The fine structure constant, α , describes the coupling between light and relativistic electrons (π). Further we benchmarked our code with a study [6]. We chose their voltage levels, $\mu = 0.42, 0.46, 0.512, 0.54 \text{ eV}$ and obtained their plots. Then we used same voltages in our code and the plots yielded are shown in Fig. 3.26; inset shows theirs [6].

These chosen voltage levels lie between 0.4 and 0.6 eV, where the $\text{Re}(\varepsilon(\omega))$ drops rapidly and the attenuation of fundamental TM mode drastically increases (*enz* effect) leading to OFF condition. As seen from these results, when compared to the layer thickness (t_g), graphene do not show a strong dependence on wavelength. This finding will be discussed further with the results of waveguide performance parameters. This weak wavelength dependence enables graphene-based modulator for broadband operation that can process hundreds of channels from different systems in the same device [6].

To summarise, in this section, we have discussed in detail the method to obtain complex dielectric constants ($\varepsilon(\omega) = \varepsilon_1 + j\varepsilon_2$) of graphene and its dependence on thickness of graphene layer and wavelength of incident light. We studied the two important contributions, *viz.*, interband and intraband, that leads to complex conductivity ($\sigma(\omega) = \sigma_1 + j\sigma_2$) which in turn results in complex $\varepsilon(\omega)$. This property is unique in graphene which threw light on other quantum-mechanical effects such as generation of surface plasmons, which is broadly classified as *Plasmonics*. Before moving on to the next chapter where we begin

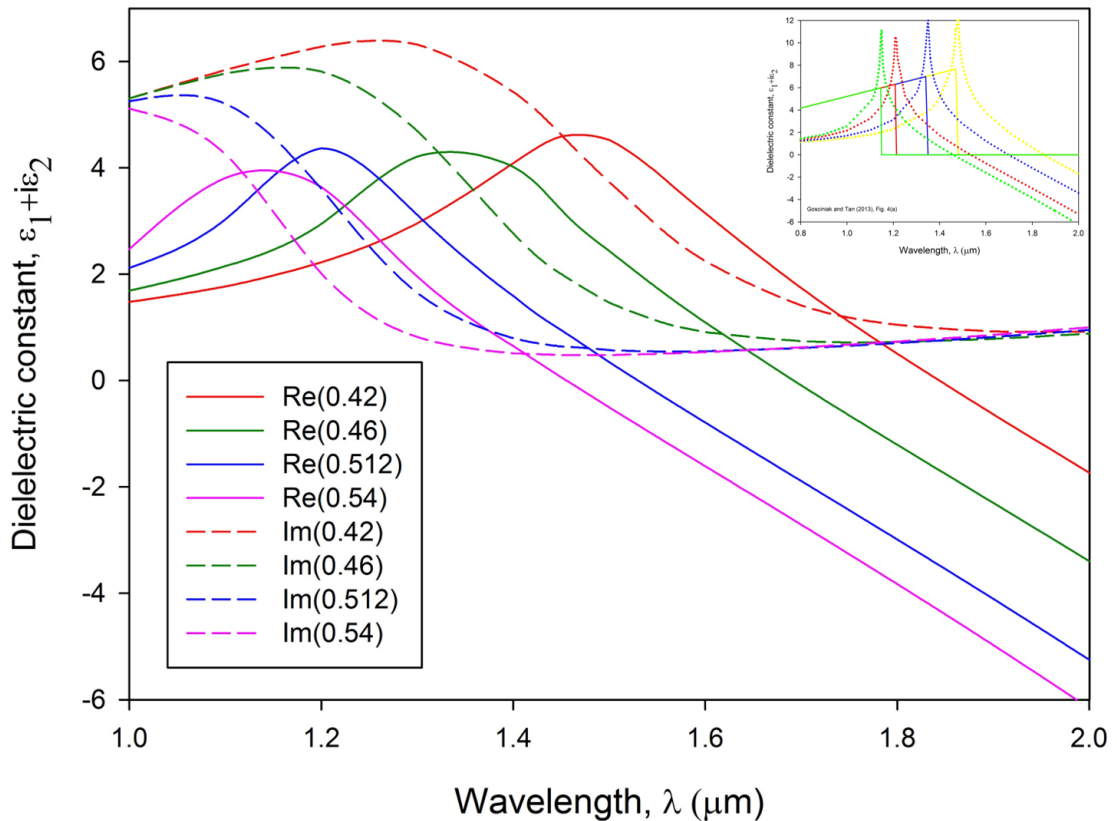


Figure 3.26: Complex $\varepsilon(\omega)$ as a function of λ , values derived using our code. Inset: Gosciniak and Tan [6] for comparison.

discussing our first part of results on the study of waveguide characteristics, we would like to present a brief note on plasmonics in the following section.

3.6 Plasmonics

The understanding of the optical response of graphene is very important for fabrication and device design for photonic and opto-electronic applications. Our study is based on characterization of electro-optic modulator wherein light-matter interaction is crucial. Electromagnetic field interacts with free electrons in metal and the study of such interactions is broadly classified as *Plasmonics*. As seen in previous section, the role of inter- and intraband absorptions plays a vital role in the effects that lead to modulation of electromagnetic wave transmitted through the thin layer of graphene, which has a sea of electrons and holes in the valence band (VB) and conduction band (CB), respectively. Electromagnetic wave composed of photons transfer its energy to electrons in CB, or holes in VB, raising those to a higher energy. Thus band transitions occur. The number of free conduction electrons and band transitions determine the optical response of metals. The

Drude model defines the optical response of the metals. A high frequency conductivity of monolayer graphene has a Drude form as follows:

$$\tilde{\sigma}(\omega) = \frac{iD}{\pi(\omega + i\Gamma)} \quad (3.71)$$

where ω is the frequency, Γ the scattering rate and D the Drude weight that has following value when neglecting electron–electron interactions,

$$D = \left(\frac{\nu_F e^2}{\hbar} \right) \sqrt{\pi |n|}$$

where ν_F is the Fermi velocity ($= 1.1 \times 10^6$ m/s) and $|n|$ the carrier density.

The electron is treated as a forced damped harmonic oscillator with angular frequency $\omega_0 = 0$ and the following equation provides solution to the motion of an electron with harmonic time-dependence for both \mathbf{E} and \mathbf{x} given by

$$\mathbf{E}(t) = \mathbf{E}_0 e^{-i\omega t} \quad x(t) = \mathbf{x}_0 e^{-i\omega t} \quad (3.72)$$

The polarisation (\mathbf{P}) caused due to the electron oscillation is given by $\mathbf{P} = -nex$, where n is the carrier concentration and e the charge of an electron. Using the relation $\mathbf{D} = \varepsilon\varepsilon_0\mathbf{E}$, the equations (3.72) are solved as follows:

$$\mathbf{D} = \varepsilon_0 \left(1 - \frac{\omega_p^2}{\omega^2 - i\gamma\omega} \right) \mathbf{E} \quad (3.73)$$

where \mathbf{D} is the electric displacement, \mathbf{E} the electric field, γ the damping constant and ω_p the plasma frequency. The dielectric function, $\varepsilon(\omega)$, of the free electron medium is given by

$$\varepsilon(\omega) = 1 - \frac{\omega_p^2}{\omega^2 - i\gamma\omega} \quad (3.74)$$

which is derived from the constitutive relations of Maxwell's equations; $\mathbf{D} = \varepsilon\varepsilon_0\mathbf{E}$.

Plasmons are quantized plasma oscillations of free electrons. This phenomena of electronic charge density oscillations occur in the bulk and at the surface of metals. When such occurring at a metal–dielectric interface are called surface plasmons. Precisely, a photon passing through a material medium couples strongly with the internal degrees of freedom inside the material and is termed as a *polariton*. In case of graphene, as plasmons are generated at the metal–dielectric interface, they are called surface-plasmon-polaritons (SPPs). The characteristic relationship between energy and plasma frequency is given by,

$$E_p = \hbar\omega_p = \hbar\sqrt{\frac{4\pi ne^2}{m_e}} \quad (3.75)$$

where n is the density of conduction electrons, e the charge of an electron, m_e the mass of an electron; ω_p is termed the plasma frequency [107]. Also, electronic oscillation is a simple harmonic function with plasma frequency,

$$\omega_p = \sqrt{\frac{ne^2}{m\varepsilon_0}} \quad (3.76)$$

Plasmon polaritons are collective excitations of photons and electrons that has the ability to confine energy of long wavelength radiation (e.g., $\lambda = 1550$ nm) at the sub-wavelength/nanoscale dimensions. For instance, in a typical waveguide with dielectric–metal–dielectric sandwich, the thickness of hBN (dielectric) and graphene are 10 and 0.7 nm, respectively. A surface plasmon polariton (SPP) is an EM wave that propagates along the surface showing a strong sub-wavelength energy confinement at metal–dielectric interface [108].

We will now move on to the next chapter discussing our results benchmarked with prominent studies. The calculated complex dielectric constants ($\varepsilon(\omega)$) from equations (3.68) and (3.69) were used to ascertain the waveguide characteristics such as mode effective index (n_{eff}) and absorption loss (α). The key figures of merit *viz.*, modulation depth or extinction ratio (ER), operation wavelength range and insertion loss (IL) are calculated.

Chapter 4

Benchmarking Graphene-based Optical Waveguides

4.1 Introduction

An electro-optic modulator is a device that allows to control the amount of light passing through the material, depending on an applied electric signal. Here, light acts as carrier of electric signal, which is coded with information, for instance ‘0s’ and ‘1s’. When a voltage is applied to a graphene–dielectric waveguide, charge carriers accumulate in the interface resulting in a chemical potential, which can be tuned with a gate voltage. Figure 4.1(a) shows a waveguide with two graphene layers separated by a dielectric material. When voltage is applied, positive and negative charges accumulate along the interfaces. This chemical potential can be tuned such that the incoming light across the material can be absorbed or allowed due to interband or intraband absorptions. When light passes through a material it perturbs the chemical potential leading to absorption, which is nothing but a quantum-mechanical effect. An artistic illustration of an EOM using light as carrier wave modulated by electrical signal is depicted in Fig. 4.1(b). Input light modulation by electrical signal carrying digital information is shown. Output is seen as light pulses i.e., 0s and 1s.

The 2D material (graphene in our study) performs the function as a self-amplitude modulator enabling ultrafast pulse generation [10]. A research group at the University of California, Berkeley, demonstrated that a waveguide could break the current speed limits in digital communications using graphene as top layer. The researchers placed graphene on top of a silicon waveguide and were able to achieve a modulation speed of 1 GHz. The speed of such modulator could theoretically reach as high as 500 GHz [20]. Many material

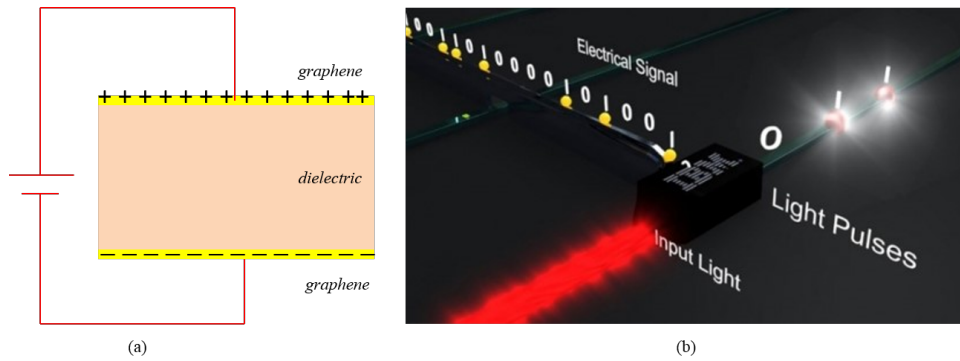


Figure 4.1: (a) Accumulation of charge carriers in graphene–dielectric interface upon applying a voltage. (b) Depiction of light modulation using electrical signal. Source: IBM T.J. Watson Research Center video.

combinations, such as cadmium sulfide (CdS), lithium niobate (LiNbO_3), ammonium dihydrogen phosphate (ADP), potassium dihydrogen phosphate (KDP), potassium titanyl phosphate (KTP), quartz (SiO_2), gallium arsenide (GaAs), indium phosphide (InP), barium titanate (BaTiO_3) and lithium tantalate (LiTaO_3), are available and can be chosen based on application. In this list, LiNbO_3 modulators possess many attractive features for modulation of visible and NIR light, making them the prime choice in many applications [109]. These modulators have several advantages over the other EOMs such as low drive power, high intrinsic modulation bandwidth and stable operation over a reasonable temperature range.

As discussed in previous chapters, the electronic band structure of graphene is responsible for the ultrafast modulation of incoming light. The interaction between charge carriers and ultrafast optical pulses produces a non-equilibrium charge carrier accumulation in VBs and CBs, which relaxes at an ultrafast timescale. This ensures wideband and ultrafast saturable absorption from Pauli blocking. Due to such

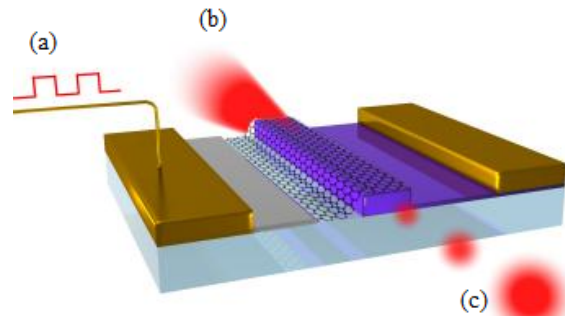


Figure 4.2: Schematic of graphene based waveguide: (a) electric signal, (b) incident light and (c) modulated light pulse. Source: [20].

nature in 2D materials, combinations of different 2D heterostructures, such as graphene–hexagonal boron nitride ($h\text{BN}$), graphene–black phosphorus, TMD– $h\text{BN}$, TMD–graphene and TMD–TMD combinations are currently explored. Of all graphene–dielectric combi-

nations, the *hBN*–graphene–*hBN* stack outperforms other 2D material combinations with its remarkable carrier transport properties [110].

In Chapter , we have discussed about photonic materials and experimental methods for exfoliating graphene layers and Chapter 2 explained the numerical method adopted to characterize the waveguide under study. Chapter 3 was devoted to discussion of graphene and its unique properties. In this chapter, we discuss the ways we adopted for studying graphene–silicon hybrid waveguides. We used two in-house solvers viz., perturbation and complex, which were written using FORTRAN codes, and were already in use for obtaining modal solutions. Firstly, we used these codes to benchmark with chosen published studies. After validation of results, we studied modal solutions of a silicon nanowire (1D and 2D) and then moved on to graphene-based waveguides in Chapter 5. In this chapter, we present the results of benchmarking and analyse the plots obtained for optimizing waveguide parameters such as effective index and absorption.

The vector \mathbf{H} -field formulation is one of the most accurate and versatile methods for studying optical waveguide problems [47]. The formulation is written as follows [45]:

$$\omega^2 = \frac{\iint (\nabla \times H)^* \cdot \hat{\varepsilon}^{-1} \cdot (\nabla \times H) d\Omega + \left(\frac{\alpha}{\varepsilon}\right) \int (\nabla \times H)^* (\nabla \cdot H) d\Omega}{\iint H^* \cdot \mu^{-1} \cdot H d\Omega} \quad (4.1)$$

where $\hat{\varepsilon}$ and $\hat{\mu}$ are the general anisotropic permittivity and permeability of the loss-free medium, respectively, α the dimensionless penalty coefficient and Ω the cross-section of the waveguide. Equation 4.1 has electric wall as natural boundary condition, expressed as $n \cdot \mathbf{H} = 0$.

Waveguides are the most basic components of an optoelectronic system. They form the building blocks of such systems. A suitable combination of active (Si, graphene) and passive materials (*hBN*, SiC, SiON) can make an efficient waveguide. For effective propagation in a waveguide, refractive index (n) of core material should be higher than other layers, such that $n_1, n_2 < n_3$ and $n_3 > n_4$. Materials are chosen based on their optoelectronic properties, response to electrical and optical signals. An electro-optic modulator requires a nonlinear material that could modulate optical signal with electrical input at ultrafast rate.

Reflecting, propagating and confining light waves within a specified volume are the fundamental characteristics of a waveguide. Materials with excellent optical and electrical

properties are of particular interest for designing waveguides. A multilayer rib waveguide is shown in Fig. 4.3. Layers with differing refractive indices reduce leaky modes. EM wave traversing through such a polarizable medium is modified by the polarization it induces and couples to it of which the coupled mode of excitation is termed a polariton. As shown in Fig. 4.3(b), optical absorption in graphene can be controlled by means of shifting its Fermi energy level through electrical gating, V_g [111, 112].

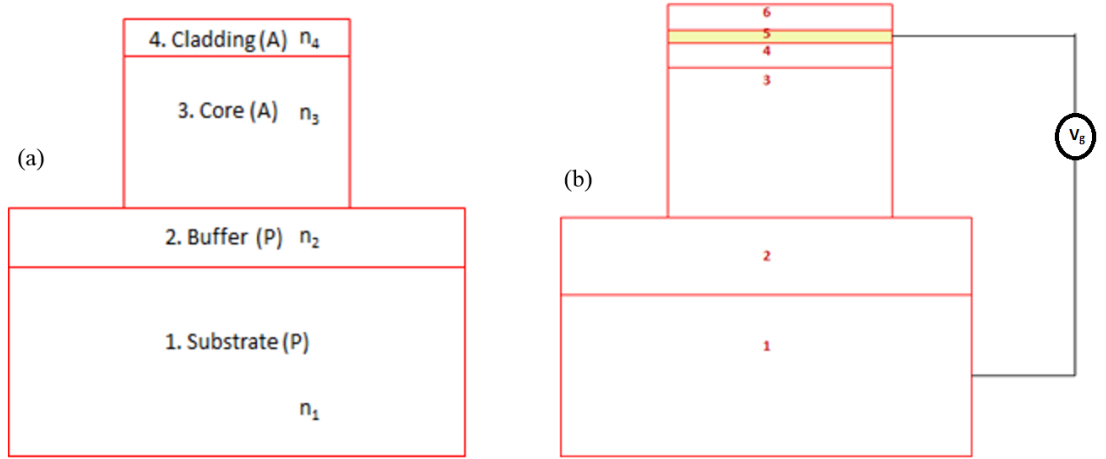


Figure 4.3: (a) Waveguide with active (A) and passive (P) materials. (b) A rib waveguide with graphene in layer 5. Layer 3 forms the core (Si), layers 1 and 2 are dielectric materials (e.g., SiO_2) and layers 4 and 6 are termed buffer materials such as hBN, Si_3N_4 or Al_2O_3 that encapsulate graphene; V_g denotes applied gate voltage.

4.2 Benchmarking

The objective of this stage is to benchmark our results (ε , n_{eff} , α) with published studies as well as choosing the suitable solver, either perturbation or complex, for further study. For this we need to simulate the chosen waveguide using both the solvers and benchmark them with published results. This stage is carried out in steps as given below:

- understanding the theory of calculating conductivity (σ) and permittivity (ε) from Kubo formula
- writing an analytical method to calculate σ and ε based on equations
- writing a MATLAB program for the analytical method
- benchmark MATLAB permittivity values obtained

- e) simulating waveguide design, using both complex and perturbation codes, as given in chosen studies from literature
- f) plot all results ($\varepsilon(\omega)$, n_{eff} , α) for chosen waveguides
- g) benchmark results with chosen studies

For benchmarking dielectric constants, the studies of Gosciniak and Tan [6], Kwon [28] and Lu and Zhao [29] are chosen. These plots are discussed in detail further. For benchmarking the solvers, studies [6], [29] and Liu *et al.* [20] are taken. Results on calculating and benchmarking effective indices and propagation loss values are presented. Studies [6] and [29] were benchmarked using in-house solvers as well as commercial package, COMSOL.

4.2.1 Study 1: Graphene-based Rib Waveguide

Initially, both solvers were subjected to analysis of a bulk waveguide, taken from Gosciniak and Tan [6], as shown in Fig. 4.4. We have adapted our solvers to represent the test structure effectively and dimensions are given in the figure. This is to analyse which solver would be accurate for studying graphene-based waveguides as graphene possesses a wide range of complex dielectric constants, $\varepsilon(\omega)$.

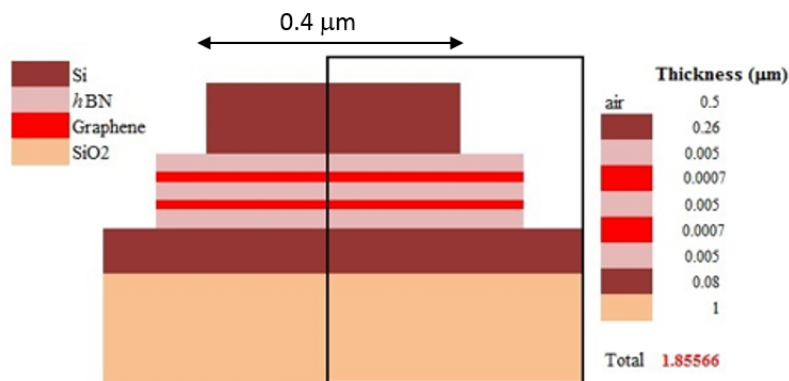


Figure 4.4: Waveguide redrawn from Ref. [6] for validating complex and perturbation solvers. Since the waveguide is symmetric, half-structure was chosen as marked.

In their study, thickness of graphene layer was taken as 0.7 nm, denoting bilayer graphene. Each graphene layer is sandwiched between dielectric materials so as to enhance dielectric optical confinement. We have discussed in previous chapters that dielectric constant of graphene, $\varepsilon(\omega)$, is complex with real and imaginary parts, $\varepsilon_1 + j\varepsilon_2$.

4.2. Benchmarking

Using perturbation and complex solvers, modal effective index (n_{eff}) and absorption (α) are obtained.

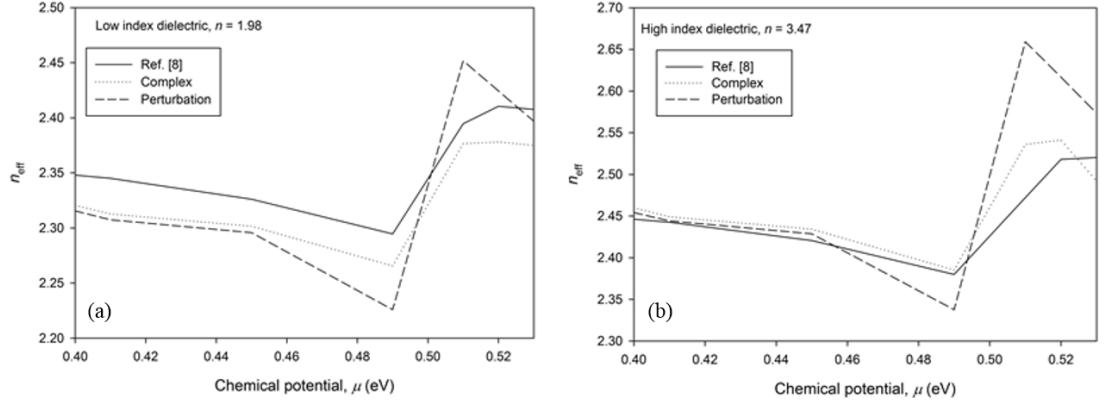


Figure 4.5: Mode effective index (n_{eff}) for validating perturbation and complex solvers.

Figures 4.5(a) and (b) show n_{eff} calculated using complex and perturbation solvers and validation against chosen points from Gosciniak and Tan [6]. Plots from both solvers show similar trend and beyond 0.45 eV, results from perturbation starts deviating from other two beyond 0.49 eV. For high-index dielectric, this deviation is prominent as shown in Fig. 4.5(b).

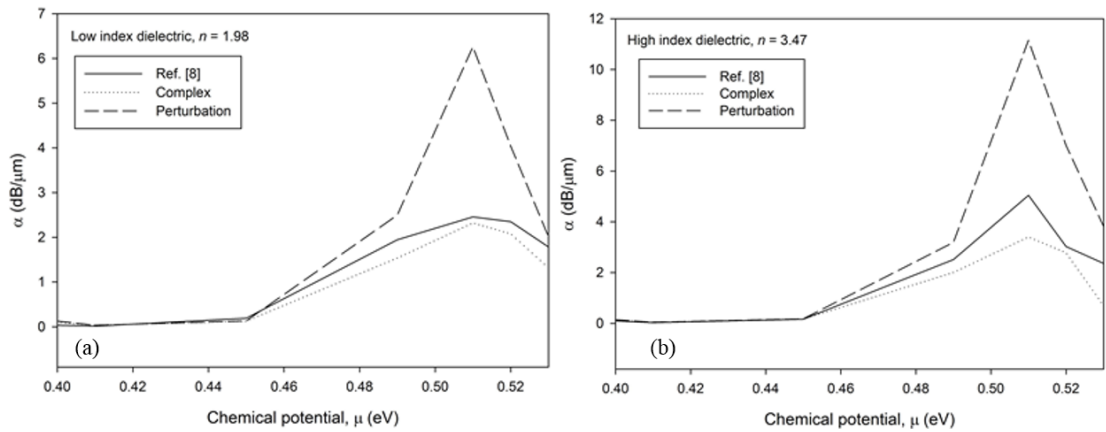


Figure 4.6: Mode absorption (α) for validating perturbation and complex solvers.

Figures 4.6(a) and (b) show mode absorption (α) calculated using both the solvers. In both high- and low-index dielectric, results from complex solver is close to that of the chosen study [6]. Results from perturbation solver varies drastically beyond 0.49 eV similar to the trend observed with n_{eff} plot in previous figure. The underlying reason is that when $\text{Re}(\varepsilon(\omega))$ becomes lesser in magnitude than $\text{Im}(\varepsilon(\omega))$, the results from perturbation solver starts deviating from the actual. Whereas, the complex solver follows the trend of reported results [6] since it remains unaffected due to the variations in real and imaginary parts of

4.2. Benchmarking

$\varepsilon(\omega)$. On the other hand, perturbation solver could accommodate a 500×500 mesh but complex solver could only reach up to 100×100 for a 2D waveguide for a given computer resources. Even though the complex solver could consider only smaller mesh divisions when compared to the perturbation code, it was taken for further benchmarking as it yields accurate results.

Figure 4.7 shows the electric field plots of quasi-TM mode. The dielectric constants chosen are as follows: ε_{low} , $\varepsilon_{\text{high}}$, ε_{enz} and $\varepsilon_{\text{metallic}}$, referring to the voltages 0, 0.4, 0.51 and 0.7 eV, respectively.

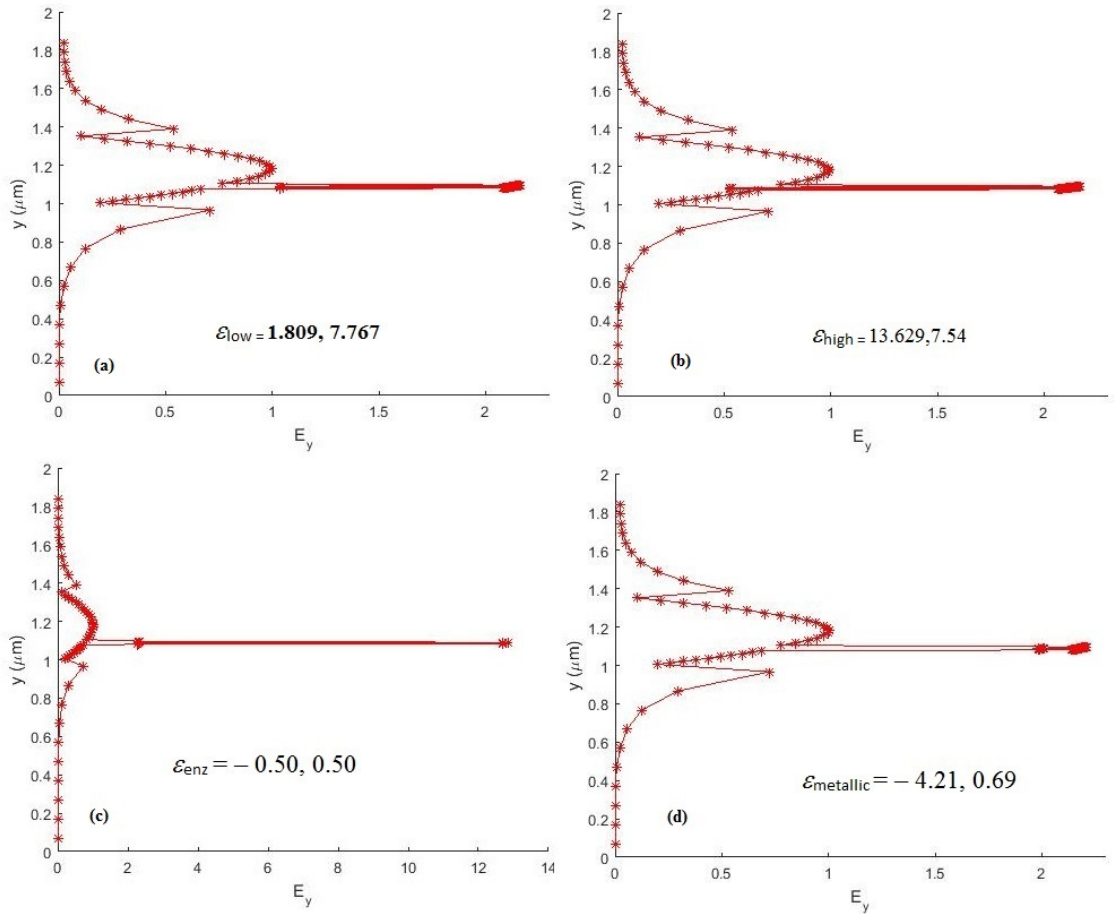


Figure 4.7: Electric field of quasi-TM E_y mode for chosen dielectric constants of graphene from Ref. [6], simulated by using the complex solver.

In above plots, the electric field in graphene layer undergoes drastic changes within the voltage range, 0–1 eV. A sharp peak is observed in all plots which represents the graphene–dielectric interface. A high degree of dielectric confinement enables good light–matter interaction. A sharp peak at ε_{enz} denotes the epsilon-near-zero (*enz*) effect, plot (c), where the absorption reaches the maximum and the real part of $\varepsilon(\omega)$ turns negative.

After 0.6 eV, graphene becomes metallic as shown in plot (d). These electric field plots are obtained using complex mode solver. A major drawback was noticed at this stage. As we have chosen a bulk waveguide (8 layers), the computation time for complex solver took to almost 40–50 minutes when the mesh size was set to 100×100 . For each step, it become time consuming to use complex solver. Therefore, COMSOL was used to obtain the modal solutions, since it is also based on FEM.

First, a template for 2D waveguide was created using COMSOL. Next, four plots from Gosciniak and Tan [6] were chosen for benchmarking the template. The flexibility in COMSOL is that once a template is built and a structure is benchmarked, the template can be reused for studying various structures. Also the computation time is only few minutes even for an “extremely fine” mesh which is a major advantage. The bulk waveguide from the chosen study was then built in COMSOL. Figures 3(a and b) and 4(c and d) were chosen from Ref. [6]. Each of these figures shows the results of both n_{eff} and α for TE and TM modes.

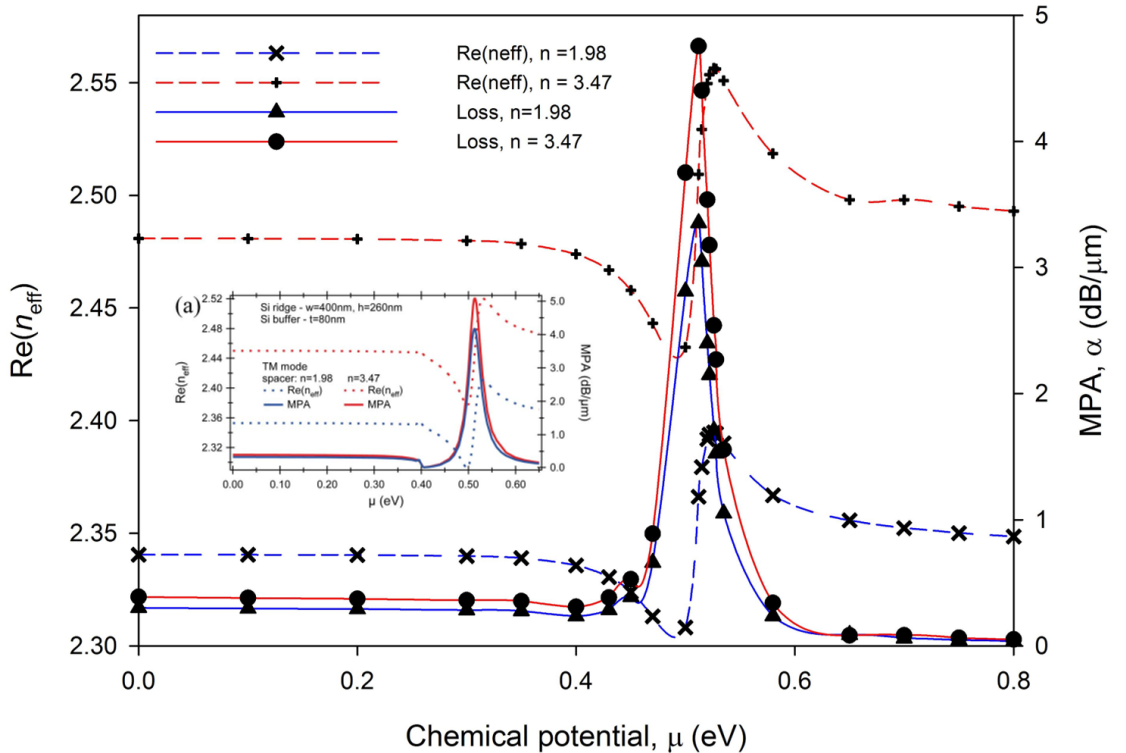


Figure 4.8: TM mode: $\text{Re}(n_{\text{eff}})$ and α for high- and low-index spacers between Si slab and Si ridge ($\lambda = 1550$ nm). Inset shows Fig. 3(a) in Ref. [6].

Figure 4.8 shows mode effective index and absorption of TM mode for the bulk waveguide having bilayer (0.7 nm) graphene as slot layers separated by *h*BN. We benchmarked

our results with that of Gosciniak and Tan [6]. Our results agreed with theirs, thus validating our template and understanding of bulk waveguides using graphene as slot layers. Core silicon in the waveguide has a width of 400 nm and height 260 nm. Low-index ($n = 1.98$) and high-index ($n = 3.47$) are taken. The latter outperforms in both n_{eff} and α as obviously a higher index will result in higher absorption.

Figure 4.9 shows plots for n_{eff} and α of TE and TM modes. This plot differs from the previous with width and height of silicon core taken as 400 and 200 nm, respectively. Note that the height of the core has been reduced by 60 nm from the previous and the dielectric with high-index, $n = 3.47$.

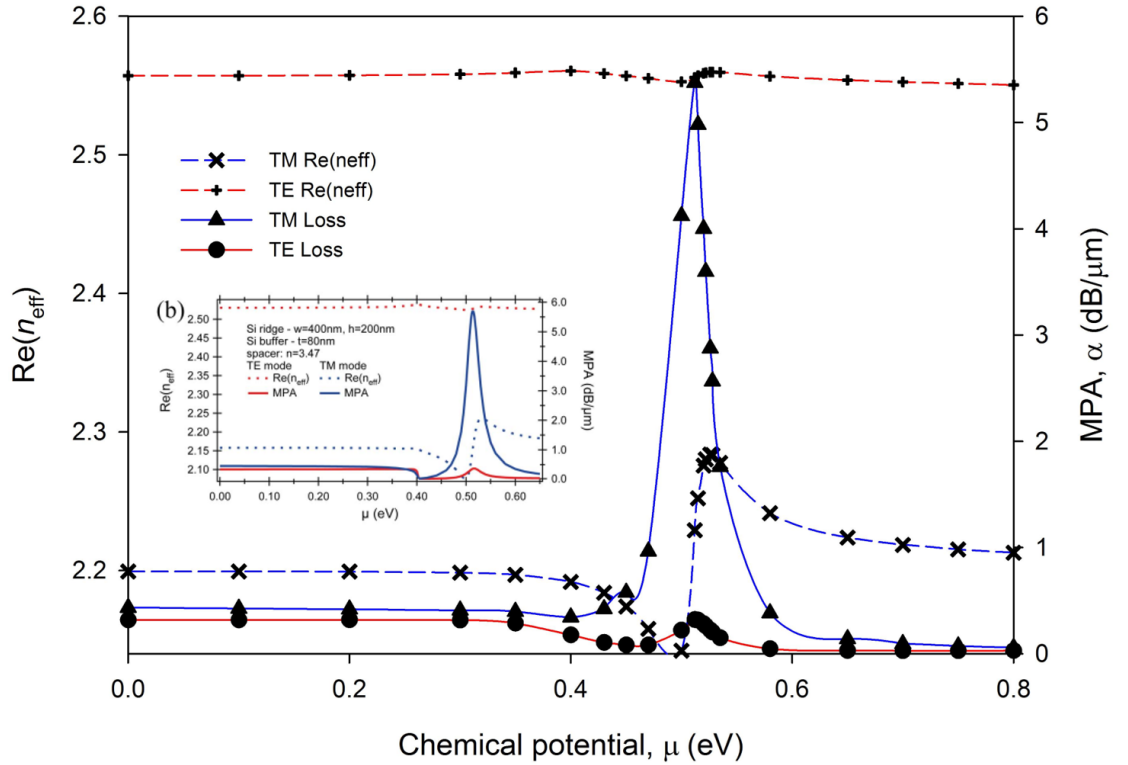


Figure 4.9: $\text{Re}(n_{\text{eff}})$ and α for two supported modes, TM and TE, for high-dielectric spacer. Inset shows Fig. 3(b) in Ref. [6].

Gosciniak and Tan [6] has stated that a 60 nm decrease in height of core results in significantly larger absorption for TM mode than that of the TE mode. All plots in both the figures denote a step fall after $\mu = 0.51\text{ eV}$, where the “dielectric” to “metallic” transition of graphene occurs. This dip in absorption is attributed to the *enz* effect.

Figure 4.10 shows the wavelength dependence of n_{eff} and α of TE mode for the bulk waveguide with high- and low-index dielectric. Waveguide dimensions are the same as those mentioned for the plots in Fig. 4.8. The chemical potential is set as $\mu = 0.512\text{ eV}$,

which refers to the OFF voltage, resulting in maximum absorption for both TE and TM modes.

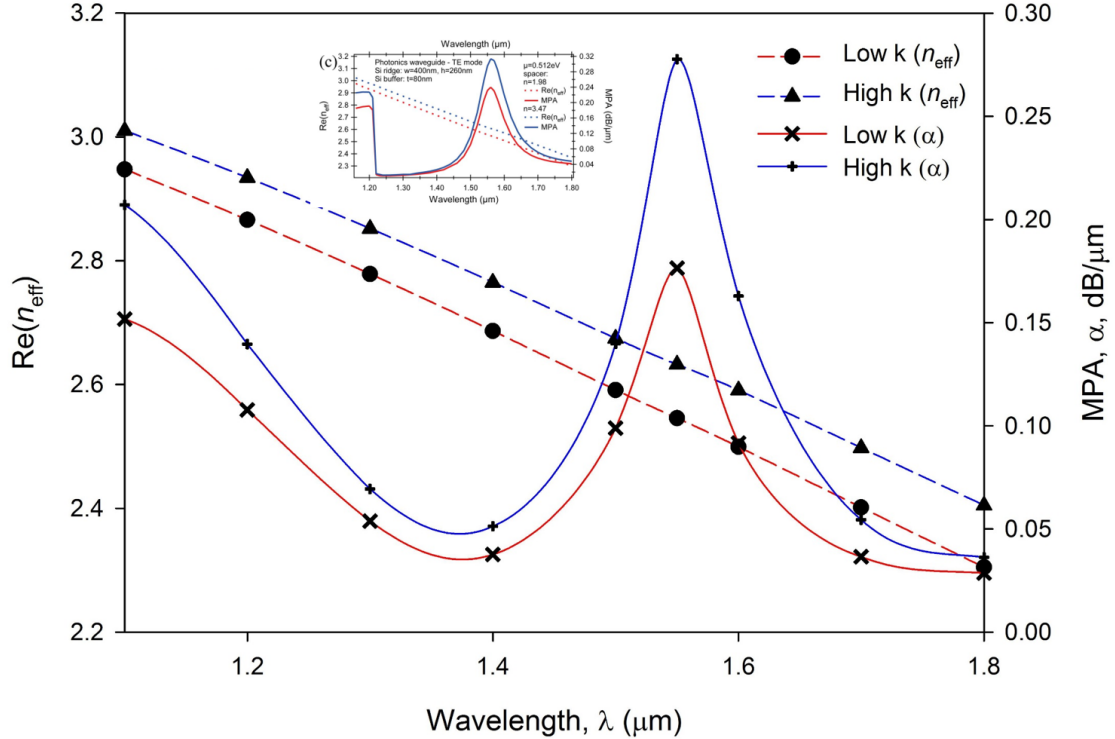


Figure 4.10: $\text{Re}(n_{\text{eff}})$ and α for high- and low-index spacers between Si slab and Si ridge for TE mode; $\mu = 0.512 \text{ eV}$. Inset shows Fig. 4(c) in Ref. [6].

Figure 4.11 shows the waveguide characteristics of TM mode for waveguide with dimensions as mentioned above. Comparing both TE and TM plots, the latter has shown a significant higher absorption reaching close to $5 \text{ dB}/\mu\text{m}$. Gosciniak and Tan [6] have calculated the $f_{3\text{dB}}$ bandwidth to be 16.5 THz for both high- and low-index dielectric spacers. This shows the strength of broadband operation of the modulator to accommodate hundreds of channels due to weak wavelength dependence.

All four plots benchmarked with Ref. [6] have shown a very good agreement with our results thus validating our understanding of a bulk waveguide with graphene as a slot layer. Graphene layer possesses high carrier mobility and high saturation velocity and therefore, the operating bandwidth is likely to be limited by the transit time of carriers. On this regard, the relaxation time (τ) is inversely proportional to the degree of crystalline disorder in graphene. Ideally, a high quality graphene layer can operate with a modulation speed in picoseconds timescale at 500 GHz [113]. Next, we consider another benchmarking study which we have considered for the understanding of graphene-based optical modulators.

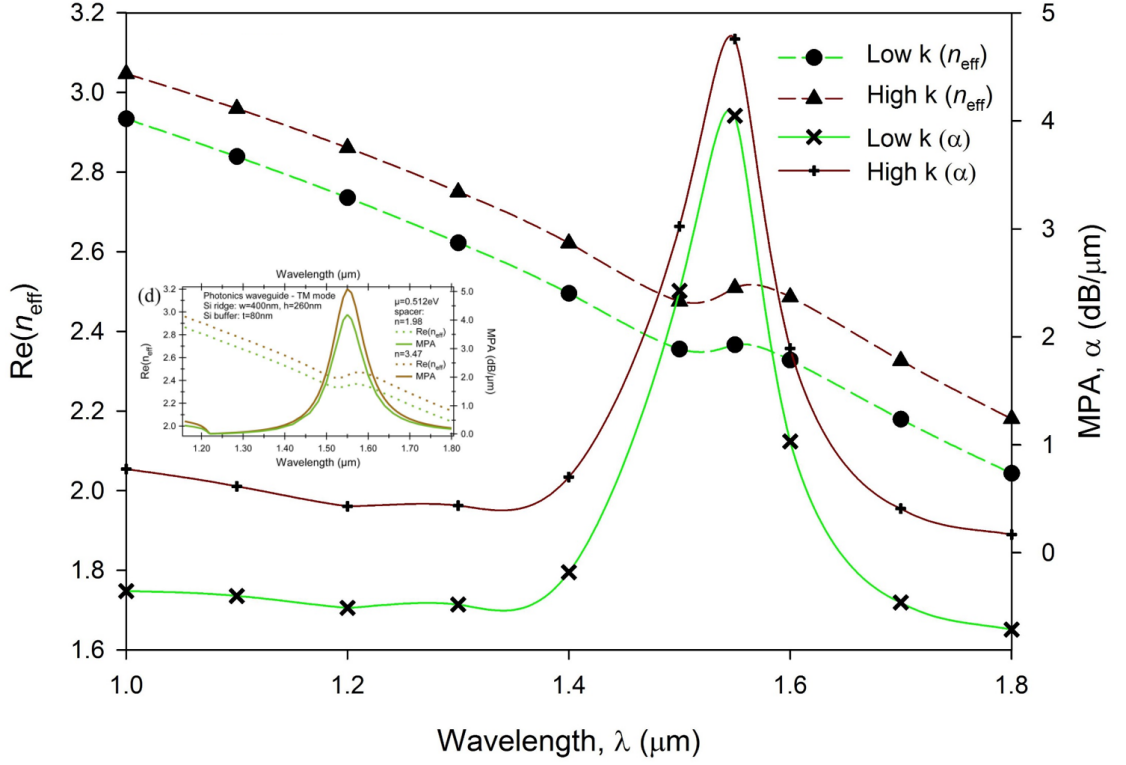


Figure 4.11: $\text{Re}(n_{\text{eff}})$ and α for high- and low-index spacers between Si slab and Si ridge for TM mode; $\mu = 0.512$ eV. Inset shows Fig. 4(d) in Ref. [6].

4.2.2 Study 2: Graphene-based Slot Waveguides

This study explores the electro-optic properties of slot waveguide in which graphene layer is sandwiched between silicon nitride (Si_3N_4) as buffer layers (Fig. 4.12). Here the thickness of buffer layers (10 nm) remained same whereas the thickness of Si layer was varied in each structure.

Lu and Zhao [29] used different structures for simulations with a 3D FDTD code. Each waveguide comprises graphene sandwiched between dielectric layers and core as Si. Thickness of graphene layer was taken as 0.7 nm. Two dielectric constants of graphene are chosen as follows: $\epsilon(0 \text{ eV}) = 0.985 + j8.077$; $\epsilon(0.515 \text{ eV}) = -0.048 + j0.323$, denoting ϵ_{enz} , representing ON and OFF voltages, respectively. Dielectric constants of rest of the materials are as follows: $\epsilon(\text{Si}) = 12.0409$; $\epsilon(\text{Si}_3\text{N}_4) = 3.9204$; $\epsilon(\text{SiO}_2) = 2.0736$; $\epsilon(\text{Cu}) = -67.86 + j10.01$. Dimensions of the waveguide (Fig. 4.13) are taken as given in Fig. 2 from Ref. [29].

First, we used our complex solver to study each of these waveguides and obtained electric field plots for the waveguides chosen. As shown earlier, the complex solver has the ability to provide accurate results even with high variations in the real and imaginary

4.2. Benchmarking

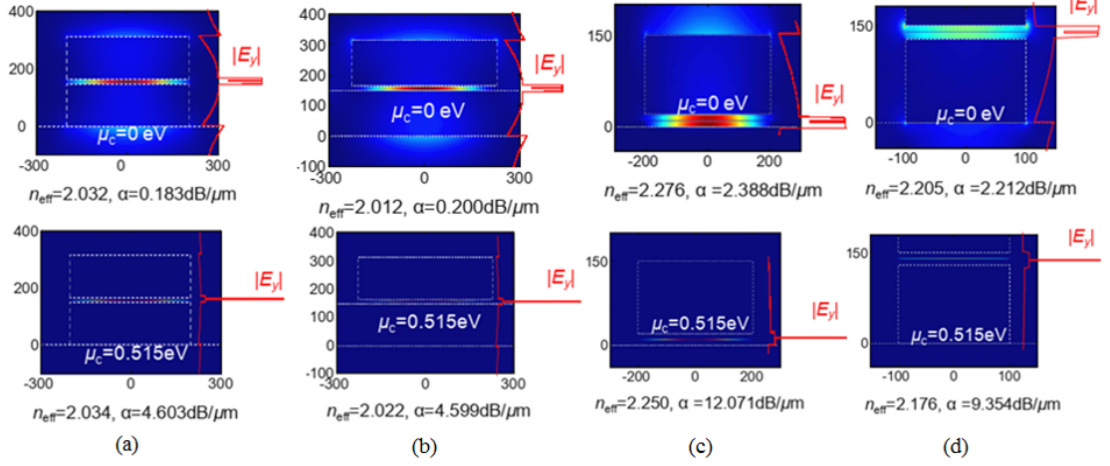


Figure 4.12: Waveguides (a), (b), (c) and (d) represents figures chosen from Fig. 2a, 2b, 2e and 2f, respectively, from Ref. [29] for benchmarking task.

parts of dielectric constant which was found lacking with perturbation solver. So we used only complex solver to obtain further results. The electric field plots of TM E_y mode are obtained for four structures (waveguides a, b, c and d shown in Fig. 4.13) with two dielectric constant values at $\mu = 0$ and $\mu = 0.515$ eV are chosen.

Figure 4.14 shows a drastic change in the electric field plots between ON and OFF states. An absorption of $\alpha = 0.183$ dB/ μm is obtained for low-loss state and in the high-absorption state, $\alpha = 4.603$ dB/ μm . Figure 4.15 shows the case of an asymmetric slot waveguide, which shows only a slight change in performance. This proves that high absorption can be achieved if graphene is encapsulated with a buffer material ($h\text{BN}$, Si_3N_4).

Figures 4.16 and 4.17 show plots obtained for waveguides with Cu as bottom layer and cladding, respectively. Here, the dielectric constant of Cu is taken as $-67.86 + j10.01$. Cu is a CMOS compatible metal and is used in all plasmonic modulators. In all these studied waveguides, the thickness of buffer layer (Si_3N_4) is fixed at 10 nm; and $\lambda = 1550$ nm.

Table 4.1 displays the mode effective index and absorption values for all waveguides benchmarked with Ref. [29]. Our results agree very closely with waveguides (a) and (b) but shows similar trend with waveguides (c) and (d). The reason is attributed to the presence of very high dielectric constant of Cu in the latter two waveguides and also the mesh limitation imposed in this solver (110×110). Complex solver needs to be tweaked for handling high complex dielectric constants and high mesh (500×500 and 1000×1000).

We further benchmarked two more plots from Lu and Zhao, using COMSOL. Waveguide (a) in Fig. 2 of Ref. [29] is chosen for benchmarking. Obtained mode profile and

4.2. Benchmarking

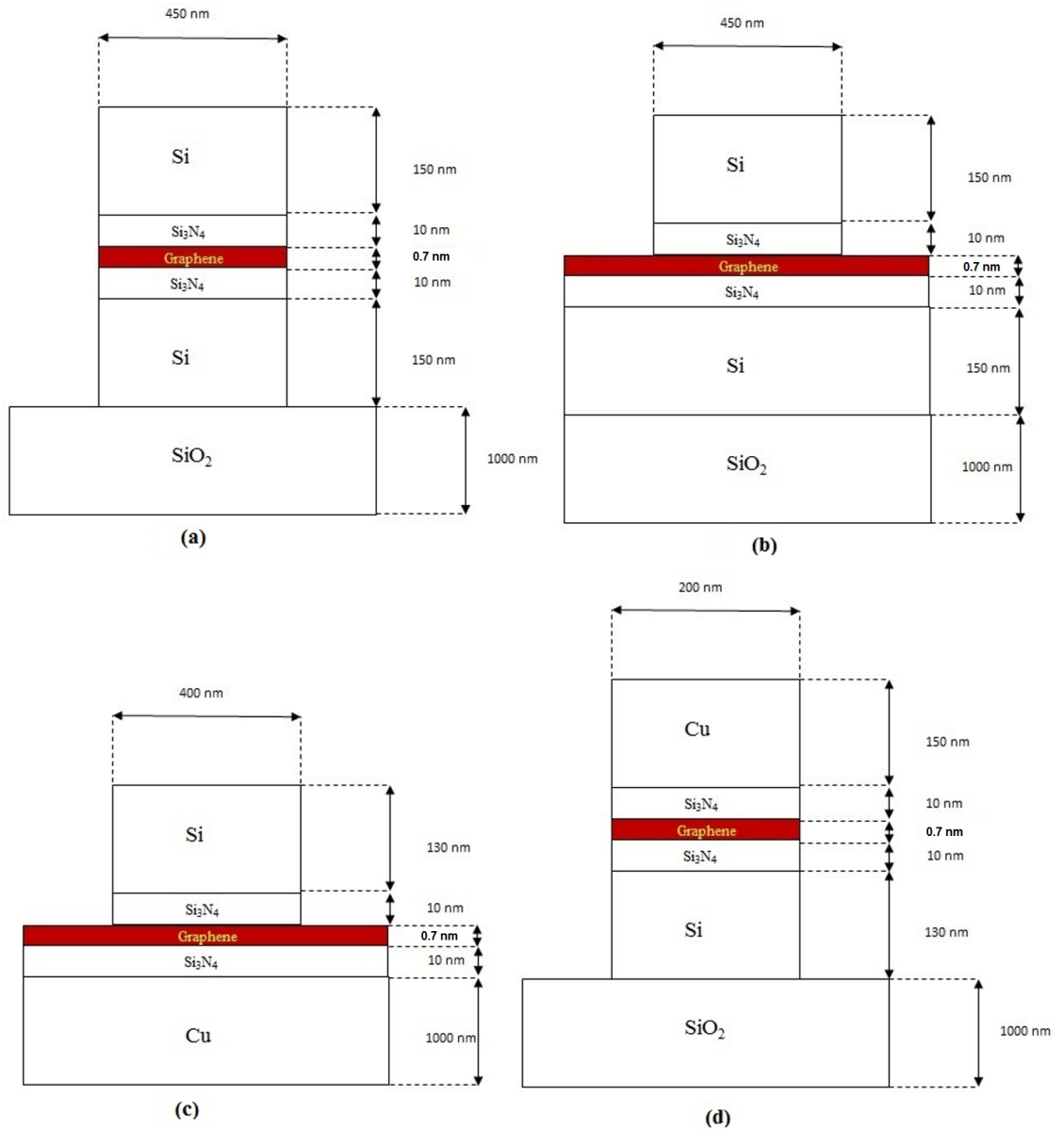


Figure 4.13: Waveguides redrawn from Fig. 2 of Ref. [29] for benchmarking using our complex code.

electric field of TM mode are shown in Fig. 4.18. These results validated our understanding and methods we followed for the analysis of graphene-based hybrid waveguides. The electric field plots for ON and OFF voltages are shown in Fig. 4.18(a) and (b), respectively.

Next, we benchmarked another waveguide of Fig. 2(b) in Ref. [29], which is shown in Fig. 4.19. The electric field plots for ON and OFF voltages are shown in Fig. 4.19(a) and (b), respectively. Tables in both Figs 4.18 and 4.19 show the values obtained for n_{eff} and α . The values show a very close agreement between theirs and ours.

On comparing the two waveguides, one having graphene layer in the slot of the core and the other with graphene layer in the slab, there is only a slight shift observed in their

4.2. Benchmarking

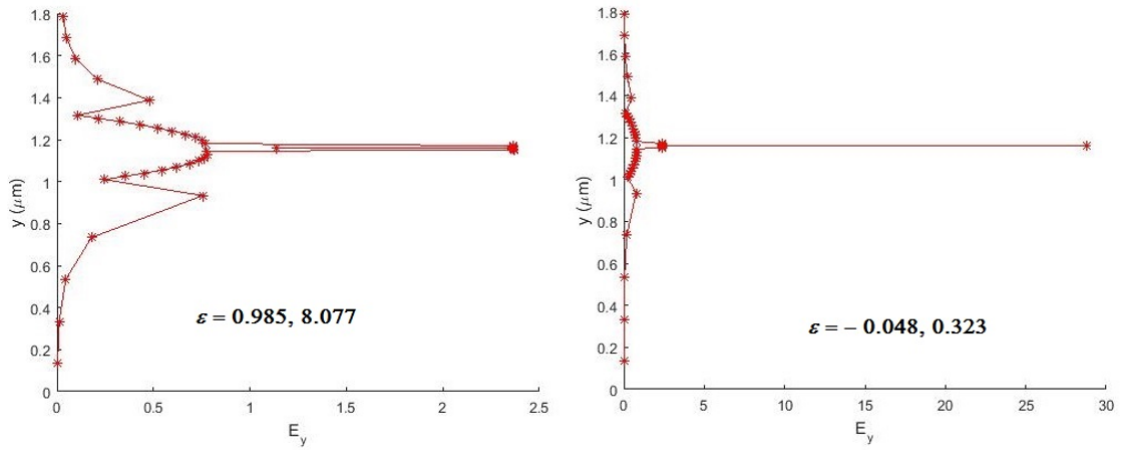


Figure 4.14: Electric field plots of TM E_y mode for waveguide (a) shown in Fig. 2(a) of Ref. [29]; Si-(graphene/dielectric)-Si.

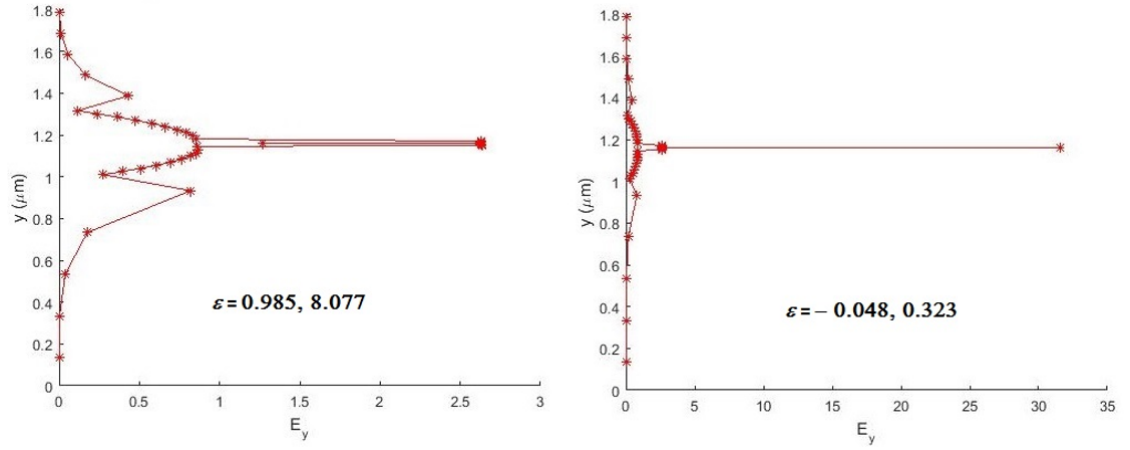


Figure 4.15: Electric field plots of TM E_y mode for waveguide (b) shown in Fig. 2(b) of Ref. [29]; Si-(graphene/dielectric)-Si, dielectric strip waveguide.

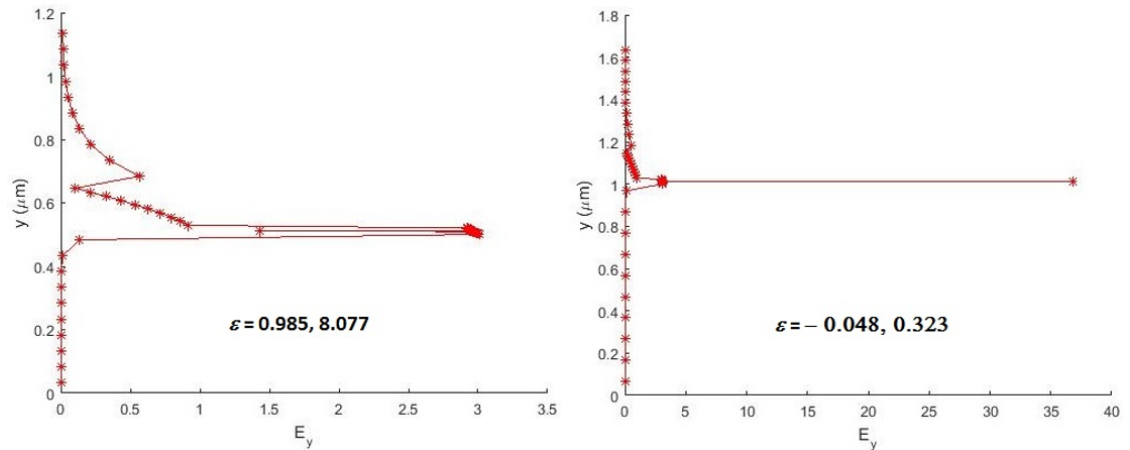


Figure 4.16: Electric field plots of TM E_y mode for waveguide (c) shown in Fig. 2(e) of Ref. [29]; Si-(graphene/dielectric)-Cu, width = 400 nm.

effective indices, for instance, 2.075 and 2.079 of ON and OFF levels, respectively. On the other hand, absorption values for these two levels are 0.166 and 4.184 dB/ μm , respectively.

4.2. Benchmarking

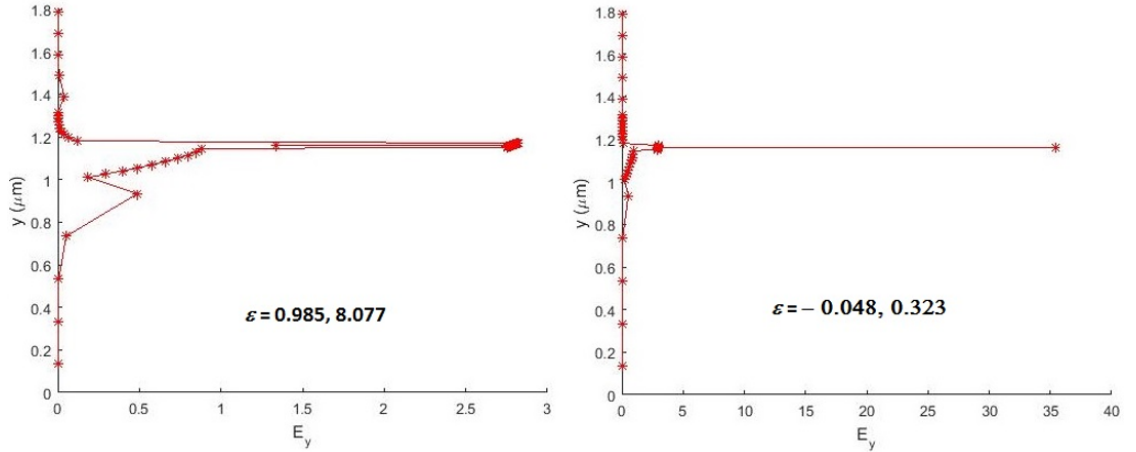


Figure 4.17: Electric field plots of TM E_y mode for waveguide (d) shown in Fig. 2(f) of Ref. [29]; Cu-(graphene/dielectric)-Si, width = 200 nm.

Table 4.1: Benchmarking of results with Lu and Zhao [29], obtained by using our complex code

$\varepsilon(\omega)$	Waveguide	Effective index, n_{eff}		Absorption, α (dB/ μm)	
		Ours	Theirs	Ours	Theirs
$0.985+j8.077$	(a)	2.01695	2.03200	0.15873	0.18300
	(b)	2.08159	2.03200	0.15873	0.18300
	(c)	2.35352	2.27600	2.28571	2.38800
	(d)	2.59330	2.20500	2.31846	2.21200
$-0.048+j0.323$	(a)	2.01913	2.03400	4.01960	4.60300
	(b)	2.08509	2.02200	4.12432	4.59900
	(c)	2.44142	2.25000	14.63280	12.07100
	(d)	2.56851	2.17600	11.39110	9.35400

Similar trend is observed in the other waveguide shown in Fig. 4.19. Absorption values for both levels are 0.176 and 4.176 dB/ μm , respectively, whereas the n_{eff} values are 2.129 and 2.132, respectively. Our results from these simulations have shown very good agreement with those of Lu and Zhao [29].

Finally, we concluded benchmarking of study 2 with plotting of absorption values as a function of wavelength and chemical potential for waveguide as shown in Fig. 4.20 and 4.21, respectively. Inset in both figures shows the plots taken from Lu and Zhao [29]. Our plots follow similar trend with theirs but shows a significant difference in absorption peak. This reason is attributed to the chosen dielectric constants at $\mu = 0.515$ eV with $\lambda = 1550$ nm. Our plot has absorption peak at $\mu = 0.515$ eV with $\lambda = 1530$ nm. Due to the difference in the analytical method followed for calculating the dielectric constants of graphene, such variations are observed in both plots. For instance, from their method,

4.2. Benchmarking

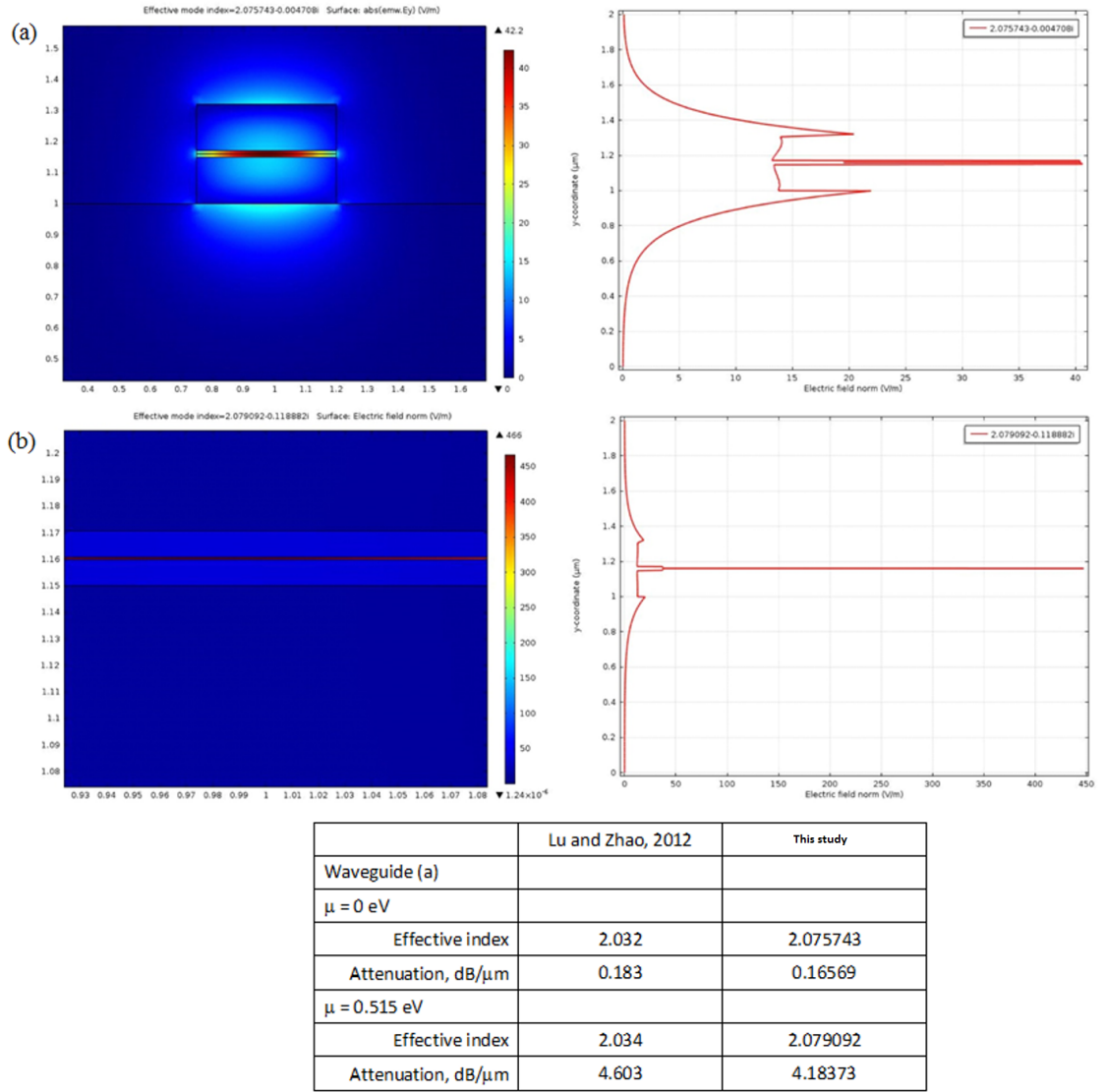


Figure 4.18: Mode profile and electric field of TM mode for waveguide in Fig. 2(a) of Lu and Zhao [29]. Table shows the comparison of n_{eff} and α values of theirs and ours.

at $\mu = 0.515$ eV, the $enz \varepsilon(\omega) = -0.048 + j0.323$; in our method, at $\mu = 0.515$ eV, the $enz \varepsilon(\omega) = -0.0967 + j0.5405$. In Table 4.1, we used their dielectric constants for $\mu = 0$ and $\mu = 0.515$ eV. The effect of these variations have already been discussed in previous chapter.

To summarise, in this section, we explained our results obtained for benchmarking the waveguide taken from literature. The results and plots of ours have shown a very good agreement with that of theirs. With this understanding, we will now move on to the third study we took for benchmarking the electric field plot.

4.2. Benchmarking

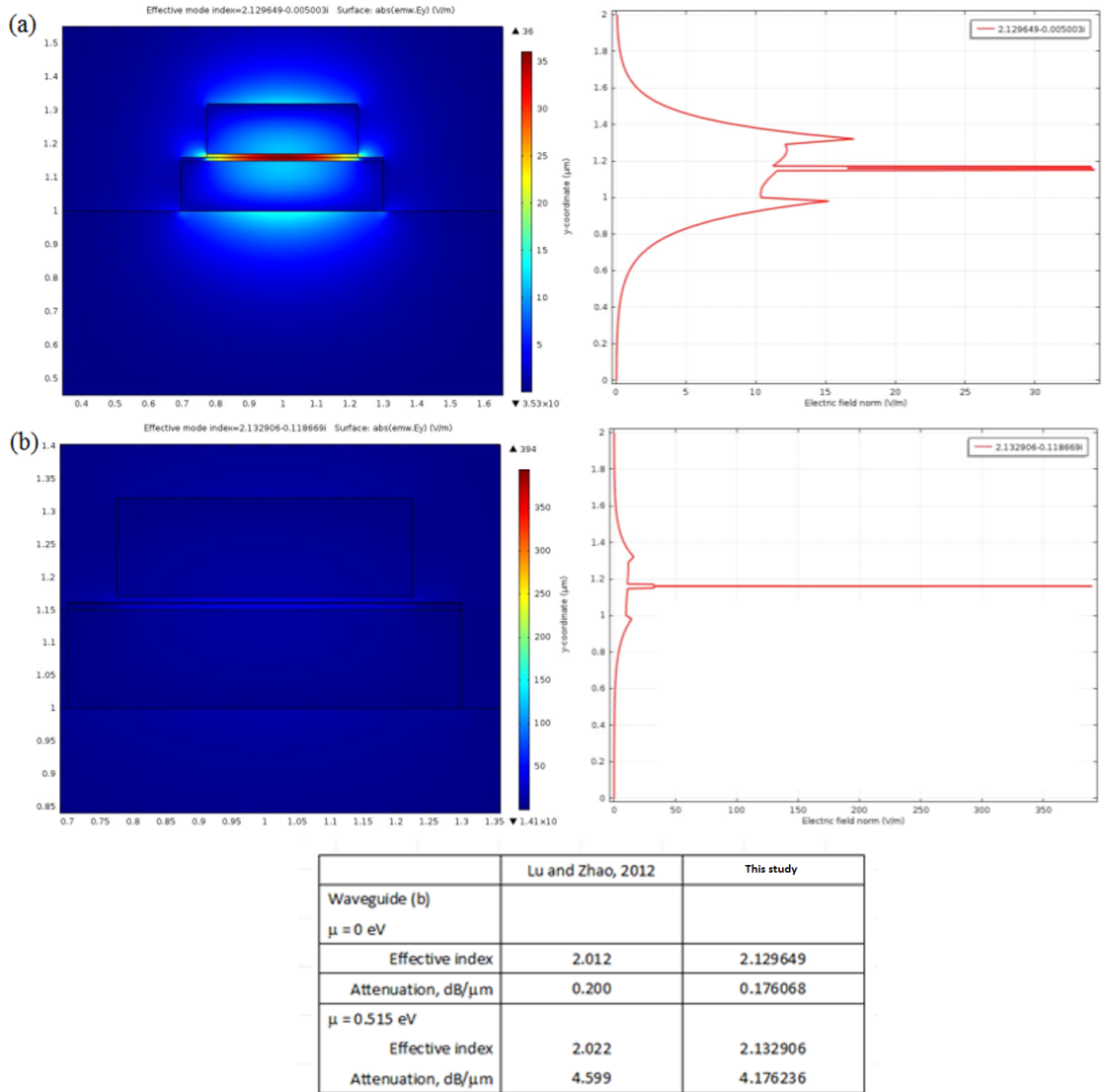


Figure 4.19: Mode profile and electric field of TM mode for waveguide in Fig. 2(b) of Lu and Zhao [29]. Inset shows the comparison of n_{eff} and α values of theirs and ours.

4.2.3 Study 3: Top Layer Graphene Waveguide

Liu *et al.* [20] reported the first waveguide-integrated graphene-based electroabsorption modulator wherein the modulation is achieved by tuning the Fermi level of a monolayer graphene sheet. Width of the Si waveguide is 600 nm and dielectric spacer (Al_2O_3) is 7 nm. Wavelength (λ) in their study was $1.53 \mu\text{m}$. Figure 4.22(a) shows the waveguide design used in their study.

Their study has not explicitly given complete details of the waveguide parameters, especially the dielectric constants of graphene. So we have used $\varepsilon(\omega)$ values from our study and followed their design specifications. Using complex solver we obtained the electric field, shown in Fig. 4.22(b). Our plot shows the same trend with their curve of

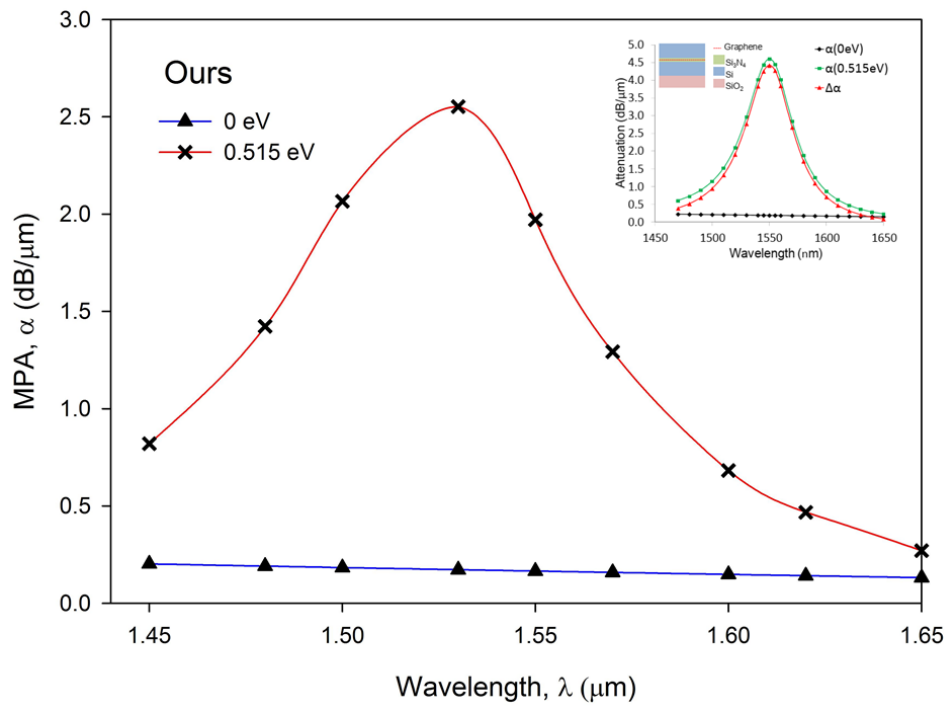


Figure 4.20: Absorption versus wavelength plot as shown in Fig. 4(a) of Lu and Zhao [29]. Inset shows their plot.

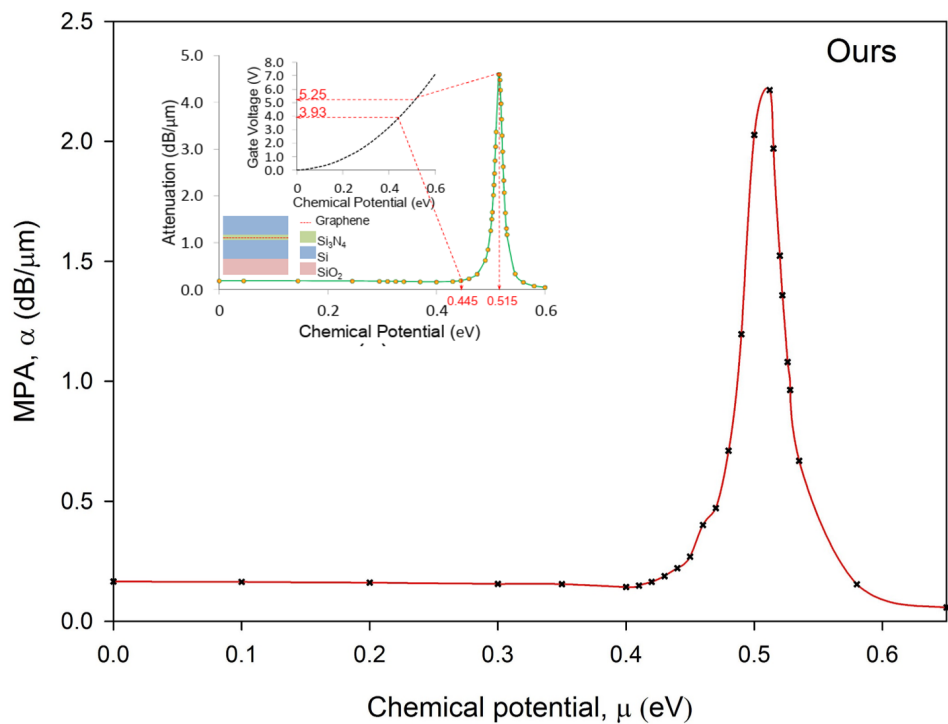


Figure 4.21: TM mode absorption as a function of chemical potential (μ) for waveguide in Fig. 4(c) of Lu and Zhao [29]. Inset shows the plot from their study.

magnitude of electric field shown in Fig. 4.22(b). In their next study, Liu *et al.* [114] proposed a bilayer graphene separated by dielectric material (Fig. 4.23). This study provides a complete description of experimental steps adopted to synthesize sheets of

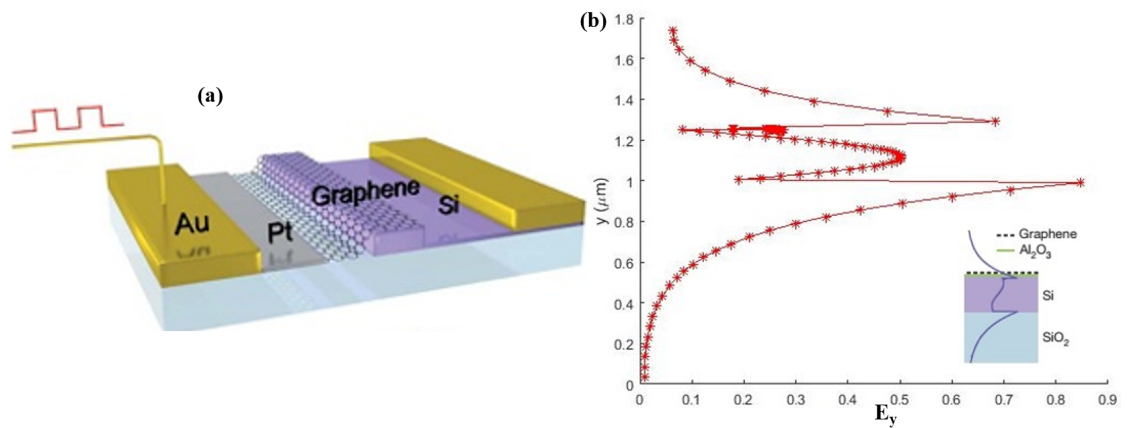


Figure 4.22: (a) Three-dimensional illustration of the modulator. Source: Ref. [20]. (b) electric field plot obtained using our complex solver for their waveguide dimensions. Inset shows the electric field plot from their study [20].

graphene. The optimized wavelength used in this study is $\lambda = 1537 \text{ nm}$. A modulation depth of $\sim 6.5 \text{ dB}$ was achieved in their study.

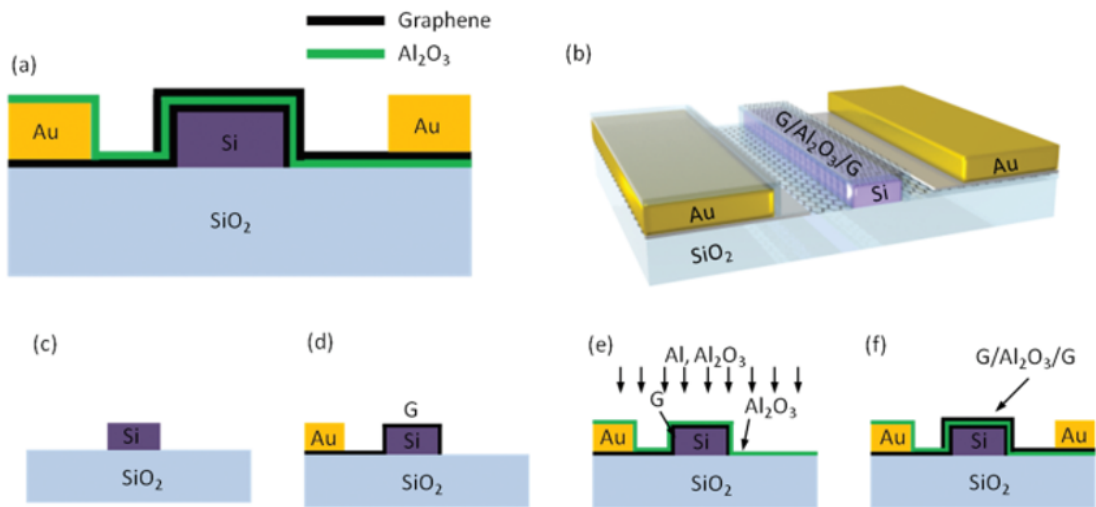


Figure 4.23: Study of Liu *et al.* [114] showing 2D (a) and 3D (b) models of double layer graphene modulator. Steps for fabrication is shown from (c) to (f). Source: [114].

Possible fabrication process of double-layer graphene is shown in Fig. 4.23(c)–(f). It can start with preparation of Si waveguide from a SOI wafer (c). A sheet of graphene prepared by CVD method can be transferred mechanically onto the waveguide (d). E-beam lithography is used at this stage and oxygen plasma removed unwanted regions. A thin layer of aluminium is deposited by thermal evaporation and Al₂O₃ by ALD method (e). Second, graphene sheet is mechanically transferred and EBL and oxygen plasma are used to define the active region (f). Metal electrodes are deposited. Here, graphene layers are separated by a 12 nm thick Al₂O₃ layer, thus forming a parallel plate capacitor

structure. A switching voltage of $V_D = 6$ V for this device was determined by dielectric constant and thickness of gate oxide.

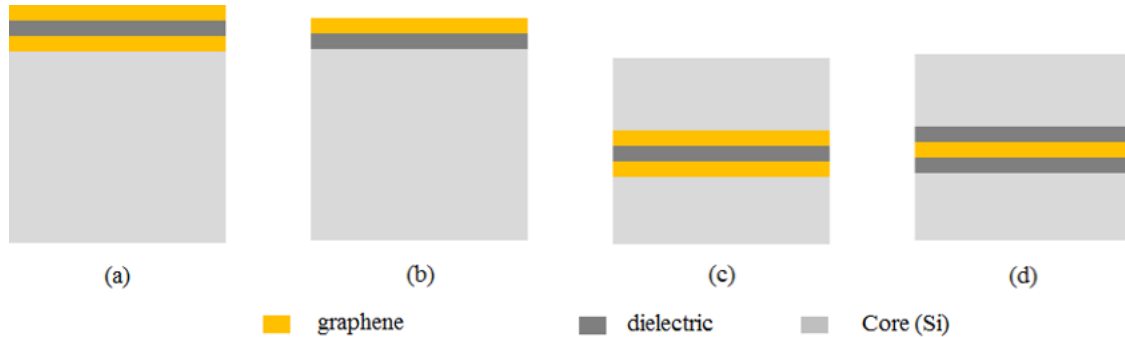


Figure 4.24: Waveguide designs taken from literature: (a) Liu *et al.* [114]; (b) Phatak *et al.* [96]; (c) Koester *et al.* [115], Hu and Wang [103]; (d) Lu and Zhao [29].

Figure 4.24 shows few structures of graphene-based waveguides proposed by different studies. Here, the placement of graphene is prominent as it is the active layer which interacts with incoming light and modulation is based on graphene's switching behaviour. So, graphene layer should be made to interact with maximum light intensity to achieve effective modulation. Plasmons or surface plasmons (SPs) which are quantisation of collective surface excitation of charge carriers play a major role in graphene-based modulators. Graphene contains intrinsic plasmons that results in high quantum efficiency of light-matter interaction [89]. Plasmons couple strongly with incoming EM waves leading to plasmon-photon coupling due to which a great amount of EM energy is confined within waveguide at subwavelength scales. Therefore, encapsulating graphene with dielectric material or having a dielectric layer between core and graphene enhances TM mode due to dielectric confinement of the EM wave.

4.3 Conclusion

We discussed the results from perturbation and complex solvers used for benchmarking with studies from the literature. Our results showed that perturbation solver may not be accurate when the real part (ε_1) of complex $\varepsilon(\omega)$ is smaller in magnitude than the imaginary part (ε_2). Whereas results from complex solver showed a very close agreement with the literature but imposes restriction on mesh dimension. Upon validating our understanding of graphene-based waveguides with literature studies, we now move on to proposing our designs and discussion of results. From benchmarking, we inferred that placement of

4.3. Conclusion

graphene layer as either slot or top layer, affects TE and TM mode absorptions, whereas effective index (n_{eff}) undergoes a minor change as a function of wavelength (λ) or gate voltage V_g . Therefore, graphene layer is the most suitable for electro-absorption modulators. Taking fabrication factors into account, in the next chapter we discuss the waveguide designs we propose and present their results.

Chapter 5

Characterization of Graphene–Silicon Hybrid Waveguides

5.1 Introduction

Light–matter interaction at nanoscale level is the unique property observed in 2D optical materials viz., graphene, phosphorene and so on. This forms a separate branch in nanophotonics termed *Plasmonics*. Due to growing state-of-the-art techniques in nanofabrication, applications such as ultrafast electro-optical modulator are envisaged. Plasmonics allow strong interaction between the free electrons and incoming light wave, breaking the diffraction limit and thus light is confined in deep-subwavelength volumes. In a graphene-based waveguide, at $\lambda = 1550$ nm, plasmonic modes are obtained in the graphene–dielectric interface, wherein thickness of bilayer graphene is just 0.7 nm.

The modal solutions of graphene-based waveguides will be discussed in this chapter beginning with finite-element characterization of a silicon nanowire. An Si nanowire waveguide is a semiconductor structure based on concept of silicon-on-insulator technology. It consists of a layer of single-crystalline silicon separated from the substrate by a layer of insulator. Here the substrate is silicon. The insulator is called buried oxide viz., SiO₂, hBN, Al₂O₃, Si₃N₄, etc. These layers are made into a simple optical waveguide (Fig. 5.1) that guides EM wave. So waveguides are the building blocks of any photonic circuit. In earlier chapters, light confinement within waveguides based on Maxwell equations were discussed.

An expression for single-mode condition (SMC) for a rib waveguide shown in Fig. 5.1

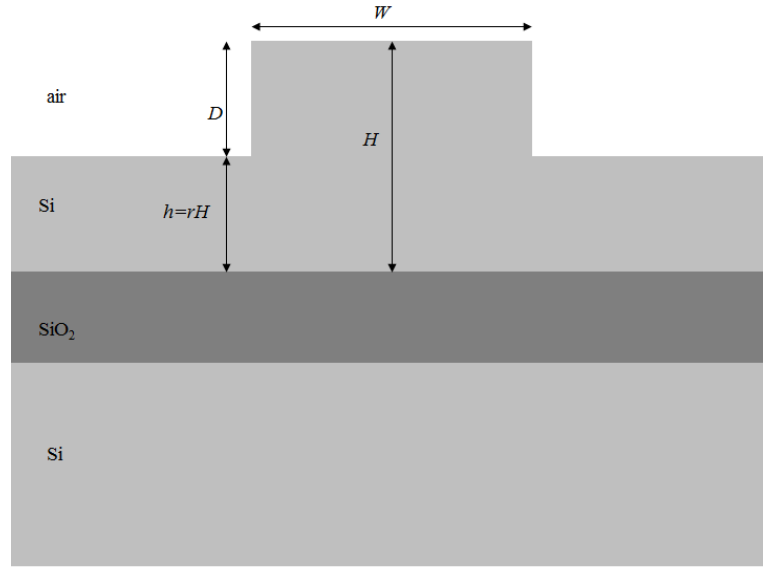


Figure 5.1: A rib waveguide in silicon-on-insulator. The refractive indices (n) air, Si and SiO_2 are 1, 3.477 and 1.444, respectively.

is given by [40]

$$\frac{W}{H} \leq 0.3 + \frac{r}{\sqrt{1-r^2}} \quad (\text{for } 0.5 \leq r < 1) \quad (5.1)$$

where r is the ratio of slab height to overall rib height, and W/H is the ratio of waveguide width to overall rib height.

5.2 Characterisation of Optical Waveguides

Waveguides form the basic building blocks of optical modulators through which the electromagnetic waves are guided. The study of guided modes, TE and TM, is of prime importance to ascertain the characteristics of modulators prior to fabrication. These characteristics depend on properties of materials used in the waveguide design. A material capable of changing its optical property such as refractive index (n) is used in such waveguides. Depending on the optical property of the material which is changed for light modulation, modulators are primarily classified as absorptive or refractive modulators. In the former, the absorption coefficient ($\text{Im}(n)$) of the material is controlled by an absorption-related effect viz., electro-absorption, Franz–Keldysh effect and the quantum confined Stark effect.

Optical waveguides are characterized by obtaining TE and TM mode profiles and corresponding plots for effective index (n_{eff}), absorption (α), extinction ratio (ER), insertion

loss (IL) and so on.

We have discussed the step-by-step characterization procedure using Finite Element Method [45] in Chapters 2 and 4. We already carried out benchmarking results of our perturbation and complex solvers. It is observed that perturbation results are not accurate when the magnitude of $\text{Re}(\varepsilon(\omega))$ is less than $\text{Im}(\varepsilon(\omega))$. So, complex solver was used for obtaining modal solutions of graphene-based wave-

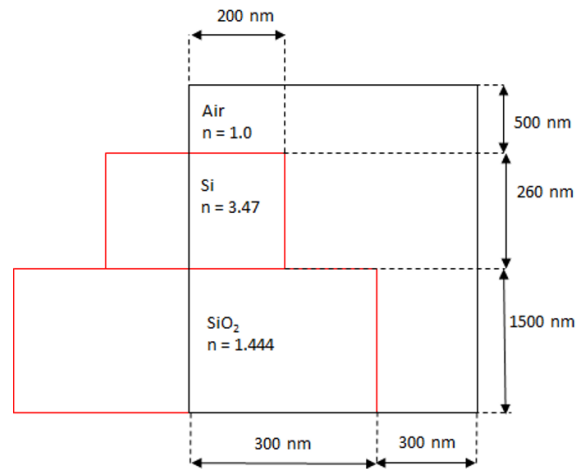


Figure 5.2: A silicon nanowire.

guides. As a first step, a silicon nanowire (Fig. 5.2) was studied using both solvers. In the figure, due to one-fold symmetry, the block as marked by solid line is considered for simulation.

5.2.1 Silicon Photonic Waveguides

In silicon photonics, a silicon nanowire is a basic waveguide structure of silicon on a substrate. This Si waveguide, prepared from a silicon-on-insulator (SOI) wafer, forms the start of fabrication process of multi-layered Si optical waveguides. The SOI waveguiding structures are more popular due to the possibility of much stronger optical confinement. These modulators have undergone significant transformation since early 1980s. Silicon is a potential material in the class of photonics materials, and also a platform for 2D materials such as graphene to realize ultrafast modulation devices for quantum computers.

TE and TM mode profiles of Si strip and rib waveguides are shown in Figs 5.4 and 5.5. The waveguide dimensions are chosen based on an earlier design optimization shown in Fig. 5.2; width, $0.4 \mu\text{m}$; thickness, $0.3 \mu\text{m}$. For the strip waveguide, the effective indices of TM and TE modes are obtained as 2.159484 and 2.412079, respectively, whereas for rib waveguide, these values are 2.755377 and 2.812342. The mode is effectively confined in rib than the strip waveguide. The reason is attributed to the presence of Si slab introduced in the rib waveguide.

Comparing TE modes in Fig. 5.4(c) and 5.5(c), the mode is moved down by the slab. This phenomena was exploited by Gosciniaik and Tan [6] who placed bilayer graphene in

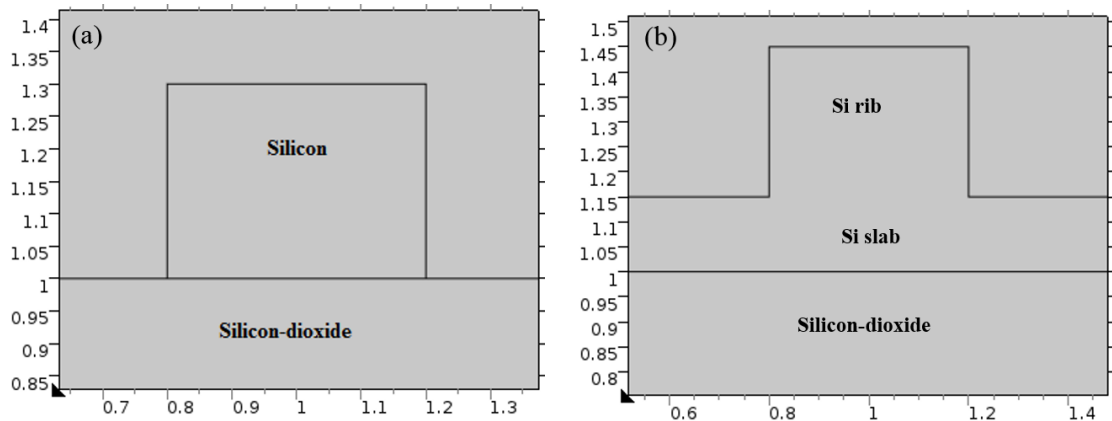


Figure 5.3: Rectangular silicon waveguides: (a) strip and (b) rib. Dimensions of Si core are width $0.4 \mu\text{m}$ and thickness $0.3 \mu\text{m}$. In (b), the Si slab is of thickness $0.15 \mu\text{m}$ and width $1 \mu\text{m}$.

the slab and ridge interface. In their study, the slab is mentioned as a low or high index buffer material with $n = 1.98$ or $n = 3.47$, respectively. Thus introducing a slab moves the maximum of the mode electric field closer to the graphene layers, thereby enhancing graphene–light interaction which is crucial for electro-optic modulation.

The optical properties of graphene namely the optical conductivity (ρ) and permittivity (ϵ) are highly influenced by the chemical potential (μ) which is fine tuned by applying a gate voltage (V_g). This is studied in the next section. This unique property of tuning of Fermi level using applied voltage forms the principle of graphene-based electro-absorption modulators.

5.2.2 Top- versus Slot-layered Graphene Waveguides

Positioning graphene layer(s) as a top-layer or slot-layer in the waveguide influences its modal properties. Experimental studies [20, 96, 114] proposed graphene as top layer. Step-by-step fabrication process was explained in [114]. Lu and Zhao [29] stated that effect of change in dielectric constant of graphene is not very manifest when graphene is placed as top layer. Gosciniak and Tan [6] discussed the benefits of positioning graphene as slot, since it increases graphene’s interaction with maximum light intensity. Effect of graphene conductivity (ρ_g) change is not very pronounced if graphene is placed far from the electric field maximum of the propagating mode. On this regard, we study the TM mode properties in both of these waveguides.

We begin characterisation of graphene-based waveguides with two designs as shown in Fig. 5.6. Dimensions of waveguide are core width $0.4 \mu\text{m}$ and height $0.3 \mu\text{m}$ which showed

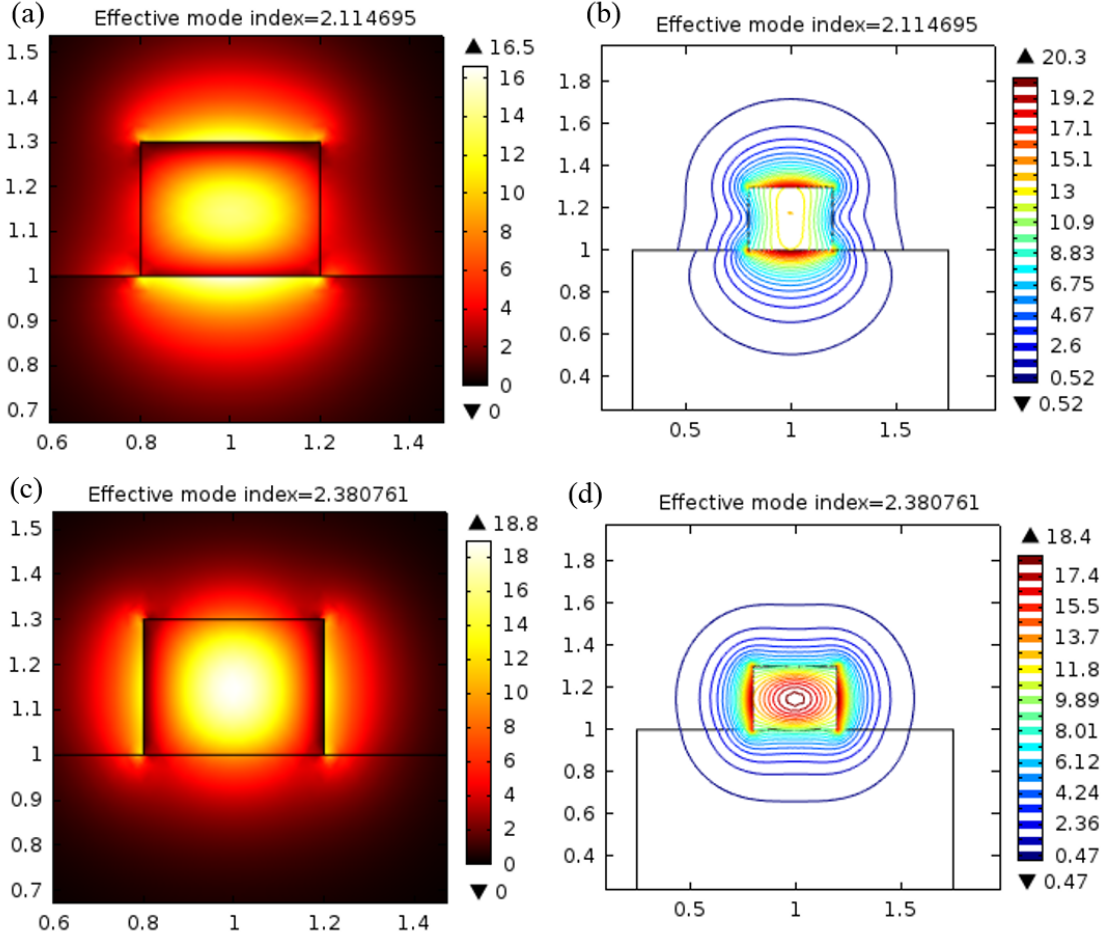


Figure 5.4: Mode profiles of Si strip waveguide: (a) TM; (b) TM contour; (c) TE; (d) TE contour.

good confinement at $\lambda = 1550$ nm. Figures 5.7 and 5.8 show n_{eff} and α variations of TM mode as a function of chemical potential (μ).

Plots in above figures show electrically tunable variations of n_{eff} and α of the TM mode in both the waveguides. These variations are due to change in complex dielectric constant, $\varepsilon(\omega) = \varepsilon_1 + j\varepsilon_2$, of the graphene layer. Between 0.4 and 0.55 eV, the magnitude of $\varepsilon(\omega)$ varies more than 30 times [6]. This is the reason for high modulation depth achieved in graphene-based modulators. The TM mode in slot-waveguide shows a steady rise and fall in both n_{eff} and α . This is attributed to the reason that graphene layer is placed at maximum light intensity of the waveguide.

Next, we consider only the waveguide with top-layer graphene in Fig. 5.6(a). The dielectric material between graphene layer and silicon chosen as one with high-index ($\varepsilon(\text{Al}_2\text{O}_3)=9.1$) and other with low-index ($\varepsilon(\text{hBN})=3.9204$). Dielectric (buffer) materials for graphene-based waveguides are chosen such that they have lattice matching with

5.2. Characterisation of Optical Waveguides

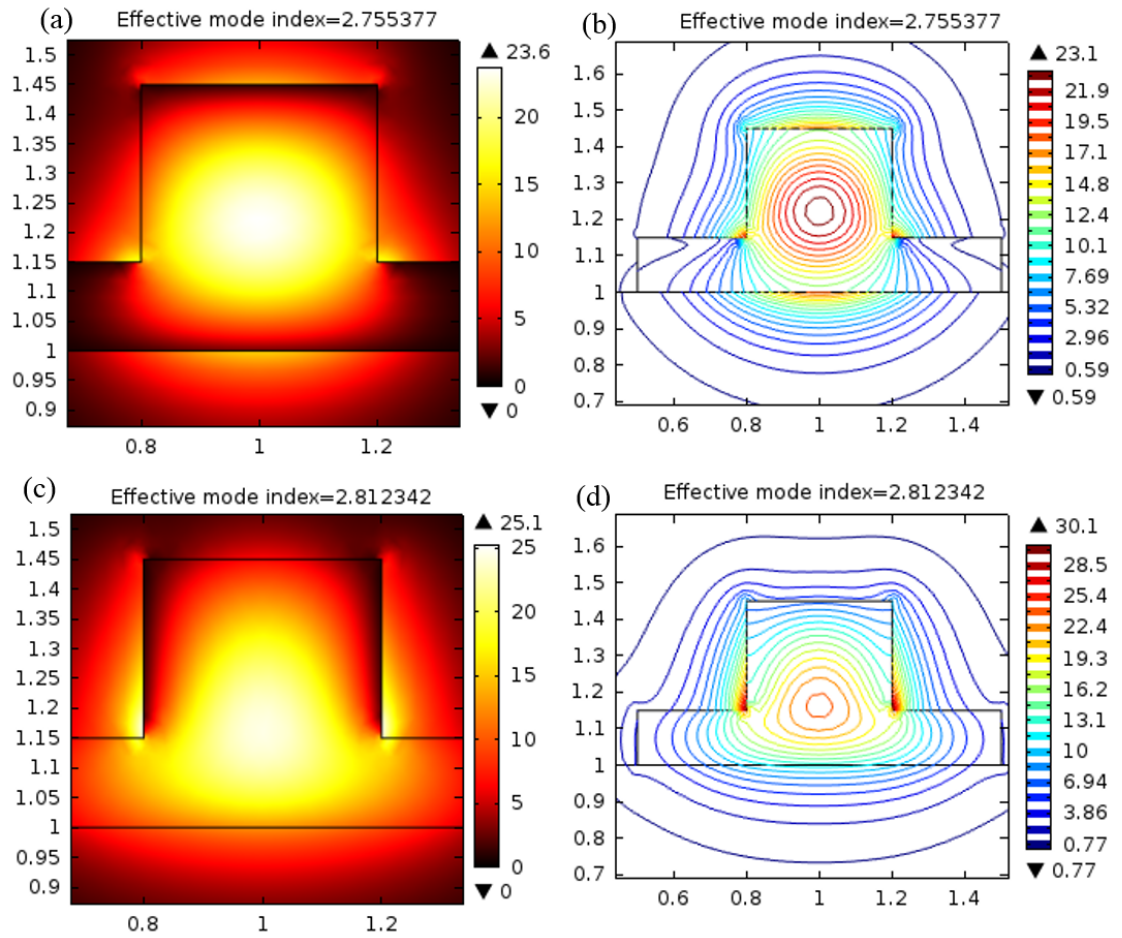


Figure 5.5: Mode profiles of Si rib waveguide: (a) TM; (b) TM contour; (c) TE; (d) TE contour.

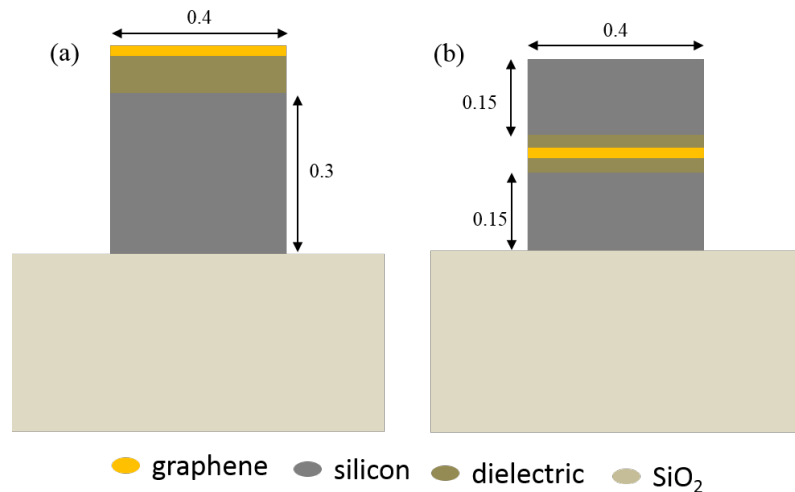


Figure 5.6: Waveguides with graphene as top (a) and slot (b) layers. $t_{\text{graphene}} = 0.69 \text{ nm}$; $\lambda = 1550 \text{ nm}$; refractive indices (n) of Si, SiO₂ and $h\text{BN}$ are 3.4777, 1.444 and 1.98, respectively.

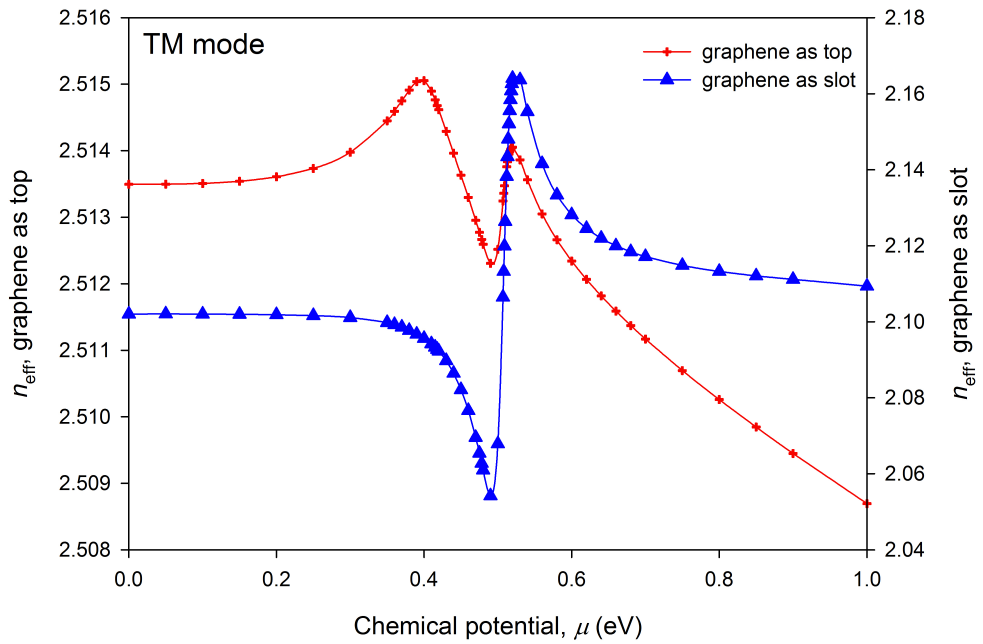


Figure 5.7: TM mode effective index plots of top-layer and slot-layer graphene.

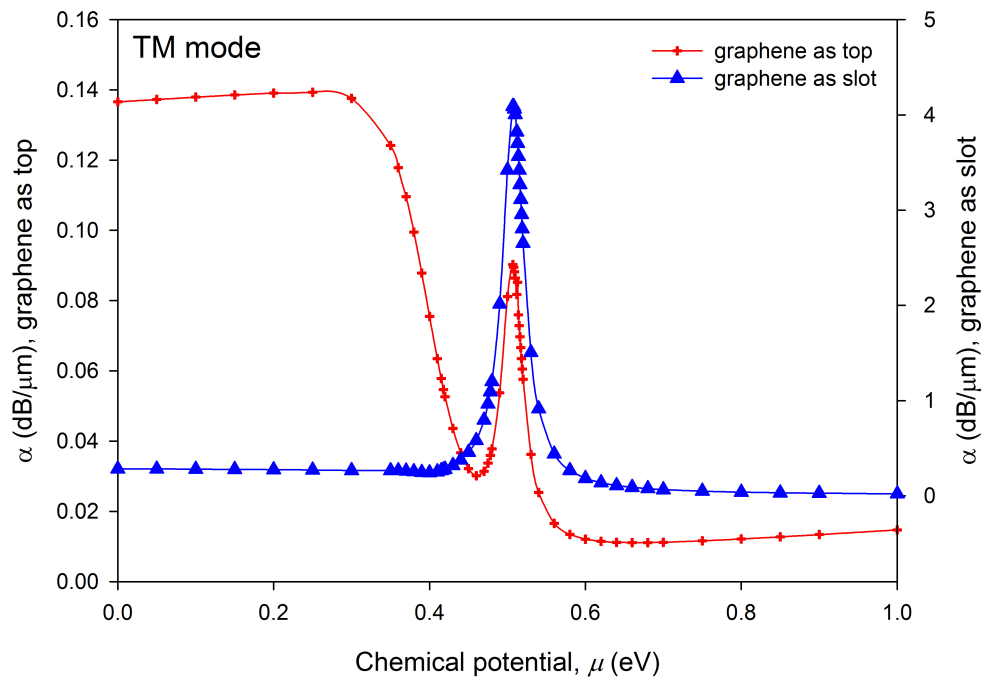


Figure 5.8: TM mode absorption plots of top-layer and slot-layer graphene.

graphene which is of hexagonal lattice. Use of this isolated layer prevent carrier injections between graphene and silicon. Also, growing graphene layer directly on silicon is not preferred due to lattice mismatch between both. The first graphene EOM proposed experimentally by Liu *et al.* [20] has Al_2O_3 as buffer layer between single layer graphene and silicon, which showed electroabsorption modulation of $0.1 \text{ dB}/\mu\text{m}$. In their next study [114], the same authors, proposed experimentally a double layer graphene modulator that has bottom graphene layer directly on silicon and the other top graphene layer separated by 5 nm thick Al_2O_3 , which showed $\sim 0.16 \text{ dB}/\mu\text{m}$. This improvement in absorption from previous design is due to the dielectric confinement of electromagnetic wave which generates surface plasmons in the dielectric interface.

Figures 5.9 and 5.10 show TE and TM mode effective index results, respectively, obtained for Si nanowire, Si-*h*BN-graphene and Si- Al_2O_3 -graphene waveguides, where $\varepsilon(\text{hBN})=3.9204$ and $\varepsilon(\text{Al}_2\text{O}_3)=9.1$. In both modes, the high-index dielectric shows distinct variation in n_{eff} while that of the low-index is marginal. The TM mode is significantly affected by change of dielectric material whereas TE does not. This task is carried out to find out the suitable dielectric material if graphene layer is placed on top of silicon core. Here, we infer that a high-index dielectric material is appropriate for waveguides with top-layer graphene. We will be discussing this finding in further sections in detail.

The increase in n_{eff} for the waveguides with dielectric materials is attributed to the dielectric confinement and that is why graphene is encapsulated by dielectric layers when used in such hybrid waveguides. In the next section we will discuss modal solutions of waveguides with graphene as slot layers. In the waveguides we discussed above, only graphene possesses a complex dielectric constant ($\varepsilon(\omega) = \varepsilon_1 + j\varepsilon_2$) which is responsible for absorption phenomena. Therefore, the absorption phenomena in graphene-based waveguides is highly influenced by the thickness of graphene as well as the refractive index of dielectric material used as isolation or buffer layer.

5.3 Characterisation of Slot Waveguides with Bilayer Graphene

Slot waveguides are suitable designs for enhancing optical confinement within the slot regions. In a plasmonic waveguide, a dielectric-metal interface generates surface plasmons in the slot which are ideal for electro-absorption phenomena. In a graphene-based waveguide,

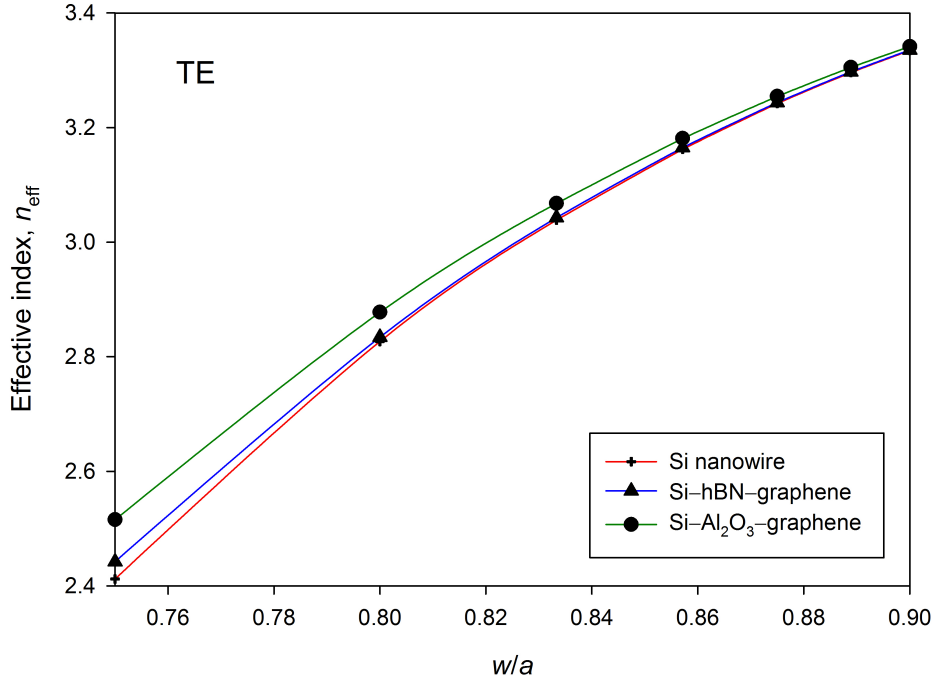


Figure 5.9: TE mode effective index plots of Si nanowire and waveguides with graphene as top layer; height-to-width ratio, w/a .

uide, absorption arises due to varying $\varepsilon(\omega)$ of graphene. Therefore, the objective in such a waveguide is always to enhance interaction between graphene and incoming light wave by placing graphene–dielectric stack in a region of maximum light intensity. Based on results presented above, we infer that graphene as a horizontal slot serves for application requiring high TM mode absorption.

Fabrication procedure for these waveguides are explained in Ref. [114]. Such design is classified as a horizontal slot waveguide. The slot layer is first deposited onto a silicon layer and then second silicon layer is grown. E-beam lithography (EBL) and oxygen plasma are used to remove unwanted region and define the active region.

In this section, we present the results of two horizontal slot waveguides, one with graphene–dielectric sandwich and the other with two graphene layers separated by a dielectric, placed in core silicon. The latter waveguide design was taken from Ref. [103]. This is to study the influence of dielectric layers on waveguide parameters such as effective index and absorption. These waveguides are shown in Fig. 5.11. Waveguide (a) is termed as the one with dielectric-encapsulated graphene and the other waveguide (b) as the one with graphene-on-graphene configuration, even though it is separated by a thin layer of dielectric material. Thickness of each layer of graphene is taken as 0.69 nm and that of

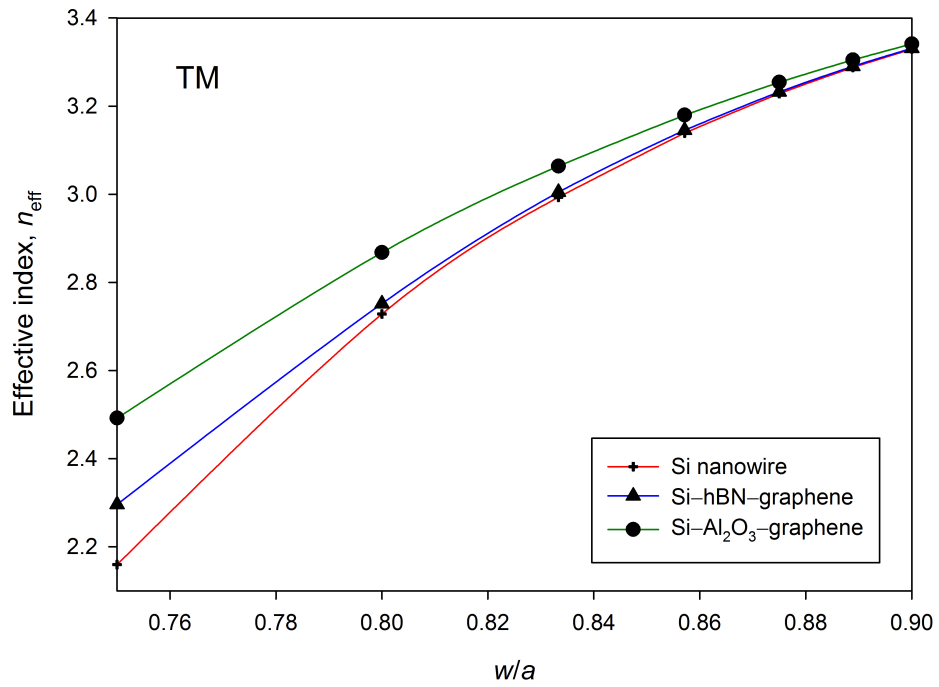


Figure 5.10: TM mode effective index plots of Si nanowire and waveguides with graphene as top layer.

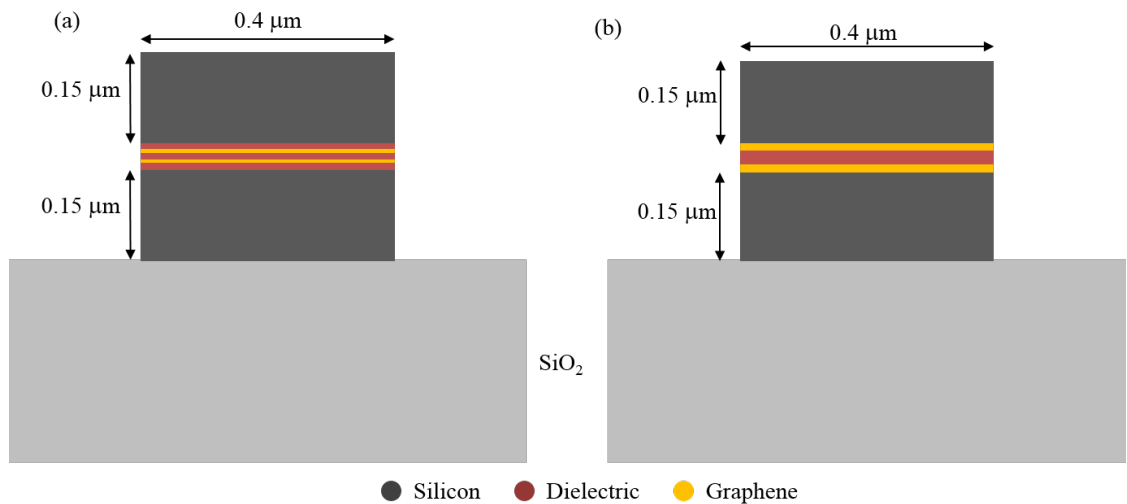


Figure 5.11: Silicon rib waveguides with graphene as slot layer: (a) graphene with encapsulated dielectric and (b) graphene directly on silicon and separated by a dielectric. Refractive indices of Si, SiO₂, hBN and Al₂O₃ are 3.477, 1.444, 1.98 and 3.017, respectively.

dielectric layers is set as 10 nm throughout the study.

The unique property of graphene is the tunable Fermi level (E_F) through which absorption of light wave can be controlled. The Fermi level is adjusted by applying a gate voltage. We study the modal properties n_{eff} and α for the voltage range from 0 to 1 eV. The dielectric constants, $\varepsilon(\omega)$, of graphene are obtained by interpolating 0–1 eV with 55 discrete voltage levels each having a complex $\varepsilon(\omega) = \varepsilon_1 + j\varepsilon_2$. The variations of n_{eff} and α for each of $\varepsilon(\omega)$ and plotted against the Fermi level, μ , as shown in Figure 5.12.

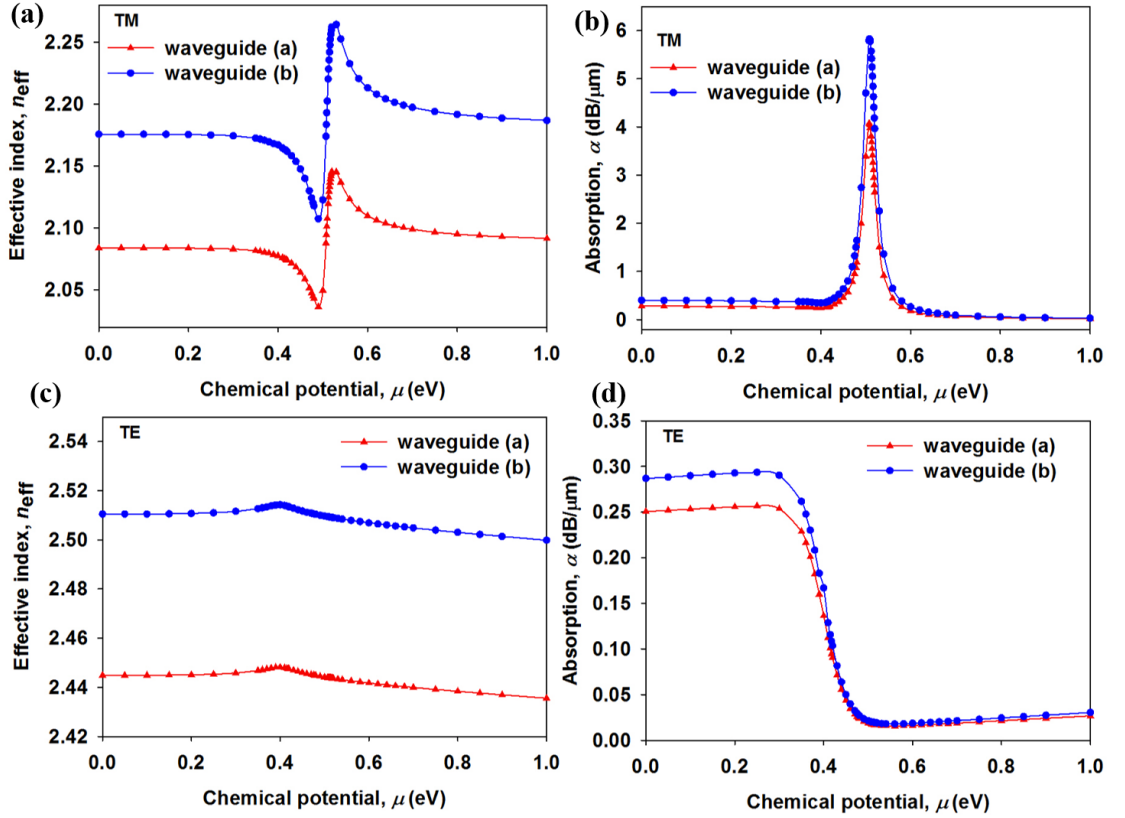


Figure 5.12: TM and TE mode effective index (a, c) and absorption (b, d) for waveguides with dielectric layer encapsulated graphene and graphene-on-graphene configuration; (a) and (c) show the change in real part of n_{eff} ; $\lambda = 1550$ nm.

Plots shown in the figure show a distinct variation between 0.4 and 0.5 eV irrespective of the type of modes. This is where peak absorption and maximum absorption occurs as shown in (b) and (d), respectively. It can be seen that waveguide (b) outperforms waveguide (a) in terms of n_{eff} . At $\mu = 0.51$ eV, a peak in TM mode absorption is achieved for both waveguides, which agrees with that of Gosciniak and Tan [6]. Due to the *enz* effect, the α undergoes rapid rise and fall within this voltage range. The change in TE mode absorption after 0.35 eV is similar to that noticed in the study by Phatak *et al.* [96].

Next we carried out the study of mode profiles of both the waveguides and their variations in n_{eff} and α as a function of w/a ratio. Height (w) of the waveguide is varied from 0.4–1.0 μm and corresponding width (a) varies from 0.3–0.9 μm and the w/a ratio is calculated accordingly.

Two voltage levels, 0.4 and 0.52 eV, corresponding to ON and OFF, respectively, are chosen. The dielectric constants ($\varepsilon(\omega)$) of graphene with $\lambda=1550$ nm at these levels are given by,

$$\varepsilon(0.4 \text{ eV}) = 4.7592 + j4.4441$$

$$\varepsilon(0.52 \text{ eV}) = -0.4998 + j0.5340$$

We have used these $\varepsilon(\omega)$ values to characterize waveguides (a) and (b) in the next sections. The reason why these voltages are chosen is that between 0.4 and 0.52 eV, the magnitude of $\varepsilon(\omega)$ of graphene varies more than 30 times [6]. This is the stage where graphene's behaviour changes from dielectric to metallic such that the electrons behave like massless Dirac fermions [90]. Mode profiles, effective index and optical absorption are studied for the TE and TM guided modes of these waveguides.

5.3.1 Dielectric-encapsulated bilayer graphene waveguide

In this section, we study the waveguide (a) shown in Fig. 5.11 wherein each of the graphene layers are encapsulated with dielectric materials such as $h\text{BN}$ and Al_2O_3 of low- and high-index, respectively. We used both dielectric materials separately and the mode profiles are shown in following figures. Plots for effective index and optical absorption are shown. For mode profiles, $h\text{BN}$ is taken for ON condition whereas Al_2O_3 for OFF condition.

TE and TM mode profiles of waveguide (a) are shown in Fig. 5.13. Mode profile (a) shows effective dielectric confinement of TM mode. Here $\mu=0.4$ eV refers to the beginning of transition state (from dielectric to metallic) where absorption in graphene undergoes drastic changes. Figure 5.14 show TM and TE mode profiles, n_{eff} and α , for waveguide (a) at $\mu=0.52$ eV. This is where the *enz* effect is observed that leads to drastic rise and fall in absorption, α . A high-index dielectric ($\varepsilon(\omega) = 9.1$) is used to obtain these results, since a high-index dielectric induces high TM mode absorption as seen in the figures.

The influence of high-index dielectric material on absorption phenomena of graphene-based waveguide is shown in above figures. The TE n_{eff} has shown an increase from 2.300564 to 2.401029 which is attributed to the high-index dielectric between the bilayer

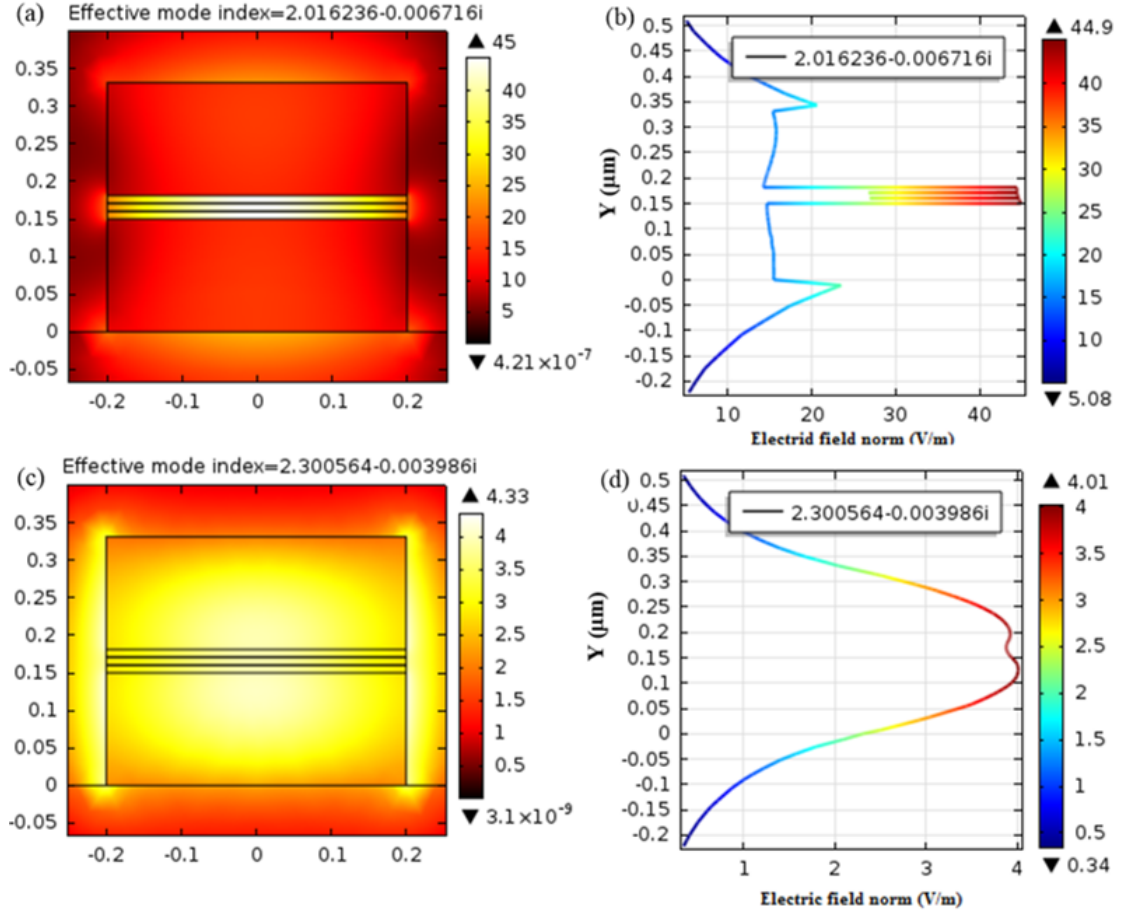


Figure 5.13: TM and TE mode profiles of low-index dielectric-encapsulated graphene layers. (a) TM; (b) TM electric field; (c) TE; (d) TE electric field. $\epsilon(h\text{BN}) = 3.9204$; ON: $\epsilon(0.4 \text{ eV}) = 4.7592 + j4.4441$; $\lambda = 1550 \text{ nm}$.

graphene. Similarly, TM mode n_{eff} increases from 2.016236 to 2.383794. In case of optical mode absorption, the TM mode undergoes drastic increase in α due to the *enz* effect. It reaches an absorption (α) of $4.585 \text{ dB}/\mu\text{m}$ at 0.52 eV from $0.236 \text{ dB}/\mu\text{m}$ at 0.4 eV . This is again attributed to the change in chemical potential as well as the high-index dielectric acting as buffer layer between graphene layers.

Next we analyse the changes in n_{eff} and α with respect to aspect ratio (w/a). Figures 5.15 and 5.18 show the effective index (n_{eff}) and absorption (α) results for TM and TE modes of low- and high-index dielectric-encapsulated graphene layers for ON and OFF $\epsilon(\omega)$ at $\lambda = 1550 \text{ nm}$.

In plots shown above, the influence of high-index dielectric material is distinct in case of TM mode n_{eff} and α . In case of TE mode, both these parameters are very close to each other for ON (0.4 eV) and OFF (0.52 eV) conditions, showing TE mode n_{eff} and α remain unaffected by the index of the dielectric material. The absorption (α) of TM

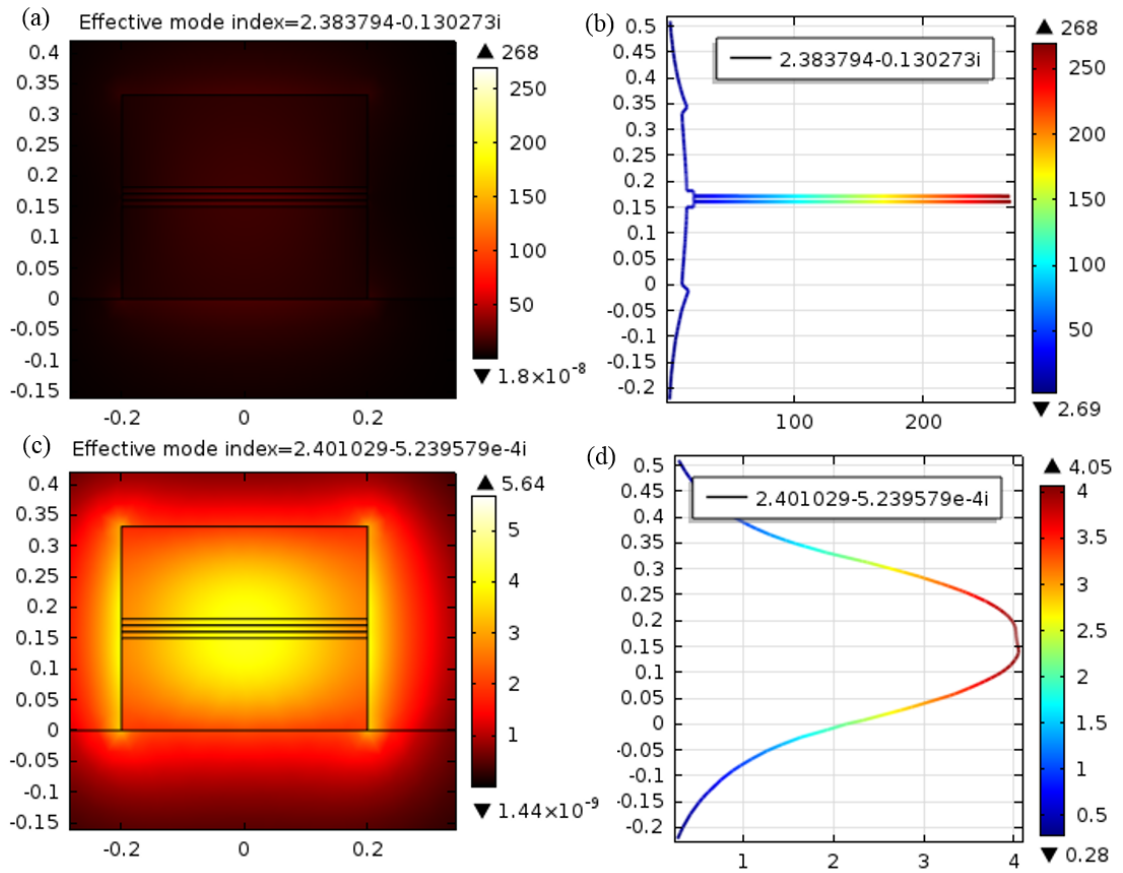


Figure 5.14: TM and TE mode profiles of high-index dielectric-encapsulated graphene layers. (a) TM; (b) TM electric field; (c) TE; (d) TE electric field. $\epsilon(\text{Al}_2\text{O}_3) = 9.1$; OFF: $\epsilon(0.52 \text{ eV}) = -0.4998 + j0.5340$; $\lambda = 1550 \text{ nm}$.

mode is significantly larger than that of the TE mode. Therefore, the change in chemical potential (μ), from 0.4 to 0.52 eV has a stronger influence on TM mode. In this study, the thickness of dielectric material was maintained at 10 nm. To bring in a change in TE modal properties, we infer that the dielectric thickness needs to be increased, which will be dealt in later sections. We have now studied the influence of μ and index of the dielectric material on modal properties of dielectric-encapsulated graphene-based waveguides.

5.3.2 Graphene-on-Graphene slot waveguide

Graphene-on-graphene configuration was first experimentally proposed by Liu *et al.* [114]. Their design had two layers of graphene separated by 5 nm thick Al_2O_3 which acted as isolation layer, placed on top of silicon core. Graphene directly on silicon is not preferred due to lattice mismatch between both. For this study, the waveguide design adapted from Ref. [103] was chosen. We follow their design of graphene- Al_2O_3 -graphene stack placed as slot as shown in Fig. 5.11(b).

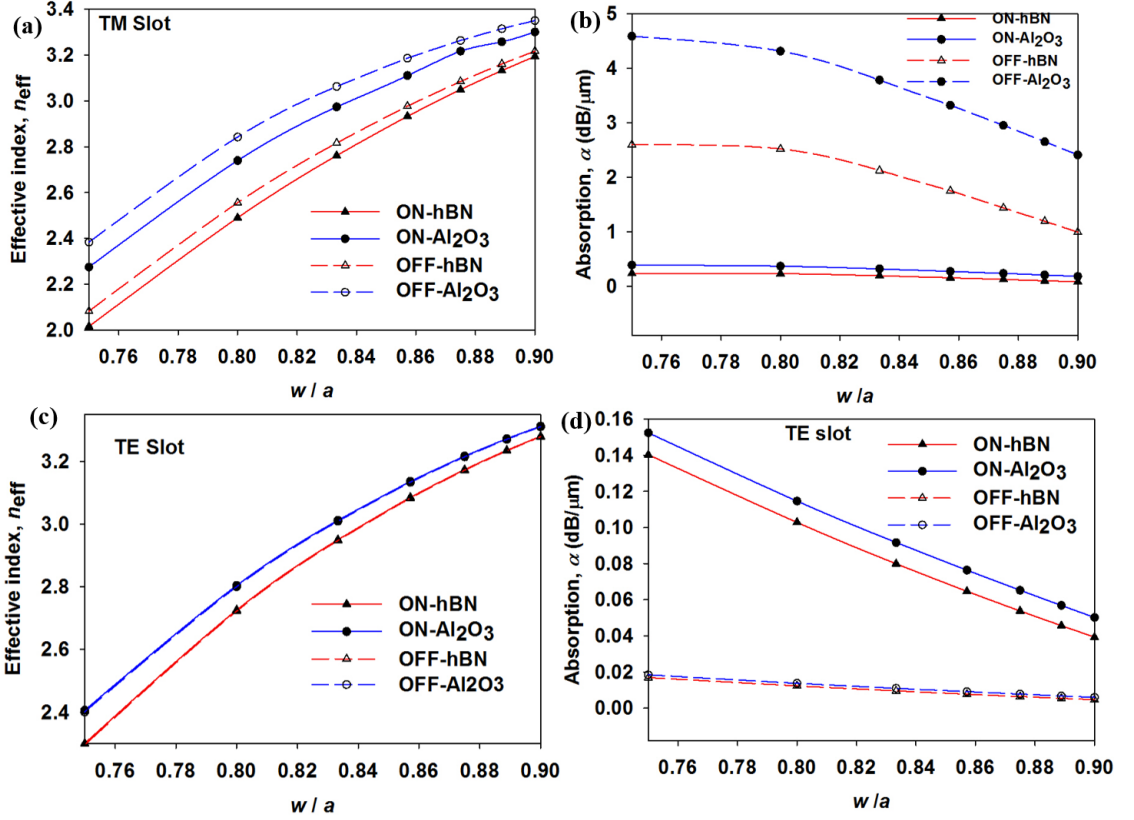


Figure 5.15: Mode effective index and absorption of TM and TE modes in a dielectric-encapsulated bilayer graphene waveguide. Plots (a) and (c) show the change of magnitude in real part of n_{eff} .

Figures 5.16 and 5.17 show TM and TE mode profiles and electric field distribution in the waveguide. The waveguide with high-index dielectric outperforms in terms of both n_{eff} and α when compared to that of low-index dielectric stack. An absorption of 4.98 dB/ μm is obtained in graphene–dielectric–graphene stack, whereas in the dielectric-encapsulated graphene waveguide, $\alpha = 4.58$ dB/ μm . This difference is attributed to the dielectric absorption that takes place in the latter, even though the difference is only marginal. On the other hand, in the latter waveguide, the dielectric layer encapsulation prevents carrier injection into silicon that arises when gate voltage is increased.

Figure 5.18 show the effective index and absorption plots obtained for graphene-on-graphene design as a function of w/a ratio. Plot (a) shows a marked difference from previous design (Fig. 5.15(a)) where n_{eff} variation for both dielectric materials are significant. In graphene-on-graphene configuration, the n_{eff} of ON- Al_2O_3 and OFF-hBN are too close. Similarly, in plot (c), n_{eff} for both dielectric materials irrespective of ON or OFF condition, lie on the same line which is similar to that of previous design. In terms of

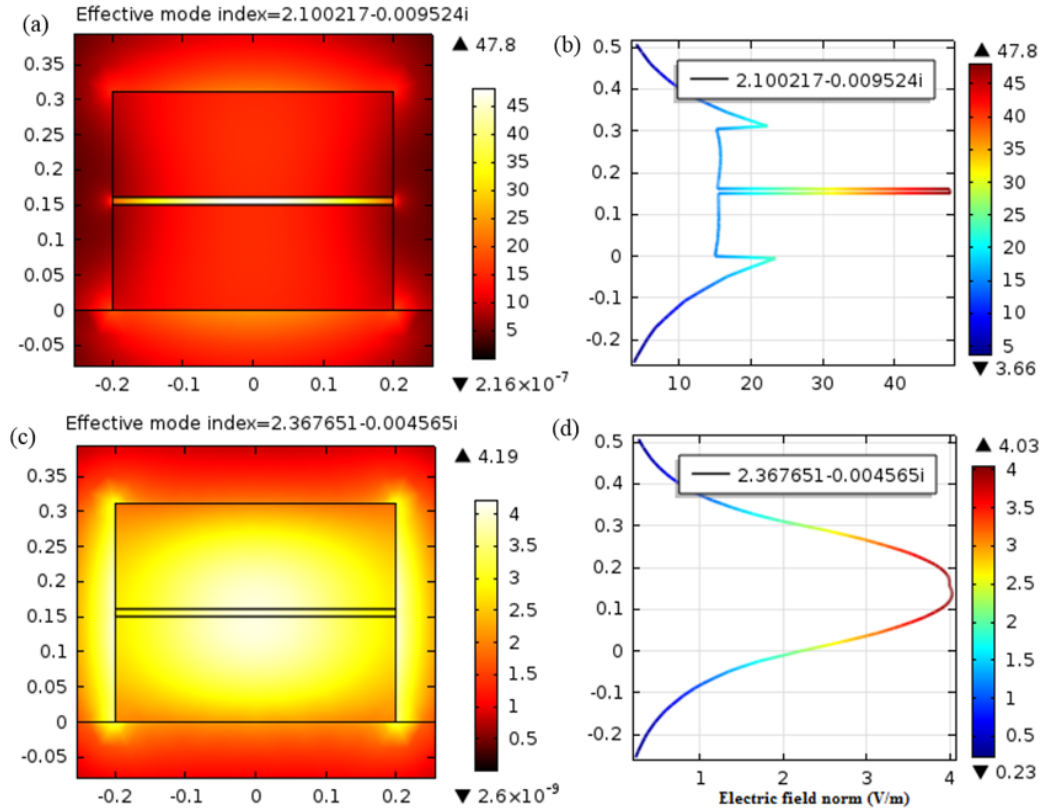


Figure 5.16: TM and TE mode profiles of waveguide with graphene-hBN-graphene stack. (a) TM; (b) TM electric field; (c) TE; (d) TE electric field. $\epsilon(h\text{BN}) = 3.9204$; ON: $\epsilon(0.4\text{ eV}) = 4.7592 + j4.4441$; $\lambda = 1550\text{ nm}$.

absorption shown in plot (b), G-on-G design shows higher absorption ($\alpha = 4.9797\text{ dB}/\mu\text{m}$) than the dielectric-encapsulated graphene waveguide ($\alpha = 4.5856\text{ dB}/\mu\text{m}$).

5.3.3 Summary

We have now analysed the modal properties of both designs viz., dielectric-encapsulated graphene and graphene-on-graphene configuration. Plots from both designs show the chemical potential (μ) dependence of $\text{Re}(n_{\text{eff}})$ and α on TM and TE modes. The change in complex dielectric constant of graphene, $\epsilon(\omega) = \epsilon_1 + j\epsilon_2$, affects the modal properties of the waveguides. Therefore, the $\epsilon(\omega)$ of graphene plays a crucial role in the electro-absorption phenomena. Electric field plots for OFF condition, shown by sharp peaks in plot (b) for both designs indicate very strong confinement within graphene layers.

Polarization-dependent loss is noted from both TM and TE mode absorption plots (b) and (d), respectively, shown in Figs 5.15 and 5.18. At dimensions of height 0.3 nm and width 0.4 nm , at 0.52 eV , TM achieves a loss of $4.9797\text{ dB}/\mu\text{m}$ whereas that of TE is $0.0201\text{ dB}/\mu\text{m}$, which proves a very strong absorption in the former. At 0.25 eV , the

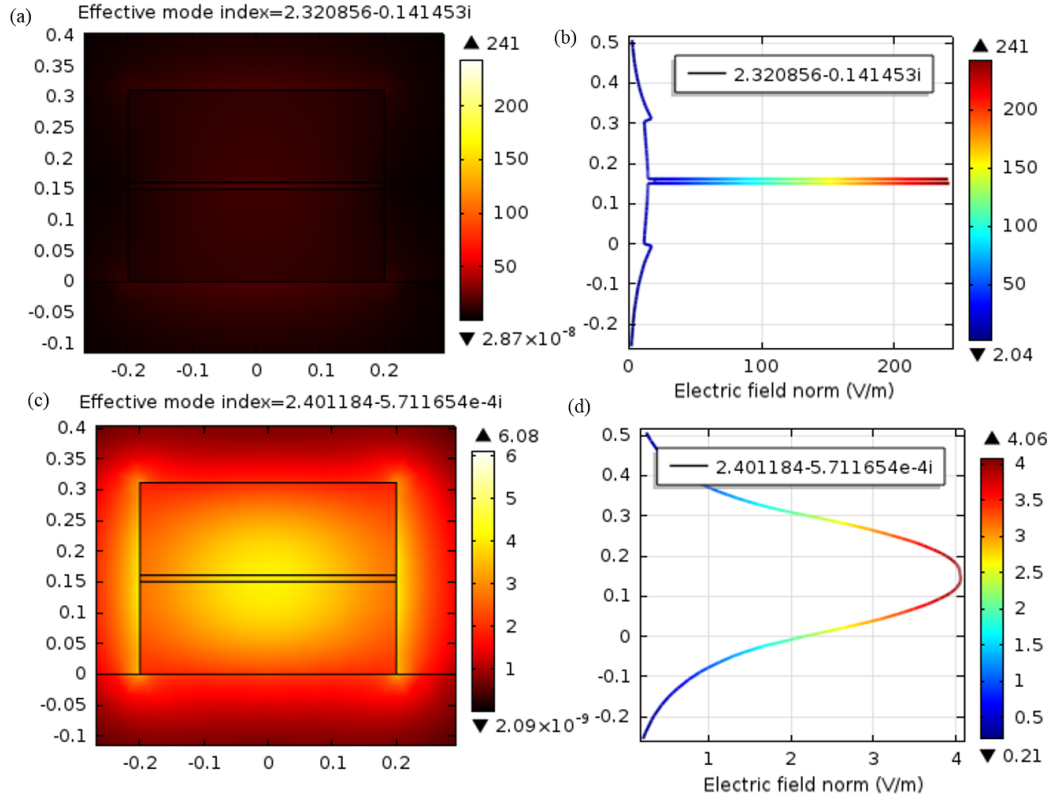


Figure 5.17: TM and TE mode profiles of waveguide with graphene–Al₂O₃–graphene stack. (a) TM; (b) TM electric field; (c) TE; (d) TE electric field. $\epsilon(\text{Al}_2\text{O}_3) = 9.1$; OFF: $\epsilon(0.52 \text{ eV}) = -0.4998 + j0.5340$; $\lambda = 1550 \text{ nm}$.

absorption in both modes are 0.2697 and $0.2566 \text{ dB}/\mu\text{m}$, respectively. Such strong polarization dependence could be utilized to realize a compact polarizer [103]. Variations in modal properties were not significantly different in both designs. In fabrication point of view, dielectric-encapsulated graphene is preferred since it eliminates performance deterioration due to carrier injections between layers.

Both waveguide designs are termed bulk since they have more than two to three layers. Fabrication of such structures possesses challenges in terms of layer alignment. Encapsulating graphene layers is inevitable as it enhances dielectric confinement and generates surface plasmons which are crucial for modulation. Graphene–dielectric–graphene layers form a parallel plate capacitor model and the maximum operating bandwidth is limited by the RC constant of the device. In terms of speed of modulation, a high quality graphene layer can operate on the timescale of picoseconds which implies that graphene-based electronics have the ability to operate at 500 GHz [6].

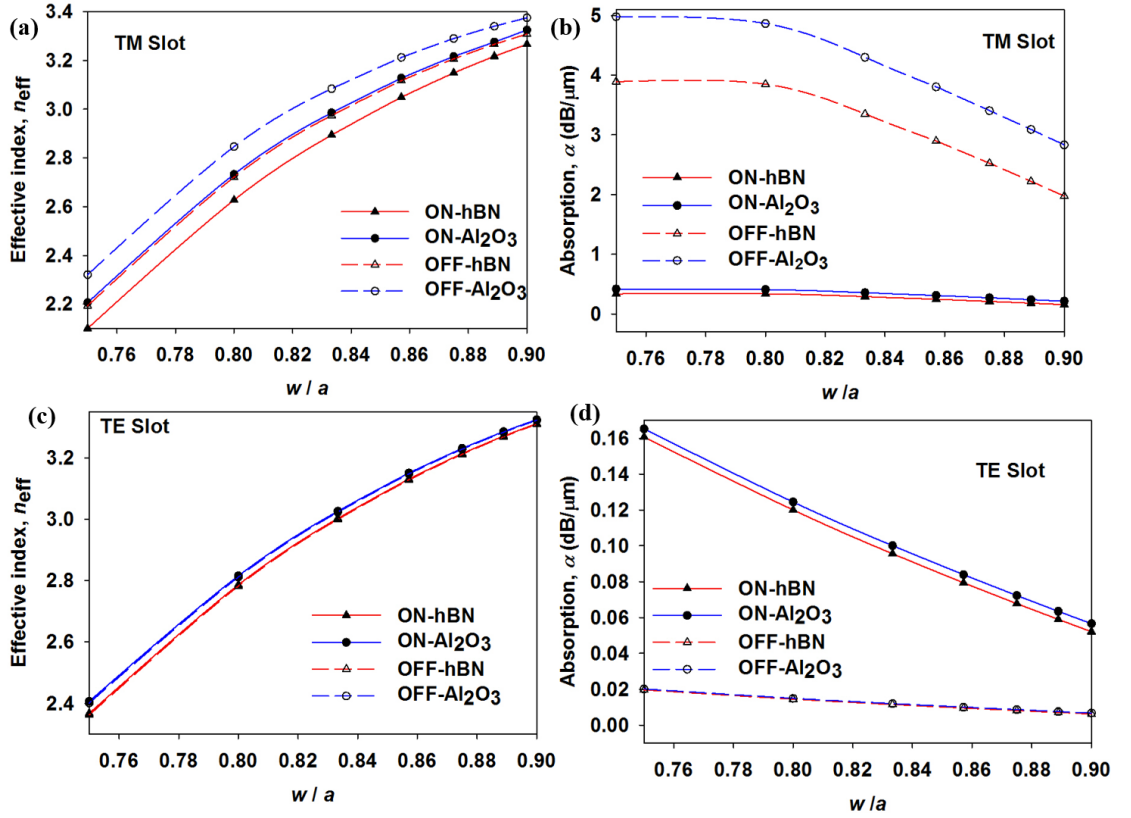


Figure 5.18: Mode effective index and absorption of TM and TE modes in a graphene-on-graphene slot waveguide. Plots (a) and (c) show the change of magnitude in real part of n_{eff} .

5.4 Characterisation of Trilayer Graphene-based Waveguides

Single layer graphene has shown a relatively small absorption of $\pi\alpha = 2.293\%$ of incident light [87, 116]. Many experimental and theoretical studies [6, 29] have proposed devices with graphene layer thickness as 0.7 nm, equivalent of bilayer graphene (BLG). Stacking of graphene layers plays an important role as the layers of graphene are shifted over the length of one C–C bonding with respect to the other. In BLG, Bernal stacking or AB is considered the most stable structure [117, 118].

In 2011, three groups have experimentally shown that ABC stacked trilayers are unique among multi-layers of graphene [81, 82, 119]. Zhang *et al.* [82] showed experimentally the quantum Hall effect in trilayer graphene. Shih *et al.* [119] demonstrated a solution-phase technique for producing large area trilayer graphene with controlled stacking. Wu [120] showed trilayer graphene with complex interlayer transitions have a rich electronic structure when compared to SLG and BLG. Sun *et al.* [121] have successfully synthesised large area of bi-, tri- and tetra-layers of graphene with Bernal stacking.

Very recently, Fan *et al.* [122] proposed a four-layer graphene electroabsorption modulator. Therefore, two- to four-layer thickness of graphene layers prove to be ideal for future electronic devices. Recently, few studies have considered thickness of graphene as 1 nm for their designs [123–125]. Simulation results are similar for graphene thickness 0.3 or 1 nm [126]. In this study, we have chosen thickness of graphene layers to be 1.12 nm [68] which is equivalent to a trilayer graphene (TLG) stack.

5.4.1 Top- and slot-graphene waveguides

We begin the study of trilayer graphene waveguides with a comparison between top and slot-layered graphene-based waveguides, which was earlier discussed in Section 5.2.2. We use similar waveguide designs as shown in Fig. 5.6, with thickness of graphene taken as 1.12 nm. Here, trilayer graphene is encapsulated with high-/low-index dielectric materials as shown in Fig. 5.19. We consider orientation is graphene as random but not confined to ABC or ABA stacking, which will be discussed in the next section.

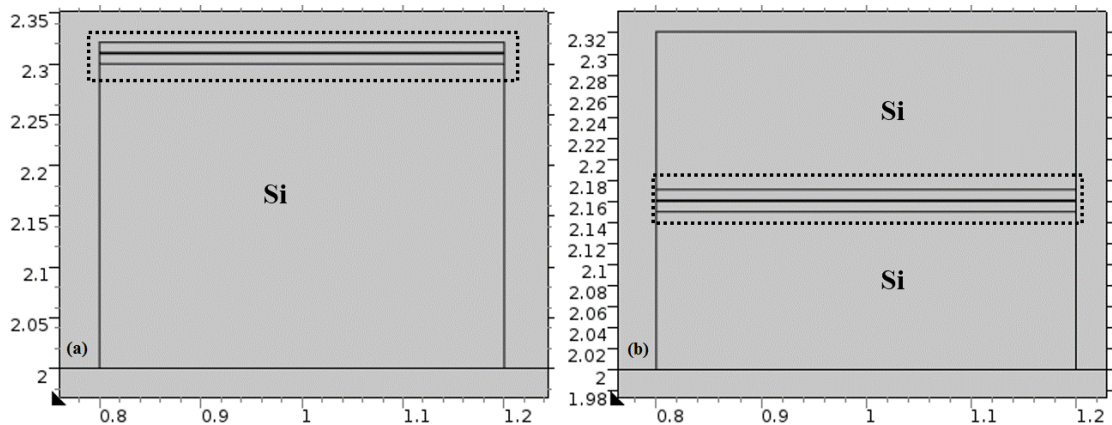


Figure 5.19: Top (a) and slot (b) waveguides with trilayer (1.12 nm) graphene, encapsulated with dielectric materials. Dotted lines indicate dielectric–graphene–dielectric stack.

In Section 5.2.2, we studied mode profiles of top *versus* slot-layered graphene waveguides, for $\mu = 0 - 1.0$ eV. In this section, we use the same waveguide designs but with trilayer graphene encapsulated with dielectric materials and calculate the mode effective index and absorption for $\mu = 0 - 2.0$ eV.

The Fermi level is extended to 2.0 eV (Fig. 5.20) to observe any distinct variations in n_{eff} and α beyond 1.0 eV. It is interesting to note that real and imaginary parts $\varepsilon(\omega)$ do not show any distinct variation beyond 1.0 eV, other than the dielectric to metallic transition stage at 0.4–0.53 eV. The dielectric layer thickness was kept constant at 10 nm.

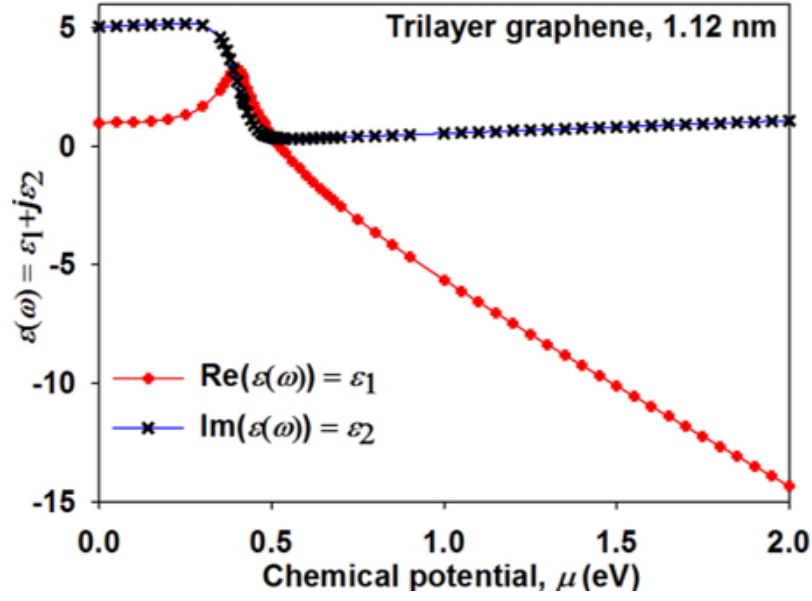


Figure 5.20: Complex dielectric constants of trilayer graphene for Fermi level up to 2.0 eV.

Width and height of the waveguide are 0.4 and 0.3 μm , respectively. Low-index dielectric is taken as $h\text{BN}$ with $\varepsilon = 3.9204$ whereas high-index dielectric is taken as Al_2O_3 with $\varepsilon = 9.1$.

5.4.1.1 Top layer graphene

Here, the dielectric–graphene–dielectric stack is placed as a layer on top of 0.3 μm thick silicon core as shown in Fig. 5.19(a)). In Section 5.2.2, we discussed the guided modes in a graphene layer on top of silicon with a buffer material (dielectric) in between. Now we are considering another dielectric film on top of graphene thus forming dielectric–graphene–dielectric stack. Figure 5.21 show plots obtained for effective index (n_{eff}) and absorption (α) as a function of chemical potential ($\mu = 0 - 2.0$ eV).

In the n_{eff} plot for TM (Fig. 5.21(a)), first peak occurs at 0.39 eV (2.804635), falls and next peak occurs at 0.53 eV (2.805636). Such a trend is observed in the graphene as top layer waveguide with only one dielectric material with first peak at 0.4 eV (2.515052) and next at 0.52 eV (2.514053) as shown in Fig. 5.7. We note that adding a dielectric layer on top of graphene shifts the high peak magnitude from first to second.

The TM mode profile in Fig. 5.22 shows a sharp peak at the dielectric–graphene interface due to enz effect. The waveguide is in OFF condition which occurs at $\mu = 0.5300$ eV with $\varepsilon(\omega) = -0.1099 + j0.3190$.

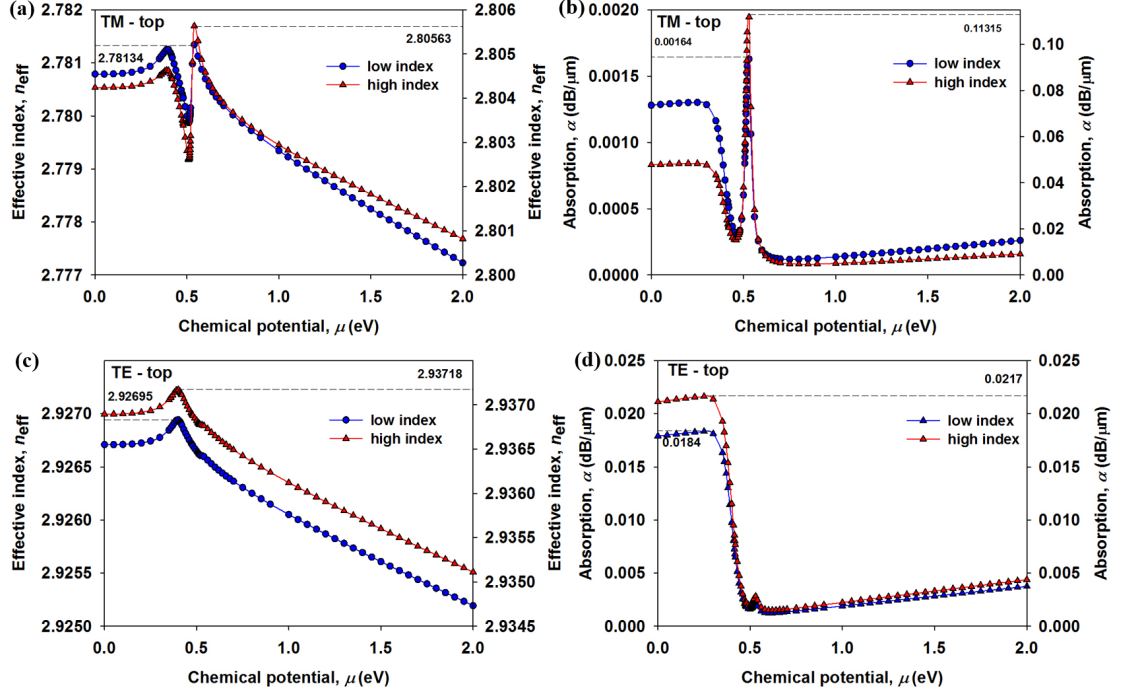


Figure 5.21: Waveguide with trilayer (1.12 nm) graphene as top layer. Plots (a) and (c) show variations of real part of n_{eff} as a function of chemical potential, μ .

5.4.1.2 Slot layer graphene

In this waveguide, trilayer graphene is placed as a horizontal slot layer in the core Si (Fig. 5.19(b)). Waveguide dimensions are as shown in Fig. 5.6(b). Figure 5.23 shows plots of n_{eff} and α for TM and TE modes of waveguide with trilayer graphene as slot layer.

TM mode absorption undergoes drastic rise, reaching up to 9.3 dB/ μm at $\mu = 0.53$ eV ($\varepsilon(\omega) = -0.1099 + j0.3190$). This rise is attributed to the *enz* effect as the magnitude of $\text{Re}(\varepsilon(\omega))$ approaches -0.1099 . For both TE and TM modes, the n_{eff} of the waveguide with high-index dielectric is larger than the one with low-index. In case of TM mode, n_{eff} shows a steady trend after the rise and fall at 0.53 eV, whereas for TE mode, n_{eff} steadily falls after the peak at 0.4 eV. Only absorption (α) shows a huge difference between TM and TE modes. Even with high-index dielectric ($\varepsilon(\text{Al}_2\text{O}_3)=9.1$), the TE mode absorption peaks only up to 0.11 dB/ μm even though the dielectric–graphene–dielectric stack is placed where there is maximum field intensity in the waveguide.

The TM mode profile and electric field intensity plots are shown in Fig. 5.24 which shows a strong peak in the graphene–dielectric interface. The waveguide with high-index dielectric achieves maximum absorption of 9.3 dB/ μm whereas the waveguide with low-index dielectric, the absorption is 6.4 dB/ μm .

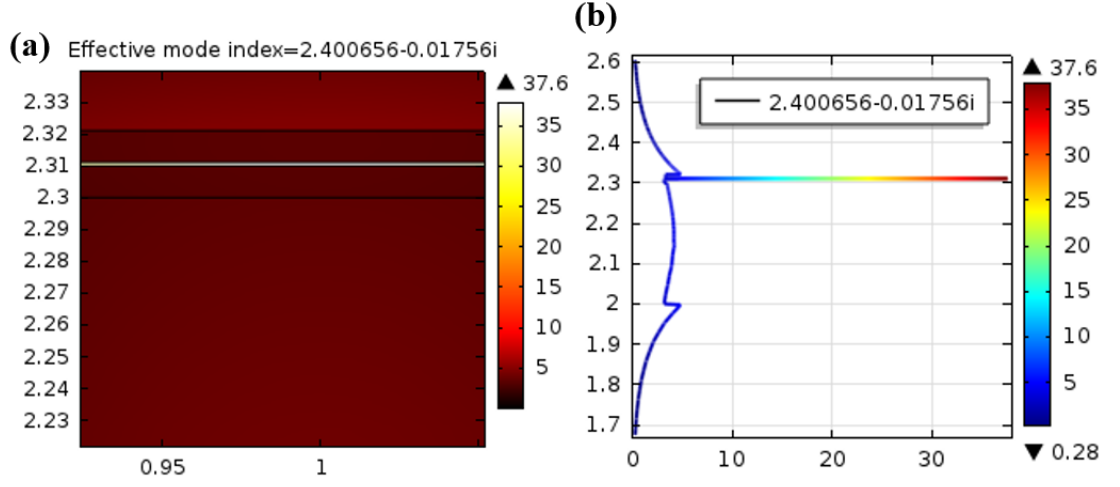


Figure 5.22: TM mode profile (a) and corresponding electric field, TM E_y (b) for trilayer graphene as top layer waveguide.

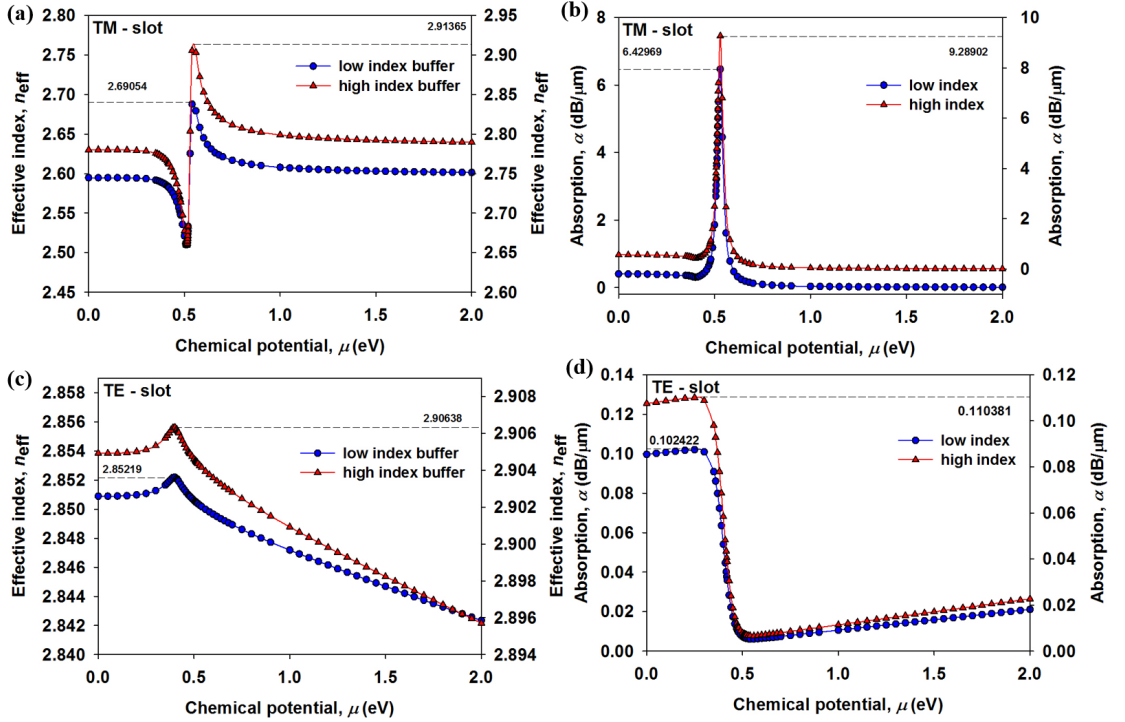


Figure 5.23: Slot waveguide with trilayer (1.12 nm) graphene. Plots (a) and (c) show variations of real part of n_{eff} as a function of chemical potential, μ .

5.4.1.3 Summary

We have now studied the modal properties of dielectric-encapsulated graphene stack, placed as top layer and as a slot layer in the waveguide. We infer that only TM mode shows a high absorption in a horizontal slot waveguide with dielectric-encapsulated graphene as slot layer. In terms of fabrication, the latter design is comparatively easier than the former. Graphene–dielectric stack as slot suffers from layer alignment. On the other hand,

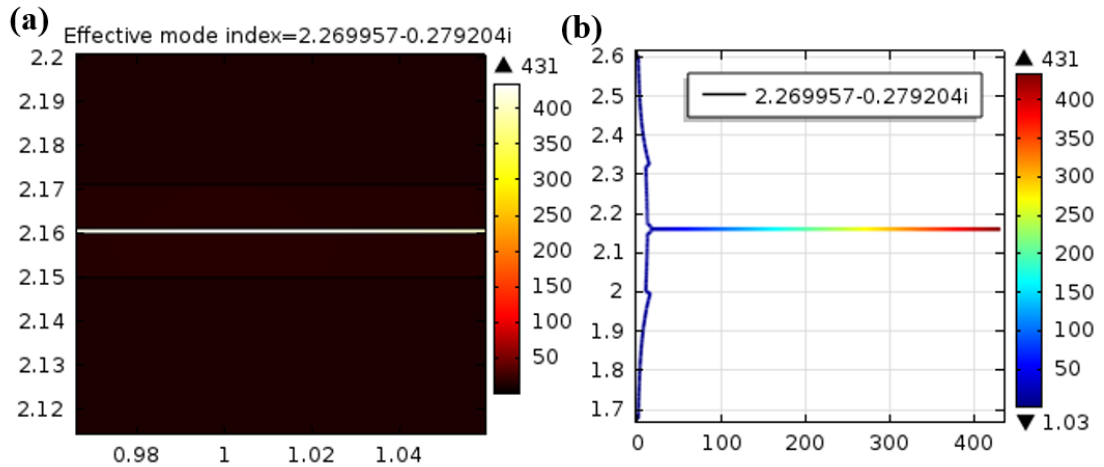


Figure 5.24: TM mode profile (a) and corresponding electric field, E_y (b) for trilayer graphene as slot layer waveguide.

graphene layers interact with maximum field intensity only when placed as a slot. This aspect is dealt in further sections and we suggest a dielectric material combination for improving TE mode absorption with graphene as top layer waveguides.

In case of effective index, the TE mode at graphene-as-top design with high-index dielectric is higher (2.93718) than that at graphene-as-slot design (2.90638). Only in terms of absorption, the latter design outperforms the former by several magnitudes. We observe that to improve modal properties in graphene-as-top layer design, it required a high-index dielectric encapsulated graphene layer placed on top of silicon.

5.4.2 ABA and ABC Stack Waveguides

Monolayer graphene is a honeycomb lattice of carbon atom with C-C bond distance 1.42 nm. Bilayer graphene is of AB or Bernal stacking with inter-layer spacing $d_0 \approx 0.334$ nm. In AB stacking, the atoms in top layer are shifted to one C-C bond distance with respect to the other. In case of trilayer graphene, similar trend is followed in ABC (rhombohedral) stacking. Here A, B and C refer to the first, second and third layers of graphene, respectively. In bi and trilayers, the inter-layer coupling leads to drastic changes in the electronic band structure of graphene. Section 3.2.3 explains the different stacking possibilities observed in bi and trilayers.

Bao *et al.* [127] have shown π -band dispersions for AAA, ABA and ABC stackings and suggest that mono- and bi-layer graphene are not suitable for electronic devices due to the absence of bandgap even under an applied electric field. Monolayer graphene has zero

density of states (DOS) at the Dirac point whereas trilayer has high density of states due to the formation of flat band at the K point near Fermi level.

In this section, after conducting a detailed study on waveguides with graphene-as-top and graphene-as-slot, we propose waveguide designs with suitable combination of dielectric materials for desired performance parameters such as extinction ratio (ER) and insertion loss (IL). So far we have presented results for graphene-based waveguides with low-index (h BN) and high-index (Al_2O_3) dielectric material combinations. Here we introduce another dielectric material, hafnium oxide (HfO_2), which is getting attention recently for use with graphene-based waveguides [128, 129]. Hafnium oxide is classified under materials with very high dielectric constant; $\varepsilon = 25$.

We carried out a brief study of two waveguides using HfO_2 as dielectric material. The objective of this study is to observe the TE (TE1, TE2, TE3) and TM (TM1, TM2, TM3) guided modes when increasing the width of the core from 0.4 to $2.0 \mu m$ at a constant height of $0.3 \mu m$. Here we studied only n_{eff} as optical mode absorption (α) is studied in further sections in detail. The results are presented as follows.

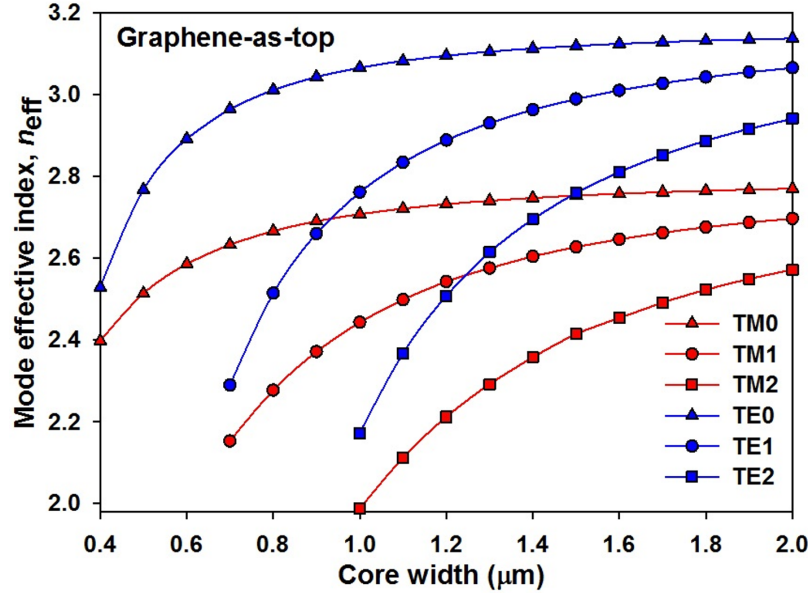


Figure 5.25: Effective refractive indices ($Re(n_{eff})$) of quasi-TE and quasi-TM modes of waveguide with HfO_2 -encapsulated trilayer graphene as top layer.

Figures 5.25 and 5.26 presents $Re(n_{eff})$ results of guided modes for waveguide with very high-index dielectric ($\varepsilon = 25$) encapsulating graphene as top layer and slot layer, respectively. Both TM and TE modes show similar increasing trend and after width $0.8 \mu m$ the increase is very minimal. This trend is different from the one observed for w/a

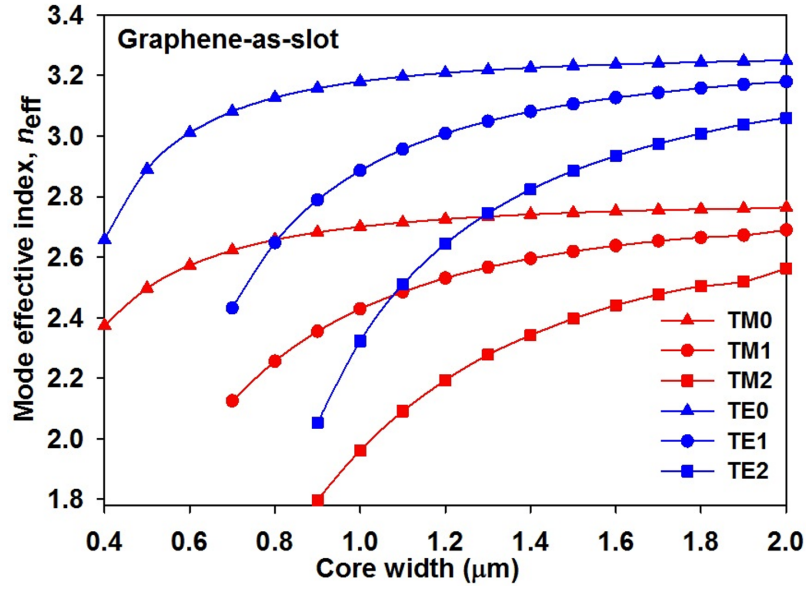


Figure 5.26: Effective refractive indices ($\text{Re}(n_{\text{eff}})$) of quasi-TE and quasi-TM modes of waveguide with HfO_2 -encapsulated trilayer graphene as slot layer.

ratio where the increase in n_{eff} was exponential since there is change in both width and height of the core.

5.4.2.1 Proposed waveguide designs

Figures 5.27(a) and (b) shows the waveguide designs proposed in this study. Dielectric-graphene-dielectric layers are denoted by $2t_D+t_G$ representing two dielectric layers encapsulating trilayer graphene. Sandwiching graphene within dielectric layers enables effective dielectric light confinement at nanoscale level and generate surface plasmons at the interface. In the energy bands of mono, bi and trilayers of graphene the conduction band (CB) and valence band (VB) meets at Dirac point. For bi and trilayers, a bandgap appears when applying gate voltage. The reason why we have chosen trilayer graphene in this study is that as monolayer graphene absorbs only 2.3% of incident light, so few layer graphene will be beneficial for electrooptic devices wherein absorption gains prominence.

Fabrication of both the proposed slot- and top-layer graphene waveguides is comparatively easier as it starts with conventional silicon-on-insulator pattern. Production of large area trilayer graphene with controlled stacking is discussed by Shih *et al.* [119]. Very recently, Sugawara *et al.* [130] has demonstrated selective fabrication of ABA and ABC stacking of trilayer graphene. hBN-graphene sheets are obtained through a two-step chemical vapour deposition (CVD) process [131]. Deposition of Al_2O_3 is carried out using ALD technique [114]. Formation of hafnium oxide-graphene hybrid was discussed by Ansell *et*

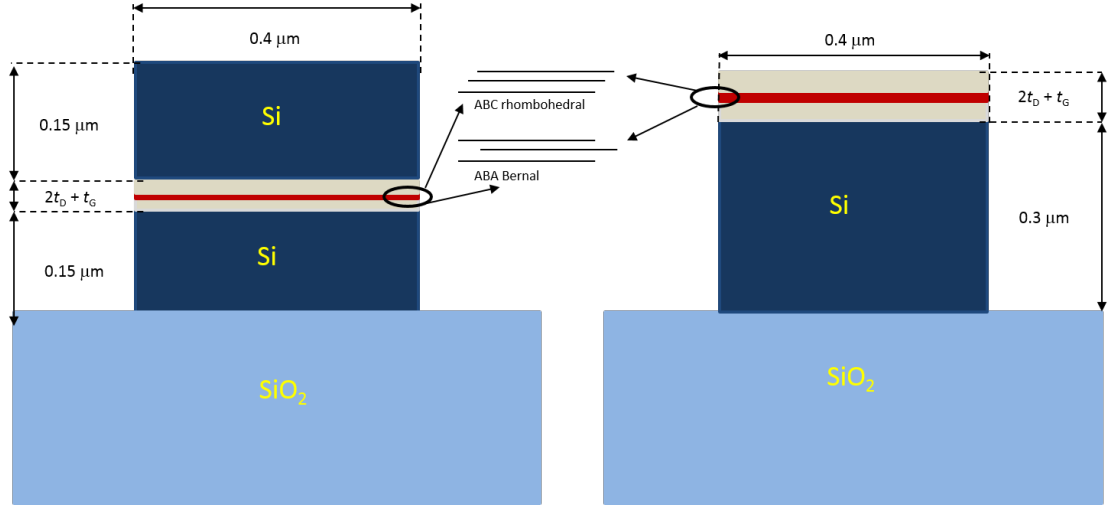


Figure 5.27: Proposed designs for trilayer graphene with ABA Bernal and ABC rhombohedral stacking order in as a dielectric-encapsulated layer placed as slot (a) and as top (b); t_D , thickness of dielectric layer; t_G , thickness of graphene.

al. [128]. Currently, various fabrication techniques are available so our designs have high degree of fabrication possibilities [114, 128].

5.4.2.2 Results and Discussion

Figures 5.28 and 5.29 show effective index and absorption plots for TE and TM modes of top- and slot-graphene (trilayer) waveguides. Here the thickness of dielectric is fixed as 10 nm throughout the study. The mode effective index follows similar trend in both designs with a peak at 0.5 eV which is clearly seen in slot-graphene ($n_{\text{eff}} = 2.55$) waveguide but a slight increase in top-graphene ($n_{\text{eff}} = 2.41$) waveguide, in case of HfO_2 buffer. This is due to 0.15 μm silicon encapsulating the graphene–dielectric sandwich in the former. On the other hand, in slot-graphene, optical absorption shows a distinct peak (12.5 dB/ μm) for HfO_2 . Whereas, for top-graphene, it reads a meagre 0.6 dB/ μm even with a very high-index dielectric such as HfO_2 ($\epsilon = 25$). This is due to the fact that, in slot design, graphene is placed at the centre of the waveguide. Many studies proposed slot waveguide placing graphene at the location of maximum light intensity [6, 105, 132].

Dielectric constants of materials used for above plots are as follows: $\epsilon(\text{hBN}) = 3.9204$; $\epsilon(\text{Al}_2\text{O}_3) = 9.1$; $\epsilon(\text{HfO}_2) = 25$. TM effective index in (a) of both figures show a significant difference in n_{eff} of very high-index dielectric. TE mode absorption in (d) of both figures, the waveguide with very high index dielectric is significantly ahead in the top-layer waveguide than that of the slot-layer. This suggests the point which we put forward for

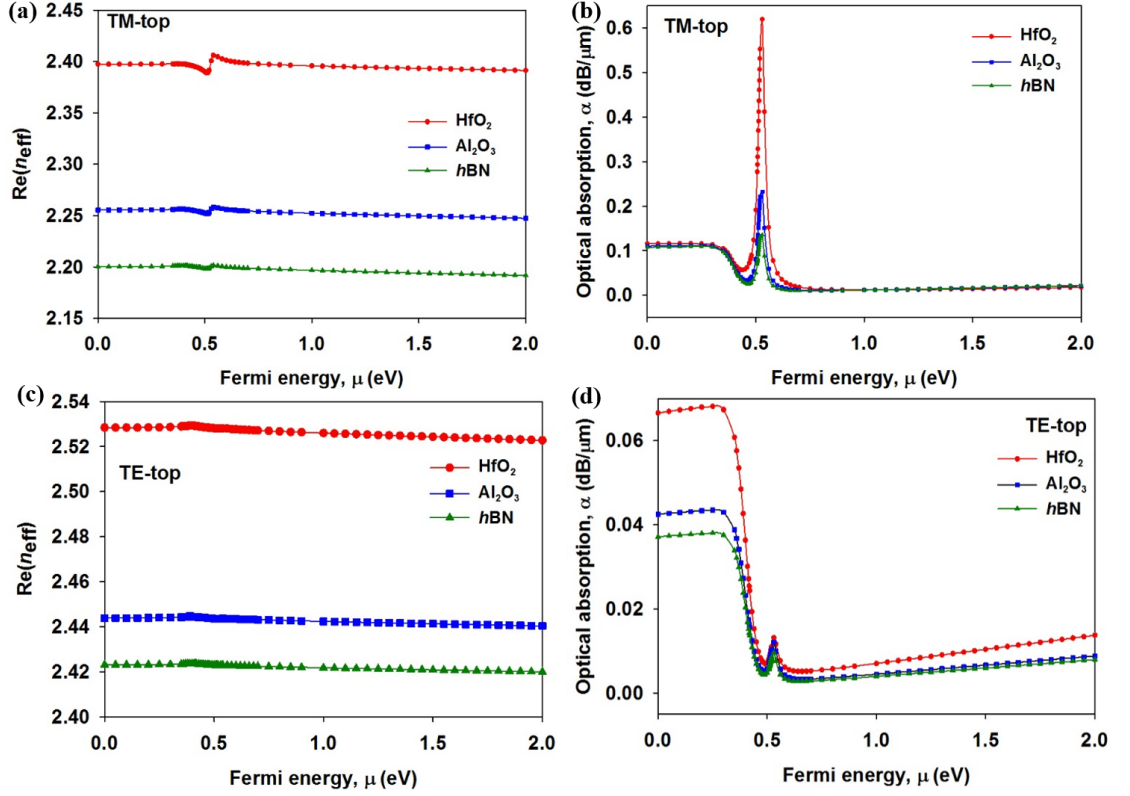


Figure 5.28: TE and TM mode effective index and optical absorption of waveguide with graphene–dielectric stack as top layer.

graphene–dielectric stack as top layer that TE mode can be enhanced to a good extent with HfO₂–graphene–HfO₂ combination on top of silicon core.

Designs proposed by Phatak *et al.* [96] and Liu *et al.* [114] have graphene as top layer. In the former study, their design involves two graphene layers separated by Al₂O₃ which involves removal of buried oxide (BOX) through hydrogen fluoride (HF) etching. This design deliver a bulk waveguide with complex fabrication steps. Therefore, in this study, we adopted a pattern of high-index dielectric (HfO₂) and trilayer graphene in our designs which is relatively simple and straightforward. By varying the dielectric layer thickness, we have shown ways to enhance TE mode absorption which is lagging in their designs.

Mode profile in Fig. 5.30(c) show the mode shifts towards graphene–dielectric stack which enhances the TE mode absorption. Our design, with HfO₂ as dielectric of thickness 50 nm achieves a TE absorption of 0.18 μm which was only 0.14 μm in Ref. [96] with complex design process. Recently, Aznakayeva *et al.* [129] proposed low voltage modulators using graphene and hafnium oxide. So, in this study, we aim to propose simple designs for graphene as slot and top layer designs and deliver ways to tune performance parameters

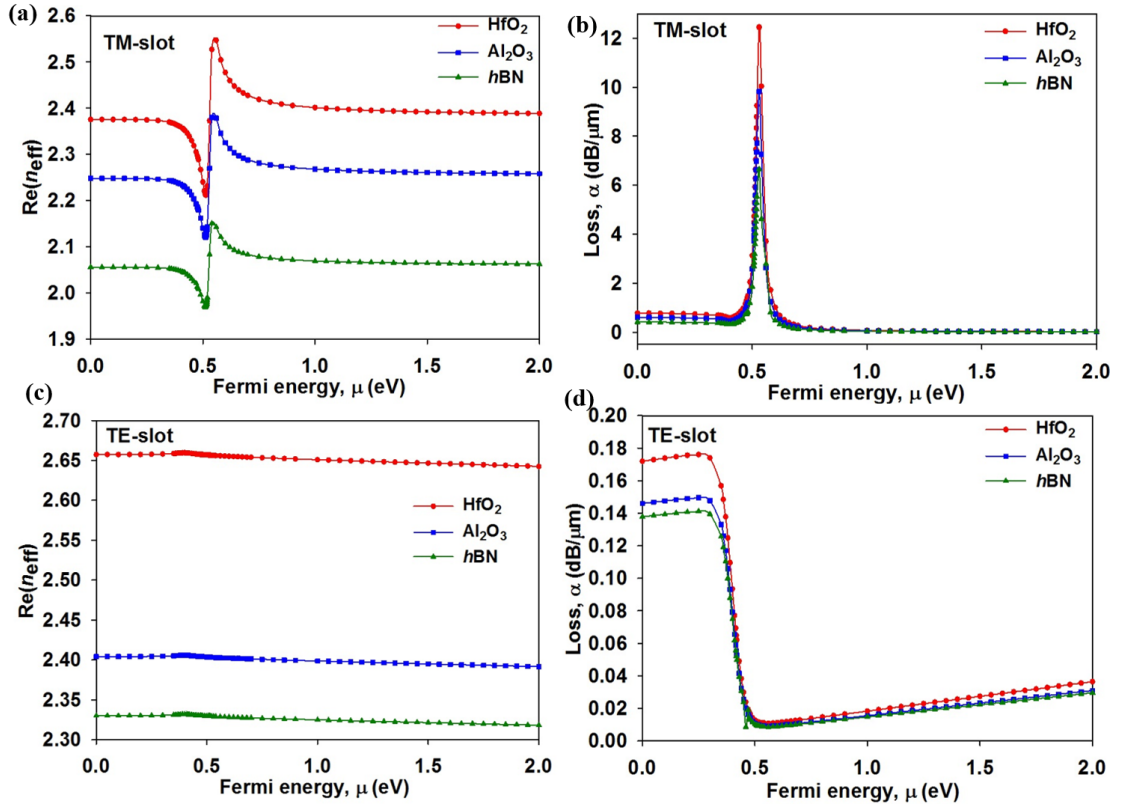


Figure 5.29: TE and TM mode effective index and optical absorption of waveguide with dielectric-graphene-dielectric stack as slot layer.

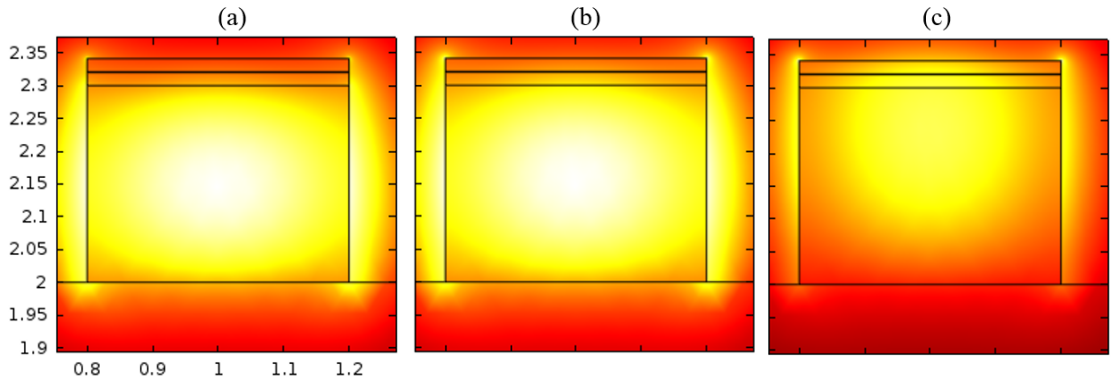


Figure 5.30: Mode profiles of dielectric-encapsulated trilayer graphene waveguide: (a) hBN ; (b) Al_2O_3 ; (c) HfO_2 . In (c) mode moves towards the graphene-dielectric stack.

by varying thickness of different dielectric materials with low- (hBN), high- (Al_2O_3) and very high-index (HfO_2). Steps for fabrication can be taken from experimental studies [81, 82, 114, 120].

We now present and discuss the results obtained for varying dielectric layer thickness (t_D) encapsulating the graphene layers and the variations as a function of change in wavelength (λ). Performance parameters such as extinction ratio (ER) and insertion loss (IL) of two proposed waveguides (slot-graphene and top-graphene) are discussed in this section.

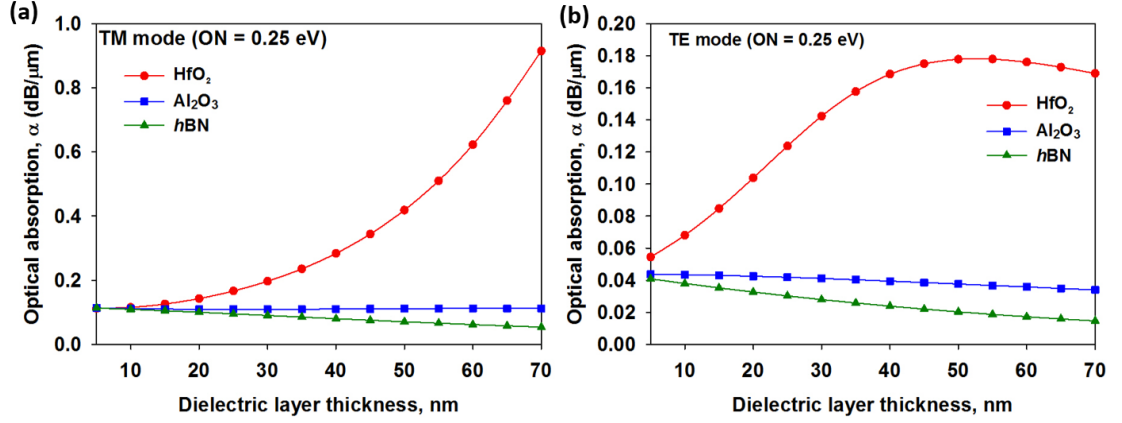


Figure 5.31: TM (a) and TE (b) mode optical absorption for varying dielectric thickness in a graphene-as-top layer waveguide.

Figure 5.31 shows optical absorption of top-graphene waveguide at $\mu = 0.25$ eV, which refers to ON voltage; $\varepsilon(\omega) = 1.3335 + j5.1690$. In both TM and TE plots, high-index dielectric shows significant rise when compared to the other two. The reason is attributed to the very high dielectric constant of HfO_2 . Waveguide with HfO_2 shows a peak absorption of $\alpha = 0.18$ dB/ μm within $t_D = 50$ – 55 nm range. This design shows a good enhancement of TE mode from the absorption of $\alpha = 0.14$ dB/ μm shown in Ref. [96]. Therefore, we propose, for a top-graphene waveguide, a high-index buffer with trilayer graphene is a suitable combination. A combination of trilayer graphene and high-index buffer proves to be a potential design for electro-optic modulation especially for low power consumption applications [129].

Next we analyse the broadband response of the waveguide and the results are shown in Fig. 5.32. Operation wavelength range is another important parameter of a modulator. Modulators are expected to operate in three major telecom windows viz., 0.85, 1.3 and 1.5 μm . Our plots have covered the wavelength from 1.3 to 1.7 μm .

Both designs show a peak at $\lambda = 1550$ nm which is in accordance with results in Ref. [6]. In top-graphene design, the TM mode absorption of high-index dielectric with $\alpha = 0.62$ dB/ μm significantly outperforms other two ($\alpha = 0.2$ dB/ μm and $\alpha = 0.1$ dB/ μm for Al_2O_3 and $h\text{BN}$, respectively). In slot-graphene waveguide, peak absorption reaching 12 dB/ μm was achieved by high-index dielectric. This is attributed to the fact that the graphene–dielectric stack is positioned at the maximum field intensity region in the waveguide. Therefore, using a high-index dielectric as buffer layer between graphene and silicon results in a very high absorption waveguide. In Fig. 5.32, the dielectric layer thickness is

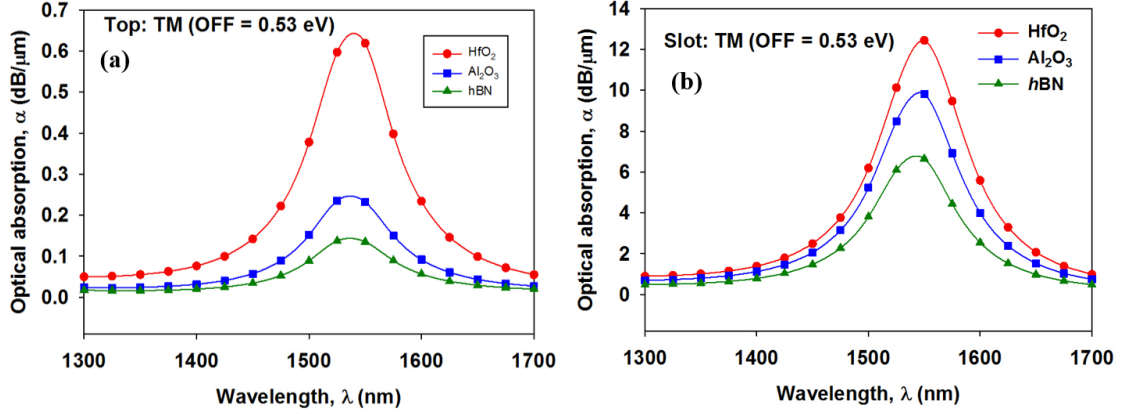


Figure 5.32: Optical absorption for TM modes of top-graphene (a) and slot-graphene (b) waveguides; $\mu = 0.53$ eV.

taken as 10 nm throughout.

Most experimental studies [114,115] have proposed waveguide designs with graphene as top layer, as it has high fabrication possibilities. In line with their results, here we propose a simple design using trilayer graphene (1.12 nm) and high-index dielectric (HfO₂, $\epsilon = 25$) combination that enhances the TE and TM mode confinements. Top-graphene achieves $n_{\text{eff}} = 2.868$ which is higher than that of a TE rib (2.798) and TM rib (2.530) designs in Ref. [96].

Broadband response of top- and slot-graphene waveguides at $\mu = 0.4$ eV are shown in Fig. 5.33. Mode effective index has shown a steady decrease for increasing wavelength in both waveguides. In slot-graphene, low- and high-index dielectrics have a high effective index of 2.38 and 2.60, respectively. Whereas in top-graphene, both have 2.60 and 2.63, respectively. Large variation in slot design is due to the reason that dielectric-graphene-dielectric layers are in the region with maximum light intensity. So the influence of dielectric layers on waveguide performance is more in slot-graphene when compared to top-graphene design. This imposes a thickness limitation of dielectric layers in slot waveguides wherein bilayer graphene layers are separated with a dielectric [6, 103] because it leads to increase in capacitance which degrades mode propagation.

The performance parameters such as insertion loss (IL) and extinction ratio (ER) are calculated as follows:

$$IL = -10\log_{10}(T_{\text{max}}) \quad ER = 10\log_{10}\left(\frac{T_{\text{max}}}{T_{\text{min}}}\right) \quad (5.2)$$

ER is obtained for both designs between the major telecom windows, 1.3–1.7 μm . The

5.4. Characterisation of Trilayer Graphene-based Waveguides

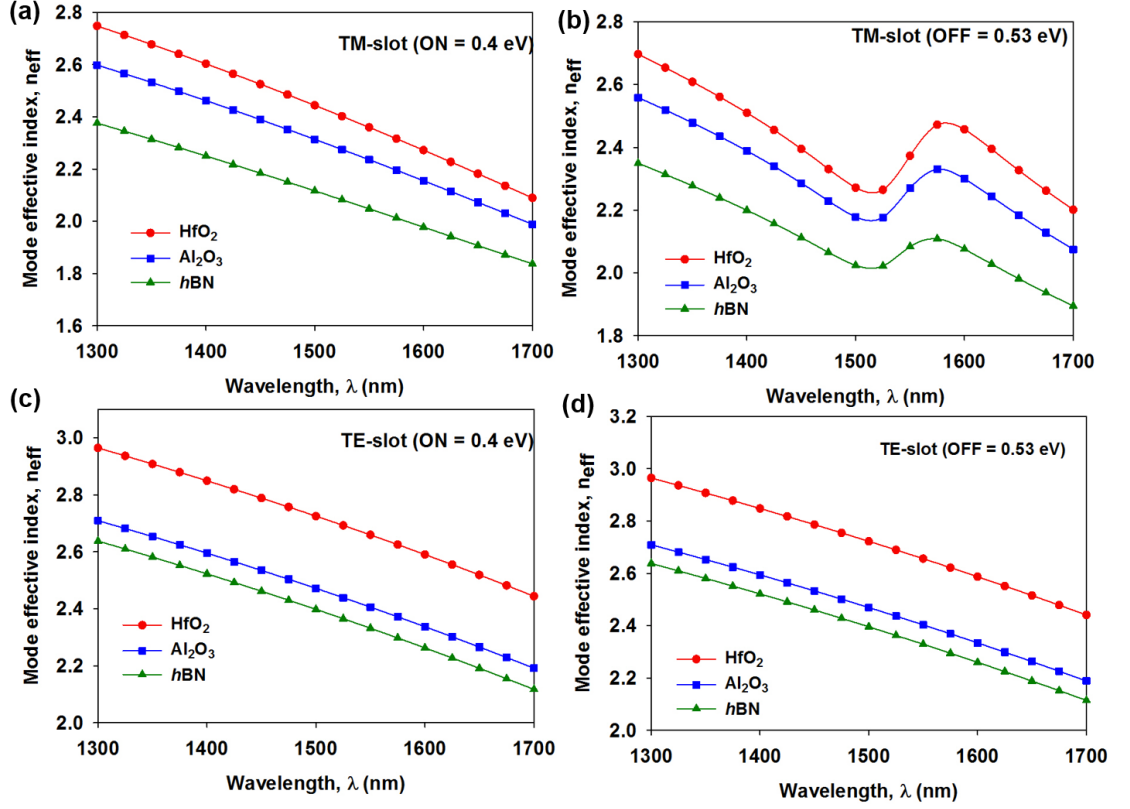


Figure 5.33: TE and TM mode effective index of graphene-slot waveguide for varying wavelength (λ): ON, 0.4 eV (a, c); OFF, 0.53 eV (b, d).

formula for ER is explained as below:

$$ER = 10 \log_{10} \left(\frac{T_{\text{max}}}{T_{\text{min}}} \right) = 10 \log_{10} \left(\frac{\exp^{-4\pi\alpha_{\text{ON}} L}}{\exp^{-4\pi\alpha_{\text{OFF}} L}} \right)$$

where α_{ON} and α_{OFF} denote the imaginary parts of n_{eff} at ON and OFF states of the waveguide, respectively, and L the length of graphene sheet.

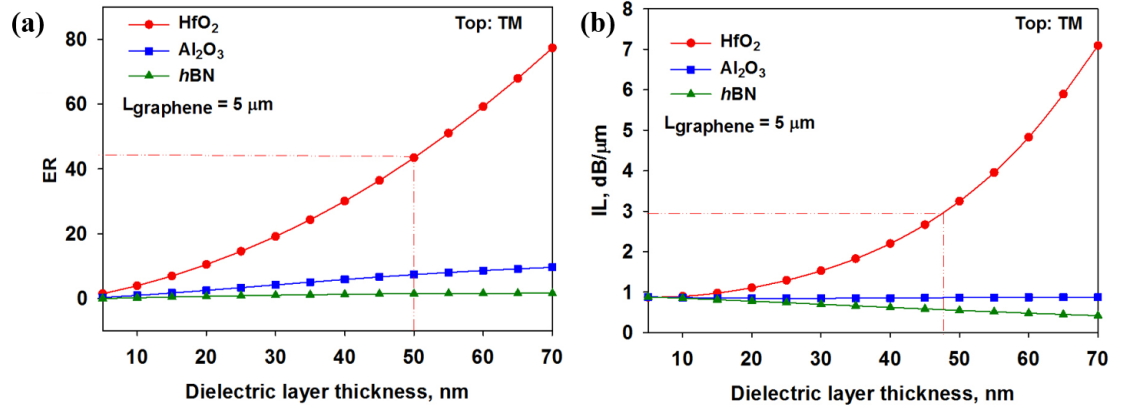


Figure 5.34: Top-graphene: TM mode (a) extinction ratio and (b) insertion loss for varying dielectric layer thickness.

Next, the influence of dielectric layer thickness ($t_{\text{D}} = 5 - 70 \text{ nm}$) on ER and IL is stud-

ied. Figure 5.34(a) and (b) show ER and IL for graphene as top layer design, respectively. Length of graphene active layer is taken as $5 \mu\text{m}$. Design with very high-index has shown a steady increase in both designs whereas high- and low-index have shown a steady decrease apart from ER. Therefore, by controlling the thickness of dielectric layers, desired waveguide performance can be achieved, say ER 40–60 dB and IL 2–3 dB/ μm . Broken marked lines in those figures show optimum ER and IL that can be obtained using high-index dielectric. This is very important as using high-index dielectric such as HfO_2 can be used for modulation around 1 V [128]. In case of high- and low-index, ER and IL variation is modest up to a thickness of 40 nm. Even after, up to 70 nm, both dielectrics vary in performance slightly. Therefore, in case of top-graphene design, the influence of high- or low-index on propagation is only minimal. This leads to the need of very high-index dielectric material to encapsulate graphene in a top-graphene design.

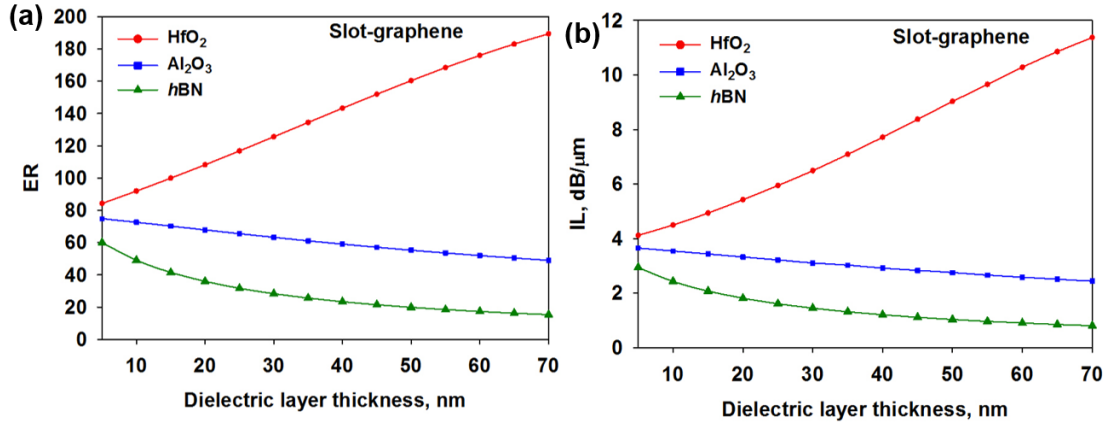


Figure 5.35: Slot-graphene: Extinction ratio (a) and insertion loss (b) for varying dielectric thickness.

Figure 5.35(a) and (b), respectively, show ER and IL for varying t_D from 5 to 70 nm. Very high-index has shown a sharp increase from 5 nm thickness whereas high- and low-index have shown a steady decrease. Also, the ER and IL variations for high- and low-index are placed apart. This proves the influence of dielectric layer being more in slot-graphene when compared to top-graphene design. Therefore, using a very high-index, $t_D = 5 \text{ nm}$ will achieve a high ER of 80 dB. On the other hand, high- and low-index dielectric materials provide optimum ER and IL within the range 20–70 and 3–4 dB/ μm , respectively. Based on these results, we infer that very high-index dielectric materials are not suitable for slot-graphene design. Also, using our results, we can ascertain the optimum dielectric thickness needed for high- and low-index to achieve desired performance that can be decided for top-

graphene and slot-graphene waveguides.

5.5 Summary

In this chapter, we presented a detailed analysis of tasks carried out in this study of graphene–silicon hybrid waveguides. Starting with characterization of silicon nanowires, we analysed the optimum dimensions of silicon on insulator will be height 0.3 nm and width 0.4 nm. Position of graphene layer in the waveguide is crucial for performance, so two designs (top- and slot-layer graphene) were studied. Then we moved on to the study of importance of dielectric layer encapsulating graphene. We observed the minute variations in mode effective index (n_{eff}) and absorption (α) with respect to low- and high-index dielectric materials.

We proposed two waveguide designs based on these results. We characterised the designs we proposed and found suitable dielectric–graphene combinations for graphene-as-top layer and graphene-as-slot layer waveguides. Our results were based on recent experimental findings on trilayer graphene [119, 120, 128, 130, 131] and the fabrication possibilities of proposed waveguide designs are straightforward.

Chapter 6

Conclusions and Suggestions for Future Research

6.1 Conclusions

In the last few decades, a new frontier has emerged in the field of optoelectronics. The advent of 1D and 2D materials such as carbon nanotubes and graphene [67] has resulted in a wide range of applications hybridising them with existing designs, for instance, optoelectronic modulators [20, 114]. Graphene is expected to play a major role in silicon nanophotonics reducing costs significantly and in increasing the communication bandwidth. Its inherent switching ability as a function of varying gate voltage makes graphene a potential material in the field of optoelectronics. Owing to its thickness (monolayer, 0.4 nm; bilayer, 0.69 nm; trilayer, 1.12 nm) [68], graphene is not a stand-alone material. Therefore, the remarkable optical properties of graphene can be utilized by integrating it with existing silicon (Si) waveguides by forming a hybrid structure.

The objectives of this study is to design and characterise graphene-based hybrid waveguides using Finite Element Method. The objectives outlined in this thesis have been successfully accomplished and a detailed analysis of waveguide designs undertaken for this study are presented. We focussed on the study of influence of dielectric materials encapsulating graphene layers in the waveguide. The positioning of this dielectric-graphene-dielectric stack is of prime importance as graphene is an active layer in the electro-optic modulation process. Benchmarking is an essential task in research as it is necessary to validate our method with published results. Theoretical and experimental studies [6, 20, 29] were chosen and using our models and understanding, we obtained their results through our mode solvers viz., complex and perturbation.

In Chapter 1, the recent trends in nanophotonics and fundamentals behind light wave propagation are explained. Thin film fabrication methods and processes involved are explained in detail. Mechanism of modulation is given a brief introduction. Study of experimental methods helped us in designing waveguides with high degree of fabrication possibilities. The designs we proposed at the end of this study are CMOS compatible and can be effectively integrated with on-chip optical interconnects. Study of waveguides is the primary objective of this research. So, in Chapter 2, we provided the fundamentals behind light-matter interaction and types of waveguides such as planar, slab and rib. Plasmonic waveguides are given a brief introduction. This thesis is based on Finite element method [45].

Graphene is a wonder material which has an inherent ability of tuning the Fermi level by applying a gate voltage. This phenomena makes graphene a unique material for designing electro-optic modulators. The speed of modulation is in picoseconds timescale [20]. Therefore a detailed study of physical, electrical and optical properties of graphene is given in Chapter 3. Graphene possesses a complex conductivity ($\sigma(\omega) = \sigma_1 + j\sigma_2$) which is used to derive the complex dielectric constant ($\varepsilon(\omega) = \varepsilon_1 + j\varepsilon_2$) values as a function of Fermi level or chemical potential (μ). The *enz* effect in graphene causes rapid rise in absorption of TM mode between 0.4 and 0.55 eV; for example, in a bilayer graphene of thickness 0.69 nm, $\varepsilon(0.51 \text{ eV}) = -0.0839 + j0.5728$. The thickness- and wavelength-dependent $\varepsilon(\omega)$ are calculated.

Dielectric constants of graphene depend on thickness of graphene layer (t_g), chemical potential (μ) and wavelength (λ). Therefore, a detailed study on physical properties of mono-, bi- and trilayers of graphene and the electronic band structure are discussed in Chapter 3. Optical conductivity ($\sigma(\omega)$) and electrical permittivity ($\varepsilon(\omega)$) are complex quantities in graphene. So the interband and intraband transitions are presented in this chapter. Our analytical method derived for calculating $\varepsilon(\omega)$ was benchmarked with three studies [6, 28, 29] which proved the validity and accuracy of our derived method. Through the MATLAB code written for the derivation, we obtained $\varepsilon_1 + j\varepsilon_2$ for 55 discrete voltage levels from 0 to 1.0 eV and further extended up to 2.0 eV.

Benchmarking task was carried out for validating and improving our perturbation and complex mode solvers. Limitations are identified for both codes. In Chapter 4,

we have presented our results of benchmarking with three published studies [6, 20, 29]. We successfully benchmarked the effective index (n_{eff}), absorption (α) and electric field intensity plots using our in-house solvers as well as COMSOL. The aspect of benchmarking helped us validate and improve our understanding before proposing new waveguide designs in line with fabrication possibilities.

We proposed two novel waveguide designs for electro-absorption modulator that forms a hybrid structure of graphene and silicon. We observed that the positioning of graphene sheets as well as the layer thickness plays a vital role in influencing the modal properties of the waveguide. Our results of performance parameters such as ER and IL will help designing waveguides for required applications. We finally proposed a combination of high-index dielectric encapsulated graphene for waveguides with graphene as top layer. For waveguides with graphene as slot layer, reduced thickness, say 5 nm, of high-dielectric material yield good results.

6.2 Suggestions for Future Research

- a) Benchmarking task exposed the limitations in our perturbation and complex mode solvers. Results from our codes indicated a close agreement with published studies. For accurate determination of modal properties, the perturbation code has to be debugged to be able to handle $\varepsilon(\omega)$ values with real part (ε_1) smaller than the imaginary part (ε_2).
- b) Complex code, even though it can handle any values of $\varepsilon(\omega)$, it needs to be improved further so that it accommodates mesh dimensions beyond 110×110 . The ability to handle mesh dimension of at least 500×500 is required using complex code.
- c) Computation time is another factor noticed while using our codes but it can be overcome by using latest versions of computers with at least 16GB RAM. Even then, both codes need to be debugged for reducing computation time when studying bulk waveguides of more than three layers.
- d) Graphene-based waveguides rely on light-graphene interaction so efficient designs are required that would position graphene stack in the field of maximum intensity.
- e) Through our findings, it is shown how dielectric materials with graphene influence

6.2. Suggestions for Future Research

modal properties of the waveguide. Now we have a range of 2D materials such as phosphorene, TMDs, silicene, etc. which can be integrated with graphene to enhance performance. Graphene–polymer combination is also a prospective combination for high speed electro-absorption modulators.

Appendix A

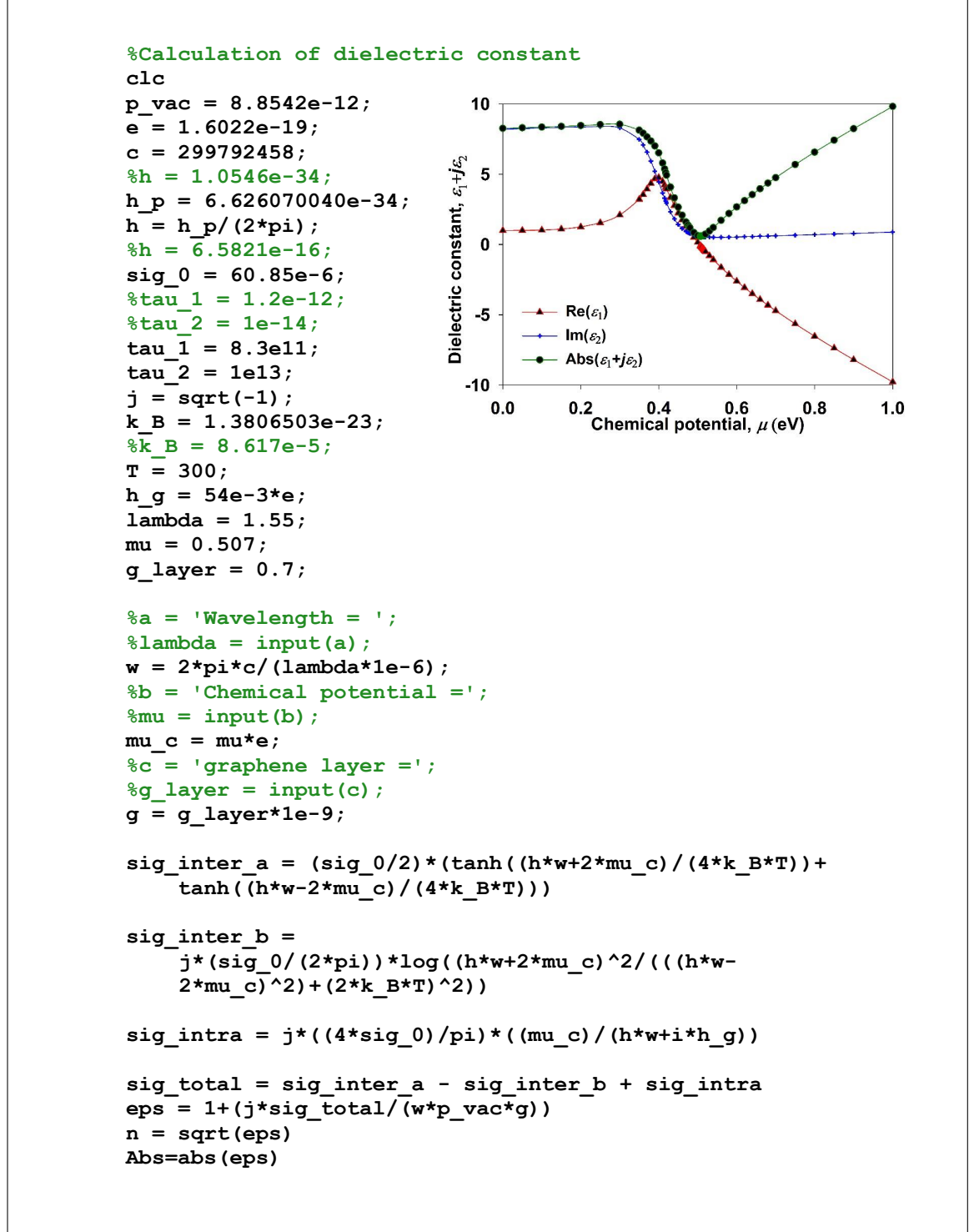
To calculate complex $\varepsilon(\omega)$ of graphene

Section 3.5.1 explains the analytical method we adopted for calculating the complex dielectric constants of graphene, $\varepsilon(\omega) = \varepsilon_1 + j\varepsilon_2$. From equation 3.69, it is noted that $\varepsilon(\omega)$ depends on wavelength (λ) and thickness of graphene layers. Figures 3.24 and 3.26 show the variations in values of $\varepsilon(\omega)$ as a function of thickness of graphene layers and wavelength, respectively. Table A.1 lists the complex $\varepsilon(\omega)$ values obtained using our MATLAB code shown in Box A.1.

μ (eV)	Re $\varepsilon(\omega)$	Im $\varepsilon(\omega)$	μ (eV)	Re $\varepsilon(\omega)$	Im $\varepsilon(\omega)$	μ (eV)	Re $\varepsilon(\omega)$	Im $\varepsilon(\omega)$
0	0.9946	8.1958	0.44	2.7704	1.8213	0.517	-0.4063	0.5409
0.05	0.9993	8.2397	0.45	2.2358	1.4276	0.518	-0.4376	0.5384
0.1	1.0245	8.2834	0.46	1.7479	1.1346	0.519	-0.4688	0.5362
0.15	1.0954	8.3268	0.47	1.3016	0.9234	0.52	-0.4998	0.534
0.2	1.2476	8.3676	0.475	1.0921	0.8425	0.53	-0.8016	0.5179
0.25	1.5413	8.3903	0.478	0.9703	0.8006	0.54	-1.09	0.5096
0.3	2.0973	8.2907	0.48	0.8906	0.7752	0.56	-1.6329	0.5077
0.35	3.2126	7.4656	0.49	0.5093	0.6737	0.58	-2.139	0.5162
0.36	3.5534	7.0707	0.5	0.1528	0.6058	0.6	-2.6158	0.5296
0.37	3.9392	6.5616	0.507	-0.0839	0.5728	0.62	-3.0687	0.5452
0.38	4.3438	5.9377	0.508	-0.1169	0.5689	0.64	-3.5019	0.5619
0.39	4.6763	5.2183	0.509	-0.1498	0.5651	0.66	-3.9185	0.579
0.4	4.7592	4.4441	0.51	-0.1825	0.5616	0.68	-4.321	0.5963
0.41	4.4779	3.6702	0.512	-0.2473	0.5549	0.7	-4.7114	0.6138
0.415	4.2318	3.301	0.513	-0.2794	0.5518	0.75	-5.6443	0.6576
0.418	4.0652	3.0887	0.514	-0.3114	0.5489	0.8	-6.5292	0.7014
0.42	3.9492	2.9517	0.515	-0.3432	0.5461	0.85	-7.3782	0.7452
0.43	3.3501	2.3291	0.516	-0.3748	0.5434	0.9	-8.1992	0.7891
						1	-9.7791	0.8767

Table A.1: Complex dielectric constant values, $\varepsilon(\omega) = \varepsilon_1 + j\varepsilon_2$, for $\mu = 0 - 1.0$ eV.

The interactive MATLAB code written for calculating these complex values of $\varepsilon(\omega)$ are given as follows:



Box A.1: Code for deriving complex values of $\varepsilon(\omega)$. Inset shows the plot obtained for $\varepsilon(\omega)$ varying within the voltage range, $\mu = 0 - 1.0$ eV

Bibliography

- [1] C. Mensink. (2018, March) Wireless power and data over inductive links: The technology for real ulp devices. Ansem. [Online]. Available: www.ulpc.nl/wp-content/uploads/2018/03/Clemens-Mensink_2
- [2] J. D. Joannopoulos, S. G. Johnson, J. N. Winn, and R. D. Meade, *Photonic Crystals: Molding the Flow of Light*. Princeton university press, 2008. 5, 8
- [3] K. S. Novoselov, A. K. Geim, S. V. Morozov, D. Jiang, Y. Zhang, S. V. Dubonos, I. V. Grigorieva, and A. A. Firsov, “Electric field effect in atomically thin carbon films,” *Science*, vol. 306, no. 5696, pp. 666–669, 2004. 6, 66, 89
- [4] H. Liu, A. T. Neal, Z. Zhu, Z. Luo, X. Xu, D. Tománek, and P. D. Ye, “Phosphorene: an unexplored 2d semiconductor with a high hole mobility,” *ACS Nano*, vol. 8, no. 4, pp. 4033–4041, 2014. 6
- [5] P. Vogt, P. De Padova, C. Quaresima, J. Avila, E. Frantzeskakis, M. C. Asensio, A. Resta, B. Ealet, and G. Le Lay, “Silicene: compelling experimental evidence for graphenelike two-dimensional silicon,” *Physical Review Letters*, vol. 108, no. 15, p. 155501, 2012. 6
- [6] J. Gosciniak and D. T. Tan, “Theoretical investigation of graphene-based photonic modulators,” *Scientific Reports*, vol. 3, p. 1897, 2013. 6, 26, 68, 85, 87, 88, 89, 90, 91, 94, 95, 96, 103, 104, 105, 106, 107, 108, 109, 122, 123, 124, 130, 131, 136, 137, 145, 148, 149, 153, 154, 155
- [7] S. Vijay, T. H. Hsieh, and L. Fu, “Majorana fermion surface code for universal quantum computation,” *Physical Review X*, vol. 5, no. 4, p. 041038, 2015. 6
- [8] Y.-F. Zhou, Z. Hou, Y.-T. Zhang, and Q.-F. Sun, “Chiral majorana fermion modes regulated by a scanning tunneling microscope tip,” *Physical Review B*, vol. 97, no. 11, p. 115452, 2018. 6
- [9] D. Litinski, M. S. Kesselring, J. Eisert, and F. von Oppen, “Combining topological hardware and topological software: Color-code quantum computing with topological superconductor networks,” *Physical Review X*, vol. 7, no. 3, p. 031048, 2017. 6
- [10] Z. Sun, A. Martinez, and F. Wang, “Optical modulators with 2d layered materials,” *Nature Photonics*, vol. 10, no. 4, p. 227238, 2016. 7, 30, 65, 68, 95, 99
- [11] E. S. Light and Optics. (2018, March). [Online]. Available: http://schoolbag.info/physics/physics_math/45.html 7
- [12] B. E. Saleh and M. C. Teich, *Fundamentals of Photonics*, 2nd ed., 2007. 10
- [13] J. C. Maxwell, *A Dynamical Theory of the Electromagnetic Field*. Philosophical Transactions of the Royal Society of London, 1865, vol. 155. 10

- [14] G. T. Reed and A. P. Knights, *Silicon Photonics: an Introduction*. John Wiley & Sons, 2004. [15](#), [16](#), [17](#), [19](#), [20](#), [21](#), [22](#)
- [15] G. T. Reed, *Silicon Photonics: the State of the Art*. John Wiley & Sons, 2008. [15](#), [23](#)
- [16] S. Sze, *VLSI Technology*, 2nd ed. McGraw-Hill, 1988, vol. 988. [17](#)
- [17] G. Celler and S. Cristoloveanu, “Frontiers of silicon-on-insulator,” *Journal of Applied Physics*, vol. 93, no. 9, pp. 4955–4978, 2003. [17](#)
- [18] B. E. Deal and A. Grove, “General relationship for the thermal oxidation of silicon,” *Journal of Applied Physics*, vol. 36, no. 12, pp. 3770–3778, 1965. [18](#)
- [19] M. J. Madou, “Fundamentals of microfabrication and nanotechnology: Manufacturing techniques for microfabrication and nanotechnology,” *Boca Raton, FL: CRC Press I Llc*, vol. 2, 2011. [19](#)
- [20] M. Liu, X. Yin, E. Ulin-Avila, B. Geng, T. Zentgraf, L. Ju, F. Wang, and X. Zhang, “A graphene-based broadband optical modulator,” *Nature*, vol. 474, no. 7349, pp. 64–67, 2011. [22](#), [26](#), [95](#), [99](#), [100](#), [103](#), [115](#), [117](#), [123](#), [127](#), [153](#), [154](#), [155](#)
- [21] K. Tharmalingam, “Optical absorption in the presence of a uniform field,” *Physical Review*, vol. 130, no. 6, p. 2204, 1963. [22](#)
- [22] D. Marcuse, *Theory of Dielectric Optical Waveguides Second Edition*. Academic Press, London, 1991. [23](#)
- [23] K. Wakita, *Semiconductor Optical Modulators*. Kluwer, USA, 1998. [23](#), [30](#), [31](#), [32](#)
- [24] D. Aspnes, *Properties of Silicon*. INSPEC IEE, London and N.Y., 1988. [23](#)
- [25] H. H. Goldstine, *A History of Numerical Analysis from the 16th through the 19th Century*. Springer Science & Business Media, 2012, vol. 2. [23](#)
- [26] Y.-C. Chang, C.-H. Liu, C.-H. Liu, Z. Zhong, and T. B. Norris, “Extracting the complex optical conductivity of mono- and bilayer graphene by ellipsometry,” *Applied Physics Letters*, vol. 104, no. 26, p. 261909, 2014. [26](#), [85](#), [88](#), [90](#)
- [27] T. Stauber, N. Peres, and A. Geim, “Optical conductivity of graphene in the visible region of the spectrum,” *Physical Review B*, vol. 78, no. 8, p. 085432, 2008. [26](#), [84](#), [85](#), [90](#)
- [28] M.-S. Kwon, “Discussion of the epsilon-near-zero effect of graphene in a horizontal slot waveguide,” *IEEE Photonics Journal*, vol. 6, no. 3, pp. 1–9, 2014. [26](#), [85](#), [90](#), [92](#), [94](#), [103](#), [154](#)
- [29] Z. Lu and W. Zhao, “Nanoscale electro-optic modulators based on graphene-slot waveguides,” *Journal of the Optical Society of America B*, vol. 29, no. 6, pp. 1490–1496, 2012. [26](#), [68](#), [85](#), [89](#), [90](#), [91](#), [94](#), [103](#), [109](#), [110](#), [111](#), [112](#), [113](#), [114](#), [115](#), [116](#), [118](#), [123](#), [137](#), [153](#), [154](#), [155](#)
- [30] D. Hondros and P. Debye, “Elektromagnetische wellen an dielektrischen drahnten,” *Annalen der Physik*, vol. 337, no. 8, pp. 465–476, 1910. [28](#)
- [31] R. N. Hall, G. E. Fenner, J. Kingsley, T. Soltys, and R. Carlson, “Coherent light emission from GaAs junctions,” *Physical Review Letters*, vol. 9, no. 9, p. 366, 1962. [28](#)
- [32] M. I. Nathan, W. P. Dumke, G. Burns, F. H. Dill Jr, and G. Lasher, “Stimulated emission of radiation from GaAs p–n junctions,” *Applied Physics Letters*, vol. 1, no. 3, pp. 62–64, 1962. [28](#)
- [33] T. M. Quist, R. H. Rediker, R. Keyes, W. Krag, B. Lax, A. L. McWhorter, and H. Zeigler, “Semiconductor maser of GaAs,” *Applied Physics Letters*, vol. 1, no. 4, pp. 91–92, 1962. [28](#)

- [34] A. Yariv and R. Leite, "Dielectric-waveguide mode of light propagation in p–n junctions," *Applied Physics Letters*, vol. 2, no. 3, pp. 55–57, 1963. [28](#)
- [35] W. Bond, B. Cohen, R. Leite, and A. Yariv, "Observation of the dielectric-waveguide mode of light propagation in p–n junctions," *Applied Physics Letters*, vol. 2, no. 3, pp. 57–59, 1963. [28](#)
- [36] I. Hayashi, M. Panish, and P. Foy, "A low-threshold room-temperature injection laser," *IEEE Journal of Quantum Electronics*, vol. 5, no. 4, pp. 211–212, 1969. [28](#)
- [37] D. Nelson and F. Reinhart, "Light modulation by the electro-optic effect in reverse-biased gap p–n junctions," *Applied Physics Letters*, vol. 5, no. 7, pp. 148–150, 1964. [28](#)
- [38] M. J. Adams, *An Introduction to Optical Waveguides*. Wiley New York, 1981, vol. 14. [29](#), [35](#)
- [39] P. M. Mathews and K. Venkatesan, *A Textbook of Quantum Mechanics*, 2nd ed. Tata McGraw-Hill Education, 2010. [30](#)
- [40] R. A. Soref, J. Schmidtchen, and K. Petermann, "Large single-mode rib waveguides in gesi-si and si-on-sio/sub 2," *IEEE Journal of Quantum Electronics*, vol. 27, no. 8, pp. 1971–1974, 1991. [35](#), [121](#)
- [41] J. Pendry, "Playing tricks with light," *Science*, vol. 285, no. 5434, pp. 1687–1688, 1999. [37](#)
- [42] A. Christ, S. Tikhodeev, N. Gippius, J. Kuhl, and H. Giessen, "Waveguide-plasmon polaritons: strong coupling of photonic and electronic resonances in a metallic photonic crystal slab," *Physical Review Letters*, vol. 91, no. 18, p. 183901, 2003. [37](#)
- [43] M. Koshiba, "Optical waveguide theory by the finite element method," 1992. [41](#)
- [44] R. G. Hunsperger, *Integrated Optics: Theory and Technology*, 2nd ed. Springer-Verlag Berlin, 1984, vol. 33. [42](#)
- [45] B. M. A. Rahman and A. Agrawal, *Finite Element Modeling Methods for Photonics*. Artech House, 2013. [43](#), [45](#), [46](#), [49](#), [101](#), [122](#), [154](#)
- [46] B. M. A. Rahman and J. Davies, "Penalty function improvement of waveguide solution by finite elements," *IEEE Transactions on Microwave Theory and Techniques*, vol. 32, no. 8, pp. 922–928, 1984. [43](#), [44](#), [45](#), [56](#)
- [47] —, "Finite-element solution of integrated optical waveguides," *Journal of Lightwave Technology*, vol. 2, no. 5, pp. 682–688, 1984. [43](#), [44](#), [45](#), [101](#)
- [48] W. English and F. Young, "An e vector variational formulation of the maxwell equations for cylindrical waveguide problems," *IEEE Transactions on Microwave Theory and Techniques*, vol. 19, no. 1, pp. 40–46, 1971. [43](#), [56](#)
- [49] K. Ferdinand, "Finite element study of the second order non-linear process of second harmonic generation in optical waveguides," Ph.D. dissertation, City, University of London, 2000. [43](#), [46](#), [48](#)
- [50] P. Silvester, "A general high-order finite-element analysis program waveguide," *IEEE Transactions on Microwave Theory and Techniques*, vol. 21, pp. 538–542, 1969. [44](#)
- [51] K. Hayata, M. Koshiba, M. Eguchi, and M. Suzuki, "Vectorial finite-element method without any spurious solutions for dielectric waveguiding problems using transverse magnetic-field component," *IEEE Transactions on Microwave Theory and Techniques*, vol. 34, no. 11, pp. 1120–1124, 1986. [44](#)

- [52] N. Mabaya and P. Lagasse, "Finite element analysis of optical waveguides." IEEE, 1981. 44
- [53] B. M. A. Rahman, M. Rajarajan, T. Wongcharoen, F. A. Katsriku, C. Themistos, P. Buah, M. Meyer, and K. T. Grattan, "Rigorous characterization of photonic devices using the finite element method," in *International Conference on Fiber Optics and Photonics: Selected Papers from Photonics India'98*, vol. 3666. International Society for Optics and Photonics, 1999, pp. 160–170. 45
- [54] B. M. A. Rahman, A. S. Kabir, M. Rajarajan, and K. T. Grattan, "Finite element modal solutions of planar photonic crystal fibers with rectangular air-holes," *Optical and Quantum Electronics*, vol. 37, no. 1–3, pp. 171–183, 2005. 45
- [55] B. M. A. Rahman, T. Wongcharoen, C. Themistos, R. Abdallah, A. Kabir, E. Ladele, N. So-masiri, M. Alam, M. Rajarajan, and K. Grattan, "Finite element characterisation of pho-tonic devices for optical communications," *IEE Proceedings-Circuits, Devices and Systems*, vol. 152, no. 5, pp. 532–538, 2005. 45
- [56] S. C. Brenner and L. Scott, *The Mathematical Theory of Finite Element Methods*. Springer-Verlag, New York, 1994. 46, 47
- [57] G. T. Reed, G. Mashanovich, F. Y. Gardes, and D. Thomson, "Silicon optical modulators," *Nature Photonics*, vol. 4, no. 8, pp. 518–526, 2010. 64
- [58] R. W. Keyes, "Power dissipation in information processing," *Science*, vol. 168, no. 3933, pp. 796–801, 1970. 64
- [59] K. Kao and G. A. Hockham, "Dielectric-fibre surface waveguides for optical frequencies," in *Proceedings of the Institution of Electrical Engineers*, vol. 113, no. 7. IET, 1966, pp. 1151–1158. 64
- [60] H. K. P. University. (2018, June) Optical communications and networking. [Online]. Available: www.alanptlau.com/Research.html 65
- [61] A. C. Ferrari, F. Bonaccorso, V. Fal'Ko, K. S. Novoselov, S. Roche, P. Bøggild, S. Borini, F. H. Koppens, V. Palermo, N. Pugno *et al.*, "Science and technology roadmap for graphene, related two-dimensional crystals, and hybrid systems," *Nanoscale*, vol. 7, no. 11, pp. 4598–4810, 2015. 65
- [62] P. R. Wallace, "The band theory of graphite," *Physical Review*, vol. 71, no. 9, p. 622, 1947. 66
- [63] H. P. Boehm, R. Setton, and E. Stumpp, "Nomenclature and terminology of graphite inter-calation compounds (iupac recommendations 1994)," *Pure and Applied Chemistry*, vol. 66, no. 9, pp. 1893–1901, 1994. 66
- [64] T. R. S. A. of Science. (2010). [Online]. Available: www.nobelprize.org/nobel~prizes/physics/laureates/2010/sciback~phy~10~2.pdf 66, 70
- [65] Q.-L. Yan, M. Gozin, F.-Q. Zhao, A. Cohen, and S.-P. Pang, "Highly energetic compositions based on functionalized carbon nanomaterials," *Nanoscale*, vol. 8, no. 9, pp. 4799–4851, 2016. 67
- [66] A. Saboori, S. K. Moheimani, M. Dadkhah, M. Pavese, C. Badini, and P. Fino, "An overview of key challenges in the fabrication of metal matrix nanocomposites reinforced by graphene nanoplatelets," *Metals*, vol. 8, no. 3, p. 172, 2018. 67
- [67] A. Geim and K. Novoselov, "The rise of graphene," *Nature Materials*, vol. 6, no. 3, p. 183, 2007. 67, 68, 76, 153

- [68] P. Nemes-Incze, Z. Osváth, K. Kamarás, and L. Biró, “Anomalies in thickness measurements of graphene and few layer graphite crystals by tapping mode atomic force microscopy,” *Carbon*, vol. 46, no. 11, pp. 1435–1442, 2008. 68, 74, 89, 93, 138, 153
- [69] A. F. Morpurgo, “Ten years of nature physics: The abc of 2d materials,” *Nature Physics*, vol. 11, no. 8, p. 625, 2015. 68, 75
- [70] C. J. Shearer, A. D. Slattery, A. J. Stapleton, J. G. Shapter, and C. T. Gibson, “Accurate thickness measurement of graphene,” *Nanotechnology*, vol. 27, no. 12, p. 125704, 2016. 68
- [71] K. W. Urban, “Electron microscopy: The challenges of graphene,” *Nature Materials*, vol. 10, no. 3, pp. 165–166, 2011. 69
- [72] M. University. (2018) Advanced quantum mechanics 2. [Online]. Available: <https://oer.physics.manchester.ac.uk/AQM2/Notes/Notes-6.4.html> 69
- [73] J.-N. Fuchs and M. O. Goerbig, “Introduction to the physical properties of graphene,” *Lecture notes*, 2008. 69, 70, 72, 74, 76
- [74] A. C. Neto, F. Guinea, N. M. Peres, K. S. Novoselov, and A. K. Geim, “The electronic properties of graphene,” *Reviews of Modern Physics*, vol. 81, no. 1, p. 109, 2009. 70, 71, 74
- [75] NanoSmiths. (2018). [Online]. Available: <https://pt.slideshare.net/landsmiths/nanotechnology1-58374363?smtNoRedir=1> 70
- [76] X. Luo, T. Qiu, W. Lu, and Z. Ni, “Plasmons in graphene: recent progress and applications,” *Materials Science and Engineering: R: Reports*, vol. 74, no. 11, pp. 351–376, 2013. 70
- [77] Z. Ni, H. Wang, J. Kasim, H. Fan, T. Yu, Y. Wu, Y. Feng, and Z. Shen, “Graphene thickness determination using reflection and contrast spectroscopy,” *Nano Letters*, vol. 7, no. 9, pp. 2758–2763, 2007. 71, 90
- [78] B. Shevitski, “Structural properties of graphene and carbon nanotubes,” *Procedia IUTAM*, vol. 28, pp. 1–8, 2010. 71, 73
- [79] J. B. Oostinga, H. B. Heersche, X. Liu, A. F. Morpurgo, and L. M. Vandersypen, “Gate-induced insulating state in bilayer graphene devices,” *Nature Materials*, vol. 7, no. 2, pp. 151–157, 2008. 74
- [80] C. H. Lui, Z. Li, K. F. Mak, E. Cappelluti, and T. F. Heinz, “Observation of an electrically tunable band gap in trilayer graphene,” *Nature Physics*, vol. 7, no. 12, p. 944, 2011. 75
- [81] W. Bao, L. Jing, J. Velasco Jr, Y. Lee, G. Liu, D. Tran, B. Standley, M. Aykol, S. Cronin, D. Smirnov *et al.*, “Stacking-dependent band gap and quantum transport in trilayer graphene,” *Nature Physics*, vol. 7, no. 12, pp. 948–952, 2011. 75, 137, 147
- [82] L. Zhang, Y. Zhang, J. Camacho, M. Khodas, and I. Zaliznyak, “The experimental observation of quantum hall effect of $l=3$ chiral quasiparticles in trilayer graphene,” *Nature Physics*, vol. 7, no. 12, pp. 953–957, 2011. 75, 137, 147
- [83] M. Craciun, S. Russo, M. Yamamoto, J. B. Oostinga, A. Morpurgo, and S. Tarucha, “Trilayer graphene is a semimetal with a gate-tunable band overlap,” *Nature Nanotechnology*, vol. 4, no. 6, pp. 383–388, 2009. 75
- [84] B. Partoens and F. Peeters, “From graphene to graphite: Electronic structure around the k point,” *Physical Review B*, vol. 74, no. 7, p. 075404, 2006. 76
- [85] T. Ando, “The electronic properties of graphene and carbon nanotubes,” *NPG Asia Materials*, vol. 1, no. 1, pp. 17–21, 2009. 80

- [86] D. Fathi, “A review of electronic band structure of graphene and carbon nanotubes using tight binding,” *Journal of Nanotechnology*, vol. 2011, 2011. 80
- [87] R. R. Nair, P. Blake, A. N. Grigorenko, K. S. Novoselov, T. J. Booth, T. Stauber, N. M. Peres, and A. K. Geim, “Fine structure constant defines visual transparency of graphene,” *Science*, vol. 320, no. 5881, p. 1308, 2008. 81, 95, 137
- [88] M. Gulde, S. Schweda, G. Storeck, M. Maiti, H. K. Yu, A. M. Wodtke, S. Schäfer, and C. Ropers, “Ultrafast low-energy electron diffraction in transmission resolves polymer/graphene superstructure dynamics,” *Science*, vol. 345, no. 6193, pp. 200–204, 2014. 81
- [89] A. Grigorenko, M. Polini, and K. Novoselov, “Graphene plasmonics,” *Nature Photonics*, vol. 6, no. 11, p. 749, 2012. 82, 118
- [90] K. Novoselov, A. Geim, S. Morozov, D. Jiang, M. Katsnelson, I. Grigorieva, S. Dubonos, and A. Firsov, “Two-dimensional gas of massless dirac fermions in graphene,” *Nature*, vol. 438, no. 7065, pp. 197–200, 2005. 82, 131
- [91] Q. Bao and K. P. Loh, “Graphene photonics, plasmonics, and broadband optoelectronic devices,” *ACS Nano*, vol. 6, no. 5, pp. 3677–3694, 2012. 82, 83
- [92] Y. Zhang, Y.-W. Tan, H. L. Stormer, and P. Kim, “Experimental observation of the quantum hall effect and berry’s phase in graphene,” *Nature*, vol. 438, no. 7065, pp. 201–204, 2005. 82
- [93] L. M. Malard, K. F. Mak, A. C. Neto, N. Peres, and T. F. Heinz, “Observation of intra-and inter-band transitions in the transient optical response of graphene,” *New Journal of Physics*, vol. 15, no. 1, p. 015009, 2013. 83
- [94] V. Gusynin and S. Sharapov, “Transport of dirac quasiparticles in graphene: Hall and optical conductivities,” *Physical Review B*, vol. 73, no. 24, p. 245411, 2006. 83, 85, 90
- [95] S. Luo, Y. Wang, X. Tong, and Z. Wang, “Graphene-based optical modulators,” *Nanoscale Research Letters*, vol. 10, no. 1, p. 199, 2015. 83
- [96] A. Phatak, Z. Cheng, C. Qin, and K. Goda, “Design of electro-optic modulators based on graphene-on-silicon slot waveguides,” *Optics Letters*, vol. 41, no. 11, pp. 2501–2504, 2016. 83, 118, 123, 130, 146, 148, 149
- [97] Hitoshi-Berkeley. (2018) Lecture notes, 221A, Landau levels. [Online]. Available: www.hitoshi.berkeley.edu/221a/landau.pdf 84
- [98] L.-J. Yin, K.-K. Bai, W.-X. Wang, S.-Y. Li, Y. Zhang, and L. He, “Landau quantization of dirac fermions in graphene and its multilayers,” *Frontiers of Physics*, vol. 12, no. 4, p. 127208, 2017. 84
- [99] Z. Jiang, E. A. Henriksen, L. Tung, Y.-J. Wang, M. Schwartz, M. Y. Han, P. Kim, and H. L. Stormer, “Infrared spectroscopy of landau levels of graphene,” *Physical Review Letters*, vol. 98, no. 19, p. 197403, 2007. 84
- [100] K. F. Mak, M. Y. Sfeir, Y. Wu, C. H. Lui, J. A. Misewich, and T. F. Heinz, “Measurement of the optical conductivity of graphene,” *Physical Review Letters*, vol. 101, no. 19, p. 196405, 2008. 85
- [101] M.-C. Chang. (2013) Chap 3 Linear response theory. [Online]. Available: https://phy.ntnu.edu.tw/~changmc/Teach/SM/ch03_.pdf 85
- [102] T. Fang, A. Konar, H. Xing, and D. Jena, “Carrier statistics and quantum capacitance of graphene sheets and ribbons,” *Applied Physics Letters*, vol. 91, no. 9, p. 092109, 2007. 87, 88

- [103] X. Hu and J. Wang, "Ultrabroadband compact graphene–silicon tm-pass polarizer," *IEEE Photonics Journal*, vol. 9, no. 2, pp. 1–10, 2017. [89](#), [118](#), [128](#), [133](#), [136](#), [149](#)
- [104] A. Vakil and N. Engheta, "Transformation optics using graphene," *Science*, vol. 332, no. 6035, pp. 1291–1294, 2011. [89](#)
- [105] J.-S. Shin and J. T. Kim, "Broadband silicon optical modulator using a graphene-integrated hybrid plasmonic waveguide," *Nanotechnology*, vol. 26, no. 36, p. 365201, 2015. [89](#), [145](#)
- [106] B. Sensale-Rodriguez, R. Yan, M. M. Kelly, T. Fang, K. Tahy, W. S. Hwang, D. Jena, L. Liu, and H. G. Xing, "Broadband graphene terahertz modulators enabled by intraband transitions," *Nature Communications*, vol. 3, p. 780, 2012. [95](#)
- [107] D. Pines, "Collective energy losses in solids," *Reviews of Modern Physics*, vol. 28, no. 3, p. 184, 1956. [98](#)
- [108] S. Ghosh and B. M. A. Rahman, "Evolution of plasmonic modes in a metal nano-wire studied by a modified finite element method," *Journal of Lightwave Technology*, vol. 36, no. 3, pp. 809–818, 2018. [98](#)
- [109] E. L. Wooten, K. M. Kissa, A. Yi-Yan, E. J. Murphy, D. A. Lafaw, P. F. Hallemeier, D. Maack, D. V. Attanasio, D. J. Fritz, G. J. McBrien *et al.*, "A review of lithium niobate modulators for fiber-optic communications systems," *IEEE Journal of Selected Topics in Quantum Electronics*, vol. 6, no. 1, pp. 69–82, 2000. [100](#)
- [110] P. Avouris, T. F. Heinz, and T. Low, *2D Materials*. Cambridge University Press, 2017. [101](#)
- [111] Z. Li, E. A. Henriksen, Z. Jiang, Z. Hao, M. C. Martin, P. Kim, H. Stormer, and D. N. Basov, "Dirac charge dynamics in graphene by infrared spectroscopy," *Nature Physics*, vol. 4, no. 7, pp. 532–535, 2008. [102](#)
- [112] Z. Fei, A. Rodin, G. Andreev, W. Bao, A. McLeod, M. Wagner, L. Zhang, Z. Zhao, M. Thiemens, G. Dominguez *et al.*, "Gate-tuning of graphene plasmons revealed by infrared nano-imaging," *Nature*, vol. 487, no. 7405, pp. 82–85, 2012. [102](#)
- [113] S. O. Koswatta, A. Valdes-Garcia, M. B. Steiner, Y.-M. Lin, and P. Avouris, "Ultimate rf performance potential of carbon electronics," *IEEE Transactions on Microwave Theory and Techniques*, vol. 59, no. 10, pp. 2739–2750, 2011. [108](#)
- [114] M. Liu, X. Yin, and X. Zhang, "Double-layer graphene optical modulator," *Nano Letters*, vol. 12, no. 3, pp. 1482–1485, 2012. [116](#), [117](#), [118](#), [123](#), [127](#), [128](#), [133](#), [144](#), [145](#), [146](#), [147](#), [149](#), [153](#)
- [115] S. J. Koester, H. Li, and M. Li, "Switching energy limits of waveguide-coupled graphene-on-graphene optical modulators," *Optics Express*, vol. 20, no. 18, pp. 20 330–20 341, 2012. [118](#), [149](#)
- [116] S. Luo, Y. Wang, X. Tong, and Z. Wang, "Graphene-based optical modulators," *Nanoscale Research Letters*, vol. 10, no. 1, p. 199, 2015. [137](#)
- [117] H. Aoki and M. S. Dresselhaus, *Physics of Graphene*. Springer Science & Business Media, 2013. [137](#)
- [118] M.-Y. Ni and K. Wakabayashi, "Stacking sequence dependence of electronic properties in double-layer graphene heterostructures," *Japanese Journal of Applied Physics*, vol. 53, no. 6S, p. 06JD03, 2014. [137](#)

- [119] C.-J. Shih, A. Vijayaraghavan, R. Krishnan, R. Sharma, J.-H. Han, M.-H. Ham, Z. Jin, S. Lin, G. L. Paulus, N. F. Reuel *et al.*, “Bi-and trilayer graphene solutions,” *Nature Nanotechnology*, vol. 6, no. 7, pp. 439–445, 2011. [137](#), [144](#), [152](#)
- [120] B.-R. Wu, “Field modulation of the electronic structure of trilayer graphene,” *Applied Physics Letters*, vol. 98, no. 26, p. 263107, 2011. [137](#), [147](#), [152](#)
- [121] Z. Sun, A.-R. O. Raji, Y. Zhu, C. Xiang, Z. Yan, C. Kittrell, E. Samuel, and J. M. Tour, “Large-area bernal-stacked bi-, tri-, and tetralayer graphene,” *ACS Nano*, vol. 6, no. 11, pp. 9790–9796, 2012. [137](#)
- [122] M. Fan, H. Yang, P. Zheng, G. Hu, B. Yun, and Y. Cui, “Multilayer graphene electro-absorption optical modulator based on double-stripe silicon nitride waveguide,” *Optics Express*, vol. 25, no. 18, pp. 21 619–21 629, 2017. [138](#)
- [123] J.-S. Kim and J. T. Kim, “Silicon electro-absorption modulator based on graphene-hexagonal boron nitride heterostructure,” *Journal of Lightwave Technology*, vol. 34, no. 22, pp. 5293–5299, 2016. [138](#)
- [124] J.-S. Shin and J. T. Kim, “Broadband silicon optical modulator using a graphene-integrated hybrid plasmonic waveguide,” *Nanotechnology*, vol. 26, no. 36, p. 365201, 2015. [138](#)
- [125] K. Tsirka, A. Katsiki, N. Chalmpes, D. Gournis, and A. S. Paipetis, “Mapping of graphene oxide and single layer graphene flakes defects annealing and healing,” *Frontiers in Materials*, vol. 5, no. 37, 2018. [138](#)
- [126] H. Shu, Z. Su, L. Huang, Z. Wu, X. Wang, Z. Zhang, and Z. Zhou, “Significantly high modulation efficiency of compact graphene modulator based on silicon waveguide,” *Scientific Reports*, vol. 8, 2018. [138](#)
- [127] C. Bao, W. Yao, E. Wang, C. Chen, J. Avila, M. C. Asensio, and S. Zhou, “Stacking-dependent electronic structure of trilayer graphene resolved by nanospot angle-resolved photoemission spectroscopy,” *Nano Letters*, vol. 17, no. 3, pp. 1564–1568, 2017. [142](#)
- [128] D. Ansell, I. Radko, Z. Han, F. Rodriguez, S. Bozhevolnyi, and A. Grigorenko, “Hybrid graphene plasmonic waveguide modulators,” *Nature Communications*, vol. 6, p. 8846, 2015. [143](#), [145](#), [151](#), [152](#)
- [129] D. Aznakayeva, F. Rodriguez, O. Marshall, and A. Grigorenko, “Graphene light modulators working at near-infrared wavelengths,” *Optics Express*, vol. 25, no. 9, pp. 10 255–10 260, 2017. [143](#), [146](#), [148](#)
- [130] K. Sugawara, N. Yamamura, K. Matsuda, W. Norimatsu, M. Kusunoki, T. Sato, and T. Takahashi, “Selective fabrication of free-standing aba and abc trilayer graphene with/without dirac-cone energy bands,” *NPG Asia Materials*, vol. 10, no. 2, p. e466, 2018. [144](#), [152](#)
- [131] Y. Miyata, E. Maeda, K. Kamon, R. Kitaura, Y. Sasaki, S. Suzuki, and H. Shinohara, “Fabrication and characterization of graphene/hexagonal boron nitride hybrid sheets,” *Applied Physics Express*, vol. 5, no. 8, p. 085102, 2012. [144](#), [152](#)
- [132] K. Kim, J.-Y. Choi, T. Kim, S.-H. Cho, and H.-J. Chung, “A role for graphene in silicon-based semiconductor devices,” *Nature*, vol. 479, no. 7373, pp. 338–344, 2011. [145](#)